The Tides in a general circulation model in the Indonesian Seas

Dwiyoga Nugroho

To cite this version:

Dwiyoga Nugroho. The Tides in a general circulation model in the Indonesian Seas . Ocean, Atmosphere. Universite Toulouse 3 Paul Sabatier (UT3 Paul Sabatier), 2017. English. NNT : . tel-01556796v2

HAL Id: tel-01556796

https://theses.hal.science/tel-01556796v2

Submitted on 7 Jul 2017

THÈSE

En vue de l'obtention du

DOCTORAT DE L'UNIVERSITÉ DE TOULOUSE

Délivré par : *l'Université Toulouse 3 Paul Sabatier (UT3 Paul Sabatier)*

Présentée et soutenue le *30/06/2017* **par :**

Dwiyoga NUGROHO

La marée dans un modèle de circulation générale dans les mers Indonésiennes

JURY

ISABELLE DADOU	Présidente	Professeur-Université Paul Sabatier,FRANCE
ERIC CHASSIGNET	Rapporteur	Professeur-Florida State University,USA
JANET SPRINTALL	Rapporteur	Senior scientist-Scripps-UC San Diego,USA
BRIAN ARBIC	Examinateur	Professeur associé-Michigan State University,USA
AGUS ATMADIPOERA	Examinateur	Maître de conférence-Bogor Agricultural University,INDONESIA
ARIANE KOCH-LARROUY	Directrice de Thése	LEGOS-IRD,FRANCE
FLORENT LYARD	Co-Directeur de Thése	LEGOS-IRD,FRANCE
PHILIPPE GASPAR	Co-Directeur de Thése	CLS,FRANCE

École doctorale et spécialité :

SDU2E : Océan, Atmosphère, Climat

Unité de Recherche :

Laboratoire d'Etudes en Géophysique et Océanographie Spatiales (UMR5566)

Acknowledgments

Alhamdulillahirabbil alamiin..... The work presented in this thesis was a huge collaborative effort from Ministry of Marine Affairs and Fisheries-Indonesia (MMAF), Institut Français Indonesia, Collecte Localisation Satellites(CLS)-France, Laboratoire d'Etudes en Géophysique et Océanographie Spatiales(LEGOS)-France, MERCATOR Ocean-France and University of Paul Sabatier-France. As a result of the large number of contributing parties, I apologize for to those whose names may be unintentionally omitted.

My sincerest gratitude goes to my advisors, first to my major advisor Dr.Ariane Koch-Larrouy for her patience and encouragement to achieve my best and for guiding me through the research presented in this thesis. Secondly, thanks to Dr.Florent Lyard as my second advisor, his insight, his beyond text book numerical skills have continuously inspired me. Thirdly thanks to Dr.Philippe Gaspar for his encouragement and support throughout my PhD study.

I would like to express the deepest appreciation to Mr. Berny Achmad Subki, Dr.Aryo Hanggono, Dr.Aulia Riza, Mrs.Yenung Secasari, Prof Dietrich Bengen(IPB), Prof Ita Widowati(UNDIP), Dr.Vincent Siregar(IPB) for all their support during the INDESO scholarship program. Appreciation is further extended to my colleagues at Agency for Marine Research and Fisheries (BALITBANG-KP) specially to Teja Arief, Elvan Ampou, Marza Ihsan, Nurazmi Ratna, Rinny Rahmania, Niken Gusmawati, Budi Gunadharma, Romy Adrianto, Indra Hermawan, Iis Triyulianti, Dendy Mahabror, Falia Maunantia, Bambang Adithya, Nurman Mbay, Pak Usep Nasrudin, Pak Imam, Pak Dono, Mba Titi Lestari and Mas Hilman Ramadhan.

I am especially grateful to my jury and reviewer members, Thanks to Prof. Eric Chassignet, Dr.Janet Sprintall as my thesis reviewer for their careful review of my manuscript, and for the comments, corrections and suggestions that ensued. Thanks to Prof Isabelle Dadou, Prof Brian Arbic and Dr.Agus Sholeh Atmadipoera for assisting me during my thesis defense.

The most important part of my time at LEGOS,CLS and MERCATOR has been knowing such an incredible group of scientist and administrative team. I feel very fortunate to have been part of them and would like to thank to Sara Fleury(LEGOS), Florence Bouille(CLS), Benoît Tranchant(CLS), Jerome Chanut(Mercator),Guillaume Reffray(Mercator), Rachid Benshila (LEGOS), Damien Allain(LEGOS), Julien Jouanno (LEGOS), the ECOLA research team (LEGOS), GESSEC LEGOS(Martine Mena, Nadine Lacroux, Brigite Cournou Agathe Barithaud) and the head of LEGOS Dr.Alexandre Ganachaud. And thanks to my friends in LEGOS: Marine Bretagnon, Cory Pegliasco, Kevin Gueriero, Marine Rogé, Michel Tchilibou, Dac Nguyen, for your friendship and surprise gift after my defense.

I would like also to thank each of those who touched my life, making Toulouse as a such a wonderful home for me. ”Terima kasih” to PPI Toulouse (Indonesian Student Association in Toulouse) and Ibu Ninik, Ibu Yunah, Ibu Bintang from AAI(Franco-Indonesian Association).

A special thanks to my lovely pretty wife, Munky Andi Kasim, my adorable daughters Azkanayra Zaida Nugroho and Azraina Zahira Nugroho for your warm hugs and kiss everyday and also my brother,my brother in-law, my sister and my sister in-law.

Finally, I dedicate this thesis to my parents Rachmat Musa and Titiek Lasmiyati and my parents in-law Nash Andi Kasim and Jenny Loenggana. I can never thank them enough for all that they have given me .....Thank you.

Abstract

In the Indonesian seas, large tidal currents interact with the rough topography and create strong internal waves at the tidal frequency, called internal tides. Part of them will eventually propagate and dissipate far away from generation sites. Their associated mixing upwells cold and nutrient-rich water that prove to be critical for climate system and for marine resources. This thesis uses the physical ocean general circulation model, NEMO, as part of the INDESO project that aims at monitoring the Indonesian marine living resources. Models not taking into account tidal missing are unable to correctly reproduce the vertical structure of watermasses in Indonesian seas. However, taking into account this mixing is no simple task as the phenomena involved in tidal mixing cover a wide spectrum of spatial scales. Internal tides indeed propagate over thousands of kilometres while dissipation and mixing occurs at centimetric to millimetric scales. A model capable of resolving all these processes at the same time does not exist. Until now scientists either parameterised the tidal mixing or used models which only partly resolve internal tides. More and more scientists introduce explicit tidal forcing in their models but without knowing where the energy is going and how the internal tides are dissipated. This thesis intends to quantify energy dissipation in NEMO forced with explicit tidal forcing and compares it to the dissipation induced by the currently used parameterization. This thesis also provides new results about the quantification of the tidal energy budget in NEMO. I first contributed to an INDESO study that aimed at validating the model against several observation data sets. In a second and third study, I investigated the mixing produced in the model by explicit tidal forcing and its impact on water mass. Explicit tides forcing proves to produce a mixing comparable to the one produced by the parameterization. It also produces a significant cooling of 0.3 °C with maxima reaching 0.8°C in the areas of internal tide generation. The cooling is stronger on austral winter. The spring tides and neap tides modulate this impact by 0.1°C to 0.3°C. The model generates 75% of the expected internal tides energy, in good agreement with other previous studies. In the ocean interior, most of it is dissipated by horizontal momentum dissipation (19 GW), while in reality one would expect dissipation through vertical possesses. This value is close to the dissipation induced by the parameterization (16 GW). The mixing is strong over generation sites, and only 20% remains for far field dissipation mainly in the

Banda and Sulawesi Seas. The model and the recent INDOMIX cruise [Koch-Larrouy et al. (2015)], which provided direct estimates of the mixing, are surprisingly in good agreement mainly above straits. However, in regions far away from the energy generation sites where INDOMIX found NO evidence of intensified mixing, the model produces too strong mixing. The bias comes from the lack of specific set up of internal tides in the model. More work is thus needed to improve the modeled dissipation, which is a theme of active research for the scientific community. I dedicated the last part of my thesis to the quantification of tidal energy sinks in NEMO. I first worked on a simple academic case: the COMODO internal tides test case, which analyses the behaviour of a vertically stratified fluid forced by a barotropic flow interacting over an idealized abyssal plain/slope/shelf topography without bottom friction. The results of the finite element T-UGOm hydrodynamic model are compared with those of NEMO. The central issue in calculating tidal energy budget is the separation of barotropic and baroclinic precesses. To this aim we developed an original method based on the projection on vertical modes. At first glance, this method compares well with the classical method of separation using the vertically averaged current. However, when looking into more details at energy budgets, vertical modes allow a cleaner and more realistic separation between barotropic and baroclinic tides. This precision will be very useful for the future SWOT mission. Also this method of separation allows quantification of the energy associated with each mode. This allowed us to identify an important bias in NEMO: The higher the mode is the shorter the NEMO wavelengths become compared to the T-UGOm wavelengths. NEMO also produces a strong numerical mixing that erodes the barotropic tides on the abyssal plain, where there is no bottom friction. The best suspect might be the 2D/3D coupling scheme implied by the NEMO's time splitting. This work pinpoints areas for reflection and investigation to improve how the model takes into account internal tides dissipation. Based on our separation method, work is in progress to better quantify tidal energy budget in the Indonesian Seas.

Keywords : INDESO, internal tides, mixing,NEMO,water masses transformation,normal modes.

Résumé

Les mers Indonésiennes sont le siège de très fort courants de marée qui interagissent avec la topographie pour créer des ondes internes à la fréquence de la marée que l'on appelle marée interne. Certaines d'entres elles, vont se propager et se dissiper loin des sources de génération. Le mélange associé provoque la remontée d'eau plus froide et plus riche en nutriments en surface qui influence le climat tropical et toute la chaine des écosystèmes marins. Surveiller les ressources marines est l'objectif du projet INDESO, dont cette thèse fait partie et qui utilise le modèle physique de circulation générale NEMO. Les modèles qui ne prennent pas en compte le mélange induit par la marée interne ne sont pas capables de reproduire les masses d'eau en Indonésie. Mais prendre en compte ce mélange n'est pas facile. En effet, le résoudre entièrement n'est pas possible car les échelles concernées par les différents processus des ondes internes varient de plusieurs milliers de kilomètres (propagation) à quelques centimètres/millimètres (dissipation). De plus en plus de scientifiques introduisent le forçage de la marée dans leur modèle mais sans savoir où va l'énergie et comment les ondes sont dissipées. Dans cette thèse nous cherchons à proposer des outils et des débuts de réponses pour participer à une meilleure compréhension de la dissipation des ondes internes dans le modèle de circulation générale d'océan NEMO. J'ai, tout d'abord, contribué à une étude d'INDESO sur la validation de NEMO grâce à de nombreux jeu de données. Ensuite, j'ai cherché à quantifier et à qualifier le mélange induit par l'introduction de la marée explicite dans le modèle, ainsi que son impact sur les masses d'eau. La transformation de masses d'eau induite par la marée explicite est comparable à celle produite par la paramétrisation des ondes internes généralement utilisée dans les mers Indonésiennes. Il produit un refroidissement de surface de 0.3°C avec des maxima atteignant 0.8°C au niveau des sites de génération des ondes internes. Le climat et les ressources marines seront certainement sensibles à ces refroidissements survenant à la fréquence de la marée. Le modèle reproduit 75% de l'énergie attendue de génération des ondes internes, en bon accord avec des études précédentes. L'essentiel de la dissipation a lieu horizontalement (19GW), alors que, dans la réalité, on s'attend principalement à une dissipation réalisée grâce à des processus verticaux. Cette valeur est proche de celle induite par la paramétrisation couramment utilisée (16GW). Quant à la structure spatiale, l'énergie se dissipe essentiellement localement, au dessus des sites de génération, et seulement 20% de l'énergie se propage avant d'être dissipée en aval des sites de génération, principalement dans la mer de Banda et la mer du Sulawesi. Le modèle, au dessus des zones de génération, est de façon surprenante en très bon accord avec les mesures in situ de dissipation obtenues lors de la campagne INDOMIX [Koch-Larrouy et al. (2015)]. Par contre, dans les régions distantes des sources de génération, le modèle surestime le mélange par rapport aux observations d'INDOMIX. Ce biais vient principalement du fait qu'il n'y a aucune prise en compte des processus associés à la dissipation des ondes internes dans le modèle. Ce point précis est un thème de recherche actif au sein de la communauté scientifique. Dans la dernière partie de cette thèse j'ai commencé à apporter des éléments de réponse à la quantification des puits d'énergie dans NEMO. J'ai pour cela travaillé avec le cas test COMODO, qui est une section d'un fluide stratifié constituée d'une plaine abyssale, d'un talus et d'un plateau, forcée par la marée et sans friction de fond. Le modèle T-UGOm, un modèle hydrodynamique de marée avec une grille en éléments finis, est comparé au modèle NEMO. Dans ce cadre, nous avons développé une méthode originale pour séparer la marée barotrope de la marée barocline. Elle repose sur la projection en modes normaux. Cette méthode donne, à première vue, des résultats similaires à ceux obtenus grâce à la méthode plus classique de soustraction par la moyenne verticale. Cependant, lorsque l'on regarde plus en détail les diagnostiques d'énergie on trouve que la méthode de projection en modes normaux offre une plus grande précision et un plus grand réalisme pour séparer la marée barotrope de la marée barocline. Cette précision sera très utile pour les futures missions SWOT. Par ailleurs, cette méthode donne accès à la décomposition d'énergie mode par mode et nous a permis d'identifier certains biais. Plus on monte dans des modes élevés plus les longueurs ondes se raccourcissent dans NEMO par rapport à T-UGOm. Par ailleurs, NEMO dissipe la marée barotrope dans la plaine abyssale, alors qu'il n'y a explicitement pas de friction. Ce ne peut pas être la diffusion verticale ou horizontale qui est à l'œuvre ici, car il n'y a pas de raison physique pour une diffusion sur un fond plat. Le meilleur candidat pour expliquer cette diffusion serait le couplage 2D/3D du time splitting de NEMO. Ce travail offre des pistes de recherche nouvelles pour améliorer la prise en compte de la marée dans les modèles de circulation générale. Un travail est en cours pour appliquer cette méthode sur l'ensemble de l'archipel Indonésien.

Mots Clés : INDESO, marée interne, mélange, NEMO, transformation de masses d'eau, modes normaux.

Contents

List of Abbreviations

AFD	Agence Française de Développement
CIS	Central Information System
CLS	Collecte Losalisation Satellites
COMODO	COmmunity MODelling Ocean
ECMWF	European Centre for Medium-Range Weather Forecasts
EEZ	Exclusive Economic Zone
ENSO	El Nino Southern Oscillation
FES	Finite Element Solution
GLS	Generic Length Scale
IA	Indonesian Achipelago
INDESO	Infrastructure Development For Space Oceanography
INDOMIX	The Indonesian Mixing program

INSTANT	International Nusantara Stratification and Transport
ITCZ	Inter Tropical Convergence Zone
ITF	Indonesian Through Flow
IUU	Illegal Unregulated Unreported
LEGOS	Laboratoire d'Études en Géophysique et Océanographie Spatiales
MMAF	Ministry of Marine Affaires and Fisheries
MODIS	Moderate-Resolution Imaging Spectroradiometer
NEMO	Nucleus for European Modeling of the Ocean
NPIW	North Pacific Intermediate Water
NPSW	North Pacific Subtropical Water
OGCM	Ocean General Circulation Model
PISCES	Pelagic Interactions Scheme for Carbon and Ecosystem Studies
PSU	Practical Salinity Unit
SAR	Synthetic Aperture Radar
SCS	South China Seas

SCSTF	South China Seas Through Flow
SEAPODYM	Spatial Ecosystem and Populations Dynamics Model
SEC	South Equatorial Current
SLA	Sea Level Anomaly
SPSW	South Pascific Subtropical Water
SSH	Sea Surface Height
SST	Sea Surface Temperature
SV	Sverdrup
SWOT	Surface Water and Ocean Topography
TUGO	Toulouse Unstructured Grid Ocean Model

Chapter 1

Thesis introduction

1.1 Introduction

1.1.1 The context of the INDESO project

The Indonesia, with its 17000 islands is the largest archipelagic country in the World. Indonesian archipelago lies at the heart of the Coral Triangle and is one of the most important reservoirs of marine biodiversity on the planet [Allen and Werner (2002); Mora et al. (2003)]. 70% of the world coral species is found in this region [Veron et al. (2009)]. The region provides several billion dollars of annual revenue through fisheries, aquaculture and tourism, with fishing and aquaculture employing almost 50 million people. Tuna fisheries are a major economical sector in Indonesia. If sustainably exploited, Indonesian seas represent a most valuable source of profit and employment. The need of monitoring and forcasting is thus vital. Work has to be done to develop sustainable use of the Indonesian marine resources while preventing unsustainable or illegal practices that undermine these resources.

This is the main objective of the INDESO project (2013-2017), funded by the Ministry of Marine Affairs and Fisheries (MMAF) of the Republic of Indonesia. To achieve this goal, INDESO has implemented a “core system” made of 3 components:

1) A satellite receiving station to operationally acquire and process SAR images. These images are used for detecting and deterring IUU fishing activities, and to monitor oil spills.

2) A suite of numerical ocean models NEMO [Madec (2008)] and PISCES [Aumont (2004)], forced by satellite and in-situ data to monitor and forecast the evolution of the ocean circulation and biogeochemistry in the Indonesian EEZ. These models are also used to drive a tuna population dynamics model SEAPODYM [Lehodey et al. (2008)] simulating the evolution of the regional distribution and abundance of skipjack, yellowfin and bigeye tuna.

3) A central information system (CIS) acquiring all data produced by the satellite receiving station, the ocean models, the fish population dynamics models and high-resolution imagery obtained from various commercial satellites.

All data are distributed to authorized users through a Web portal. Based on this core system, INDESO aims at providing indispensable information allowing sustainable use of marine resources in Indonesia. INDESO more specifically focuses on seven key application domains (see figure 1.1): Combating illegal fishing, Managing fish stocks (especially tuna), Monitoring and management of coastal regions and Marine Protected Areas, Monitoring and protection of coral reefs Monitoring and support to shrimp producers and industrial aquaculture, Monitoring and support to seaweed farming, Monitoring and prevention of oil spills.

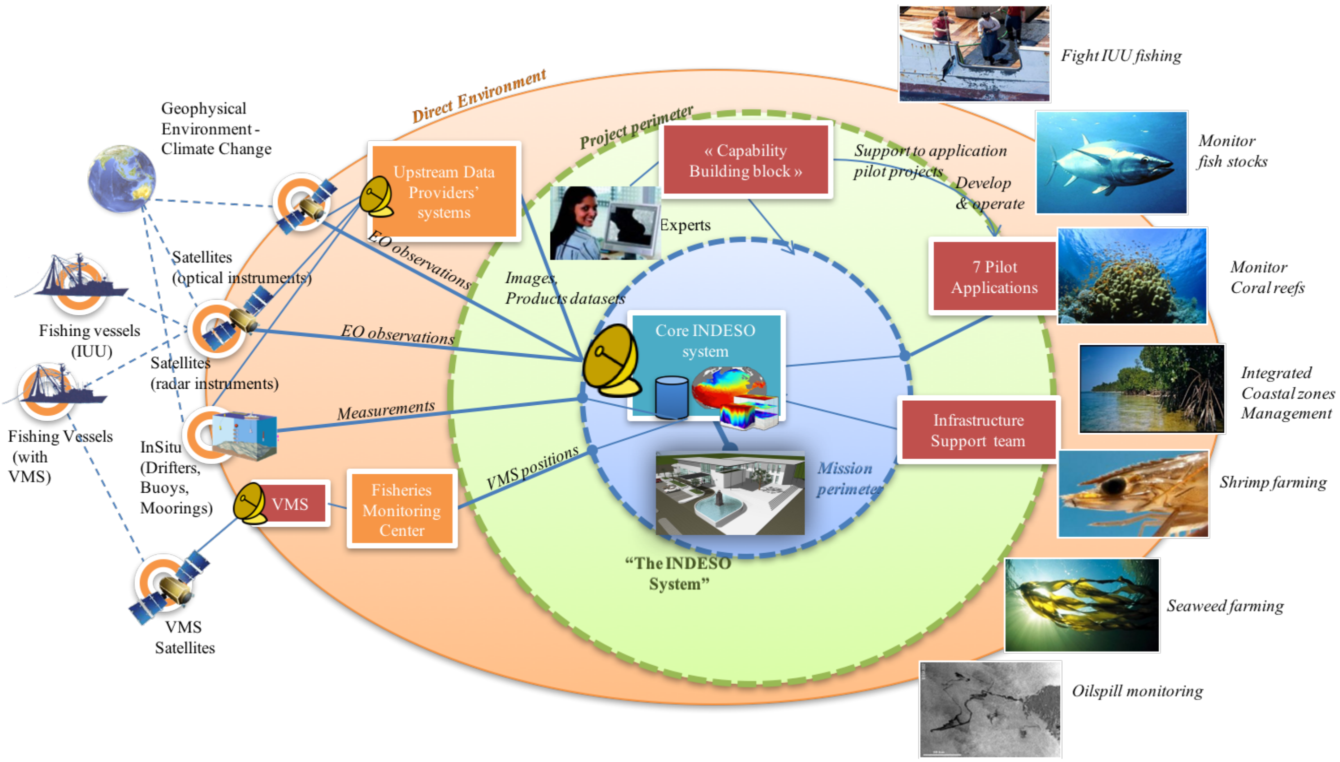

Figure 1.1: The INDESO project "Eye-Concept" and its environment ; Source:www.cls.fr

1.1.2 The context of this thesis

The wind stress and the ocean tides are believed to be the only significant sources of mechanical energy driving the deep ocean mixing necessary to sustain the global overturning circulation [Wunsch and Ferrari (2004)]. The overall tidal energy budget is estimated to be about 3.5 TW. Tidal energy is provided by the astronomic bodies (Earth, Moon and Sun) through gravitational forces work. 2.6 TW of this (mostly barotropic) energy is dissipated through to bottom friction and 0.9 TW are converted into internal tides, which will further dissipate locally or after propagation.

Internal tides generation occurs in the area where barotropic flows interact with strong topographic gradient and create isopycnal heaving at tidal frequency. Barotropic horizontal motions are converted into vertical velocities over the topography. Part of internal tides could dissipate and produce vertical mixing locally just after generation, or later after propagation.

Many studies try to quantify the energy generation of the internal tides. For the global ocean tidal hydrodynamic model with data assimilation [Lyard et al. (2006)] and through inverse calculation using altimeter data [Egbert and Erofeeva (2002)] indicates that 0.7 TW or roughly 25% − 35% of the barotropic M2 tidal energy is converted through internal tides generation. Barotropic hydrodynamical models are not capable to resolve explicitly internal tides, hence energy conversion is parameterized as a wave drag based on bottom topography slope and barotropic currents, acting as a barotropic energy sink [Lyard et al. (2006); Shriver et al. (2012); Buijsman et al. (2015)].

In the recent years, OGCMs have been used to estimate internal tides energy in realistic stratification [Niwa and Hibiya (2001a); Niwa (2004); Lorenzo (2006); Jan et al. (2007, 2008); Carter et al. (2008); Jan and Chen (2009); Zilberman et al. (2009); Arbic et al. (2010); Niwa and Hibiya (2011); Carter et al. (2012); Kang and Fringer (2012a); Muller et al. (2012a); Shang et al. (2015); Nagai and Hibiya (2015)]. In that case, the model explicitly solves internal tides, with more or less accuracy. Indeed, the mechanism of internal tides dissipation is still highly controversial, however it is usually admitted that a great parts of the energy get finally converted into ocean mixing.

The proportion of barotropic tides energy converted into baroclinic tides has been discussed for a long time. Today, the precise quantification of internal tide generation (through energy budget computation) and the fate of internal tide energy remain open questions. This thesis constitutes a contribution to the investigation relative to these questions in the context of the

INDESO project.

The Indonesian archipelago is the only region of the world with strong internal tides generation in a semi-enclosed area. As a result, all of the internal (or baroclinic) tidal energy remains trapped locally inside the archipelago and is available for dissipation. Thus, the archipelago is one of the regions in the World with the largest internal tides generation (10% of the global value). As a results water mass is transformed when entering the archipelago producing colder and fresher thermocline water and saltier and colder surface water [Ffield and Gordon (1996); Hautala et al. (2001); Koch-Larrouy et al. (2007)]. Vertical diffusivity of 1–$2.10^{-4}m^2/s$ have been estimates from observations to be necessary in order to explain the water mass transformation in the archipelago [Ffield and Gordon (1992)].

Recently, the INDOMIX cruise provided direct estimates of internal tides mixing [Koch-Larrouy et al. (2015)] with higher values ($10^{-2}m^2/s$) in the shallow and narrow passage (Ombai Strait and Halmahera portals) in comparison to lower values in the inner Halmahera Sea ($10^{-4}m^2/s$) or further away from generation sites ($10^{-6}m2/s$) in the Banda Sea. This new results show that the mixing induced by internal tides in the Indonesian archipelago is highly heterogeneous in space, with high values above straits and low values further away from generation sites. In addition, it demonstrates that internal tides mixing is also strong at the surface.

Modelling in the region is quite challenging because of the numerous processes acting and the very complex bathymetry. Koch-Larrouy et al. (2007), implemented a tidal parameterization adapted to the specificities of the Indonesian archipelago. Introduced in an Oceanic General Circulation Model (OGCM), this parameterization allows the model to better represent the properties of the water mass evolution in each sub-basin, in good agreement with the observations [Koch-Larrouy et al. (2007)]. It produces heterogeneous vertical diffusivity as large as $10.10^{-4}m^2/s$, with an average of $1.5.10^{-4}m^2/s$. This is in quite good agreement with previous estimates deduced from observations [Ffield and Gordon (1996)]. This suggests that the total energy input provided by the tidal parameterization has the right order of magnitude.

This tidal mixing parameterization also cools the sea surface by 0.5°C in annual average, which reduces the deep convection, and the rain activity (by 20%) [Koch-Larrouy et al. (2007, 2010); Sprintall et al. (2014)]. The impact on biological activity has not yet been studied, but it could be guessed from these results that the vertical mixing would have a significant impact on blooms of phytoplankton by upwelling water richer in nutrients at the surface.

However, this parameterisation was a first step towards taking into account the mixing induced by the internal tides, as in reality, the dissipation may not occurs exclusively locally but some fraction could dissipate in the far field. Also this dissipation may vary in time following the cycles of variability of the surface tides. Such limitations and the increase of resolution encourage scientists to force their Ocean General Circulation Models (OGCMs) by the explicit tidal forcing (eg: in Indonesian seas: [Castruccio et al. (2013); Kartadikaria et al. (2011); Nagai and Hibiya (2015)], in Luzon : [Niwa and Hibiya (2001b); Jan et al. (2008); Wang et al. (2016); Alford et al. (2015)], in Global : [Niwa and Hibiya (2011); Arbic et al. (2012); Simmons et al. (2004); Shriver et al. (2012)]. The resolution of these models is generaly between 1 to 10 km. Niwa and Hibiya (2011) show that using a 9km (1/12°) resolution the model is able to generate only 75% of the internal tides. With a 4km (1/36°) resolution, the model generates 90% of the internal tides. With such relatively coarse resolution the processes involved in the dissipation of the internal tides can't be resolved. However, studies in the Indonesian archipelago [Castruccio et al. (2013); Kartadikaria et al. (2011); Nagai and Hibiya (2015)] show that the addition of explicit tidal forcing produces mixing that improves the water mass, reproducing the homohaline Indonesian Water. The question is how the model is able to create mixing when no specific parameterization is active in the model. Is it done at the correct rate along the lifetime of the internal tides?

In order to respond at these questions we performed simulations with and without tides and calculate the kinetic and potential energy dissipations. Validation of these tidal energy estimates are done using the INDOMIX recent cruise. But these estimates rely on the hypothesis that the physic induced by wind and hydrodynamic forcing is identical with and without tides, which may not be entirely true. Also the need of a precise tidal budget in NEMO is needed. The last part of this thesis work has been achieve in order to provide a method and diagnostics to better quantify the tidal energy budget in NEMO. The results are presented in this manuscript on a simple test case and some work is in progress to apply it over the Indonesian region.

The central issue in calculating tidal energy budget is the separation of barotropic and baroclinic processes, in terms of velocity and pressure. Although intuitive, this issue is nothing but trivial and needs to define precisely the meaning of ”barotropic dynamics” and ”baroclinic dynamics” terms. A universal, precise definition does not exist and still trigger some controversy among researchers. Kelly and Nash (2011) gives a revolutionary comprehension to show the complexities and the importance of barotropic and internal tides separation in order to remove spurious tidal energy budget. His study lead to incertitude of the common methods that has been first introduced by [Baines (1982)] and followed by researchers until now [Niwa and Hibiya

(2001a); Jan et al. (2008); Carter et al. (2008); Kang (2010); Zilberman et al. (2009); Niwa and Hibiya (2011); Jeon et al. (2014); Nagai and Hibiya (2015); Alford et al. (2015); Wang et al. (2016)].

The main objectives of the thesis are thus: Provide quantification of the energy generation, dissipation of the tides in NEMO over the Indonesian region; Establish the impact of the associated dissipation on water mass, surface cooling and its associated variability; Provide knowledge, tools and diagnostics to better describe the energy route of the tidal fields.

This thesis manuscript is organized as follows: Chapter 2 will first review the currentology, and hydrography, as well as the tidal properties of the Indonesian seas. The evaluation on the INDESO physical model is then presented in Chapter 3. Chapter 4 presents results on the effect on explicit tidal forcing on surface properties, while Chapter 5 shows a more detailed study that investigate the energy of generation and dissipation of the tides in the model. Chapter 6 presents the controversy on the tidal energetic calculation. Finally, the conclusions of this thesis are presented in Chapter 7, while a discussion and perspectives to this work are provided in Chapter 8.

1.2 Introduction(in French)

1.2.1 Le contexte du projet INDESO

Avec ses 17 000 îles, l'Indonésie, est le plus grand pays archipélagique du monde. L'archipel indonésien, au coeur du triangle de corail, est un des principaux réservoirs de la biodiversité marine au niveau mondial [Allen and Werner (2002); Mora et al. (2003)]. On y trouve 70% des espèces de corail connues [Veron et al. (2009)]. La pêche et l'aquaculture emploient près de 50 millions de personnes et constituent, avec le tourisme, une source de revenu importante pour l'Indonésie. La pêche thonière, en particulier, est un secteur d'activité majeur. Si elles sont exploitées de façon durables, les mers indonésiennes représentent donc une source de richesse et d'emploi inestimable. Il est donc indispensable de suivre et de prévoir leur évolution afin de pouvoir développer une exploitation durable des ressources marines, tout en contrôlant et en décourageant les activités illégales qui menacent ces ressources. C'est l'objectif principal du projet INDESO (2013-2017), financé par le ministère des Affaires maritimes et des Pêches de la République d'Indonésie. Pour atteindre cet objectif, INDESO a mis en place un "système central" composé de 3 composants:

1) Une station de réception d'images satellitaires permettant d'acquérir et de traiter, de manière opérationnelle, des images SAR. Ces images sont utilisées pour détecter les activités de pêche illégales et les pollutions par hydrocarbures.

2) Une série de modèles numériques d'océan (NEMO [Madec (2008)] et PISCES, [Aumont (2004)], forcés par des observations satellitaires et in situ pour simuler et prévoir l'évolution de la circulation océanique et de la bio-géochimie dans la ZEE indonésienne . Les sorties de ces deux modèles sont également utilisés pour forcer SEAPODYM [Lehodey et al. (2008)], un modèle de dynamique de la population simulant l'évolution de l'abondance et la distribution spatiale des 3 principales espèces de thons exploitées en Indonésie : la bonite, le thon jaune et le thon obèse.

3) Un système d'information central (CIS) qui stocke toutes les données acquises par la station de réception d'images satellitaires ou produites par les différents modèles numériques. Le CIS distribue également ces données aux utilisateurs autorisés grâce à un serveur Web. INDESO vise ainsi à fournir des informations indispensables permettant une utilisation durable des ressources marines en Indonésie. INDESO se concentre plus spécifiquement sur sept domaines d'application clés (voir figure 1.1): Lutte contre la pêche illégale, gestion des stocks de poissons (en particulier le thon), surveillance des régions côtières et des aires marines protégées, surveillance des récifs coralliens, surveillance et support à la crevetticulture et à l'aquaculture industrielle, surveillance et support à l'algoculture, surveillance des pollutions par hydrocarbures.

1.2.2 Le contexte de cette thèse

Le vent et les marées sont les principales sources d'énergie mécanique provoquant le mélange de nécessaire pour maintenir la circulation de retournement globale [Wunsch and Ferrari (2004)]. L'apport global d'énergie par la marée est estimé à environ 3,5 TW. Cette énergie est fournie par les corps astronomiques (Terre, Lune et Soleil) grâce au travail des forces gravitationnelles. 2.6 TW de cette énergie (principalement barotrope) est dissipée par frottement du fond et 0.9 TW sont convertis en marées internes, qui se dissiperont localement ou après propagation. La génération de la marée interne se produit dans les zones où des écoulements barotropes interagissent avec un gradient topographique fort et créent un soulèvement isopycnal à la fréquence des marées. Les mouvements horizontaux barotropes sont convertis en vitesses verticales sur la topographie. Une partie des marées internes peut se dissiper et produire un mélange vertical localement juste après la génération, ou plus tard après la propagation. De nombreuses études tentent de quantifier la génération d'énergie liée aux marées internes. Lyard et al. (2006), avec un modèle hydrodynamique de marée global assimilant des données et Egbert and Erofeeva (2002), avec un calcul inverse utilisant des données altimétriques, estiment que 0,7 TW ou environ 25% à 35% de l'énergie de la composante barotrope de la marée M2 est converti par génération de marée interne. Les modèles hydrodynamiques barotropes n'étant pas capables de résoudre explicitement la marée interne, le transfert d'énergie vers la marée interne y est paramétrée sous forme de frottement de fond lié à la pente du fond et à la vitesse du courant barotrope [Lyard et al. (2006); Shriver et al. (2012); Buijsman et al. (2015)]. Au cours des dernières années, des modèles de circulation générale (OGCM) ont été utilisés pour estimer l'énergie interne des marées dans une stratification réaliste [Niwa and Hibiya (2001a); Niwa (2004); Lorenzo (2006); Jan et al. (2007, 2008); Carter et al. (2008); Jan and Chen (2009); Zilberman et al. (2009); Arbic et al. (2010); Niwa and Hibiya (2011); Carter et al. (2012); Kang and Fringer (2012a); Muller et al. (2012a); Shang et al. (2015); Nagai and Hibiya (2015)]. Dans ce cas, le modèle résout explicitement les marées internes, avec plus ou moins de précision. En effet, le Dans ce cas, le modèle résout explicitement les marées internes, avec plus ou moins de précision. En effet, le mécanisme de la dissipation interne des marées est encore très controversé, mais on admet généralement que qu'une part importante de l'énergie est dissipée par mélange vertical. La proportion de l'énergie des marées barotropes converties en marées baroclines a été discutée depuis longtemps. Aujourd'hui, la quantification précise de la génération de la marée interne et le devenir de l'énergie y associée restent des questions ouvertes. Cette thèse constitue une contribution à l'enquête relative à ces questions dans le cadre du projet INDESO. L'archipel indonésien est la seule région du monde avec une forte génération de marées internes dans une zone semi-fermée. En conséquence, toute l'énergie de marée interne (ou barocline) reste piégée localement à l'intérieur de l'archipel et est disponible pour la dissipation. Ainsi, l'archipel indonésien est l'une des régions du monde avec la plus grande génération de marées internes (10% de la valeur globale). En conséquence, les masses d'eau se transforment en entrant dans l'archipel : les eaux profondes de la thermocline deviennent plus chaudes et moins salées alors que les eaux de surfaces se refroidissent et deviennent plus salées [Ffield and Gordon (1996); Hautala et al. (2001); Koch-Larrouy et al. (2007)]. Il a été estimé qu'une diffusivité verticale de 1 à 2 10-4 m2/s était nécessaire pour expliquer la transformation des masses d'eau dans l'archipel [Ffield and Gordon (1992)]. Récemment, la croisière INDOMIX a fourni des estimations directes du mélange induit par la marée interne [Koch-Larrouy et al. (2015)]. Des valeurs élevées de diffusivité ($10^{-2} m^2/s$) ont été mesurées dans des passages peu profonds et étroits (détroit d'Ombai et Halmahera) et des valeurs faibles ont été observées à l'intérieur de la mer d'Halmahera ($10^{-4}m^2/s$) ou plus loin des sites de production ($10^{-6}m2/s$) dans la mer de Banda. Ces nouveaux résultats montrent que le mélange induit par les marées internes dans l'archipel indonésien est très hétérogène dans l'espace, avec des valeurs élevées au-dessus des détroits et des valeurs faibles plus loin des sites de production. En outre, il démontre que le mélange interne des marées est fort à la surface. La modélisation des mers indonésiennes est très difficile en raison des nombreux processus qui agissent et de la bathymétrie très complexe. Koch-Larrouy et al. (2007) , a mis en place une paramétrisation des marées adaptée aux spécificités de l'archipel indonésien. Introduite dans un OGCM, cette paramétrisation permet au modèle de mieux représenter l'évolution des propriétés de de la masse d'eau dans chaque sous-bassin, en accord avec les observations [Koch-Larrouy et al. (2007)]. Cette paramétrisation produit une diffusivité verticale hétérogène atteignant $10.10^{-4}m^2/s$, avec une moyenne de $1.5.10^{-4}m^2/s$. Cela suggère que l'apport énergétique total fourni par la paramétrisation des marées a le bon ordre de grandeur. Cette paramétrisation du mélange des marées refroidit également la surface de la mer de 0,5 ° C en moyenne annuelle, ce qui réduit la convection profonde et la pluviosité (de -20%) [Koch-Larrouy et al. (2007); Sprintall et al. (2014)]. L'impact sur l'activité biologique n'a pas encore été étudié, mais on peut penser que le mélange vertical aurait un impact significatif sur les blooms de phytoplancton grâce à l'apport en surface d'eaux profondes riches en nutriments. Cependant, cette paramétrisation n'est qu'une première étape vers la prise en compte du mélange induit par les marées internes. En réalité, la dissipation ne se produit pas exclusivement localement mais une fraction de l'énergie peut se dissiper dans le champ lointain. Cette dissipation peut également varier dans le temps suivant les cycles de variabilité des marées de surface. De telles limitations et l'augmentation de la résolution encouragent les scientifiques à inclure dans leurs OGCM une modélisation explicte de la marée (par exemple dans les mers indonésiennes: [Castruccio et al. (2013); Kartadikaria et al. (2011); Nagai and Hibiya (2015)] ; à Luzon : [Niwa and Hibiya (2001b); Jan et al. (2008); Wang et al. (2016); Alford et al. (2015)], au niveau global: [Niwa and Hibiya (2011); Arbic et al. (2012); Simmons et al. (2004); Shriver et al. (2012)]. La résolution de ces modèles se situe entre 5 et 10 km. Niwa and Hibiya (2011) montrent qu'en utilisant une résolution de 9 km (1/12 °), le modèle ne peut générer que 75% des marées internes. Avec une résolution de 4 km (1/36 °), le modèle génère 90% des marées internes. Avec une résolution relativement grossière, les processus impliqués dans la dissipation des marées internes ne peuvent pas être complètement résolus. Cependant, des études dans l'archipel indonésien [Castruccio et al. (2013); Kartadikaria et al. (2011); Nagai and Hibiya (2015)] montrent que l'ajout d'un forçage de marée explicite produit un mélange qui améliore la structure de la masse d'eau et reproduisent l'eau indonésienne homohaline. La question est de savoir comment ce type de modèle peut créer du mélange en l'absence d'une paramétrisation spécifique. Est-ce que cela se fait à un taux correct pendant toute la durée de vie des marées internes? Afin de répondre à ces questions, nous avons effectué une simulation avec marée et une autre sans marée. Nous avons ensuite comparé la dissipation de quantité de mouvement et d'énergie potentielle dans ces 2 simulations. La validation de ces estimations de la dissipation est effectuée à l'aide des résultats de la croisière INDOMIX. Mais ces estimations s'appuient sur l'hypothèse que la physique induite par le forçage éolien et hydrodynamique est identique avec et sans la marée, ce qui n'est probablement pas entièrement vrai. De plus, le besoin d'un budget de marée précis dans NEMO est nécessaire. Dans la dernière partie de cette thèse, des travaux ont été réalisés afin de fournir une méthode et des diagnostics permettant de mieux quantifier le budget énergétique de la marée dans NEMO. Les résultats sont présentés dans ce manuscrit sur un cas de test simple. Des travaux sont en cours pour l'appliquer sur la région indonésienne. Le problème central dans le calcul du budget énergétique de la marée est la séparation des processus barotropes et baroclines, en terme de vitesse et de pression. Bien qu'intuitif, ce problème est loin d'être trivial et nécessite une définition précise de la dynamique barotrope et de la dynamique barocline. Une définition universelle et précise n'existe pas et déclenche encore une certaine controverse parmi les chercheurs. Kelly and Nash (2011) propose une compréhension ≪ révolutionnaire ≫ de ces problèmes afin de mettre en évidence la complexité et l'importance de la séparation barotrope/barocline dans le cadre de l'étude du budget énergétique de la marée. Son travail questionne la validité des approches courantes introduites par Baines (1982) et suivies jusqu'à présent par la plupart des chercheurs [Niwa and Hibiya (2001a); Jan et al. (2008); Carter et al. (2008); Kang (2010); Zilberman et al. (2009); Niwa and Hibiya (2011); Jeon et al. (2014); Nagai and Hibiya (2015); Alford et al. (2015); Wang et al. (2016)]. Les principaux objectifs de cette thèse sont donc de 1) Quantifier, dans NEMO, la production et la dissipation d'énergie liée à la marée dans les mers indonésiennes 2) Etablir l'impact de la dissipation sur les masses d'eau simulées et sur le refroidissement en surface et sa variabilité 3) Fournir de nouvelles connaissances, des méthodes et des diagnostics permettant de mieux décrire les processus de transfert d'énergie liés à la marée.

Ce manuscrit de thèse est organisé comme suit: le chapitre 2 passe en revue la courantologie, l'hydrographie, et les marées dans les mers indonésiennes. L'évaluation du modèle physique utilisé dans INDESO est ensuite présentée au chapitre 3. Le chapitre 4 étudie l'impact de la modélisation explicite de la marée sur les propriétés de surface, tandis que le chapitre 5 présente une étude plus détaillée consacrée à la génération et la dissipation de l'énergie liée à la marée. Le chapitre 6 présente la controverse existant sur le calcul du bilan en énergie de la marée. Les conclusions de cette thèse sont présentées au chapitre 7. Enfin, une discussion finale et les perspectives de ce travail sont fournies au chapitre 8.

Chapter 2

Scientific context

contents

2.1 The indonesian archipelago a unique region of the world

Indonesian Archipelago (IA) is the only area where two major oceans, the Pacific and the Indian, are connected near the Equator. The IA plays at least two important roles in the global ocean. The first, concerns its role in the climate system. It encompasses some of the warmest surface temperatures of the world ocean that drive intense atmospheric convection [Clement et al. (2005)] and is therefore able to influence climate on the global scale via atmospheric teleconnections [Neale and Slingo (2003)].

The atmospheric deep convection is the center of the Walker and Hadley Circulation and is one of the main driving forces of the tropical atmospheric circulation. The Indonesian Seas contribute to this deep convection as heat and moisture source [Kawamura and Matsuura (2003)]. As such, the volume of surface heat content in IA is known to impact the state of the Pacific and Indian oceans as well as air–sea exchange and gives influence to coupled ocean–climate system [Godfrey (1996); Lukas et al. (1996); Lee et al. (2002); Vranes et al. (2002); Jochum and Potemra (2008); Koch-Larrouy et al. (2010); Sprintall et al. (2014)].

The second important role is its oceanic pathway in the Pacific to Indian interocean exchange which is known as Indonesian Through flow (ITF) that transports 10–20 Sv of warm and fresh waters [Murray and Arief (1988); Fieux et al. (1994); Meyers (1996); Gordon and Fine (1996); Hautala et al. (2001); Molcard et al. (2001); Susanto and Gordon (2005); Sprintall et al. (2009)].

The IA bathymetry is very complex (see Figure. 2.1), with numerous narrow straits, shallow submarine mounts and semi-enclosed basins with sharp shelf break down to 4000m depth (Sulawesi, Molucca and Seram Seas). IA is the only region of the world where strong internal tides remains trapped in the semi enclosed seas, so that a large amount of tidal energy remains available for vertical mixing [Koch-Larrouy et al. (2007, 2008)].

Vertical mixing within the Indonesian seas allow a very strong water mass transformation of the incoming Pacific waters into Indonesian water. Salinity maximums of the North Pacific Subtropical Waters (NPSW) of 34.8 PSU (practical salinity unit) and the South Pacific Subtropical Waters (SPSW) 35.4 PSU, are eroded during their residence in the Indonesian seas. The Indonesian water enterring into the Indian Ocean are characterized by a homohaline water mass with a salinity of 34.45 PSU. As a result, the tropical Indian Ocean thermocline is cooled and freshened by the ITF [Song and Gordon (2004); Gordon (2005)].

2.2 Topography and The Indonesian Through Flow

The INDESO model domain cover most of southeast asian waters including full part of IA. The Bathymetry in Indonesian Archipelago is shown in figure 2.1. Model latitude varies from 15^0 south in Indian Ocean to pacific ocean in 22^0 north. Model longitude covers Andaman seas in the west (95^0 East) to eastern Papua island in 144^0 East.

The model region consists of more than 16000 islands and is lying over a complex bottom topography. Shallow bottom topography of less than 50 meters can be found in Java seas and Arafura seas whereas deep bottom topography of more than 6000 meters can be found in the Indian Ocean, the Pacific Ocean and in the interior of Banda Sea. The region is also formed by a complex coastline and many straits that create sharp topography gradient. Typical strong bottom gradient can be found in the region facing the Pacific ocean such as Luzon, Halmahera and Sangihe Straits and in the region facing to Indian Ocean such as Sunda, Lombok, Alas, Flores and Timor straits. In the interior seas, the topography is even more complicated as the small islands are current feature in this region.

The IA is the only low latitude upper passage in the global thermohaline circulation, known as the Indonesian Through Flow (ITF). To reach the interior of Indonesian seas, Pacific water must deal with deep gap along Phillipines and New guinea. The main entrance portals to the the interior seas are the Luzon straits, the Sangihe Straits and the Halmahera seas [Gordon and Fine (1996); Gordon (2005)]. ITF flow rate average is ranging from 10 - 15 Sv (1 Sv $\equiv 10^6 m^3 s^{-1}$)[Potemra (1999); Gordon (2005); van Aken et al. (2009); Gordon et al. (2010); Wijffels et al. (2008)].

ITF transport has been measured from INSTANT program between 2004-2006 by deploying three years of moorings at 5 stations along the route : Lombok, Makassar, Lifamatola, Ombai and Timor straits. The ITF route from Pacific Ocean to Indian ocean can be divided into western and eastern route into the interior of IS and through south china seas via Luzon Strait and its total transport can be seen in figure 2.1.

The western route mainly concerns North Pacific waters that flow through the Sulawesi Sea into the Makassar Strait. Within Makassar Strait, the 680 m deep Dewakang sill permits only the upper thermocline waters to enter the Flores Sea and flow eastward to the Banda Sea, or to directly exit into the Indian Ocean via the shallow (300 m) Lombok Strait. The transport in Makassar strait was measured 11,6 Sv southward direction [Gordon et al. (2010)].

Smaller contributions of Deeper Pacific water may also take an “eastern” route through the Maluku Sea and over the deeper (1940 m) sill of Lifamatola Strait into the Banda Sea. The 3-years mooring data in Lifamatola strait during INSTANT programme [van Aken et al. (2009)] reflect vigorous horizontal and vertical motion in the lowest 500m over the 2000m deep sill, with speeds regularly surpassing 100 cm/s. The strong residual flow over the sill in the passage and internal, mainly diurnal, tides contribute to this bottom intensified motion. The average volume transport of the deep throughflow from the Maluku Sea to the Seram Sea below 1250m is 2.5 Sv. At shallower levels, between 1250m and the sea surface, the flow is directed towards the Maluku Sea, north of the passage. The typical residual velocities in this layer are low (3cm/s), contributing to an estimated northward flow of 0.9–1.3 Sv. Finally as secondary entrance to the IA, South Pacific waters may enter through from Halmahera Sea, as well as water from fresh water Java.

Lombok Strait, Ombai Strait, and Timor Passage convey the full-depth transport and stratification profile of the ITF from the Pacific Ocean to the Indian Ocean [Sprintall et al. (2009)]. Total mean transport over the 3-year period is 2.6 Sv in Lombok Strait (i.e., toward the Indian Ocean), 4.9 Sv in Ombai Strait, and 7.5 Sv in Timor Passage. The transport in Timor Passage is nearly twice as large as historical estimates and represents half of the 15 Sv full-depth ITF transport that enters the Indian Ocean.

To first order, the seasonal cycle of transport in the thermocline (100–150 m) in all three exit straits is dominated by regional monsoon forcing, with maximum ITF during the southeast monsoon. During the northwest monsoon, the surface transport relaxes in Timor and weakly reverses in Ombai and Lombok, so the main core of the ITF is subsurface.

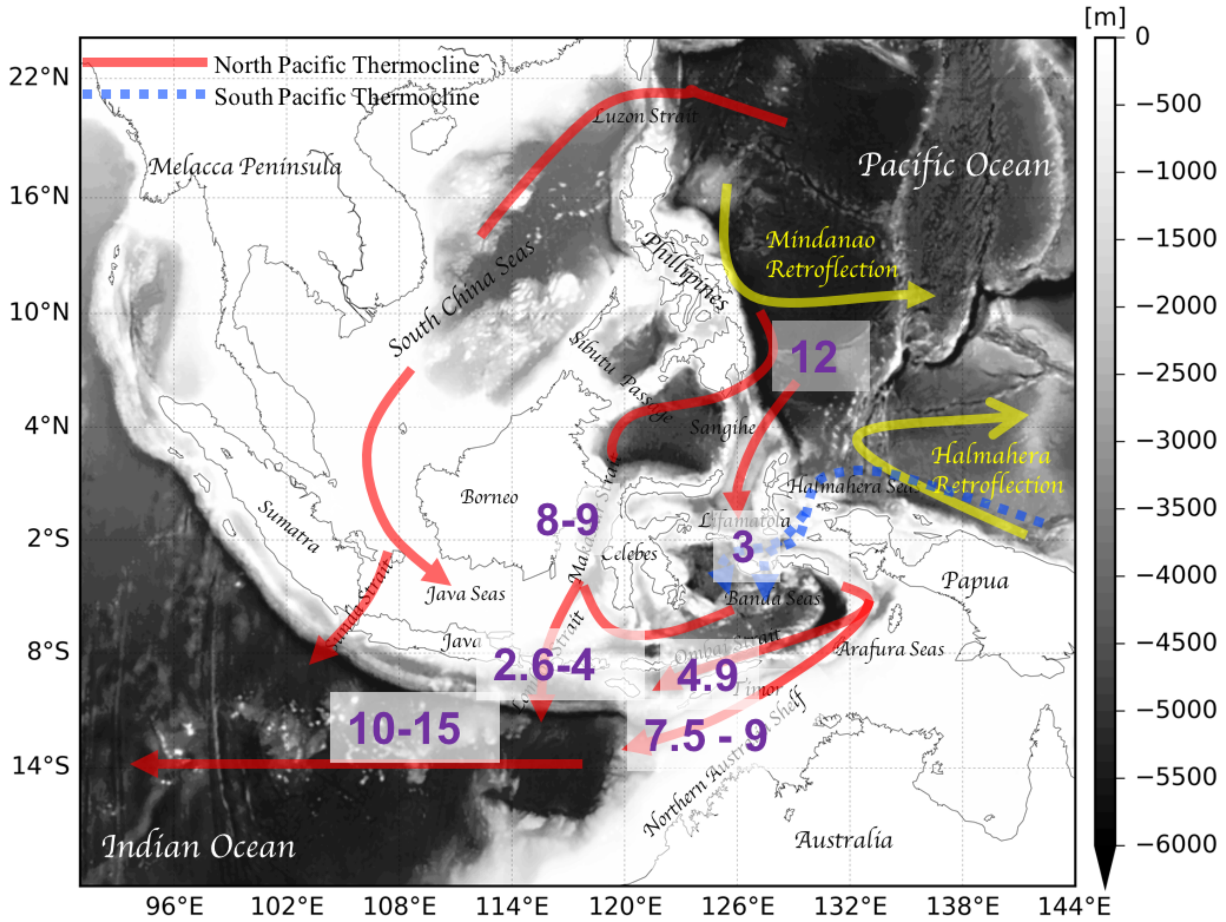

Figure 2.1: Main circulation of the Indonesian Through Flow (ITF) and its Volume Transport (in Sv, 106 m3/s). ITF net transport is of between 10 and 15 Sv. It passes through the shallow Makassar Strait (9 Sv), through the deep Lifamatola Strait (3 Sv). Another 0.5 to 1.5 Sv passes through Halmahera seas, and 0.5 to 1.5 through Java sea. 3 to 4 Sv flow out through the shallow Lombok Strait, and 8 to 9 Sv out distributed among the deep Savu, Sumba, and Timor Straits [Gordon (2005); Talley and Sprintall (2005); van Aken et al. (2009); Sprintall et al. (2014)]. Bathymetry in 1/12 deg resolution interpolated from Etopo2 (www.ngdc.noaa.gov)

2.3 Surface Properties

The IA experiences a seasonal cycle due to monsoonal winds (figure 1.2), with the principal rainy season centered on December- February (DJF), and the dry season peaking in July-August [Aldrian and Dwi Susanto (2003); Chang et al. (2005)]. The ITCZ (Inter Tropical Convergence Zone) follows this moonsonal cycle and is over the South China Sea from July to September, and is over the Sunda Island archipelago, dipping into northern Australia from January to March.

Monsoonal pattern of sea surface temperature and sea surface salinity is shown in figure 2.3. The monsoonal winds shift the lowest surface salinity into the Java Sea and Southern Makassar

Strait from January to March, and into the South China Sea from July to September.

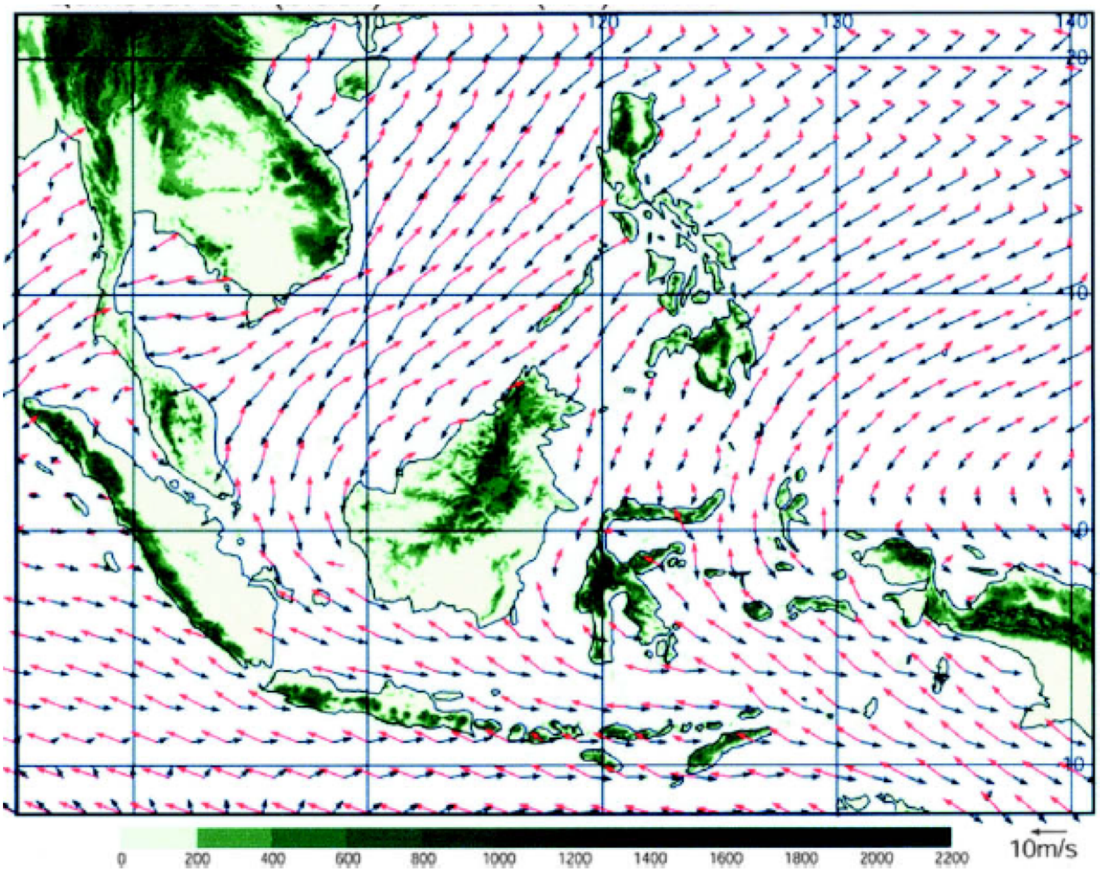

Figure 2.2: Mean QuikSCAT wind for Jan (black) and Jul (red), and topography (m).[Chang et al. (2005)]

At the sea surface, the warmest waters also shift with the seasons: they are further north from July to September, and further south from January to March. In the austral summer (Dec, Jan, Feb), winds blow from the north. They are known as the north west monsoon winds and they bring cold air temperature and tend to cool SST in south china seas and north part of Indonesia. In summer season, the winds are coming from the south west and they tend to warm the SST in southern part of IA. In the Austral winter from June to August, SST is warmer in the northern part of IA, while over Australia the air temperature is colder during winter season. During southeast monsoon upwelling south of the Java islands, nusatenggara islands, and Banda Sea are seen.

Wind is the strongest sources that induced seasonal cycle in Indonesian archipelago. Sea surface salinity reveal the shifts of low salinity water in response to the monsoonal winds (black arrows) and precipitation patterns. The warm sea surface temperature (SST) of these seas serves as one of major sources of heat and moisture for the Austral SummerMonsoon [Kawamura and Matsuura (2003)] and small differences in the SST can lead to significant changes in the magnitude of the atmospheric deep convection and climate [Wijffels (2012); Koch-Larrouy et al. (2010); Sprintall et al. (2014)].

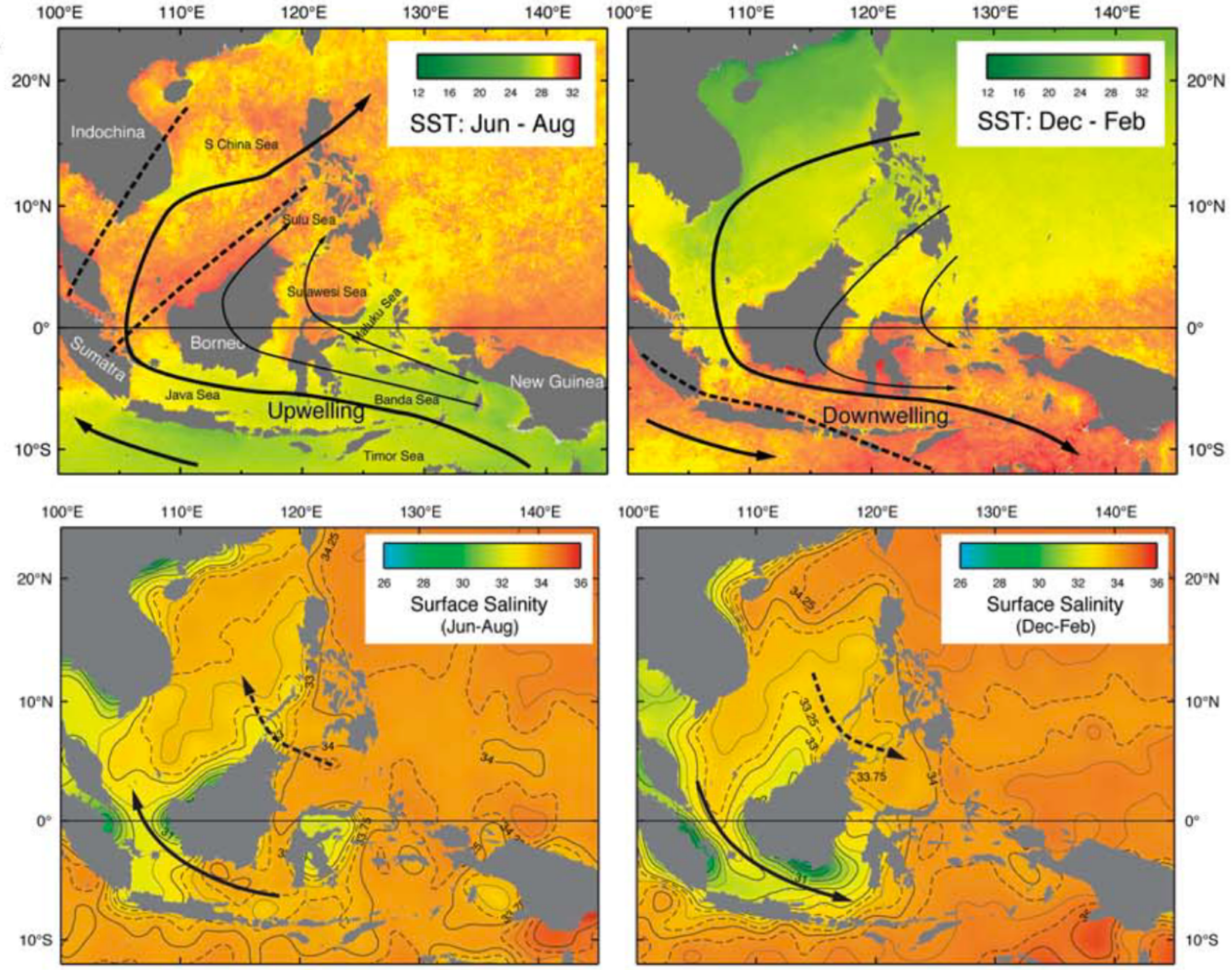

Figure 2.3: Sea surface temperature (SST, top panels) and Sea Surface Salinity (SSS, bottom panels)(left: southeast monsoon; right: northwest monsoon) based on archived hydrographic data.[Gordon (2005)]

2.4 Barotropic and Internal Tides in Indonesian Seas

2.4.1 Barotropic tides

Egbert and Erofeeva (2002) assimilated Topex/Poseidon altimeter data into a global barotropic model by using the method of a generalized inversion scheme. The Semidiurnal M2 constituents is the largest semidiurnal tidal influence in IA. Map of M2 tides from model-observation can be seen in figure 2.4(left).

From the co-tidal phase contour, the propagation of semidiurnal tides is dominated from Indian Ocean into the interior of Indonesian seas. Amplitude varies between 20 cm to 50 cm in the open ocean where the lowest amplitude (less than 10cm) is found in the South china sea and Java sea. Semidiurnal tides have lower amplitude in the Pacific ocean and enter the Indonesian seas by Luzon strait and Halmahera Sea.

Concerning the diurnal tides, K1 is the largest one in the IA. Map of K1 from the model from the model and observations can be seen in figure 2.4(right). In contrast with M2, the tidal pattern in K1 is simpler. Tidal height range from 10 cm in the open seas to 40 cm in the interior seas. High tidal amplitude up to 65 cm is found in the continental shelf, where in particular in Karimata Strait, Sunda Shelf and northwestern Australia coast. From the phase lag contours, we can sea that K1 is mainly passing from Pacific Ocean through IA through Sangihe Strait and Halmahera Sea. M2 is coming from the Indian Ocean, passes along the shore of the Java Island and enters to the interior seas through the Nusa Tenggara islands, Ombai and Timor straits. High amplitudes are found in Indian ocean before entering inner Indonesian seas.

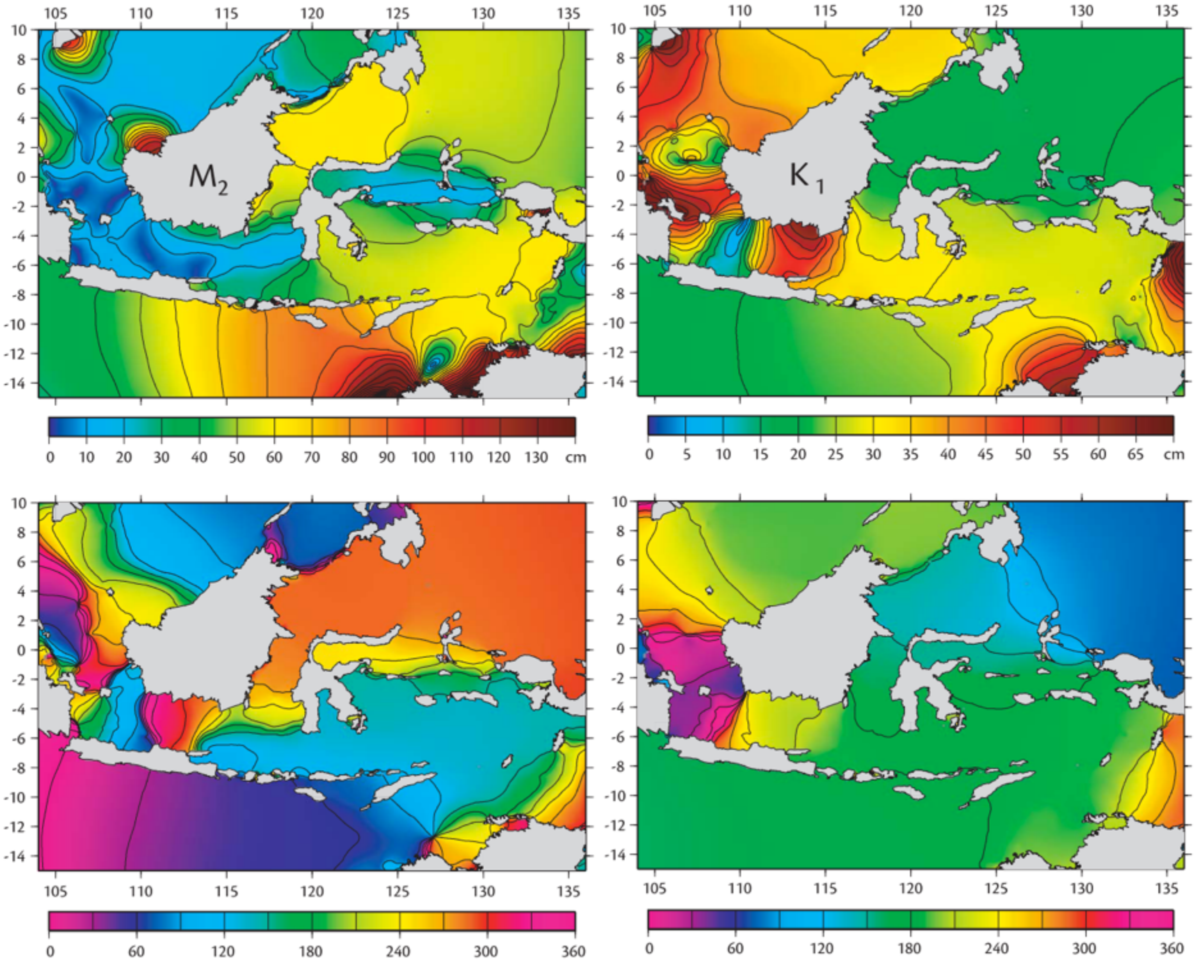

Figure 2.4: The Cotidal charts of the largest semidiurnal tide M2 (left) and diurnal tide K1(right) for sea surface amplitude (top) and greenwich phase lags (bottom). Charts are based on ten years of sea-level measurements from the Topex/Poseidon satellite altimeter into a nonlinear hydrodyamic model. Figure is coming from Egbert and Erofeeva (2002).

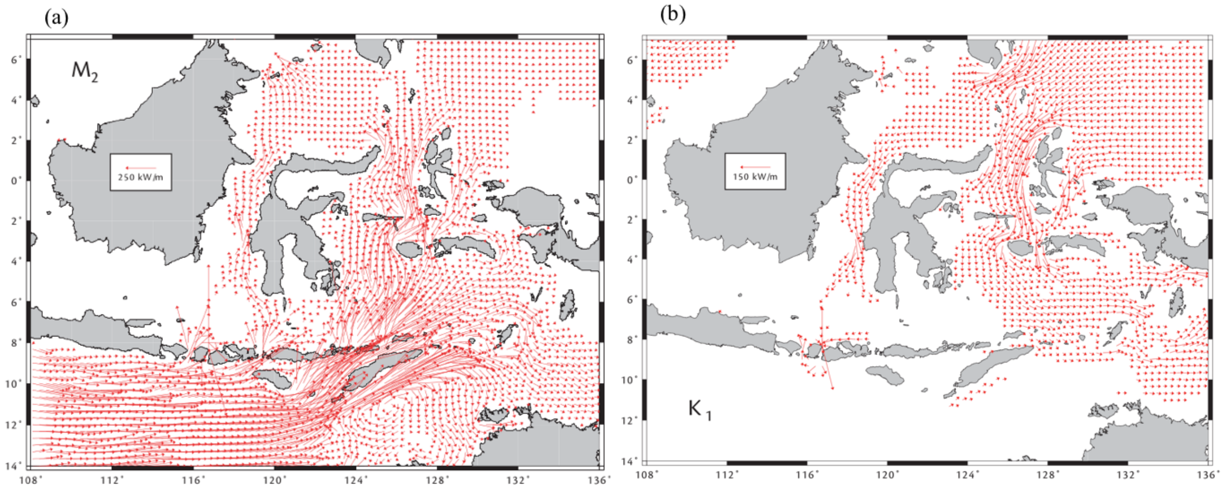

Figure 2.5: Mean barotropic energy flux vectors for the M2 (left). Mean barotropic energy flux vectors for the M2 tiden(right). Fluxes smaller than 20 kW m-1 are not drawn. Figure is copied from Egbert and Erofeeva (2002).

The mean M2 barotropic energy flux can be seen in figure 2.5. The figure show that M2 is mainly coming from the Indian ocean, while K1 is coming from the Pacific. The barotropic M2 flux enter the interior IA through the islands of Nusa Tenggara and Flores. It is amplified when entering narrow strait such as Lombok strait, Alat strait 10 150 kW m-1 and exceeding 500 kW m-1 in Ombai and Timor strait. K1 barotropic flux is higher in Sangihe and Lifamatola straits.

2.4.2 Internal tides

The INDESO domain covers regions with strong internal tides generation. Indeed, regions that have been reported as sources of internal tides are : Lombok strait, Halmahera seas, Sangihe strait, Sulu straits, Ombai strait, Makassar strait and Luzon strait [Mitnik et al. (2000); Aiki et al. (2011); Sari Ningsih (2008); Susanto et al. (2005); Matthews et al. (2011); Robertson and Ffield (2005, 2008)]. Vertical displacement induced by Internal tides can reach up to 150m in 5 min. This strong vertical heaving may supply nutrients from the deep ocean that nourish coral reefs and pilot whale populations that forage in their wakes [Moore and Lien (2007); Jan and Chen (2009); Alford et al. (2015)]. The surface signature from internal tides in IA is detected from Moderate Resolution Imaging Spectroradiometer (MODIS) satellite with the SAR images [Jackson (2007)] The example of captured internal tides from MODIS image data is shown in Figure 2.6. Three selected ”less cloud cover” image were captured in South China Sea, Sulawesi Sea and Banda Seas. In Sulawesi Sea, there are packets of internal tides propagated to the west that may come from the generation of Sangihe strait.There are also internal tides packet that propagate to southeast coming from the generation site of Sibutu Strait. In the South China sea, the internal wave packets is coming from the northern Luzon strait. Finally, internal tides in Banda seas are coming from the Ombai strait.

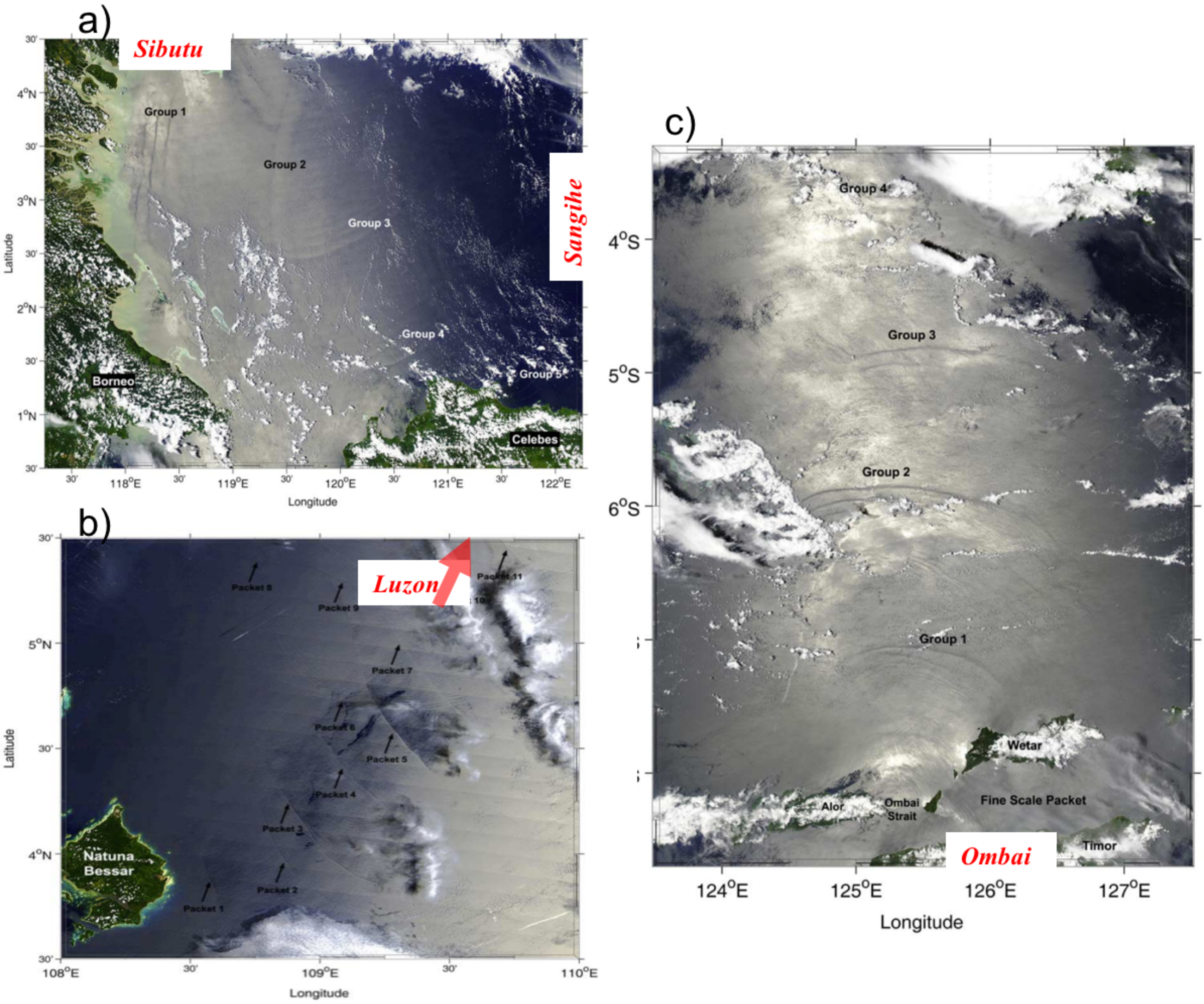

Figure 2.6: True-color MODIS image of (a) the Sulawesi Sea acquired on 6 March 2006 at 5:25 (b) the southwestern South China Sea acquired on 6 March 2003 at 3:20 UTC (c) the Banda Sea acquired on 24 February 2004 at 5:05 UTC. (more details in Jackson (2007)

Internal tides surface signature is also detected in Luzon strait from ENVISAT ASAR images and some ERS-2 SAR images from 2005 to 2010 [Wang et al. (2011)]. Internal waves not only occur in the Northern South China Sea (between Luzon Strait and Hainan Island), but are also found in Western South China Sea (along the Vietnamese coast) and Southern South China Sea as shown in figure 2.7.

The internal tides coming from the Luzon Strait on the eastern margin of the South China Sea are the largest waves documented in the global oceans [Alford et al. (2015)]. They shoal onto the continental slope to the west, the downward displacement of the ocean's layers associated with these solitary waves can exceed 150 meter in 5 min [Ramp et al. (2004)].

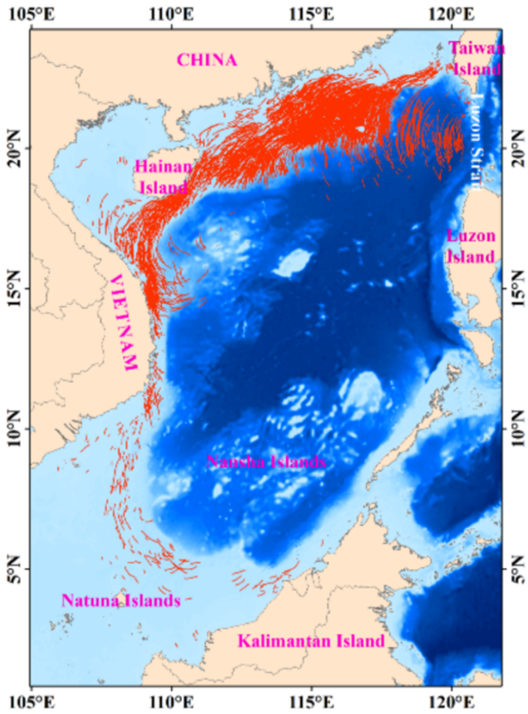

Figure 2.7: The spatial distribution map of internal waves in South China Sea from 2005 to 2010 from Wang et al. (2011)

2.5 Mixing and Watermass Transformation

Many previous studies have suggested that the most likely factor causing the strong water mass transformation in the IA would be the internal tides and their associated mixing [Schiller (2004); Hatayama (2004); Robertson and Ffield (2005)]. IA is the only region of the world where strong internal tides remain trapped in semi-enclosed seas, so that a large amount of tidal energy remains available for vertical mixing [Schiller (2004); Alford et al. (1999); Koch-Larrouy et al. (2008, 2007); Robertson and Ffield (2008); Robertson (2010); Nagai and Hibiya (2015)].

Temperature and salinity distributions within Indian ocean thermocline depth (figure 2.3) depict that the IA acts as a ”mix master” that cools and freshen the thermocline water from Pacific Ocean [Gordon and Fine (1996); Gordon (2005)]. Watermass transformation looking at Temperature Salinity diagrams within the IA is shown Figure 2.9. The NPSW found in the north pacific input box has a salinity of about 34.9 psu and a temperature of about 230C . In contrast, the SPSW found in the South Pacific input box is characterized by a higher salinity maximum of around 35.45 psu and the temperature reaches 21.5 ^{0}C. Strong vertical mixing in IS forms the unique, nearly homohaline ITF profile in Indian Ocean, with a salinity of 34.45 PSU. It is interesting to note that SPSW has lost the signature of the salinity maximum already in the Seram Sea, suggesting that most of the mixing must occur in the Halmahera and Seram Sea.

First estimates of the integrated vertical mixing in the IA has been done using *in-situ* water mass properties and a simple advection–diffusion model [Ffield and Gordon (1992)]. They show that a mixing ten times larger than in the open ocean ($Kz \approx 10^{-4} m^{-2} s^{-1}$) was necessary in order to reproduce the water-mass transformations. Estimates from microstructure measurements in the Indonesian Archipelago was carried out by [Alford et al. (1999)] in Banda seas indicating only weak vertical mixing $Kz \approx 10^{-5} m^{-2} s^{-1}$ in the upper 300 m. The first microstructure and finestructure estimates of the mixing in the regions of high internal tide generation in the Indonesian archipelago were carried out by [Koch-Larrouy et al. (2015)] during the INDOMIX 2010 cruise. They show that mixing is very heterogeneous with very high values of $Kz \approx 10^{-2} m^{-2} s^{-1}$ (station 1, 3, 5 figure 2.10) in regions of generation. In contrast, region further away from generation sites (station 2 and 4, figure 2.10) depict smaller or inexistent mixing in good agreement with Alford et al. (1999)

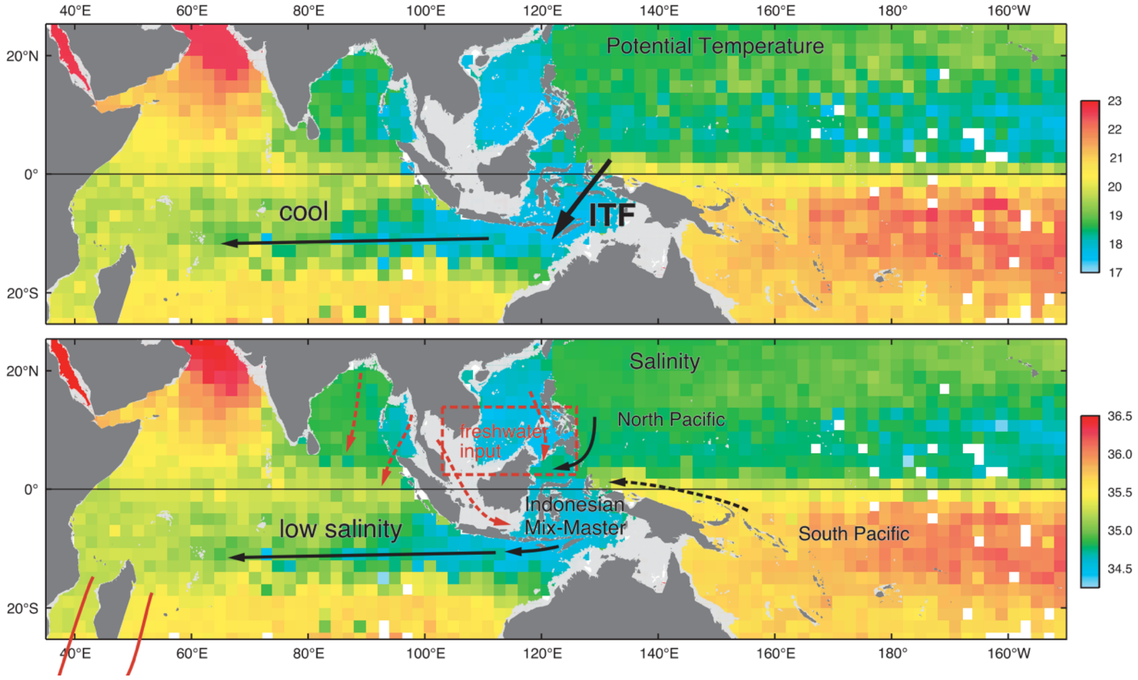

Figure 2.8: Temperature (upper) and Salinity (lower) in $\sigma = 25$ which lies within the upper thermocline. (Figure from Gordon (2005))

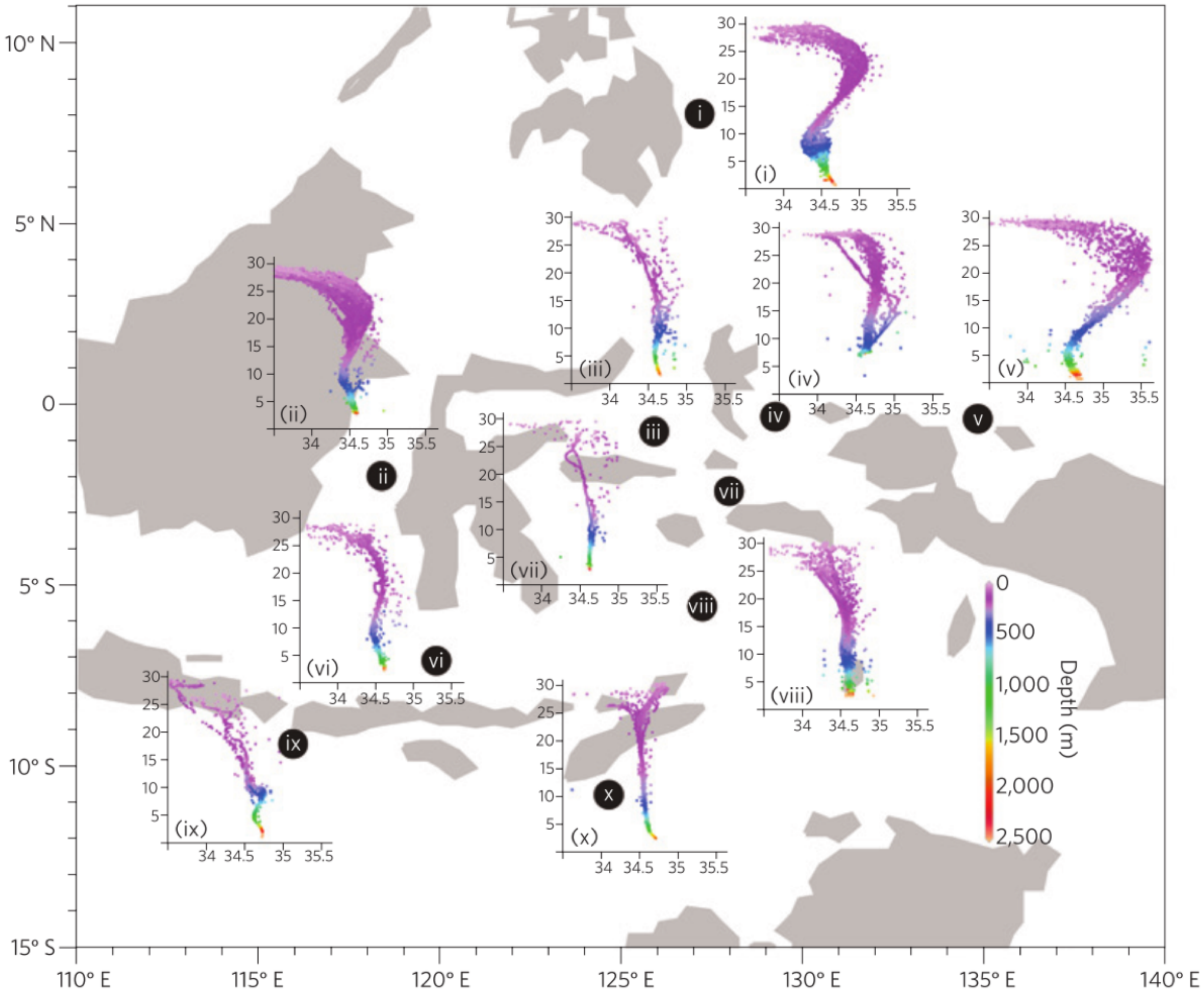

Figure 2.9: Temperature Salinity diagram in the IA.The data were derived from the World Ocean Data Base 2001 and additional regional CTD data. (Figure is from Sprintall et al. (2014) figure.2)

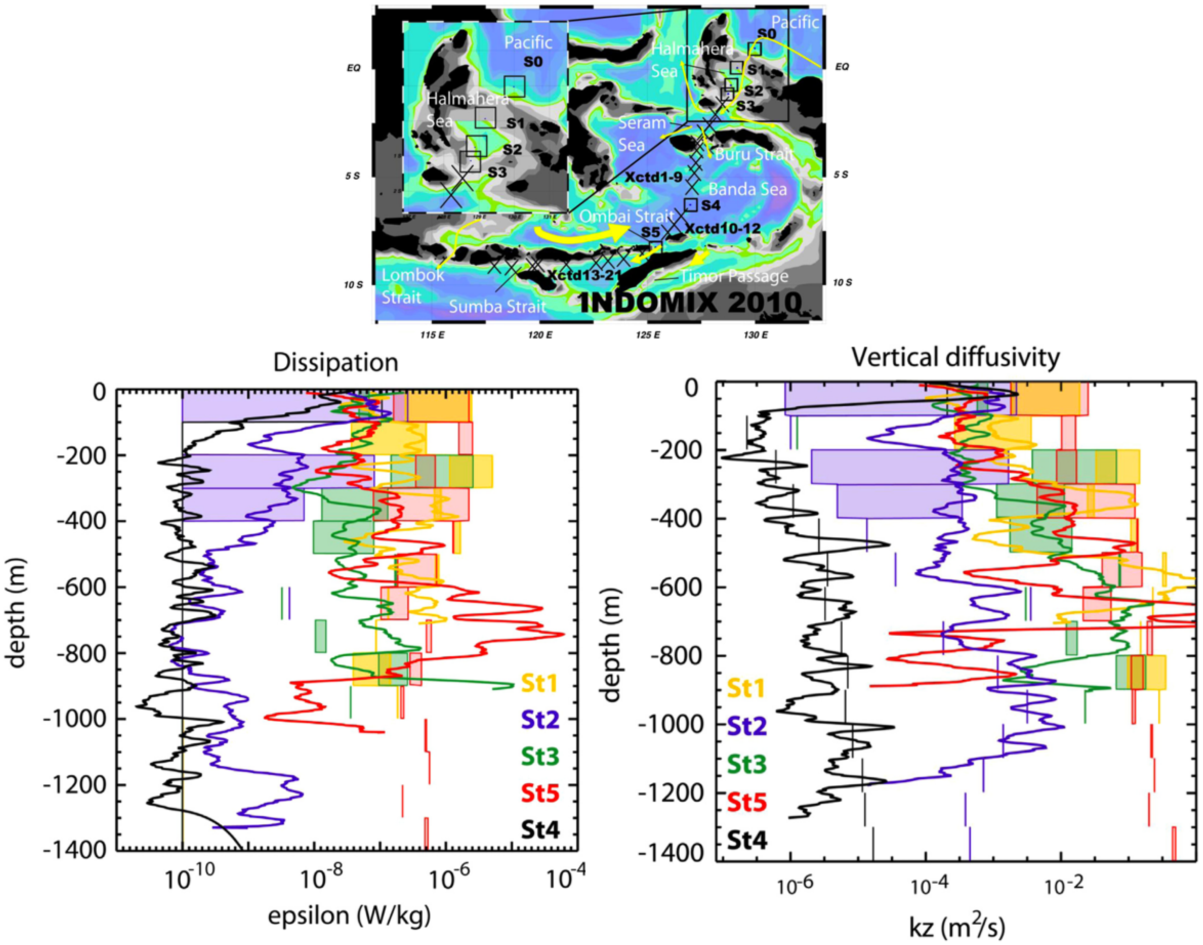

Figure 2.10: Vertical dissipation (left) and vertical difusivity (right) in Wkg^{-1} averaged for each of the 5 stations during INDOMIX cruise [Koch-Larrouy et al. (2015)]

Chapter 3

Evaluation of an operational ocean model configuration at $(1/12^0)$ spatial resolution for the Indonesian seas - Part 1: Ocean physics (published article)

3.1 Introduction

In the framework of the INDESO project, a regional configuration of the NEMO/OPA 9.0 physical ocean model (Madec et al., 1998) has been developed. It covers the whole Indonesian EEZ (Exclusive Economic Zone) and is now running every week in a fully operational mode. This NEMO configuration (named INDO12) has an horizontal resolution of 1/12°. It is coupled with the biogeochemical model PISCES, (Aumont et al., 2006) and fish population dynamics model SEAPODYM (Lehodey et al, 2008). INDO12, which is the model used throughout this thesis, is presented in this paper and its results are validated against several observation data sets.

The model started in January 2007 from initial hydrographic conditions derived from the operational global ocean forecasting system (at 1/40) operated by Mercator Océan. Atmospheric forcing fields (3-hourly ECMWF model outputs) and the inverse barometer effect are used as surface forcing. Explicit tidal forcing is extracted along ocean boundaries from TPXO6 global tidal model. The model is also forced by the fresh water flux from major rivers in Indonesia and along Malaya peninsula.

To take into account internal tidal mixing, the model explicitly solves the barotropic tides. At the resolution of the model, only part of the baroclinic energy will be generated (Niwa and Hibiya, 2011). An additional parameterisation of tidal mixing is thus used to reproduce the effect of internal tides. This parameterisation has been especially developed for OPA/NEMO in Indonesian seas (Koch-Larrouy et al., 2007, 2008, 2010). Comparison of the model results with various data sets, including outputs of the parent model, climatologies, in situ temperature and salinity measurements, and satellite data, show that:

- The general circulation around and through the Indonesian archipelago is well reproduced by the INDO12 ocean model.
- The simulated tides agree reasonably well with the TOPEX/POSEIDON, JASON 1 and JASON2 crossover observations.
- The relative volume transport in the three major outflow passages in the INDO12 simulation is very close to one calculated from the INSTANT estimates
- The simulated vertical mixing is able to erode the South and North Pacific subtropical water salinity maximum. Compared to climatologies, the inflow coming from North Pacific seems too salty for NPSW (give full name) and too fresh in surface for NPIW.

(give full name) Compared to data collected during the INDOMIX cruise, an excessively strong vertical mixing occurs in Halmahera Sea, on the other hand, T –S profiles fit quite well in the Banda Sea and the Ombai Strait. Finally, all T –S dia- grams in the Indonesian Archipelago show that the parent model has definitively not enough efficient vertical mixing and that a higher resolution model including explicit tides is needed to mix correctly the Pacific waters in the Indonesian Archipelago.

In summary, in spite of a few weaknesses, INDO12 proves to be able to provide a very realistic simulation of the ocean circulation and water mass transformation through the Indonesian Archipelago.

3.2 Scientific paper :

Evaluation of an operational ocean model configuration at $(1/12^0)$ spatial resolution for the Indonesian seas (NEMO2.3/INDO12) – Part 1: Ocean physics

Benoit Tranchant[1], Guillaume Reffray[2], Eric Greiner[2], Dwiyoga Nugroho[3,4], Ariane Koch-Larrouy[3] and Philippe Gaspar[1]

1 CLS, Ramonville Saint-Agne, France

2 Mercator Océan, Ramonville Saint-Agne, France

3 IRD/LEGOS 18 av. Ed. Belin, 31401 Toulouse, France

4 Agency of Research and Development for Marine And Fisheries, MMAF, Jakarta, Indonesia

Published in Geoscientific Model Development Journal, 10 March 2016

Geosci. Model Dev., 9, 1037–1064, 2016
www.geosci-model-dev.net/9/1037/2016/
doi:10.5194/gmd-9-1037-2016

Geoscientific
Model Development
Open Access

Evaluation of an operational ocean model configuration at 1/12° spatial resolution for the Indonesian seas (NEMO2.3/INDO12) – Part 1: Ocean physics

Benoît Tranchant[1], Guillaume Reffray[2], Eric Greiner[1], Dwiyoga Nugroho[3,4], Ariane Koch-Larrouy[3], and Philippe Gaspar[1]

[1]CLS, Ramonville Saint-Agne, France
[2]Mercator Océan, Ramonville Saint-Agne, France
[3]IRD/LEGOS 18 av. Ed. Belin, 31401 Toulouse, France
[4]Agency of Research and Development for Marine And Fisheries, MMAF, Jakarta, Indonesia

Correspondence to: Benoît Tranchant (btranchant@cls.fr)

Received: 12 June 2015 – Published in Geosci. Model Dev. Discuss.: 19 August 2015
Revised: 19 February 2016 – Accepted: 22 February 2016 – Published: 10 March 2016

Abstract. INDO12 is a 1/12° regional version of the NEMO physical ocean model covering the whole Indonesian EEZ (Exclusive Economic Zone). It has been developed and is now running every week in the framework of the INDESO (Infrastructure Development of Space Oceanography) project implemented by the Indonesian Ministry of Marine Affairs and Fisheries.

The initial hydrographic conditions as well as open-boundary conditions are derived from the operational global ocean forecasting system at 1/4° operated by Mercator Océan. Atmospheric forcing fields (3-hourly ECMWF (European Centre for Medium-Range Weather Forecast) analyses) are used to force the regional model. INDO12 is also forced by tidal currents and elevations, and by the inverse barometer effect. The turbulent mixing induced by internal tides is taken into account through a specific parameterisation. In this study we evaluate the model skill through comparisons with various data sets including outputs of the parent model, climatologies, in situ temperature and salinity measurements, and satellite data. The biogeochemical model results assessment is presented in a companion paper (Gutknecht et al., 2015).

The simulated and altimeter-derived Eddy Kinetic Energy fields display similar patterns and confirm that tides are a dominant forcing in the area. The volume transport of the Indonesian throughflow (ITF) is in good agreement with the INSTANT estimates while the transport through Luzon Strait is, on average, westward but probably too weak. Compared to satellite data, surface salinity and temperature fields display marked biases in the South China Sea. Significant water mass transformation occurs along the main routes of the ITF and compares well with observations. Vertical mixing is able to modify the South and North Pacific subtropical water-salinity maximum as seen in T–S diagrams.

In spite of a few weaknesses, INDO12 proves to be able to provide a very realistic simulation of the ocean circulation and water mass transformation through the Indonesian Archipelago. Work is ongoing to reduce or eliminate the remaining problems in the second INDO12 version.

1 Introduction

INDO12, a 1/12° regional version of the NEMO/OPA 9.0 (Madec et al., 1998) physical ocean model covering the whole Indonesian EEZ (Exclusive Economic Zone) has been developed in a fully operational mode. It is now running every week in the framework of the INDESO (Infrastructure Development of Space Oceanography) project. This project has been devised and funded by the Indonesian Ministry of Marine Affairs and Fisheries to support sustainable exploitation of Indonesian marine resources. The Indonesian infrastructure within this project has been designed and dimensioned for an operational system at 1/12°. Compared to

Published by Copernicus Publications on behalf of the European Geosciences Union.

ORCA12 (Global configuration at 1/12°), INDO12 includes the tide effect that induces important processes in the Indonesian region. Moreover, it is easier to modify and tune the parameters in a regional configuration, and afterwards make the global ORCA12 configuration to benefit from the improvements of the regional configuration. INDESO actually includes the development of a series of coupled ocean models including a biogeochemical model and a fish population dynamics models covering three commercially important tuna species (skipjack, yellowfin and bigeye tunas). Results of the biogeochemical model are presented in a companion paper (Gutknecht et al., 2015) while simulations of tuna population dynamics will be discussed in a further paper. More details about the INDESO projects can be found at http://www.indeso.web.id.

The Indonesian Archipelago is the only area where two major oceans, the Pacific and the Indian, are connected near the Equator. An additional complicating factor comes from the internal variability associated with ENSO. The complex geometry of the coastlines, the strong tides and the seasonal reversal of monsoonal winds make it difficult to obtain a detailed and realistic representation of the ocean circulation. Numerical models of the oceanic circulation through the Indonesian Archipelago have been developed and prove to be rather successful.

In this paper, we focused on the physics. A realistic modelling of the circulation in the Indonesian Archipelago helps to understand the role of the Indonesian throughflow (ITF) at global scale. ITF carries water from the tropical Pacific into the Indian Ocean in a region where (i) the bottom bathymetry is complicated (see Fig. 1), (ii) numerous narrow straits and deep interior (semi-enclosed) basins down to 4000 m depth (Sulawesi, Molucca and Seram seas) exist and (iii) tidal mixing permits the transformation of incoming Pacific source waters into different water masses. Thus, vertical mixing within the Indonesian Archipelago makes substantial changes to the incoming stratified Pacific thermocline waters.

The major input of the ITF is the Mindanao Current that provides water from the upper thermocline (North Pacific Subtropical Water, NPSW) and North Pacific Intermediate Water (NPIW). This branch fills the archipelago through the Sulawesi Sea and then flows through the Makassar Strait (Gordon, 1986; Murray and Arief, 1988; Gordon and Fine, 1996). Because the Makassar Strait is only 600 m deep, waters below this depth are prevented from progressing southward. About 80 % of the ITF transport is flowing through the shallow Makassar Strait (mainly the thermocline waters) (Gordon et al., 2010). This branch of the ITF flows out of the archipelago through the Lombok Strait (about 20 % of the Makassar transport) or eventually reaches the Flores or Banda seas to finally exit through Ombaï Strait or Timor Passage (Gordon and Fine, 1996).

Two secondary eastern routes exist. The first route is taken by South Pacific Intermediate Water (SPIW) going from the South Equatorial Current (SEC) through the Maluku (or Molluca) Sea and the Lifamatola Strait into the Banda Sea and further through the Ombaï Strait or the Timor Passage into the Indian Ocean. The South Pacific Subtropical Water (SPSW) from the SEC takes the second route through the Halmahera and Seram seas and eventually joins the first eastern route waters in the Banda Sea.

Finally, an important path of the ITF is the flow through the SCS (South China Sea) and is referred as South China Sea throughflow (SCSTF). The cold and salty water inflow through the Luzon Strait becomes a warm and fresh water outflow through the Mindoro and Karimata straits, with a net volume transport of 2–4 Sv ($1\,\mathrm{Sv} = 10^6\,\mathrm{m^3\,s^{-1}}$) (see Qu et al., 2004).

The Indonesian Archipelago is characterised by strong internal tides, which are trapped in the different semi-enclosed seas of the archipelago, inducing a strong mixing of water masses. Susanto et al. (2005) observed internal solitary waves generated in stratified water by interaction of successive semi-diurnal tidal flows with the sill south of the Lombok Strait. These waves create large vertical displacements of water masses that are important to vertical transport and the mixing of biogenic and non-biogenic components in the water column (Munk and Wunsch, 1998).

Vertical mixing within the Indonesian seas can alter the incoming stratified Pacific thermocline waters. Salinity maximums of Pacific waters, 34.8 PSU (practical salinity unit) in the North Pacific and 35.4 PSU in the South Pacific, are eroded during their residence in the Indonesian seas. The ITF waters entering into the Indian Ocean are characterised by a unique water mass associated with a unique tropical stratification with a salinity of 34.6 PSU. As a result, the tropical Indian Ocean is cooled and freshened by the ITF (Song et al., 2004; Gordon, 2005). Previous studies show that the vertical mixing occurs mainly in regions of sharp topography such as sills or narrow straits (Ffield and Robertson, 2008; Koch-Larrouy et al., 2007). However, the exact location of water mass transformations remains unclear (Koch-Larrouy et al., 2007). Different measurements of turbulent dissipation rates made during the INDOMIX 2010 cruise (Koch-Larrouy et al., 2015) could certainly help to increase our knowledge and understanding of vertical eddy diffusivity values for use in numerical models.

To take into account internal tidal mixing, the model explicitly solves the barotropic tides. At the resolution of the model, only part of the baroclinic energy will be generated (Niwa and Hibiya, 2011). Nevertheless, how this energy will dissipate in the model remains unclear and the tidal mixing remains insufficient. To this end, an additional parameterisation of tidal mixing is used to reproduce the effect of internal tides. This parameterisation has especially been developed for OPA/NEMO in Indonesian seas and gives satisfying results compared to observations (Koch-Larrouy et al., 2007, 2008, 2010).

This paper compares the result of the first INDESO simulation against previous results from literature detailed above

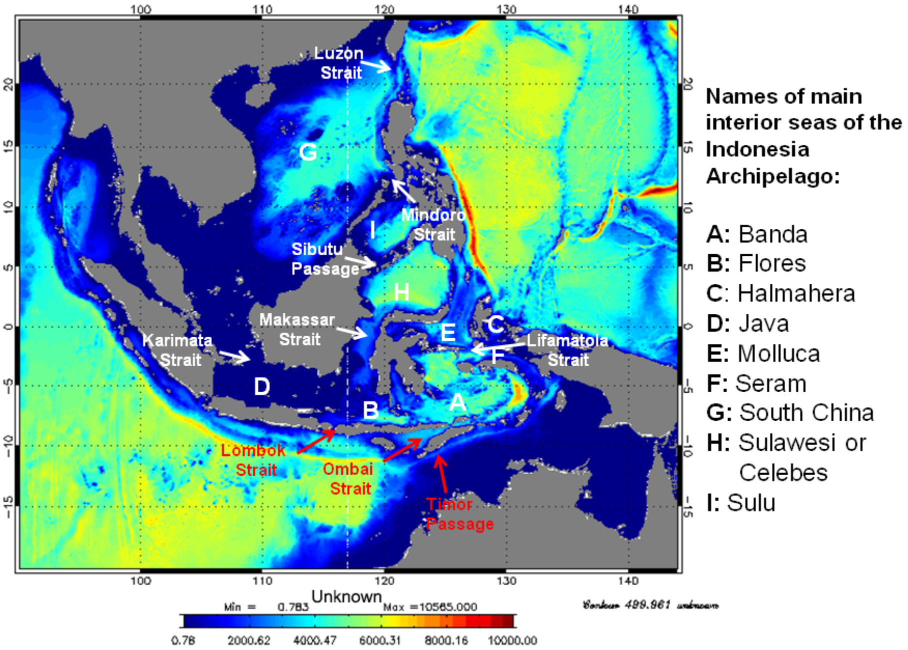

Figure 1. Bathymetry (in metre) of the INDO12 configuration (latitudes: 20° S–25° N and longitudes: 90–145° E) based on ETOPOV2g/GEBCO1 + in-house adjustments in straits of major interest. Three ITF exits are indicated in red. Main straits/passages are indicated in white.

in Indonesian seas. It is organised as follows. Section 2 describes the INDO12 configuration. Section 3 shows different model comparisons with different relevant data sets in the area. We assess INDO12 dynamics against recent scientific literature. We compare meso-scale variability and tides with altimeter data and tide gauges. Comparisons with satellite data such as sea surface temperature (SST) and sea surface salinity (SSS) are done. We also make comparisons with monthly gridded fields combining ARGO (Array for Real-time Geostrophic Oceanography) floats, Triangle Trans-Ocean Buoy Network (TRITON), and available conductivity–temperature–depth (CTD). We compare model volume transport with transport estimates from the INSTANT campaign. Regarding the water mass transformation in the Indonesian seas, we compare T–S (temperature–salinity) diagrams of the INDO12 simulation to the parent and to observational data such as climatology, the recent INDOMIX 2010 cruise (Koch-Larrouy et al., 2015) and instantaneous data in 2013. Finally, Sect. 4 provides a summary of the results of this work.

2 The INDO12 configuration

2.1 The NEMO ocean model

The regionalised configuration of the Indonesian seas using the OPA/NEMO model (Madec et al., 1998; Madec, 2008) in its NEMO2.3 version called INDO12 and developed at Mercator Océan is the circulation model used in the INDESO project. This NEMO2.3 version has already been successfully applied to the IBI (Iberian–Biscay–Ireland) area (Maraldi et al., 2013). It deals with the addition of high-frequency processes such as tide and the atmospheric pressure forcing. Specific numerical schemes such as time-splitting, non-linear free surface (Levier et al., 2007) and open-boundary algorithms have been implemented or improved. Specific physical parameterisations for regional modelling have been added such as the GLS (generic length scale) turbulence model (Umlauf and Burchard, 2003) including wave impact and logarithmic bottom friction. In addition, the vertical mixing induced by internal tides is taken into account using the parameterisation of Koch-Larrouy et al. (2007) by artificially enhancing the vertical viscosity and the diffusion coefficients. In semi-enclosed seas, an approximate value of $1.5\,\mathrm{cm}^2\,\mathrm{s}^{-1}$ for eddy diffusivity has been estimated by Koch-Larrouy et al. (2007). Note that this background diffusivity is of the same order of magnitude as that used by Jochum and Potemra (2008).

The domain covers 20° S–25° N and 90–144° E (Fig. 1) and includes the entire EEZ of Indonesia. The horizontal grid is an extraction of the global ORCA (the global tripolar grid used in NEMO) grid at 1/12° developed at Mercator Océan. It is a quasi-regular grid over the Indonesian area and with a mesh approximately equal to 9 km. In the vertical direction, the model uses a partial step z coordinate (Barnier et al., 2006). The vertical grid is spread over 50 levels and has a depth-dependent resolution (1 m at surface to 450 m at

Table 1. Sill depths (m) of the key straits and passages in the Indonesian seas from the scientific literature and those used in INDO12.

Straits or passages	Observed estimate	INDO12
Inflow passages		
Sanhigihe Ridge (divides Pacific Ocean and Sulawesi Sea)	1350[a]	1250
Makassar Strait (Dewakang sill)	680[a]	675
Halmahera Sea passages	580[a]	551
Lifamatola Passage	1940[b]	1950
Outflow passages		
Lombok Strait	300[a]	200
Strait between Alor and Atauro islands (upstream of Ombaï Strait)	1450[d]	1400
Wetar Strait (upstream of Ombaï Strait)	2450[c]	2050
Sumba Strait (north of Sumba Island)	900[d]	800
Savu Strait (connection between Savu Sea and Indian ocean)	1150[d]	1100
Timor Passage (southern end)	1890[d]	1800

Source for sill depths: [a] Gordon et al. (2003a), [b] van Aken et al. (1988), [c] Sprintall et al. (2010), [d] Sprintall et al. (2009).

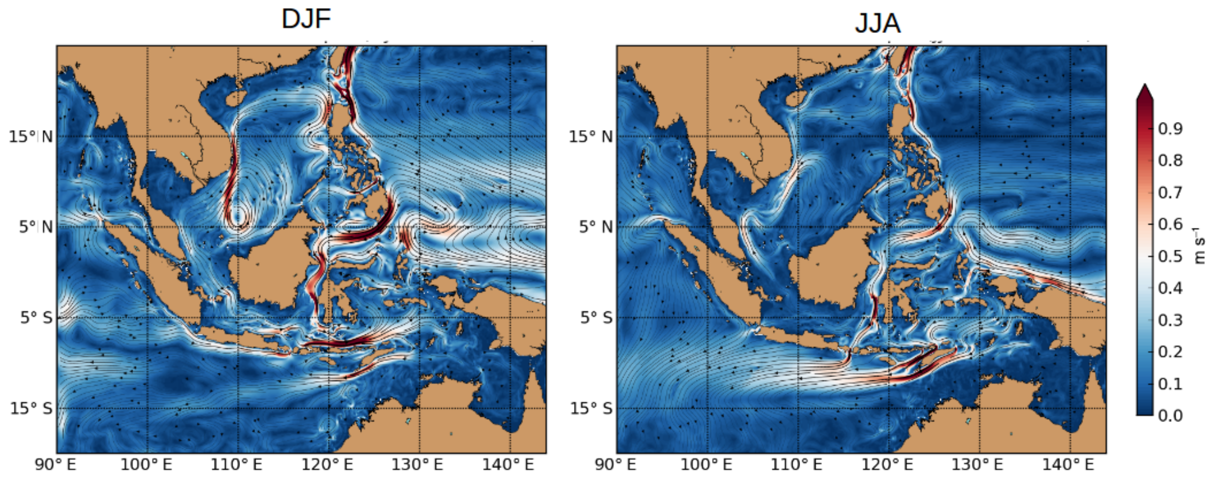

Figure 2. Mean circulation at surface (16 m depth) during boreal winter or DJF (left) and boreal summer or JJA (right) during the 2008–2013 period.

the bottom). In the first 10 m, the layer thickness is less than 2 m, then rise to about 10 m at a depth of 50 m.

The bathymetry used in this configuration is based on ETOPO2V2g (2′) and GEBCO (1′) and has been interpolated on the NEMO grid without any smoothing. Due to missing foreshore in the model, a minimal threshold value of 7 m depth has been fixed. The bathymetry has been locally modified by hand editing mainly in the straits and passages where the sill depths have a major influence and constrain the transports. As in Metzger et al. (2010), we report sill values in Table 1 and compare them to scientific literature. Note that correct sill depths are essential for proper model simulation (Gordon et al., 2003a). Without these changes, the outflow passages were quite incorrect with most of the flow that goes through the Lombok Strait instead flowing through the Ombaï Strait and the Timor Passage. Note that the INDO12 configuration is coupled "online" to the biogeochemistry model PISCES (Pelagic Iteraction Scheme for Carbon and Ecosystem Studies) (see Gutknecht et al., 2015).

2.2 External forcings

Atmospheric forcing fields come from the European centre (European Centre for Medium-Range Weather Forecasts, ECMWF) and have a high frequency (3 h). "Bulk" formulae from CORE are used to model the atmosphere–ocean interface (Large and Yeager, 2004). The surface atmospheric pressure forcing is also explicitly considered.

This configuration includes explicit tidal forcing. INDO12 has geopotential tidal forcing for M2, S2, N2 and K2 (the four largest semi-diurnal constituents) and for K1, O1, P1 and Q1 (the four largest diurnal constituents). As in Maraldi

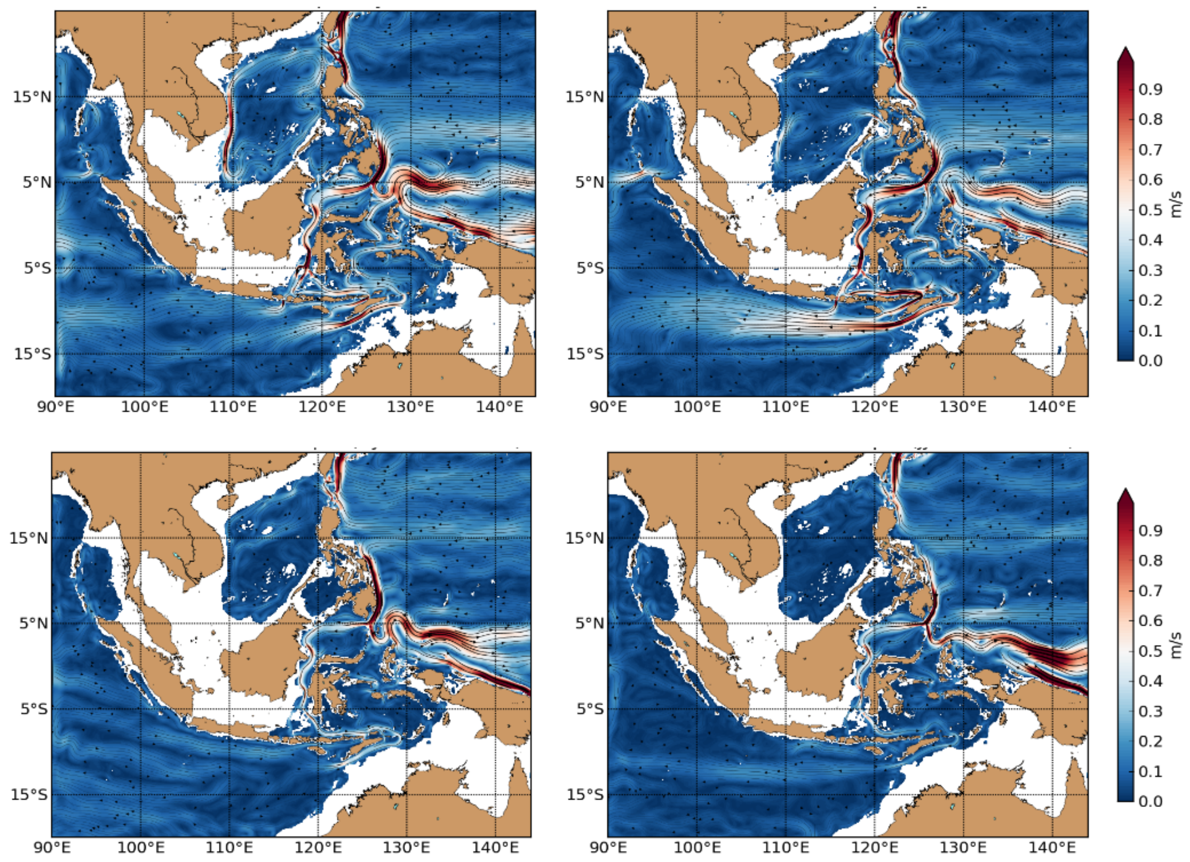

Figure 3. Mean circulation at 100 m (top) and 300 m (bottom) during boreal winter or DJF (left) and boreal summer or JJA (right) during the 2008–2013 period.

et al. (2013), two long-period tides Mf and Mm and one non-linear constituent (compound tides) M4 are also added. These 11 tidal constituents, which come from the astronomical forcing TPX0.7 data set (Egbert and Erofeeva, 2002), are used to force open boundaries.

A monthly runoff climatology is built with data on coastal runoffs and 99 major rivers from Dai and Trenberth (2002) and prescribed with a flux formulation. In addition, two important rivers (Mahakam and Kapuas on Borneo island) with large enough rates (class 3) were added to this database.

The penetration light scheme used in this simulation is based on a 4-bands decomposition of the light; 54 % of the solar radiation is trapped in the surface layer with an extinction depth of 0.35 m and the other part is decomposed following the red, green and blue wavelengths (Jerlov, 1968). The climatological chlorophyll values, required to calculate the absorption coefficients, were deduced from the global 1/4° input file built from the monthly SeaWifs climatological data (McClain et al., 2004).

The longest available period to force the INDO12 model and to achieve the operational target set by the INDESO project was the Mercator Océan Global Ocean Forecasting System at 1/4° (PSY3V3R3) (Lellouche et al., 2013), data from 2007 to 2013. Therefore, the INDO12 simulation starts on the 3 January 2007 with initial conditions coming from the PSY3V3R3 run started 3 months before from a Levitus climatology (WOA 2005), see Antonov et al. (2006).

These conditions include temperature, salinity, currents and sea surface height (SSH). Open-boundary conditions (OBCs) are located on a relaxation band of 10 grid points ($\sim 1°$) and come from daily output of the Global Ocean Forecasting System at 1/4° of Mercator Océan.

3 INDO12 assessment

In order to evaluate the quality of the INDO12 simulation, several diagnostics were performed on different variables such as temperature, salinity and currents. Our performance analysis confronts the model results to the distinct available data sets. The first year (2007) of the simulation is considered as the model spin-up phase. Consequently, only the 2008–2013 simulated period is assessed.

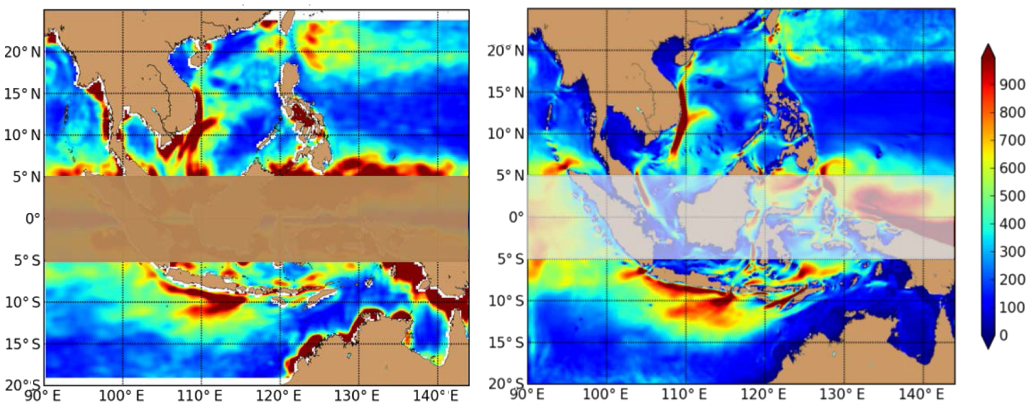

Figure 4. Mean EKE ($m^2 s^{-2}$) derived from altimetric data (AVISO products) (left) from INDO12 (right) for 2010–2013 period. EKE from altimetry is not reliable within a band of 5° on both sides of the Equator due to geostrophic approximation.

3.1 The mean circulation

As noted by Ueki el al. (2003), the NGCC (New Guinea Coastal Current) exhibits a seasonal variability correlated to the monsoonal wind variation with a north-east wind stress during the boreal winter and a south-west wind stress during the boreal summer. It flows northward usually at the surface and is intensified during the boreal summer. It flows southeastward during the boreal winter (see Fig. 2). The New Guinea Coastal Under Current (NGCUC) flows steadily northwestward during the whole year in the sub-surface thermocline layer (100–300 m) with an intensification during the boreal summer (see Fig. 3).

In the Pacific region (Fig. 2), the intensity of SEC and (North Equatorial Counter Current) NECC increase during boreal winter, and are weaker during boreal summer. The SEC and NECC are closely linked to the ITCZ (Inter Tropical Convergence Zone). They are stronger from August to December and weaker from March to May (see McPhaden et al., 1998).

Between the surface and ~ 100 m depth, the seasonal variability is well represented in the major exit passages of the Lombok Strait, Ombaï Strait and Timor Passage with a maximum velocity (maximum transport) during the SEM (South East Monsoon) (Sprintall et al., 2009).

In the SCS, the circulation at the surface is cyclonic during the boreal winter and weakly anti-cyclonic during boreal summer; see (Fig. 2).

In the Indian Ocean, the eastward surface current, the SJC (South Java Current) flows along the Indian Ocean coast of Sumatra and Java only during the NEM (North East Monsoon). During the SEM, the SJC is mostly in the same direction as the westward flowing ITF (Sprintall et al., 2010), which is well reproduced in our simulation. The deeper South Java UnderCurrent (SJUC) flows also along the coast (400–800 m) in the model. It clearly seems that it is driven by Kelvin waves as mentioned by Sprintall et al. (2010) since it flows mainly eastward whatever the monsoon period.

3.2 EKE

In order to describe the mesoscale and the eddy variability, the mean Eddy Kinetic Energy (EKE) is calculated. The EKE calculation is performed over the last 3 years (2010–2013) of the INDO12 simulation and compared to altimetry data (AVISO products), see Fig. 4.

Saraceno et al. (2008) point out the difficulty of representing coastal processes with conventional altimeter data. It is mainly due to intrinsic difficulties such as corrections applied to the altimeter data near the coast (the wet tropospheric component, high-frequency oceanographic signals, tidal corrections, etc.). The Indonesian seas are no exception to the rule due to the presence of numerous islands and an active atmospheric convection during the monsoons. In addition, in the equatorial band (5° S–5° N), the geostrophic approximation is not valid since the Coriolis force vanishes.

Except in coastal regions, the EKE from INDO12 and the EKE derived from altimeter data have the same patterns for strongest values. They are localised along the Vietnam coast, near the Luzon Strait (Kurushio intrusion in the SCS) and all along the Java coast (upwelling signature). In the INDO12 simulation, stronger values are found in all the straits and in the main exits (Lombok, Ombaï and Timor). As in Castruccio et al. (2013), large EKE values are also found within the Indonesian seas, Celebes Sea, Flores Sea, Molluca Sea and the southern part of the Banda Sea. In the Pacific, Halmahera and Mindanao eddies as well as the NGCC also show a strong signature in the EKE field. On both sides of Luzon Strait, the EKE from INDO12 exhibits weaker values than the EKE derived from altimeter data (AVISO). These weak EKE values corroborates the weak inflow as mentioned in the Sect. 3.6.

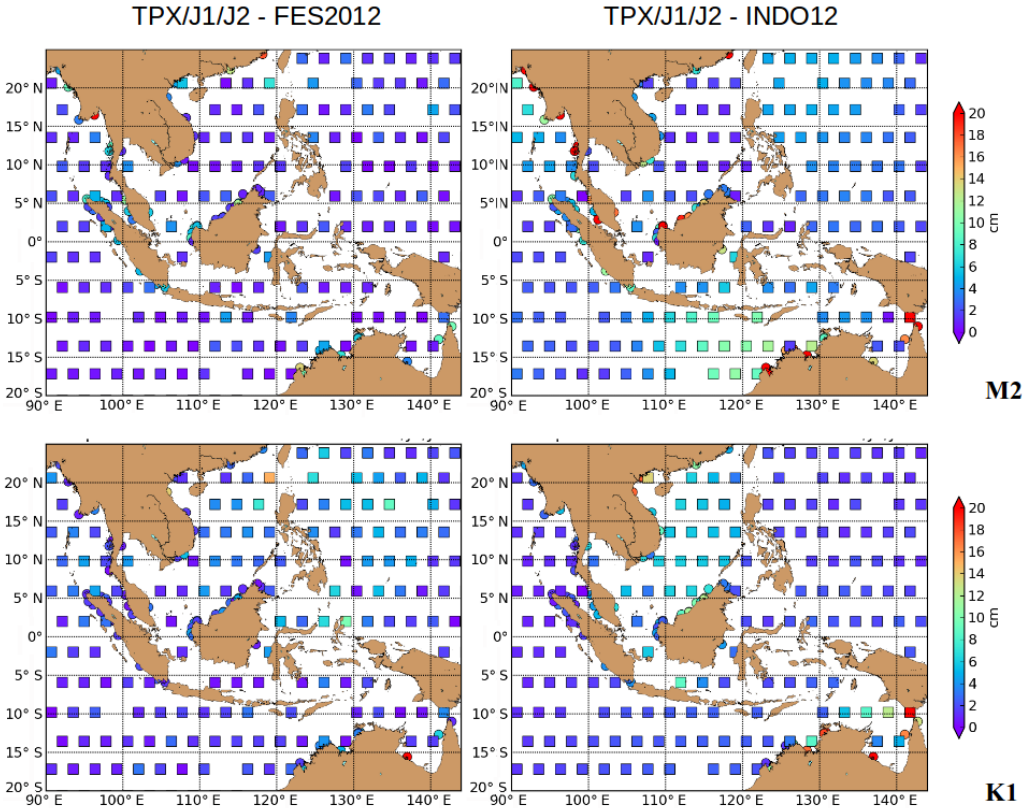

Figure 5. Surface tidal elevation complex differences at crossing points between TPX/J1/J2 and FES2012 (left) and INDO12 (right) symbolised by squares. Surface tidal elevation complex differences between tide gauges and FES2012 (left) and INDO12 (right) symbolised by circles. Units are in centimetres. M2 (top) and K1 (bottom) tidal components.

3.3 Tides

The four primary tidal components, namely M2, S2, K1 and O1 are found to be the major components that drive tidal forcing in the Indonesian seas (Ffield and Robertson, 2008; Kartadikaria et al., 2011). In this section, we present only two primary tidal components, M2 and K1, the largest amplitude semidiurnal and diurnal constituents. Kartadikaria et al. (2011) have fully described the evolution of the M2 and the K1 tides in the Indonesian seas. They show that (i) the propagation of the K1 is simpler than that of the M2 component (ii) and the K1 amplitude is smaller than that of M2. Here, the K1 and M2 constituents are compared to a hydrodynamic model of the barotropic tides constrained by satellite altimetry FES2012 (Carrère et al., 2012; Stammer et al., 2014). The INDO12 tidal sea surface elevation amplitude and phases were calculated as a complex amplitude using standard harmonic analysis applied to the sea surface height. Differences of tidal elevation between satellite altimeter data (TOPEX/POSEIDON, JASON 1 and JASON2) at crossover locations and models (INDO12 and FES2012) are shown in Fig. 5. For the M2 constituent, FES2012 is closest to the observations excepted in the SCS. On the contrary, for the K1 constituent, INDO12 is closest to the observations except in the SCS and along the Australian coast. Differences in tidal elevation between tides gauges (circles) and models are also given in the same figure. Closer to the coast, the discrepancy between tide gauges and INDO12 is larger than between tide gauge and FES2012. This can be attributed to the lack of resolution along the coast in INDO12 compared to the finite element FES2012.

Figure 6 shows a power-spectrum analysis of hourly SSH from tide gauges and from simulated moorings. As in Castruccio et al. (2013), at low frequencies (period larger than 10 days), the model is in very good agreement with the observations. The spectral analysis shows that SSH fluctuations depict the same peaks at the dominant tidal frequencies, the diurnal (O1 and K1) and semidiurnal (M2 and S2). The same intensity is found in the model and in the observations. It confirms that tides are a dominant forcing in the area, and that the tidal current is dominated by the diurnal (O1 and K1) and semidiurnal (M2 and S2) frequencies. Non-linear constituents are represented by additional peaks at the higher harmonics that contain less energy in the model than the observations. As mentioned in Ffield and Robertson (2008), model errors are mainly due to a topography, stratification, resolution, and tidal forcing. Indeed, tide gauges are very close to the coast where the INDO12 model is less able to

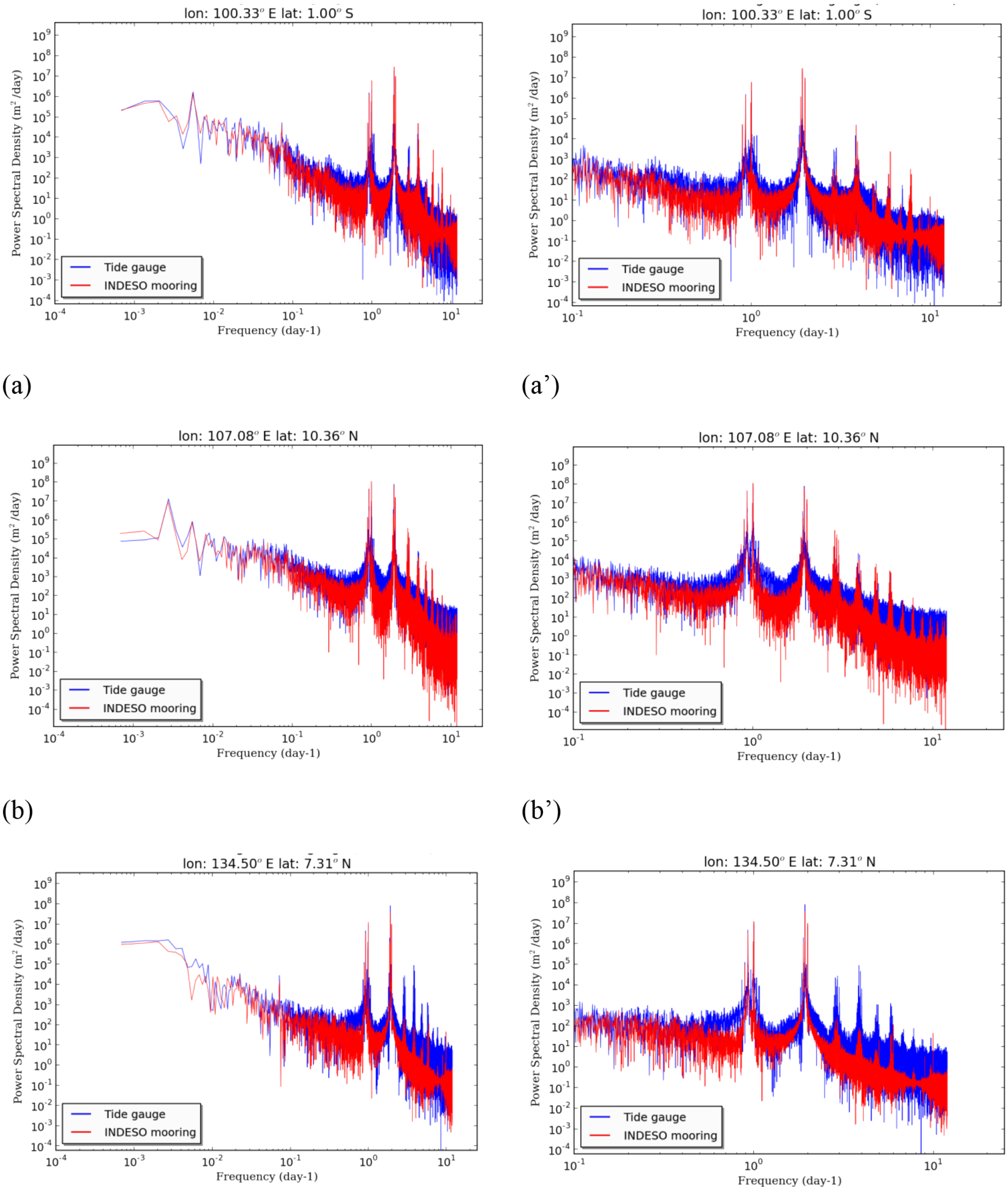

(a) (a')

(b) (b')

(c) (c')

Figure 6. Power spectral density of the SSH for the model (red solid line) and for Tide gauges (blue solid line) at different locations (**(a)** Padang (East Sumatra), **(b)** Vung Tau (SCS/South Vietnam) and **(c)** Malakal (Pacific)), calculated during 2009–2012 period. Right panel is a detailed view of the left panel.

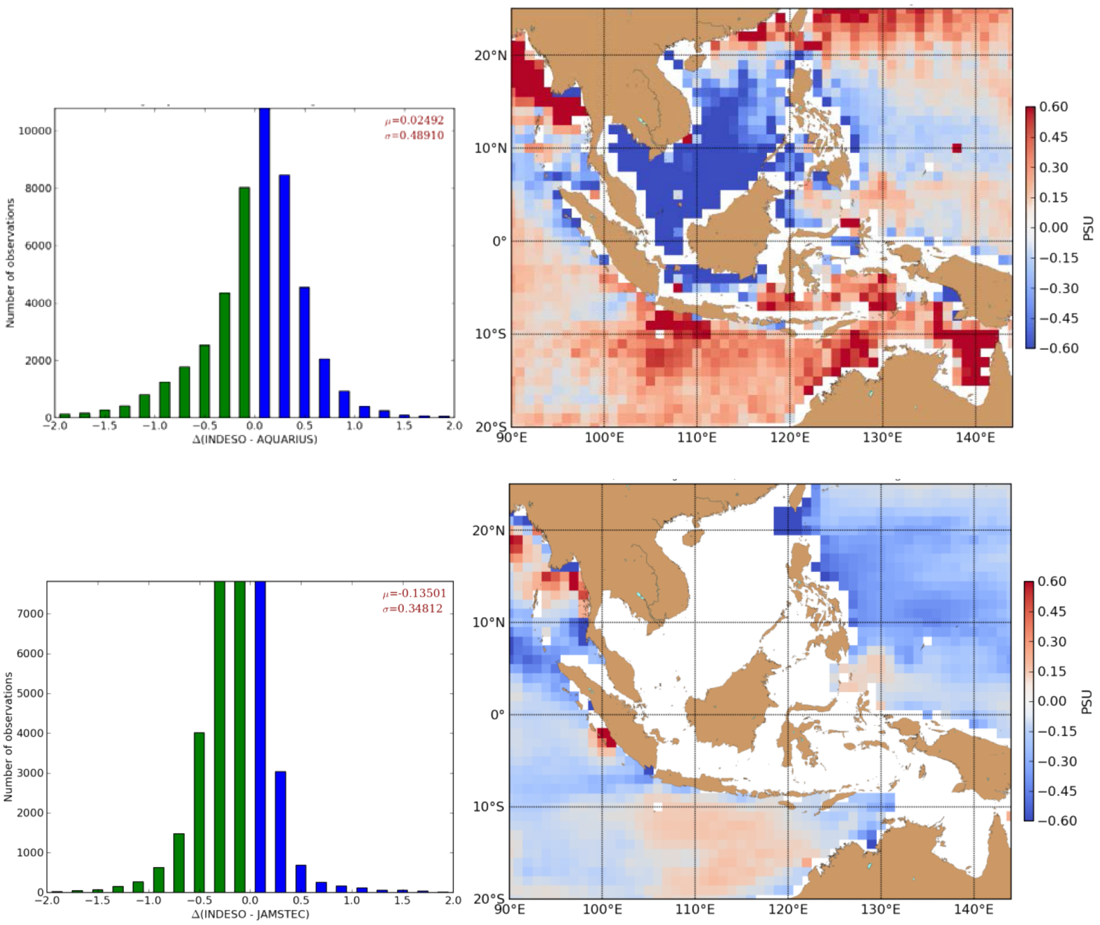

Figure 7. Mean bias (PSU) of the INDO12 SSS (monthly means) relative to Aquarius L3 (V3.0) (top) and JAMSTEC (ARGO + TRITON + CTD) (bottom) from August 2011 to December 2013.

well represent non-linear processes. Finally, non-linear tides seems also to have more energy in the model near the east of Sumatra coast (Fig. 6a) than in the Pacific (Fig. 6c).

3.4 SSS: comparisons with Aquarius and Argo monthly data

Due to the important role of the low salinity surface layer waters (coming from the SCS southward throughflow) on the ITF (Gordon et al., 2012), it is important to assess the SSS fields of INDO12.

3.4.1 Aquarius data

We used the Aquarius Level 3 SSS standard mapped image data that contain gridded 1° spatial resolution SSS averaged over 1 month. This particular data set is the monthly sea surface salinity product for version 3.0 of the Aquarius data set, which is the official second release of the operational data from AQUARIUS/SAC-D mission. A summary of improvements to this new version of the Aquarius data is available.

For the previous version (V2.0), the estimated error for (monthly mean) was around 0.3–0.4 PSU (Lagerloef and the Aquarius team, 2013). A recent paper of Menezes et al. (2013) shows that root mean square (rms) difference between the Aquarius (7-day Level-3 product version 2.0) and Argo is about 0.28 PSU in the tropical eastern basin of the Indian ocean (5–20° S; 90–140° E), i.e. in a region where the fresh ITF is spread westward. In addition, in a very recent paper, Tang et al. (2014) show that the monthly rms difference with respect to Argo between 40° S and 40° N for all Aquarius SSS data products (V2.0) can be reduced to below 0.2 PSU with some limitations.

3.4.2 JAMSTEC data

As in Tang et al. (2014), we use a monthly gridded data set of global oceanic salinity on 1° × 1° grid processed and delivered by the Japan Agency for Marine-Earth Science and Technology (JAMSTEC) (Hosoda et al., 2008). This product is derived from the use of the optimal interpolation (OI)

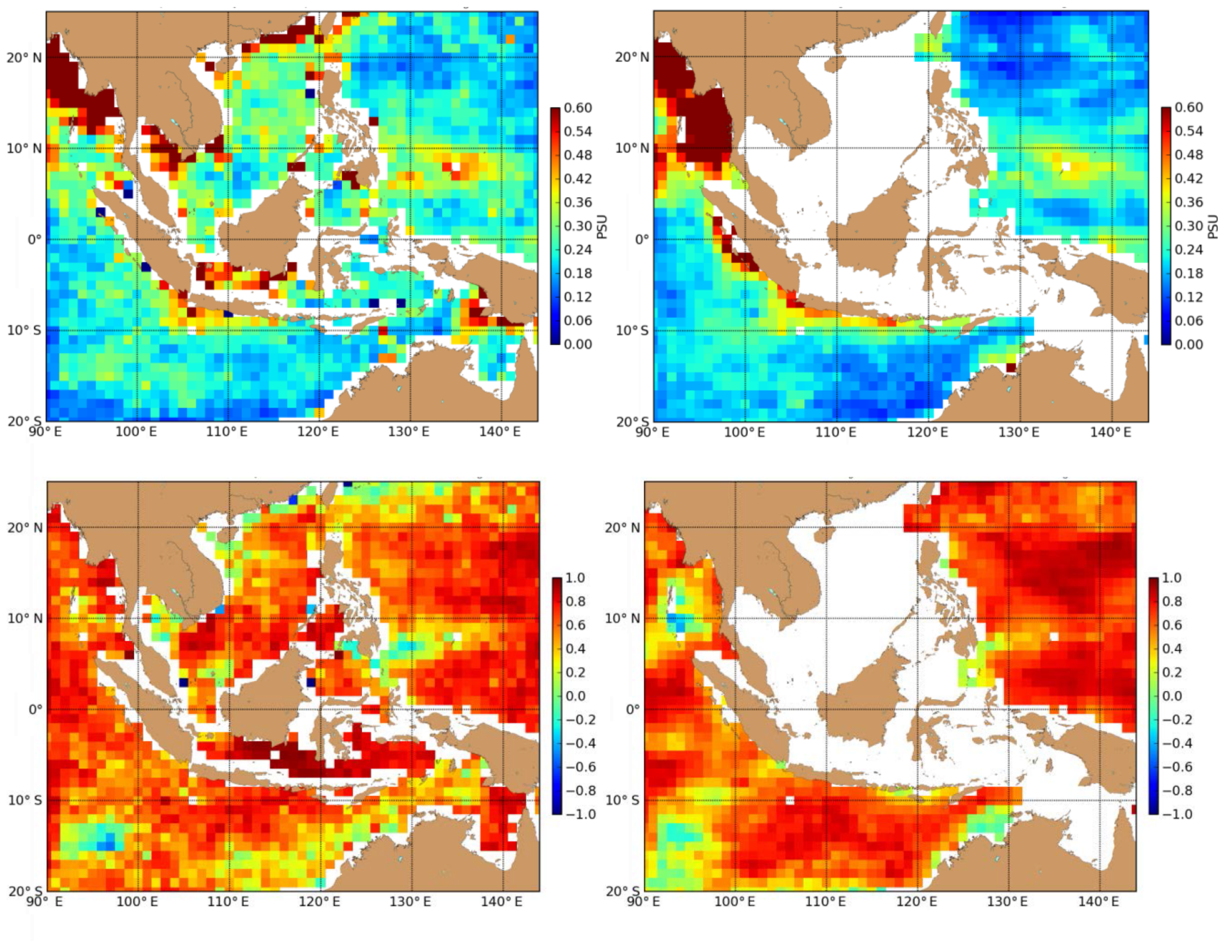

Mean correlation = 0.579

Mean correlation = 0.607

Figure 8. RMSD (top) and correlation (bottom) of INDO12 with respect to Aquarius (left) and JAMSTEC (ARGO + TRITON + CTD) (right) monthly map from August 2011 to December 2013.

method that builds the gridded fields from ARGO floats, TRITON and available CTD.

The salinity values at 10 m depth from INDO12 are compared with the first level of JAMSTEC salinity at 10 dbar (∼ 10 m depth).

The advantage of the monthly Aquarius data is the spatial coverage. Monthly JAMSTEC data do not cover the Indonesian seas due to a lack of in situ data.

3.4.3 Results

For both data sets, a negative bias exist in the Pacific region (Fig. 7) except near the Mindanao loop current where a positive bias exist mainly in winter. It is more pronounced with the Aquarius data set. We show that the probability density function (pdf) of the SSS misfit is biased and non-symmetric, which corroborates the fact that processes and/or water masses into the Pacific and Indian oceans are different. The biases relative to each data set are consistent for the same coverage except in the northern Pacific (above 10° N) where Aquarius SSS data are probably polluted by strong RFI (Radio Frequency Interference); see Kim et al. (2014) and Le Vine et al. (2014). They are quite similar but stronger for Aquarius. In the Indian Ocean, a positive bias exists just after the ITF exit. It becomes negative near the Eastern Gyral Current (EGC) that flows eastward near 15° S. In the upper ocean, a strong salinity front exists between the fresh water from the ITF in the SEC and the salty subtropical waters (Menezes et al., 2013). Note also that the ITW joins the SEC and spreads westward in the Indian Ocean by advection and diffusion (Gordon et al., 1997).

Un-correlated biases near the west-Sumatra coast are located in the vicinity of many islands that could pollute the Aquarius signal. The RMSD (root mean square deviation) between JAMSTEC and INDO12 in this region is higher (Fig. 8) than the RMSD between Aquarius and INDO12.

A strong negative bias (too fresh) exists in the SCS, which is more (in winter) or less (in summer) important depending on the season (not shown here). It could be related to an $E–P$

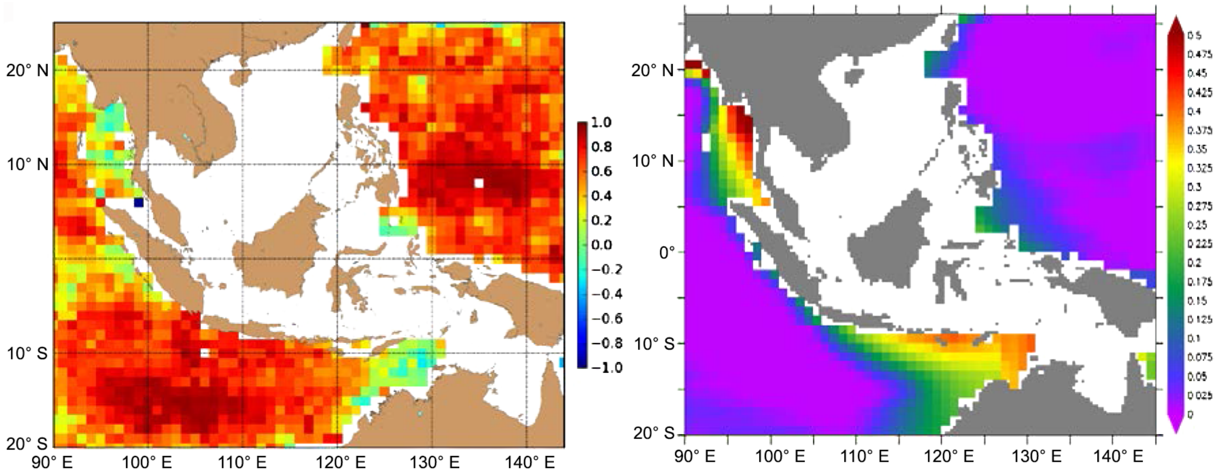

Figure 9. Mean temporal correlation between the (INDO12-Aquarius) SSS bias and the (INDO12-JAMSTEC) SSS bias and salinity interpolation error of JAMSTEC (ARGO + TRITON + CTD) calculated from August 2011 to December 2013.

(evaporation–precipitation) bias in the ECMWF precipitation flux where the model simulation of precipitation is particularly poor over Indonesia (see Kidd et al., 2013; Dee et al., 2011). In a recent paper, Zeng et al. (2014) argue that the smaller LST (Luzon Strait Transport) is a plausible cause of the freshening in 2012. In our model, the too strong freshening could also be due to a too weak transport at Luzon.

A positive bias exists in the southern tropical Indian Ocean except during April–May–June when the bias tends to be negative. There is a seasonal variation of the bias into the Pacific. In the interior domain, the bias is less pronounced and there is not a seasonal signal.

RMSD and correlations in SSS between Aquarius and INDO12 are quite similar to those between JAMSTEC and INDO12 in the Pacific and Indian oceans. In the interior domain, RMSD/correlation (Fig. 8) between Aquarius and INDO12 are larger/smaller in the Java Sea (monsoon variability), in the Gulf of Thailand and in the Taiwan Strait (probably due to land contamination).

A region in the Indian Ocean (95° E–15° S) is characterised by a smaller correlation between both INDO12 and both data sets. It is certainly due to a systematic bias in the boundary conditions. This bias can be related to a lesser accuracy of MDT (mean dynamic topography) (Rio et al., 2011) in the South Indian Ocean. Indeed, the MDT is involved in the process of SLA (sea level anomaly) data assimilation in the parent ocean forecasting system. From Fig. 9 (left), we show that in the Indian Ocean, the three main opposite differences (statistically significant) between the two data sets (uncorrelated biases) are in the Timor Sea, in the Andaman Sea and on the west-coast of Sumatra. These differences can be partially explained by the salinity interpolation errors shown on Fig. 9 (right) since the maximums are found at the same locations. The Timor Sea is mainly located on the continental shelf, which would results in the large interpolation errors due to the absence of ARGO floats. An uncorrelated bias exists at the entrance of the Indonesian domain, in the Celebes Sea and corresponds to the maximum of the salinity interpolation errors.

Due to the lack of JAMSTEC data in the interior domain, it is difficult to conclude on the quality of Aquarius data. Nevertheless, comparisons in the SCS (Sect. 3.5.3) have shown that the INDO12 model is fresher than the in situ data at the surface, which is corroborated here with Aquarius data.

3.5 SST: comparisons to AMSR-E and Argo monthly data

The SST of the Indonesian seas is of major interest to air–sea interaction at regional and global scales (see for example Sanchez et al., 2008). This is due largely to the convection process.

3.5.1 AMSR-E data

We use the SST data retrieved from observations of the satellite microwave radiometer Advanced Microwave Scanning Radiometer on board EOS (AMSR-E). The advantage of using microwave data instead of infrared data is that the clouds' influence can be neglected. For this study, in order to be close to the horizontal resolution (1° × 1°) of JAMSTEC (see above), we use the nighttime monthly averages SST map (1° × 1°) from the AMSR-E version 7 SSTs (see www.remss.com). The TAO array shows AMSR-E to have very small biases (−0.03 °C) and SD (0.41 °C) (Gentemann et al., 2010).

3.5.2 JAMSTEC data

As in Tang et al. (2014), we use a monthly gridded data set of global oceanic temperature on 1° × 1° grid processed and de-

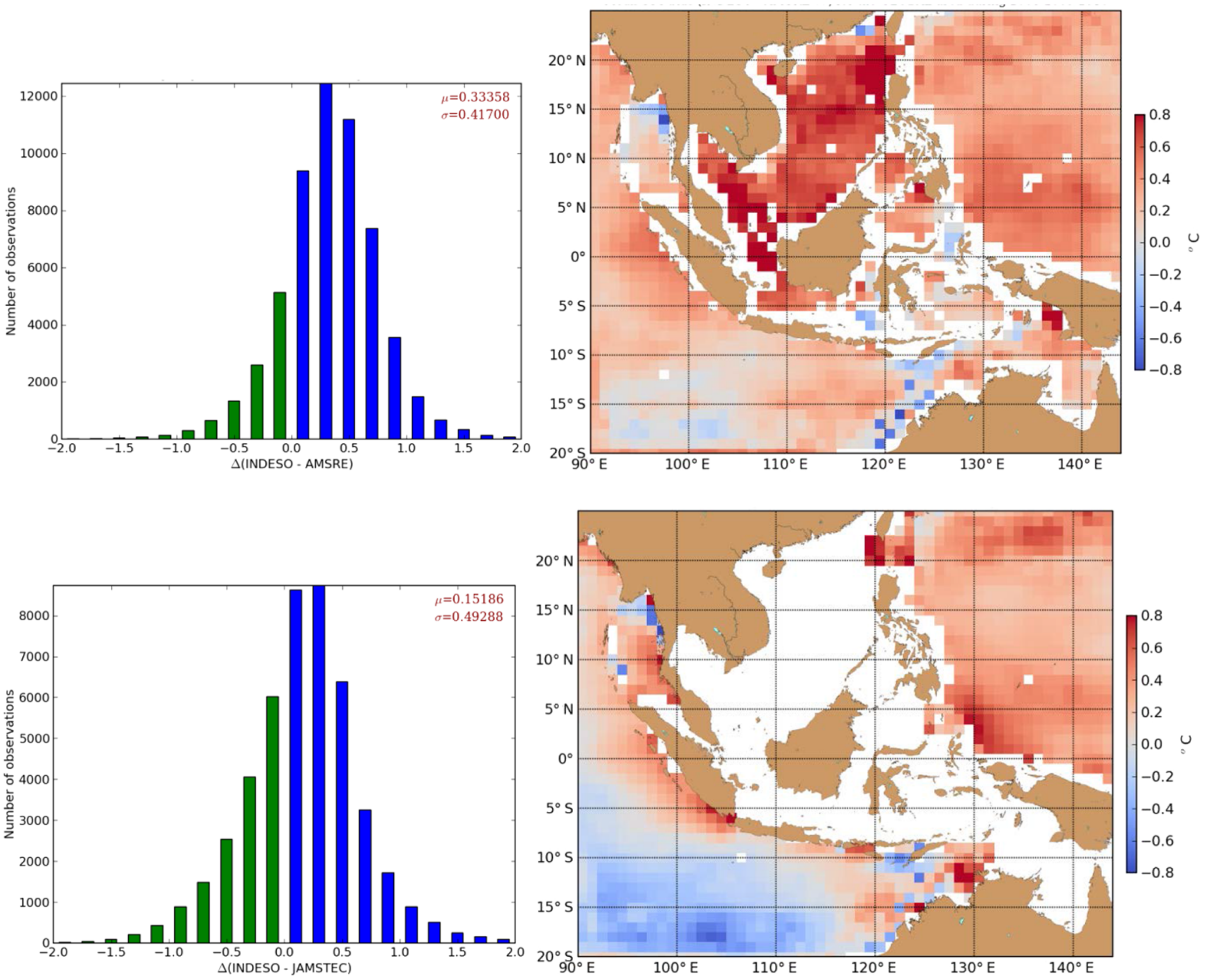

Figure 10. Mean bias (°C) of the INDO12 SST (monthly means) relative to AMSR-E (V7.0) (top) and JAMSTEC (ARGO + TRITON + CTD) (bottom) for the years 2008–2010.

livered by the JAMSTEC (Hosoda et al., 2008). This product is derived from the use of the OI method that builds the gridded fields from ARGO floats, TRITON, and available CTD.

The temperature values at 10 m depth from INDO12 are used to compare with the first level of JAMSTEC temperature at 10 dbar (∼ 10 m depth).

3.5.3 Results

Compared to both data sets, the SST in the model is too warm overall (Fig. 10). The SST bias is larger in the SCS where the influence of SCSTF is important (Qu et al., 2006) through the Luzon Strait. Positive biases are of similar amplitude between the two data sets and are mainly located in the Pacific region. This increased the confidence in the positive bias in the SCS and corroborates the negative bias in the SSS. A too weak deep-water overflow in the Luzon Strait can also explained this large bias. Zhao et al. (2014) show that enhanced mixing in the SCS is a key process responsible for the density difference between the Pacific and SCS, which in turn drives the deep circulation in the Luzon Strait.

There is only one important region where the INDO12 SST is significantly too cold, it is in the southern part of the INDO12 domain, i.e. in the southern tropical Indian Ocean. The negative bias relative to JAMSTEC is larger than the bias relative to AMSR-E as it is for the RMSD (Fig. 11). It is localised in the Eastern Gyral Current (EGC) that flows eastward near 15° S, i.e. in the same region where a positive SSS bias exist (see previous section). In the Indonesian Archipelago, the SST bias relative to AMSR-E is slightly positive except in the Flores and Molluca seas and in the Timor Passage where the bias is slightly negative. The Timor Passage is the only region where a non-correlated bias exists between the two data sets (Fig. 12a). It still corresponds to the maximum of the temperature interpolation errors (Fig. 12b) in JAMSTEC. The temporal correlation (Fig. 11) is rather high everywhere and consistent between

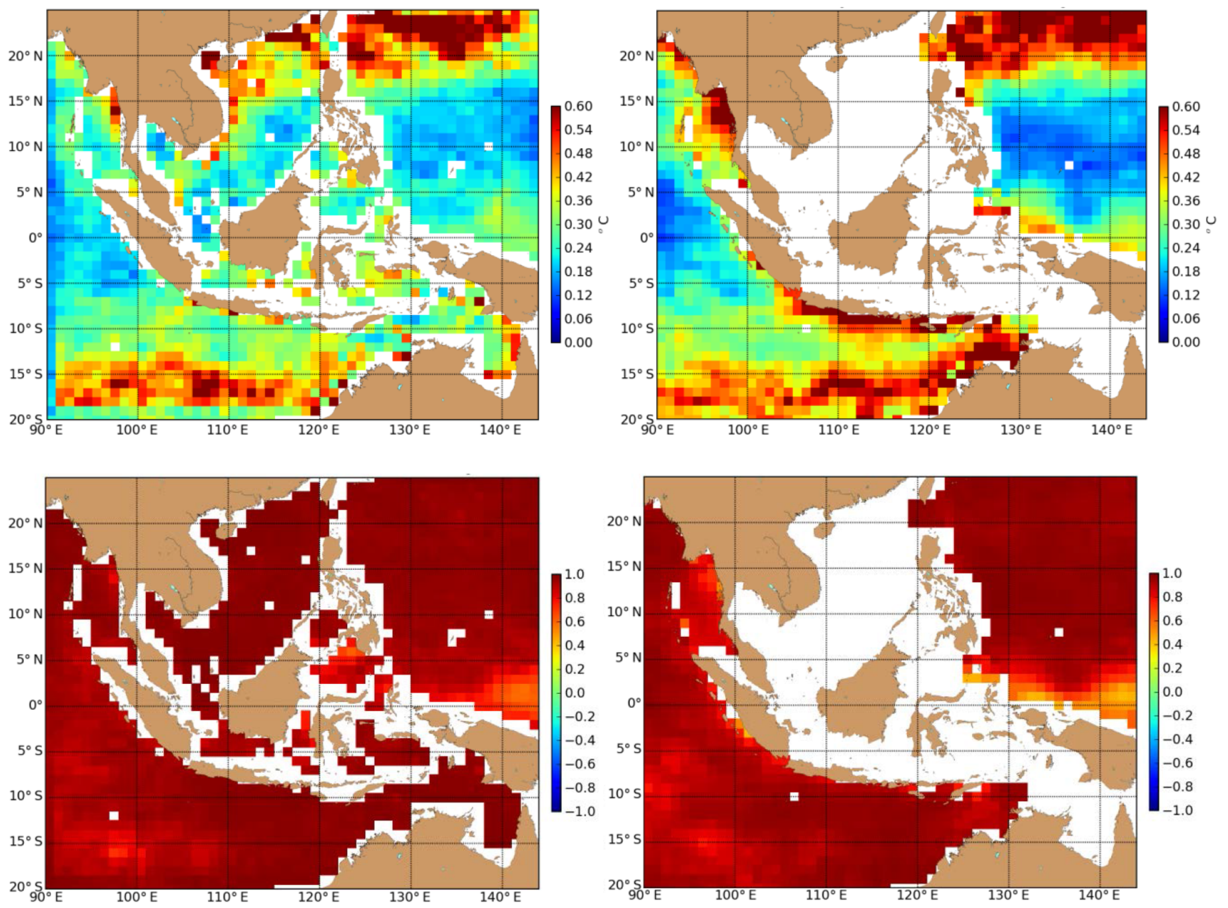

Figure 11. RMSD (top) and correlation (bottom) of INDO12 SST with respect to AMSR-E (left) and JAMSTEC (ARGO + TRITON + CTD) (right) calculated from monthly means (2008–2010).

two data sets. Only one region located near the Halmahera eddy and along the SEC seems less correlated.

3.6 Volume transport (ITF and SCSTF)

The ITF flows along three main routes (Sprintall et al., 2004) and a good representation is given in (Gordon et al., 2012; Fig. 1).

The main western route is the flow taken by the North Pacific Subtropical Water coming from the North Equatorial Current (NEC) via the Mindanao Current through the Celebes Sea, along the Makassar Strait, into the Flores Sea and the Lombok or the Ombaï straits into the Indian Ocean. In the southern part of the Makassar Strait, only the upper thermocline waters can flow southward into the Flores and Banda seas due to the Dewakang sill (650 m).

The second path is taken by the South Pacific subthermocline water, going from the SEC through the Maluku Sea and the Lifamatola Strait into the Banda Sea and further through the Ombaï Strait or the Timor Passage into the Indian Ocean. The Lifamatola Strait, at 1940 m, regulates the flow of deep Pacific water into the interior Indonesian seas. Talley and Sprintall (2005) show that the IIW (Intermediate Indonesian Water) attains most of its characteristics immediately downstream of the Lifamatola Strait as a result of the diapycnal mixing of the intermediate Pacific Ocean water masses. They also estimate a large total southward transport (∼ 3 Sv). Below 1250 m, the average volume transport through Lifamatola during INSTANT (about 1.5 years between January 2004 and July 2005) was 2.5 ± 1.5 Sv (van Aken and Brodjonegoro, 2009). It is a fairly robust number with an uncertainty of ∼ 5 % below 1250 m, which is not the case above 1250 m with an uncertainty that exceeds 50 % (Gordon et al., 2010). Finally, the total transport measured by INSTANT (El Niño period) below 200 m is 1.1 Sv. In our simulation (2008–2013), the total transport is quite null and flows northward (1.6 ± 3 Sv) below 1250 m with no inter-annual variability. Above 1250 m, the net inflow is southward and varies with ENSO (El Niño–Southern Oscillation). It is stronger during La Niña and weaker during El Niño. From Fig. 13, we show that the upper thermocline waters flow southward. The flow is northward between 400 and 1400 m. The only deep water flowing southward is located below 1400 m with a maximum near 1700 m depth in spite

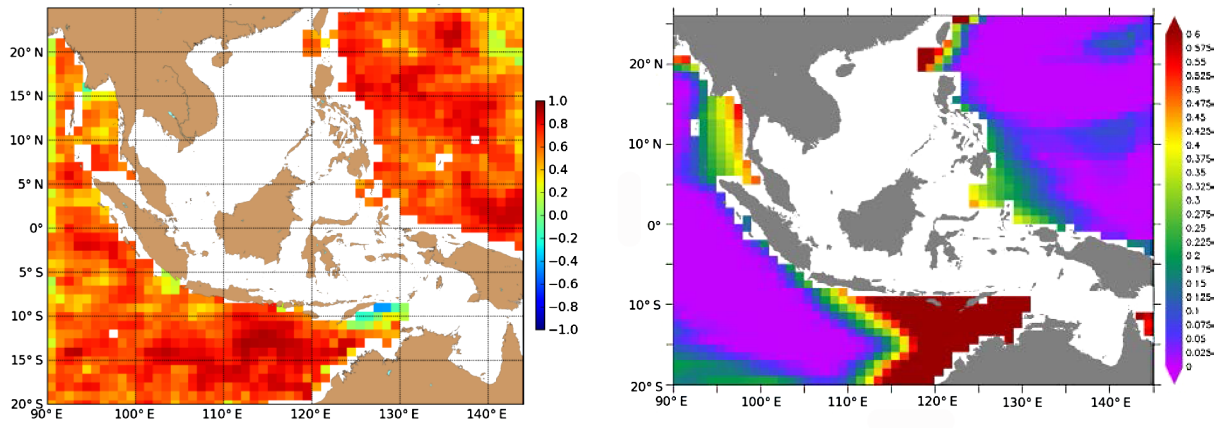

(a) (b)

Figure 12. Mean temporal correlation between the (INDO12-AMSR-E) SST bias and the (INDO12-JAMSTEC) SST bias **(a)** and temperature interpolation error of JAMSTEC (ARGO + TRITON + CTD) **(b)** calculated from 2008 to 2010.

Table 2. Mean volume transport in the ITF (Sv and Ratio) for Lombok Strait, Ombaï Strait and Timor passages. Mean values from INSTANT (2004–2006) and from the INDO12 simulation (2008–2013).

Straits	INSTANT (2004–2006)		INDO12 (2008–2013)	
	Sv	%	Sv	%
Lombok	2.6	17.3	2.07	16.7
Ombai	4.9	32.7	2.76	22.2
Timor	7.5	50	7.58	61.1
Total	15		12.41	

of the presence of an opposite flow on the eastern side of the strait. It is a strong discrepancy with measurements and can be attributed to the bathymetry located upstream of the strait or to the open-boundary conditions.

The SPSW (South Pacific Subtropical Water) from the SEC takes the third route through the Halmahera and Seram seas and joins the second route waters in the Banda Sea.

We consider the transport through the three major outflow passages of Lombok, Ombaï and Timor to determine the ITF transport estimates as in Sprintall et al. (2009). Table 2 gives absolute values of transport in each strait and total transport for the 2008–2013 simulated period compared to the INSTANT estimates (Gordon et al., 2010). The total value measured by INSTANTS (15 Sv) is stronger than in the model (12.4 Sv). This might be attributed to the prescribed ocean forcing fields given by the Mercator Océan Global Ocean Forecasting System at 1/4° (PSY3V3R3) and to an inaccurate bathymetry in the important straits. Also, INSTANT estimates and simulated INDO12 volume transports are not calculated over the same period and therefore have different ENSO signals.

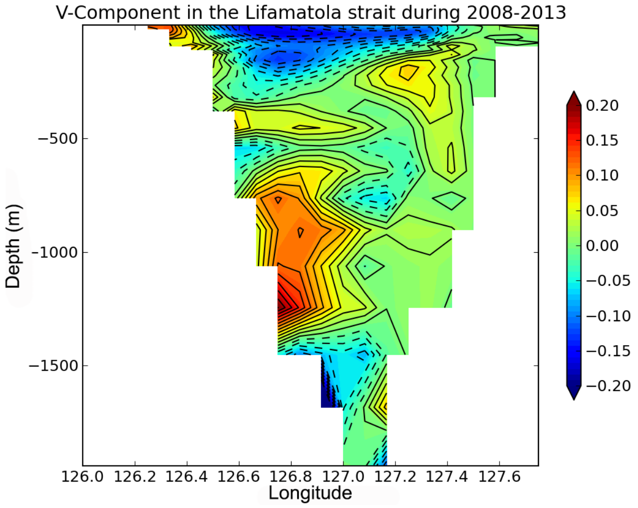

Figure 13. Mean of the along-strait velocity ($m\,s^{-1}$) in the Lifamatola Strait (2008–2013). Contour (dashed lines) means a negative value (southward flow). Contour (solid lines) means a positive value (northward flow).

Significant transport variability during the INSTANT period is linked to the ENSO and to the IOD (Indian Ocean Dipole) phenomena (Sprintall et al., 2009; Gordon et al., 2008; Van Sebille et al., 2014). The INSTANT estimates also reveal inter-annual fluctuation; see Table 1 of Gordon et al. (2010). Nevertheless, Sprintall and Revelard (2014) argue that the 3-year time series alone is not sufficient to comprehensively resolve the inter-annual signal. In the INDO12 simulation, Fig. 14 shows that a strong inter-annual variability exists and is more or less pronounced depending both on locations and on competing ENSO/IOD events. In 2008 and 2013, ENSO and IOD signals are generally weak but the simulated ITF transports are among the largest in the pe-

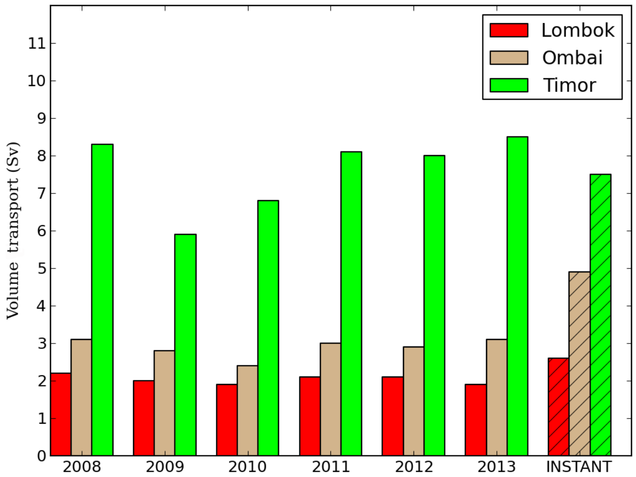

Figure 14. Model volume transport (Sv) into three main exits: Lombok (red), Ombaï (Brown), Timor (green) at different years. The Instant estimates (2004–2006) are shaded.

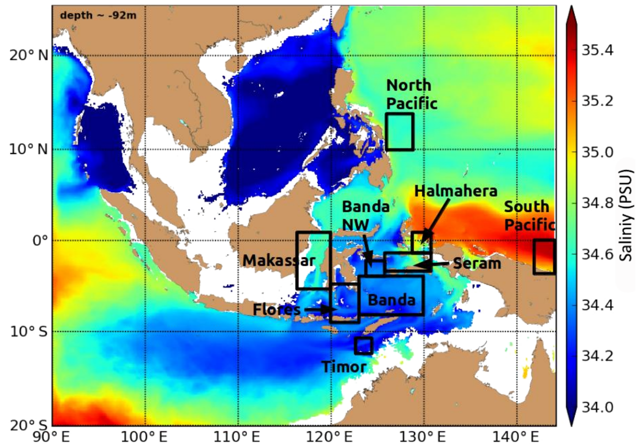

Figure 15. Main areas of water mass transformation. Colour shading indicates salinity at 92 m depth.

riod, particularly in the Ombaï and Timor straits. In 2011 and 2012, there is no ENSO event and a positive IOD, and it gives quite equivalent total transports. In 2009, the only El Niño of the simulation period takes place and no IOD event; consequently, the weakest ITF transport of the period occurs that year. In 2010, La Niña coincides with a negative IOD. In this case, the ITF transport is reduced with the weakest transport in Ombaï and the negative IOD seems to prevail. In a recent paper, Sprintall and Revelard (2014) argue that Indian Ocean dynamics likely win out over the Pacific Ocean dynamics during concurrent ENSO and IOD events. Indeed, the ITF transport variability would be linked both to spatial patterns of SLA and to zonal wind stress anomalies. During concurrent La Niña and negative IOD events (e.g. 2010), a stronger SSH signature exists in both the Pacific and Indian Oceans with higher SLA throughout the Indonesian Archipelago. At the same time, a westerly wind anomaly (September–December) in the tropical Indian Ocean would reverse the upper layer of the ITF transport (Lombok, Ombaï and Timor) via the downwelling Kelvin waves. Whereas during a solo La Niña event, only a slight SLA imbalance exists in the Pacific latitude bands around 5–10°. This leads to off-equatorial Rossby waves, which result in an increase in Timor volume transport as suggested by McClean et al. (2005). Note that during the INDO12 simulation (2008–2013), there was no such event.

In order to better compare the relative transport in each of the three exit straits, we give the ratio with regard to the total mean transport volume and compare them with INSTANT estimates (Gordon et al., 2010); see Table 2.

On the one hand, this ratio (%) in the INDO12 simulation is very close to the INSTANT estimates values for Lombok Strait, but on the other hand this ratio is lower for the Ombaï Strait and stronger in the Timor Passage. However, if we compare the absolute volume transport (Sv) in the Timor Passage, it compares favorably to INSTANT estimates, whereas the Ombaï Strait transport is substantially weaker than INSTANT estimates; see also Fig. 14. In a recent paper, Oke et al. (2013) found the same kind of differences with a longer reanalysis.

The SCSTF affects the near-surface flow in the Makassar Strait (Qu et al., 2006). It leads to the subsurface maximum in the southward current of the Makassar Strait. Gordon et al. (2003b) showed that the intrusion of freshwater from the SCS effectively inhibits the Makassar Strait surface water from freely flowing southward. As a consequence, the ITF heat transport is significantly reduced during the northeast monsoon season. The Luzon Strait is the major pathway between the SCS and the Pacific Ocean. The LST is estimated to be westward and about -4 ± 5.1 Sv at 120.75° E (Hsin et al., 2012). In the INDO12 simulation, this volume transport is westward and around -0.4 Sv. This leads to a lack of salt water coming from the Pacific Ocean. Recent studies suggested different ways of improvement. Hurlburt et al. (2011) shows that simulations are very sensitive to model resolution and to the accuracy of the topography and sill depths within the narrow straits in the Philippine Archipelago. More recently, Zhao et al. (2014) show that the transport of the deep circulation increases with diapycnal diffusivity in the deep SCS and Luzon Strait.

3.7 Water masses transformation

In this section, we deal with the water masses transformation in the Indonesian seas. We compare INDO12 T–S diagrams with WOA 2013 climatology and with parent model (PSY3) in several sub-basins along the pathways within the Indonesian Archipelago as in Koch-Larrouy et al. (2007); see Fig. 15. T–S diagrams of parent and INDO12 models are compared to INDOMIX CTD data in July 2010 (Koch-

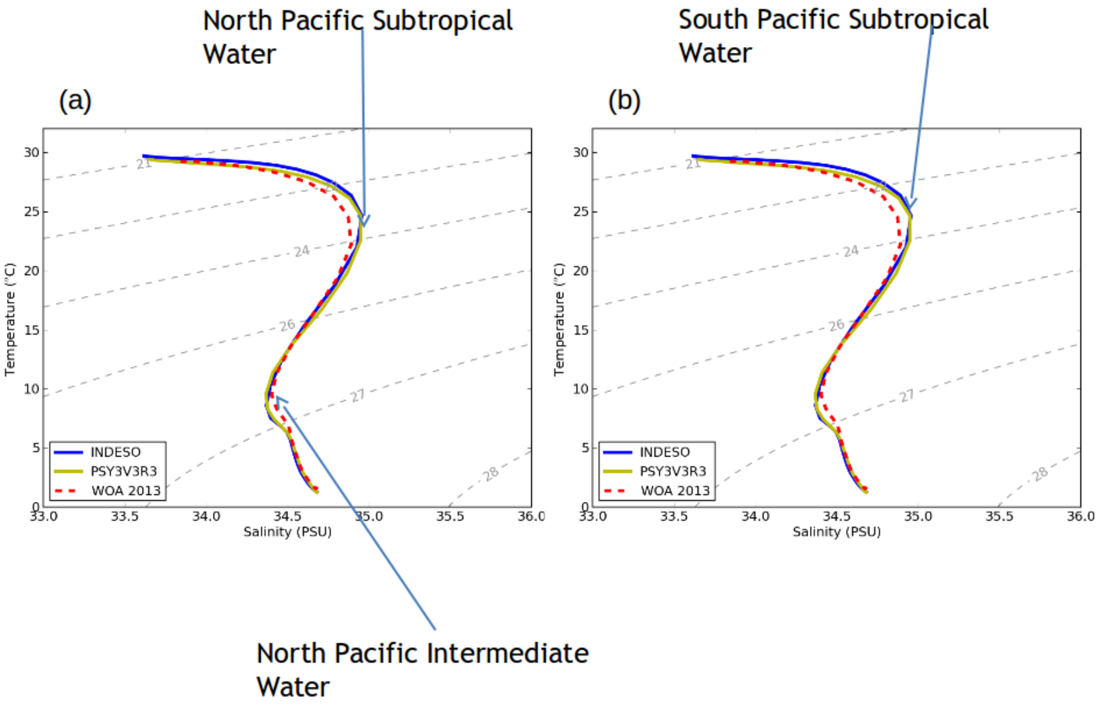

Figure 16. T–S diagrams from INDO12 simulation (green line) averaged on the North Pacific area **(a)** and the South Pacific area **(b)** and compared to climatologies WOA 2009 (dotted line) and PSY3V3R3 (yellow) in 2012. Salinity (PSU) and temperature (°C) are plotted along x and y axes, respectively.

Larrouy et al., 2015). Model and climatology (WOA2009) T–S diagrams are also compared to instantaneous data (WOD 2013) on both sides of Luzon Strait.

In addition to these T–S diagrams, we highlight different biases into the MLD (mixed layer depth) that give indications on upper ocean stratification.

3.7.1 Comparisons with parent model and WOA2013 climatology

Water masses from the INDO12 simulation (averaged all over the period from 2008 to 2013) are compared with those of the WOA 2013 climatology (Boyer et al., 2013) and with those of the parent model (PSY3V3R3) in main areas of water mass transformation, see Fig. 15.

At the main entrance, the Mindanao Current drives the North Pacific water characterised by a salinity maximum (34.8 PSU), the NPSW and a minimum of 34.2 PSU (North Pacific Intermediate Water, NPIW). Coming from the North Pacific, the NPSW is saltier in the INDO12 simulation than in the WOA 2013 climatology. The NPIW and the surface water are fresher (Fig. 16a).

SPSW enter also into the Indonesian seas and are characterised by a salinity maximum around 35.45 PSU. Compared to the WOA 2013 climatology, the SPSW in the INDO12 simulation are slightly too warm at the surface and at the sub-surface (Fig. 16b).

Because open-boundary conditions are close to the North and South Pacific waters properties, the INDO12 and parent model (PSY3V3R3) differ from WOA 2013 climatology in the same way.

When comparing T–S diagram in the interiors seas between the regional model that includes tidal mixing to the parent model that does not include any additional mixing, we find that the tidal mixing of the SPSW has occurred before entering the Banda Sea (Fig. 17a, b, c). In the Banda, Seram and Timor regions, the North and the South Pacific subtropical salinity maximums are strongly attenuated in the INDO12 simulation. It is not the case for the parent simulation.

In particular, the SPSW salinity maximum is strongly eroded from its entrance in the Halmahera Sea and vanishes already in the Seram Sea as noted by Koch-Larrouy et al. (2007). The tidal mixing strongly improves the water masses. However, there are still some biases between the climatology and the INDO12 simulation that could come from observed biases at the entrance of the domain.

During their residence in the Indonesian Archipelago, the incoming Pacific waters are transformed to produce a unique water mass associated with a unique homohaline tropical stratification (34.58 PSU, below 20 °C); see T–S diagrams in the Timor region on Fig. 18. In the Timor and Banda regions, at the surface there is a strong freshening compared to the climatology. But comparisons do not take into account the

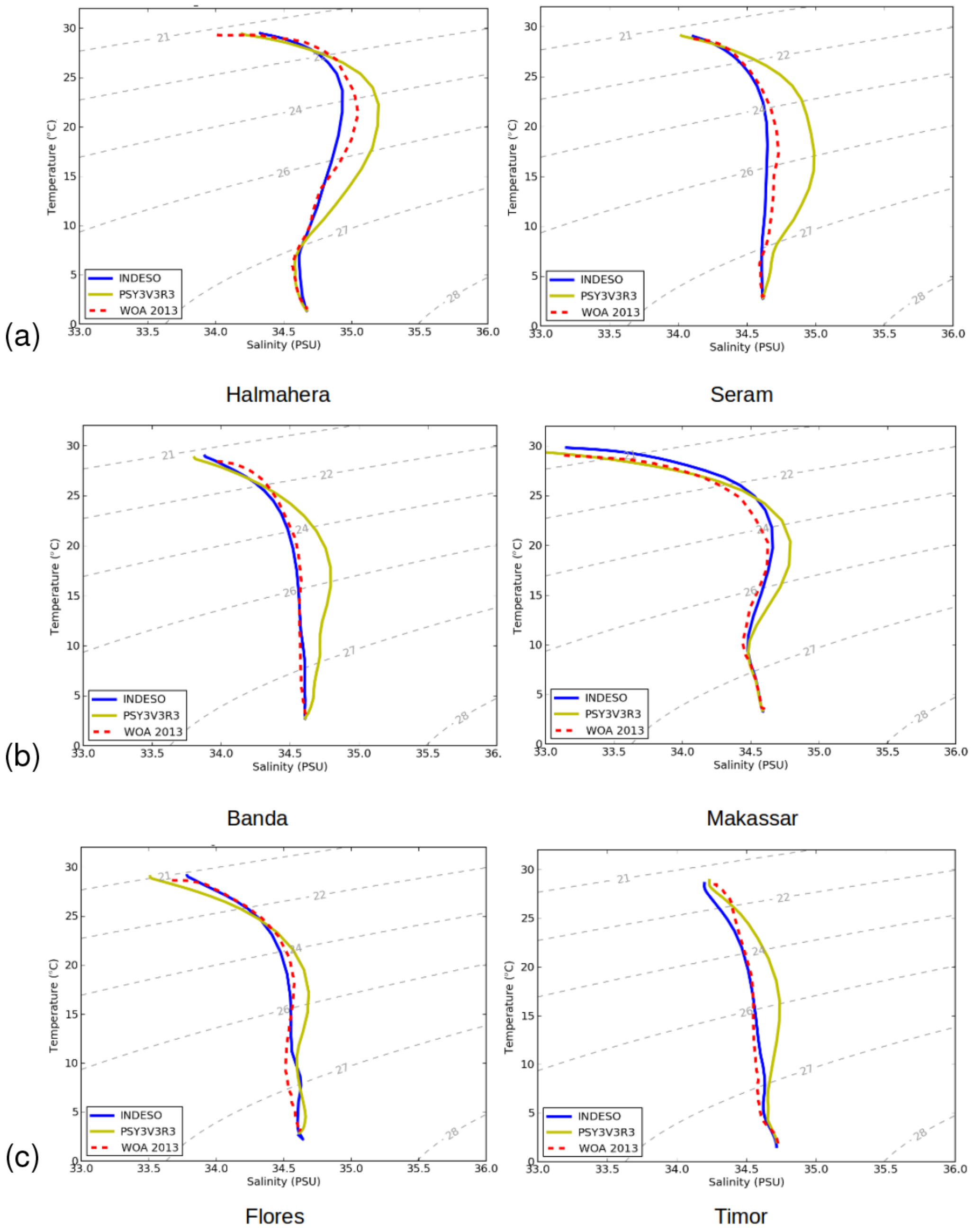

Figure 17. T–S diagrams from INDO12 simulation (blue line) averaged on different areas, **(a)** Halmahera Strait and Seram Sea, **(b)** Banda Sea and Makassar Strait, **(c)** Flores Sea and Timor Passage compared to climatologies WOA 2013 (red dotted line) and PSY3V3R3 (yellow line) for the 2008–2013 period. Salinity (PSU) and temperature (°C) are plotted along x and y axes, respectively.

inter-annual variability and some disparities exist depending on the year (Figs. 8 and 12). This freshening is not observed at the entrance of the Indonesian domain (NPW). It is due to the surface fresh water coming from the Java Sea water that represents the major freshwater input (70 %, Koch-Larrouy et al., 2008). Moreover, a too strong freshening is observed in the model (see Sect. 3.7.3 and 3.4.1). Surface water of Makassar Strait and Flores Sea are lower than 33.8 PSU. It is certainly due to a lack of salt water coming from the Pacific Ocean; see Sect. 3.6 and 3.7.3. This behaviour is enhanced in 2011 (Fig. 18) when the LST is the strongest (−1.19 Sv) in the INDO12 simulation. The effect of a too strong mixing in the Banda Sea (Fig. 17b) can also enhance the too strong freshening at the surface.

Comparing the model over a limited period of time to a climatology that suffers from a lack of data to properly

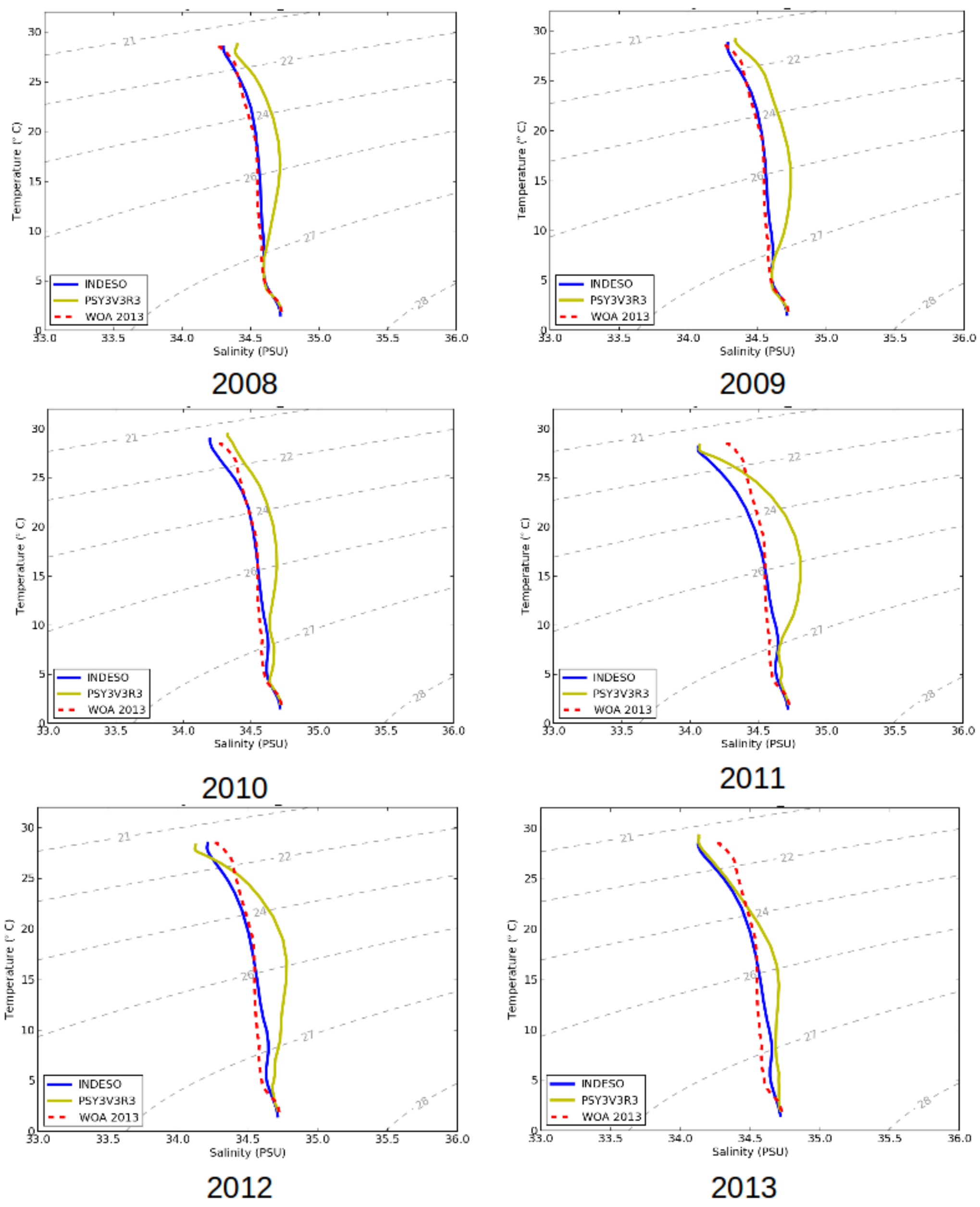

2008 2009 2010 2011 2012 2013

Figure 18. T–S diagrams from INDO12 simulation (blue line) averaged on the Timor region and compared to climatologies WOA 2013 (red dotted line) and PSY3V3R3 (yellow line) for years 2008 to 2013. Salinity (PSU) and temperature (°C) are plotted along x and y axes, respectively.

represent inter-annual variability and regional rapid changes between the seas of the archipelago, is an imperfect exercise to validate the model. Fortunately, the INDOMIX cruise occurred during the period of our simulation, providing a unique data set to validate the model.

3.7.2 Comparisons with CTD from INDOMIX campaign

The INDOMIX cruise (July 2010, Koch-Larrouy et al., 2015) recovers in situ measurements in one of the most energetic section for internal tides through the Halmahera Sea and the Ombaï Strait. Classical fine-scale CTD/LADCP measurements have been performed together with micro-structure measurements at five locations, two at the entrance of the Halmahera Sea (S0, S1), two in the Halmahera Sea (S2, S3),

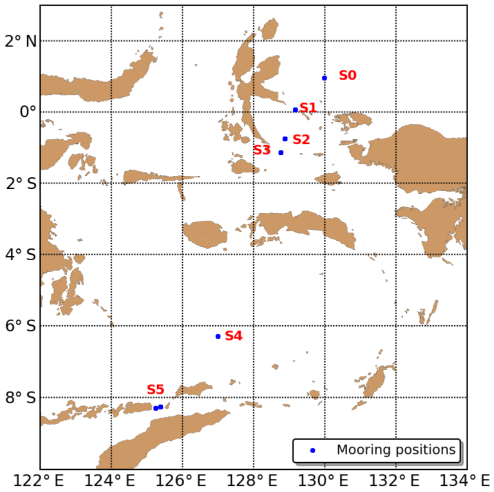

Figure 19. Locations of CTD moorings during the INDOMIX campaign (July 2010).

one in the Banda Sea (S4) and two (S5a/S5b) in the Ombaï Strait (Fig. 19).

Koch-Larrouy et al. (2007) argued that the vertical mixing due to internal tides of the SPSW occurs mainly within the Halmahera and Seram seas before entering the Banda Sea.

In the following section, we compared instantaneous INDOMIX profiles (July 2010) to parent model (daily mean) and to the INDO12 simulation (hourly instantaneous) profiles. We see that before entering the Halmahera Sea (Fig. 20/S0), a maximum of salinity is present, and is in better agreement with observations in INDO12 simulation compared to the parent model. The combined effect of the horizontal resolution and explicit tides has a crucial role. The INDO12 model exhibits a zigzag shape profile that suggests intense lateral mixing probably produces by the explicit tides.

In the Halmahera Strait (Fig. 20/S1), the salinity maximum has already been reduced both in the observations and in the simulations. The vertical mixing seems to be too strong in the INDO12 simulations since the mixed layer is too salty and the lower thermocline is warmer and fresher. It is in better agreement with observation than the parent model that exhibits strong salinity a maximum.

At the S2 and S3 locations in the Halmahera Sea (Fig. 20), T–S profiles display temperature and salinity structure with “wiggles” and step features in the thermocline (more pronounced than in S1 location). Ffield and Robertson (2008) found a similar temperature fine structures associated to the straits, the shallow shelves, and the proximity of the shelf-slope boundary in the Indonesian seas. This phenomenon seems to be amplified during the windy JJA southeast Monsoon time period when the upper thermocline is less stratified, especially during La Niña years that which corresponds to July 2010. They associated this temperature fine structure with internal wave activity that can be a precursor to turbulent vertical mixing. It is not clear if the horizontal and vertical resolution of INDO12 prevents the reproduction of this wave activity or if it occurs slightly away of the station location.

As in S1, the mixing seems too strong since the mixed layer is too salty and the lower thermocline is warmer and fresher.

INDO12 T–S diagrams compare quite well with the INDOMIX data in the Banda Sea (S4). It is the result of the mixing and the advection of water masses coming from the Java and the Flores seas. In the Ombaï Strait (S5), INDO12 fits very well with the INDOMIX data below the pycnocline. The NPIW (density 26.5) seems to be well mixed in the observations, certainly by isopycnal mixing but it is no the case in the INDO12 simulation where the NIPW signature is still present.

Finally, all T–S diagrams in the interior domain show that the parent model has definitively not enough efficient vertical mixing and that a higher-resolution model including explicit tides is needed to mix correctly Pacific waters in the Indonesian Archipelago.

It is also interesting to know where are located the most important bias and errors in the vertical. This gives an additional indication about the upper ocean stratification. In Fig. 21a, b, c, d, most of the salinity biases for INDO12 show two significant maximums, a negative bias in the mixed layer (0–50 m) and a positive bias at 150–200 m depth. The model is fresher than the observations in the lower thermocline where salty waters from SPSW penetrate into the Indonesian seas. Moreover, this twice as large for S0 (Fig. 21a) as for S1, S2 and S3 (Fig. 21b, c, d). As previously mentioned, this indicates that an excessively strong mixing occurs in the Halmahera Strait and the Seram Sea. The parent model shows a systematic negative bias over the whole water column for salinity with two pronounced peaks near the SPSW penetration and in the mixed layer. Except in S0 where two peaks exist, maximum errors (RMSD) are found below the mixed layer depth (near 100 m), i.e. in the upper thermocline. In S4 (Fig. 21e), a positive salinity bias exists only in the mixed layer depth for INDO12 whereas in S5 (Fig. 21e) a slight salty bias exists over the whole water column with a maximum in the upper thermocline. Except in S0, INDO12 temperature at S1, S2 and S3 is too warm (negative bias) down to 300 m depth, i.e. in the lower thermocline. Below 600 m depth, a cold bias exists (positive) with a gradually increase at S2 (Fig. 21c). In S4 (Banda Sea), it is quite different since two opposite biases exist in the lower and upper thermocline and no more significant positive bias for deep layers. As previously mentioned, the NIPW signature is present at S5 location (Fig. 21f) with a larger bias near 800 m depth but with also a larger variability since the RMSD is larger.

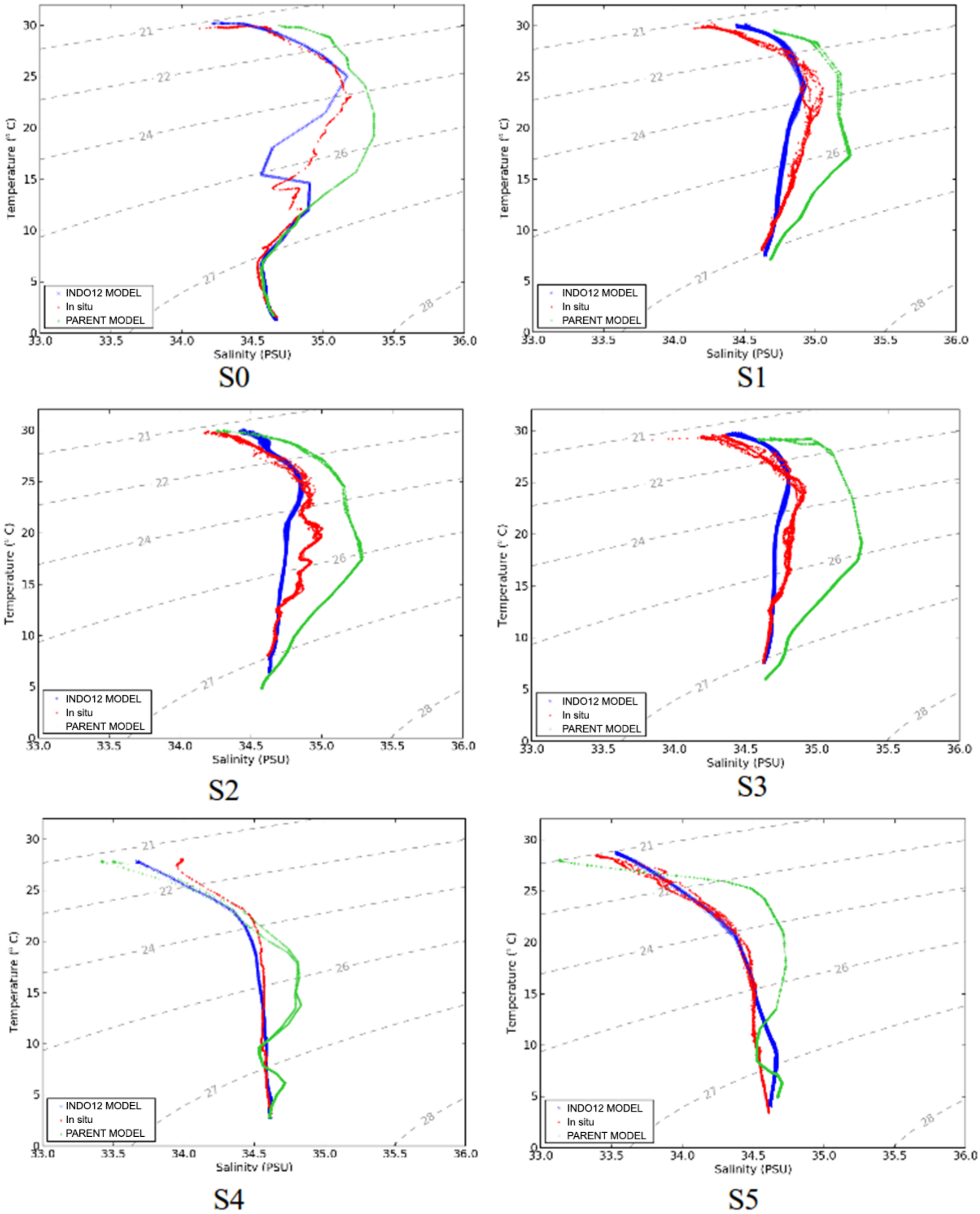

Figure 20. Collocated T–S diagrams to INDOMIX data (red) from hourly fields of INDO12 simulation (dark blue) and from daily mean fields of parent model PSY3 (green) in July 2010 at all mooring locations. Salinity (PSU) and temperature (°C) are plotted along x and y axes, respectively.

3.7.3 Comparisons to in situ data in the SCS (October–December 2013)

Comparisons of INDO12 simulations and WOA 2009 climatology collocated with real in situ profiles (WOD 2013) have been done in on both sides of the Luzon Strait for the autumn 2013 (October–December). We focus on the SCS region that is connected to the Pacific Ocean through the Luzon Strait in the northern part. In the southern part of the basin, the region links with the Java Sea through the Karimata Strait, and with the Sulu Sea through mainly through the Mindoro Strait. The fresh SCS water entering the Java Sea through the Karimata Strait inhibits the warm surface water from the

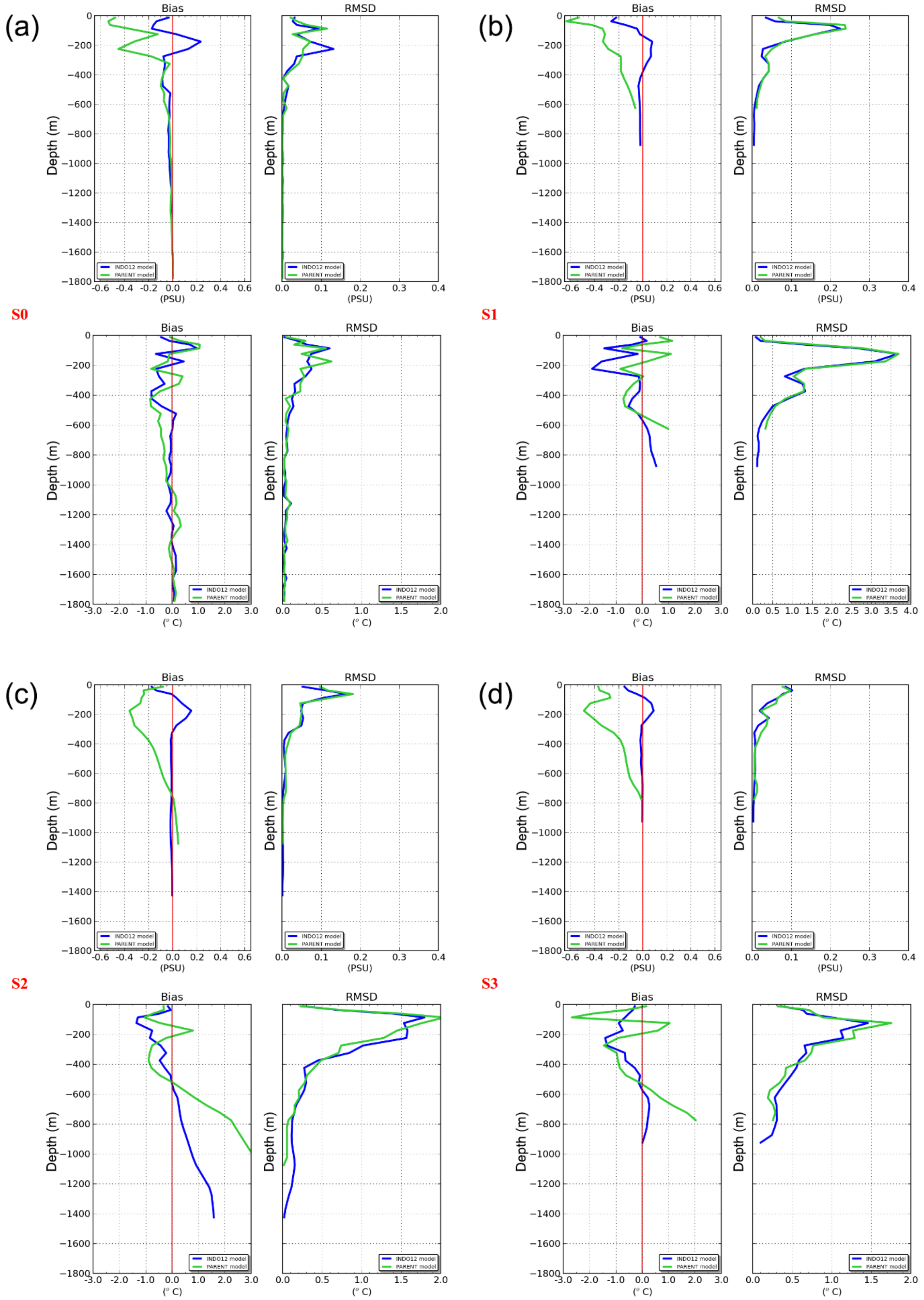
(a)
(b)
(c)
(d)
S0
S1
S2
S3
Bias
RMSD
Depth (m)
0
−200
−400
−600
−800
−1000
−1200
−1400
−1600
−1800
-0.6 -0.4 -0.2 0.0 0.2 0.4 0.6
0.0 0.1 0.2 0.3 0.4
(PSU)
-3.0 -2.0 -1.0 0.0 1.0 2.0 3.0
0.0 0.5 1.0 1.5 2.0
0.0 0.5 1.0 1.5 2.0 2.5 3.0 3.5 4.0
(° C)
INDO12 model
PARENT model

Figure 21.

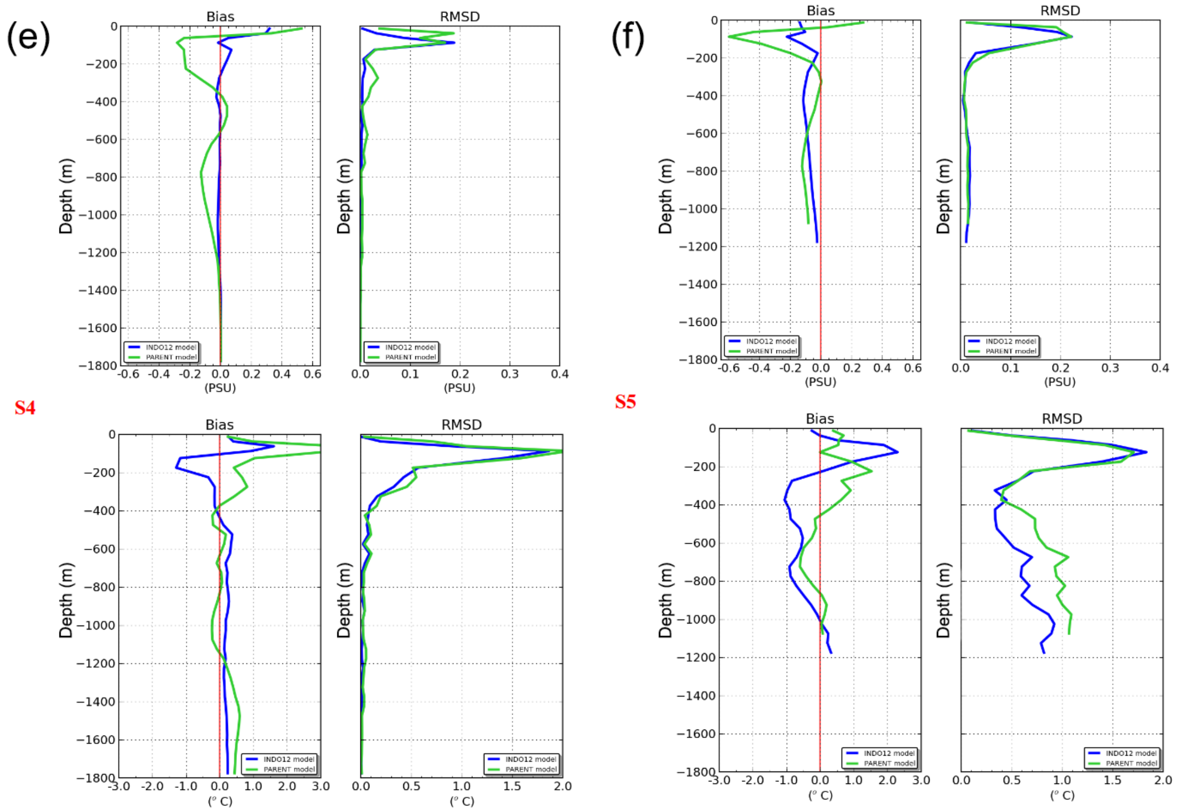

Figure 21. Bias and RMSD of salinity (up) and temperature (bottom) between INDOMIX data and INDO12 (blue line) and parent model PSY3 (green line) at at all mooring locations. Data are binned in 25 m depth intervals for the first 100 m depth and in 50 m depth interval for deeper layers.

Pacific flowing southward in the Makassar Strait during the boreal winter (Gordon et al., 2003b; Qu et al., 2006; Tozuka et al., 2007). As the Makassar throughflow amounts to 80 % of the total ITF, the SCS effect is a major contributor to the overall variability of the ITF vertical structure. Whereas that the Karimata transport is mostly seasonal (Fang et al., 2010), the circulation of the SCS demonstrates an inter-annual variation related to the ENSO. Gordon et al. (2012) suggest that the building of a “freshwater plug” in the western Sulawesi Sea (via the Sibutu Passage) during prolonged El Niño periods inhibits the Mindanao surface layer injection into the Makassar Strait. On the contrary, during La Niña the “freshwater plug” is dissipated, which leads to the penetration of surface water from the tropical Pacific Ocean.

On both sides of the Luzon Strait (Fig. 22), the INDO12 model tends to be fresher mainly at the surface. This indicates that not enough Pacific waters enter into the SCS and it corroborates the too weak volume transport of thermocline waters observed at the Luzon Strait, see Sect. 3.6. The INDO12 model (Fig. 22a) show NPSW and NPIW already shown previously (Fig. 16a) and it is quite close to observations. In the SCS (Fig. 22b), the INDO12 model is too fresh. T–S profiles shows that vertical mixing acts by disrupting the NPSW but in a too strong way by the INDO12 model. The SCS region is known as a place where the representation and the localisation of internal waves and their associated vertical mixing is still difficult to quantify. Recently Alford et al. (2015) made new measurements in the Luzon Strait to better understand the formation of the world’s strongest known internal waves.

As in the previous section, the bias and the RMSD of salinity and temperature are shown on both sides of the Luzon Strait; see Fig. 23a, b. On the eastern side of Luzon Strait (Fig. 23a), salinity biases are mainly located in the first 50 m and are significant for the INDO12 model only. After the Luzon Strait, salinity biases are larger and spread deeper down to 200 m for the INDO12 model only. The climatology seems to have no significant biases and RMSD of salinity is equivalent for the climatology and the INDO12 model. For temperature biases, opposite biases exist for the INDO12 models and in a lesser extend for the WOA 2009 climatology. From too cold (positive bias) on the eastern side of the Luzon Strait, the sea surface temperature becomes too warm (negative bias) on its western side and systematically too cold from the upper thermocline to the bottom. It is not the case for the

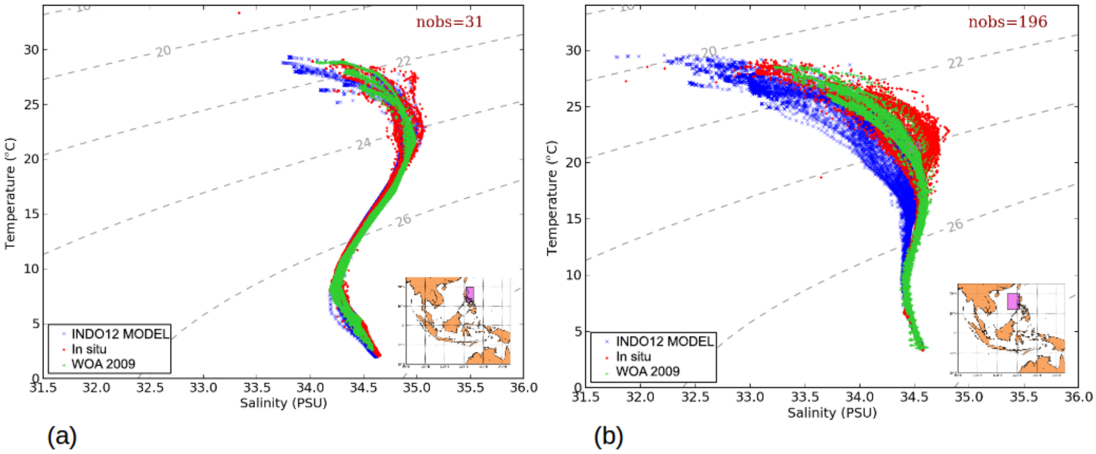

Figure 22. Collocated T–S diagrams to in situ data (red) from INDO12 simulation (blue) and from climatology WOA2009 (green) on both sides of the Luzon Strait (purple square) from October to December 2013. Salinity (PSU) and temperature (°C) are plotted along x and y axes, respectively.

WOA 2009 climatology that is systematically too cold (positive bias) over the whole water column.

4 Summary

The INDESO operational system has been designed to monitor the evolution of the circulation, biogeochemistry and fish population dynamics within the Indonesian seas. Practically, INDESO addresses the needs of the Balitbang KP for a complete new oceanographic centre in Perancak, Bali, from the building to the computer systems, the satellite antenna, and the transfer of expertise to the Indonesian experts. Since mid-September 2014, the entire system (Ocean, Biogeochemistry and Fish population dynamics) is fully operational in Perancak (see http://www.indeso.web.id) and delivers 10-day forecast/2 weeks hindcast on a weekly basis. In order to validate the ocean physic, the INDO12 model based on NEMO 2.3 was integrated during 7 years (2007–2013). This period is fairly short but it was the longest operational period able to be constrained by the global ocean forecasting system at 1/4° (PSY3V3R3).

Overall, the mean circulation induced by the main equatorial and coastal currents (i.e. NGCC, SEC, NECC, SJC) is well reproduced by the INDO12 ocean model. Except in coastal regions, the EKE from INDO12 and the EKE derived from altimeter data share the same patterns. On both sides of the Luzon Strait, the weak EKE values from INDO12 corroborates the weak SCSTF. The model estimations of complex elevation amplitudes (amplitude and phase) agree reasonably well with the TOPEX/POSEIDON, JASON 1 and JASON2 crossover observations, with better agreement for the diurnal constituents K1 than the semidiurnal constituent M2. A power-spectrum analysis of the hourly SSH from tide gauges and from simulated moorings shows that the model is in very good agreement with the observations at low frequencies. It confirms that tides are a dominant forcing in the area, and that the tidal current is dominated by the diurnal (O1 and K1) and semidiurnal (M2 and S2) frequencies. The non-linear constituents (higher harmonics) contain less energy in the INDO12 model than the observations due to a lesser accuracy of non-linear processes near the coast. Compared to two different SST data sets, one from space (AMSR-E) and one from an in situ product (JAMSTEC), an overall warm bias exists and it is quite equivalent between the two data sets. It is also consistent with the SSS bias (fresh bias). Stronger values of the SST biases are located in the SCS. Only one region is too cold, it is in the southern tropical Indian Ocean. In the Indonesian Archipelago, it is difficult to discern a general trend due to the large interpolation errors and the lack of data.

We need to improve the large discrepancy in the SCS both for SSS and SST that are influenced both locally by the monsoons and remotely by the SCSTF/ITF. As mentioned by Qu et al. (2009), despite the considerable progress that has been made in the past years, our understanding of the SCSTF is far from complete. They also pointed out that Mindoro Strait can play a significant role by shifting the NEC bifurcation (Mindanao Eddy) and then the Kurushio intrusion. This enhances the importance to have realistic Pacific open-boundary conditions, which influences the position of the Mindanao Eddy. We show that monthly SSS from space (Aquarius V3.0) and from an in situ product (JAMSTEC) are quite consistent. This shows that the INDO12 model SSS is too low in the SCS and it corroborates the too weak volume transport of thermocline waters observed in the Luzon Strait. A positive bias exists in the southern tropical Indian Ocean (95° E–15° S) where a smaller correlation between both INDO12 and both the observation data sets exist. It is certainly due to a systematic

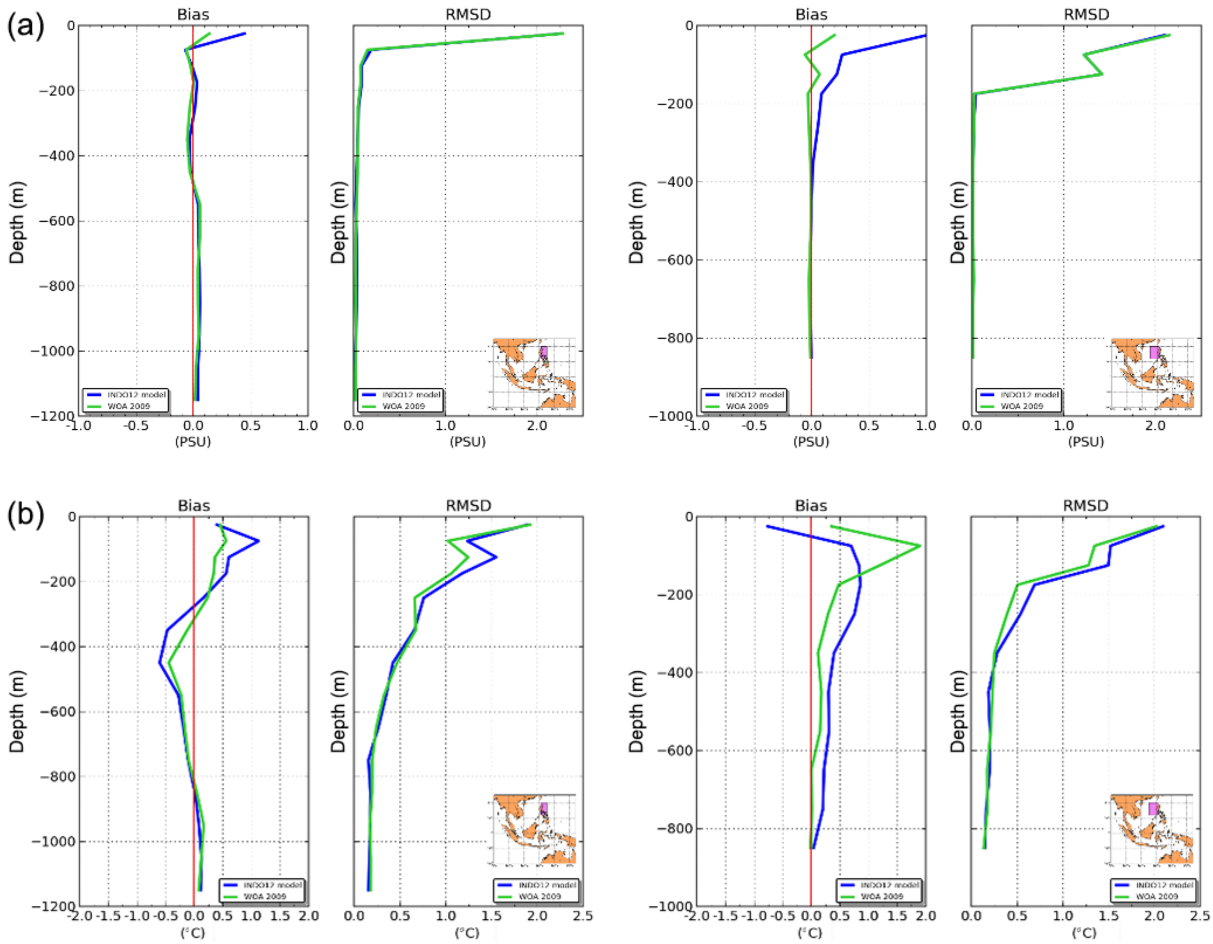

Figure 23. Bias and RMSD of salinity between real data (WOD 2013) and INDO12 (blue) and WOA 2009 (green) on both sides of Luzon Strait (purple squares) from October to December 2013. Data are binned in 50 m depth intervals for the first 200 m depths and in 100 m depth interval for deeper layers.

bias in the eastern boundary conditions related to a lesser accuracy of the MDT.

Zhao et al. (2014) show that the enhanced mixing in the SCS is a key process responsible for the density difference between the Pacific and the SCS, which in turn drives the deep circulation in the Luzon Strait.

The relative volume transport in the three major outflow passages in the INDO12 simulation is very close to one calculated from the INSTANT estimates. There is still an imbalance between the Timor Strait (too strong) and the Ombaï Strait (too weak). The LST is westward but still too weak. It could be due to the model resolution and to the accuracy of the topography in the Philippine Archipelago as suggested by Hurlburt et al. (2011). In a recent study, Zhao et al. (2014) argue that an increase of the diapycnal diffusivity in the deep SCS and the Luzon Strait enhances the transport of the deep circulation. A strong discrepancy exists between the few existing measurements and the INDO12 simulation in the Lifamatola Strait. As for the LST, it might be attributed to the bathymetry located upstream of the strait but also to the prescribed ocean forcing fields given by the Operational Ocean Forecasting System at 1/4° (PSY3V3R3). This could also explain the fact that the total transport in the INDO12 model is lower. Note also that the INSTANT estimates and the simulated INDO12 volume transports are not calculated over the same period (different ENSO/IOD signals).

The model is forced by explicit tides, which are able to generate part of the total internal tides energy. Accordingly to Niwa and Hibiya (2011), only 60 % of the baroclinic energy can be generated with a 1/12° model. The model is also forced by an existing parameterisation of the mixing (Koch-Larrouy et al., 2007). The resulting vertical mixing is able to erode the South and North Pacific subtropical water-salinity maximum as seen in the T–S diagrams. Compared to climatologies, the inflow coming from North Pacific seems too salty for NPSW and too fresh in surface for NPIW, the inflow coming from South Pacific seems too salty and too warm in surface and sub-surface. The SPSW salinity maximum is strongly eroded from its entrance in the Halmahera Sea and vanishes in the Seram Sea. A too fresh surface water mass coming from the SCS throughflow and also a too strong mixing in the Banda Sea could explain a strong surface freshening into the Timor water masses. Nevertheless, an interannual variability exists depending on the year.

Compared to data collected during the INDOMIX cruise, an excessively strong vertical mixing occurs in the INDO12 model into the Halmahera Sea, which is not able to reproduce the observed "wiggles" and step features in the thermocline. On the other hand, T–S profiles fit quite well in the Banda Sea and the Ombaï Strait. Finally, all T–S diagrams in the Indonesian Archipelago show that the parent model has definitively not enough efficient vertical mixing and that a higher-resolution model including explicit tides is needed to mix correctly the Pacific waters in the Indonesian Archipelago.

Compared to WOD (2013) in situ data, the INDO12 model tends to be fresher mainly at the surface in the SCS. This confirms what it has been previously observed in the SCS with SSS and SST satellite data. It is certainly the consequence of a too weak transport of Pacific water at the Luzon Strait.

Different possible ways of improving the INDO12 model can be suggested. A recent and better tidal forcing (FES 2012; see Carrère et al., 2012) could improve tidal currents. New boundary conditions from the 1/12° global ocean forecasting model are also planned and should be more consistent (same horizontal resolution and same bathymetry). In addition, the new 1/12° global ocean forecasting system will start from the WOA 2013 climatology. This new initialisiation should improve the deeper T–S biases found in the Indonesian Archipelago where there is not enough observation data to efficiently constrain the model with the data assimilation system. They could give us some indications of the Mindanao Eddy influence on the LST. Next developments should also include an improved bathymetry in major straits (entrance and exit). A specific study on vertical mixing induced by internal waves is necessary in order to improve the current tidal mixing parameterisation.

Finally, although the ITF has a major impact on the global ocean circulation and climate variability, there are still too few measurements in the Indonesian Archipelago.

Code and data availability

The INDO12 configuration is based on the NEMO2.3 version developed at Mercator Océan. All specificities included in the NEMO code version 2.3 are now freely available in the recent version NEMO 3.6; see the NEMO web site http://www.nemo-ocean.eu. The INDO12/NEMO2.3 configuration and all the input files used in the present paper are available upon request (please contact benoit.tranchant@cls.fr).

World Ocean Database and World Ocean Atlas are available at https://www.nodc.noaa.gov. Aquarius data L3 (V3.0) data are available at http://podaac.jpl.nasa.gov/dataaccess. AMSR data are produced by Remote Sensing Systems and sponsored by the NASA Earth Science MEaSUREs DISCOVER Project and the NASA AMSR-E Science Team. Data are available at www.remss.com. JAMSTEC data are available at http://www.jamstec.go.jp/ARGO/argo_web/prod/oi_prs_e.html

Acknowledgements. This work was funded by the INDESO project. The authors thank Nathalie Verbrugge, Loren Carrère and Antoine Delepoulle for fruitful discussions and for sharing data. Comments by two anonymous reviewers and the editor greatly improved the paper. The author would like to thank Marc Lucas for his valuable help in correcting the manuscript's english.

Edited by: S. Valcke

References

Alford, M. H., Peacock, T., MacKinnon, J. A., Nash, J. D., Buijsman, M. C., Centuroni, L. R., Chao, S.-Y., Chang, M.-H., Farmer, D. M., Fringer, O. B., Fu, K.-H., Gallacher, P. C., Graber, H. C., Helfrich, K. R., Jachec, S. M., Jackson, C. R., Klymak, J. M., Ko, D. S., Jan S., Johnston, T. M. S., Legg, S., Lee, I.-H., Lien, R.-C., Mercier, M. J., Moun, J. N., Musgrave, R., Park, J.-H., Pickering A. I., Pinkel, R., Rainville, L., Ramp, S. R., Rudnick, D. L., Sarkar, S., Scotti, A., Simmons, H. L., St Laurent, L. C., Venayagamoorthy, S. K., Wang, Y.-H., Wang, J., Yang, Y. J., Paluszkiewicz, T., and Tang, T.-Y. D.: The formation and fate of internal waves in the South China Sea, Nature, 521, 65–69, doi:10.1038/nature14399, 2015.

Antonov, J. I., Locarnini, R. A., Boyer, T. P., Mishonov, A. V., and Garcia, H. E.: World Ocean Atlas 2005, Vol. 2: Salinity, in: NOAA Atlas NESDIS 62, edited by: Levitus, S., US Government Printing Office, Washington, DC, 182 pp., 2006.

Barnier, B., Madec, G., Penduff, T., Molines, J.-M., Treguier, A.-M., le Sommer, J., Beckmann, A., Biastoch, A., Boning, C., Dengg, J., Derval, C., Durand, E., Gulev, S., Remy, E., Talandier, C., Theetten, S., Maltrud, M., McClean, J., and de Cuevas, B.: Impact of partial steps and momentum advection schemes in a global circulation model at eddy permitting resolution, Ocean Dynam., 56, 543–567, doi:10.1007/s10236-006-0082-1, 2006.

Boyer, T. P., Antonov, J. I., Baranova, O. K., Coleman, C., Garcia, H. E., Grodsky, A., Johnson, D. R., Locarnini, R. A., Mishonov, A. V., O'Brien, T. D., Paver, C. R., Reagan, J. R., Seidov, D., Smolyar, I. V., and Zweng, M. M.: World Ocean Database 2013, edited by: Levitus, S. and Mishonov, A., NOAA Atlas NESDIS 72, 209 pp., 2013.

Carrère, L., Lyard, F., Cancet, M., Guillot, A., and Roblou, L.: FES2012: a new global tidal model taking advantage of nearly 20 years of altimetry, in: Proceedings of meeting, 20 years of altimetry, Venice-Lido, Italy, 24–29 September 2012, 6 pp., 2012.

Castruccio, F. S., Curchitser, E. N., and Kleypas, J. A.: A model for quantifying oceanic transport and mesoscale variability in the Coral Triangle of the Indonesian/Philippines Archipelago, J. Geophys. Res.-Oceans, 118, 6123–6144, doi:10.1002/2013JC009196, 2013.

Dai, A. and Trenberth, K. E.: Estimates of freshwater discharge from continents: Latitudinal and seasonal variations, J. Hydrometeorol., 3, 660–687, 2002.

Dee, D. P., Uppala, S. M., Simmons, A. J., Berrisford, P., Poli, P., Kobayashi, S., Andrae, U., Balmaseda, M. A., Balsamo, G., Bauer P., Bechtold, P., Beljaars, A. C. M., van de Berg, L., Bidlot, J., Bormann, N., Delsol, C., Dragani, R., Fuentes, M., Geer, A. J., Haimberger, L., Healy, S. B., Hersbach, H., Holm, E. V., Isaksen, L., Kallberg, P., Kohler, M., Matricardi, M., McNally, A. P., Monge-Sanz, B. M., Morcrette, J.-J., Park, B.-K., Peubey, C., de Rosnay, P., Tavolato, C., Thepaut, J.-N., and Vitart, F.: The ERA-Interim reanalysis: configuration and performance of the data assimilation system, Q. J. Roy. Meteor. Soc., 137, 553–597, doi:10.1002/qj.828, 2011.

Egbert, G. D. and Erofeeva, S. Y.: Efficient inverse modeling of barotropic ocean tides, J. Atmos. Ocean. Tech., 19, 183–204, 2002.

Fang, G., Susanto, R. D., Wirasantosa, S., Qiao, F., Supangat, A., Fan, B., Wei, Z., Sulistiyo, B., and Li, S.: Volume, heat, and freshwater transports from the South China Sea to Indonesian seas in the boreal winter of 2007–2008, J. Geophys. Res., 115, C12020, doi:10.1029/2010JC006225, 2010.

Ffield, A. and Robertson, R.: Temperature finestructure in the Indonesian Seas, J. Geophys. Res., 113, C09009, doi:10.1029/2006JC003864, 2008.

Gentemann, C. L., Wentz, F. J., Brewer, M., Hilburn, K. A., and Smith, D. K.: Passive microwave remote sensing of the ocean: an overview, in: Oceanography from Space, revisited, edited by: Barale, V., Gower, J. F. R., and Alberotanza, L., Springer, Heidelberg, 13–33, 2010.

Gordon, A. L.: Interocean exchange of thermocline water, J. Geophys. Res., 91, 5037–5046, doi:10.1029/JC091iC04p05037, 1986.

Gordon, A. L.: Oceanography of the Indonesian Seas and their throughflow, Oceanography, 18, 14–27, doi:10.5670/oceanog.2005.01, 2005.

Gordon, A. L. and Fine, R. A.: Pathways of water between the Pacific and Indian oceans in the Indonesian seas, Nature, 379, 146–149, 1996.

Gordon, A. L., Ma, S., Olson, D. B., Hacker, P., Ffield, A., Talley, L. D., Wilson, D., and Baringer, M.: Advection and Diffusion of Indonesian Throughflow within the Indian Ocean South Equatorial Current, Geophys. Res. Lett., 24, 2573–2576, 1997.

Gordon, A. L., Giulivi, C. F., and Ilahude, A. G.: Deep topographic barriers within the Indonesian Seas, in: Physical Oceanography of the Indian Ocean during the WOCE Period, editetd by: Schott, F., Deep-Sea Res. Pt. II, 50, 2205–2228, 2003a.

Gordon, A. L., Susanto, R. D., and Vranes, K.: Cool Indonesian throughflow as a consequence of restricted surface layer flow, Nature, 425, 824–828, doi:10.1038/nature02038, 2003b.

Gordon, A. L., Susanto, R. D., Ffield, A., Huber, B., Pranowo, A. W., and Wirasantosa, S.: Makassar Strait Throughflow, 2004–2006, Geophys. Res. Lett., 35, L24605, doi:10.1029/2008GL036372, 2008.

Gordon, A. L., Sprintall, J., Van Aken, H. M., Susanto, R. D., Wijffels, S., Molcard, R., Ffield, A., Pranowo, W., and Wirasantosa, S., The Indonesian throughflow during 2004–2006 as observed by the INSTANT program, Dynam. Atmos. Oceans, 50, 115–128, doi:10.1016/j.dynatmoce. 2009.12.002, 2010.

Gordon, A. L., Huber, B. A., Metzger, E. J., Susanto, R. D., Hurlburt, H. E., and Adi, T. R.: South China Sea throughflow impact on the Indonesian throughflow, Geophys. Res. Lett., 39, L11602, doi:10.1029/2012GL052021, 2012.

Gutknecht, E., Reffray, G., Gehlen, M., Triyulianti, I., Berlianty, D., and Gaspar, P.: Evaluation of an operational ocean model configuration at 1/12° spatial resolution for the Indonesian seas (NEMO2.3/INDO12) – Part 2: Biogeochemistry, Geosci. Model Dev. Discuss., 8, 6669–6706, doi:10.5194/gmdd-8-6669-2015, 2015.

Hosoda, S., Ohira, T., and Nakamura, T.: A monthly mean dataset of global oceanic temperature and salinity derived from Argo float observations JAMSTEC Rep. Res. Dev., 8, 47–59, 2008.

Hsin, Y.-C., Wu, C.-R., and Chao, S.-Y.: An updated examination of the Luzon Strait transport, J. Geophys. Res., 117, C03022, doi:10.1029/2011JC007714, 2012.

Hurlburt, H. E., Metzger, E. J., Sprintall, J., Riedlinger, S. N., Arnone, R. A., Shinoda, T., and Xu., X.: Circulation in the Philippine Archipelago simulated by 1/12° and 1/25° Global HYCOM and EAS NCOM, Oceanography, 24, 28–47, doi:10.5670/oceanog.2011.02, 2011.

Jerlov, N. G.: Optical oceanography, American Elsevier Publ. Co., Inc., New York, 194 pp., 1968.

Jochum, M. and Potemra, J. T.: Sensitivity of tropical rainfall to Banda Sea diffusivity in the Community Climate System Model, J. Climate, 21, 6445–6454, 2008.

Kartadikaria, A. R., Miyazawa, Y., Varlamov, S. M., and Nadaoka, K.: Ocean circulation for the Indonesian seas driven by tides and atmospheric forcings: comparison to observational data, J. Geophys. Res., 116, C09009, doi:10.1029/2011JC007196, 2011.

Kidd, C., Dawkins, E., and Huffman, G.: Comparison of precipitation derived from the ECMWF operational forecast model and satellite precipitation datasets, J. Hydrometeorol., 14, 1463–1482, doi:10.1175/JHM-D-12-0182.1, 2013.

Kim, S.-B., Lee, J. H., de Matthaeis, P., Yueh, S., Hong, C. S., Lee, J.-H., and Lagerloef, G.: Sea surface salinity variability in the East China Sea observed by the Aquarius instrument, J. Geophys. Res.-Oceans, 119, 7016–7028, doi:10.1002/2014JC009983, 2014.

Koch-Larrouy, A., Madec, G., Bouruet-Aubertot, P., Gerkema, T., Bessières, L., and Molcard, R.: On the transformation of Pacific Water into Indonesian throughflow water by internal tidal mixing, Geophys. Res. Lett., 34, L04604, doi:10.1029/2006GL028405, 2007.

Koch-Larrouy A., Madec, G., Blanke, B., and Molcard, R.: Quantification of the water paths and exchanges in the indonesian archipelago, Ocean Dynam., 58, 289–309, doi:10.1007/s10236-008-0155-4, 2008.

Koch-Larrouy, A., Atmadipoera, A., Van Beek, P., Madec, G., Aucan, J., Lyard, F., Grelet, J., and Souhaut, M.: Estimates of tidal mixing in the Indonesian archipelago from multidisciplinary INDOMIX in-situ data, Deep-Sea Res. Pt. I, 106, 136–153, doi:10.1016/j.dsr.2015.09.007, 2015.

Lagerloef and the Aquarius team: Aquarius Salinity Validation Analysis, Aquarius Project Document: AQ-014-PS-0016, 18 February 2013.

Large, W. and Yeager, S.: Diurnal to decadal global forcing for ocean and sea-ice models: the data sets and ux climatologies.

CGD Division of the National Center for Atmospheric Research, NCAR Technical Note, NCAR/TN-460+STR, 2004.

Lellouche, J.-M., Le Galloudec, O., Drévillon, M., Régnier, C., Greiner, E., Garric, G., Ferry, N., Desportes, C., Testut, C.-E., Bricaud, C., Bourdallé-Badie, R., Tranchant, B., Benkiran, M., Drillet, Y., Daudin, A., and De Nicola, C.: Evaluation of global monitoring and forecasting systems at Mercator Océan, Ocean Sci., 9, 57–81, doi:10.5194/os-9-57-2013, 2013.

Levier, B., Tréguier, A. M., Madec, G., and Garnier, V.: Free surface and variable volume in the NEMO code, MERSEA IP report WP09-CNRS-STR03-1A, 47 pp., 2007.

Le Vine, D. M., de Matthaeis, P., Ruf, C.S., and Chen, D. D.: Aquarius RFI detection and mitigation algorithm: Assessment and examples, IEEE T. Geosci. Remote, 52, 4574–4584, 2014.

Madec, G.: NEMO ocean engine, Note du Pole de modélisation, Institut Pierre-Simon Laplace (IPSL), France, No. 27, ISSN No. 1288–1619, 2008.

Madec, G., Delecluse, P., Imbard, M., and Lévy, C.: OPA 8.1 Ocean General Circulation Model reference manual, Note du Pole de modélisation, Institut Pierre-Simon Laplace (IPSL), France, No 11, 91 pp., 1998.

Maraldi, C., Chanut, J., Levier, B., Ayoub, N., De Mey, P., Reffray, G., Lyard, F., Cailleau, S., Drévillon, M., Fanjul, E. A., Sotillo, M. G., Marsaleix, P., and the Mercator Research and Development Team: NEMO on the shelf: assessment of the Iberia–Biscay–Ireland configuration, Ocean Sci., 9, 745–771, doi:10.5194/os-9-745-2013, 2013.

McClain, C. R., Feldman, G. C., and Hooker, S. B.: An overview of the SeaWiFS project and strategies for producing a climate research quality global ocean bio-optical time series, Deep-Sea Res. Pt. II, 51, 5–42, 2004.

McClean, J. L., Ivanova, D. P., and Sprintall, J.: Remote origins of interannual variability in the Indonesian Throughflow region from data and a global parallel ocean program simulation, J. Geophys. Res., 110, C10013, doi:10.1029/2004JC002477, 2005.

McPhaden, M. J., Busalacchi, A. J., Cheney, R., Donguy, J. R., Gage, K. S., Halpern, D., Julian, M. Ji, P., Meyers, G., Mitchum, G. T., Niiler, P. P., Picaut, J., Reynolds, R. W., Smith, N., and Takeuchi, K.: The Tropical Ocean-Global Atmosphere observing system: A decade of progress, J. Geophys. Res., 103, 14169–14240, 1998.

Menezes, V. V., Phillips, H. E., Schiller, A., Domingues, C. M., and Bindoff, N. L., Salinity dominance on the Indian Ocean Eastern Gyral current, Geophys. Res. Lett., 40, 5716–5721, doi:10.1002/2013GL057887, 2013.

Metzger, E. J., Hurlburt, H. E., Xu, X., Shriver, J. F., Gordon, A. L., Sprintall, J., Susanto, R. D., and van Aken, H. M.: Simulated and observed circulation in the Indonesian Seas: 1/12° global HYCOM and the INSTANT observations, Dynam. Atmos. Oceans, 50, 27–300, 2010.

Munk, W. and Wunsch, C.: Abyssal Recipes II: energetics of tidal and wind mixing, Deep-Sea Res., 45, 1976–2000, 1998.

Murray, S. P. and Arief, D.: Throughflow into the Indian Ocean through the Lombok Strait, January 1985–January 1986, Nature, 333, 444–447, 1988.

Niwa, Y. and Hibiya, T.: Estimation of baroclinic tide energy available for deep ocean mixing based on three-dimensional global numerical simulations, J. Oceanogr., 67, 493–502, doi:10.1007/s10872-011-0052-1, 2011.

Oke, P. R., Griffin, D. A., Schiller, A., Matear, R. J., Fiedler, R., Mansbridge, J., Lenton, A., Cahill, M., Chamberlain, M. A., and Ridgway, K.: Evaluation of a near-global eddy-resolving ocean model, Geosci. Model Dev., 6, 591–615, doi:10.5194/gmd-6-591-2013, 2013.

Qu, T., Kim, Y. Y., Yaremchuk, M., Tozuka, T., Ishida, A., and Yamagata, T.: Can Luzon Strait Transport play a role in conveying the impact of ENSO to the South China Sea?, J. Climate, 17, 3643–3656, 2004.

Qu, T., Yan, D., and Hideharu, S.: South China Sea throughflow: a heat and freshwater conveyor, Geophys. Res. Lett., 33, L23617, doi:10.1029/2006GL028350, 2006.

Qu, T., Song, T., and Yamagata, T.: An introduction to the South China Sea throughflow: Its dynamics, variability, and implication for climate, Dynam. Atmos. Oceans, 47, 3–14, doi:10.1016/j.dynatmoce.2008.05.001, 2009.

Rio, M. H., Guinehut, S., and Larnicol, G.: New CNES-CLS09 global mean dynamic topography computed from the combination of GRACE data, altimetry, and in situ measurements, J. Geophys. Res., 116, C07018, doi:10.1029/2010JC006505, 2011.

Sanchez Gomez, E., Cassou, C., Hodson, D. L. R., Keenlyside, N., Okumura, Y., and Zhou, T.: North Atlantic weather regimes response to Indian-western Pacific Ocean warming: a multi-model study, Geophys. Res. Lett., 35, L15706, doi:10.1029/2008GL034345, 2008.

Saraceno, M., Strub, P. T., and Kosro, P. M.: Estimates of sea surface height and near-surface alongshore coastal currents from combinations of altimeters and tide gauges, J. Geophys. Res., 113, C11013, doi:10.1029/2008JC004756, 2008.

Song, Q., Gordon, A. L., and Visbeck, M.: Spreading of the Indonesian throughflow in the Indian Ocean, J. Phys. Oceanogr., 34, 772–792, doi:10.1175/1520-0485(2004)034<0772:SOTITI>2.0.CO;2, 2004.

Sprintall, J. and Revelard, A.: The Indonesian throughflow response to Indo-Pacific climate variability, J. Geophys. Res.-Oceans, 119, 1161–1175, doi:10.1002/2013JC009533, 2014.

Sprintall, J., Wijffels, S., Gordon, A. L., Ffield, A., Molcard, R., Susanto, R. D., Soesilo, I., Sopaheluwakan, J., Surachman, Y., and van Aken, H. M.: A New International Array to Measure the Indonesian Throughflow: INSTANT, EOS Transactions, 85, 369–376, 2004.

Sprintall, J., Wijffels, S. E., Molcard, R., and Jaya, I.: Direct estimates of the Indonesian Throughflow entering the Indian Ocean: 2004–2006, J. Geophys. Res., 114, C07001, doi:10.1029/2008JC005257, 2009.

Sprintall, J., Wijffels, S. E., Molcard, R., and Jaya, I.: Direct evidence of the South Java Current sustem in Ombai Strait, Dynam. Atmos. Oceans, 50, 140–156, 2010.

Stammer, D., Ray, R. D., Andersen, O. B., Arbic, B. K., Bosch, W., Carrère, L., Cheng, Y., Chinn, D. S., Dushaw, B. D., Egbert, G. D., Erofeeva, S. Y., Fok, H. S., Green, J. A. M., Griffiths, S., King, M. A., Lapin, V., Lemoine, F. G., Luthcke, S. B., Lyard, F., Morison, J., Müller, M., Padman, L., Richman, J. G., Shriver, J. F., Shum, C. K., Taguchi, E., and Yi, Y.: Accuracy assessment of global barotropic ocean tide models, Rev. Geophys., 52, 243–282, doi:10.1002/2014RG000450, 2014.

Susanto, R. D., Mitnik, L., and Zheng, Q.: Ocean internal waves observed in the Lombok Strait, Oceanography, 18, 80–87, doi:10.5670/oceanog.2005.08, 2005.

Talley, L. D. and Sprintall, J.: Deep expression of the Indonesian throughflow: Indonesian intermediate water in the South Equatorial Current, J. Geophys. Res., 110, C10009, doi:10.1029/2004JC002826, 2005.

Tang, W., Yueh, S. H., Fore, A. G., Hayashi, A., Lee, T., and Lagerloef, G.: Uncertainty of Aquarius sea surface salinity retrieved under rainy conditions and its implication on the water cycle study, J. Geophys. Res.-Oceans, 119, 4821–4839, doi:10.1002/2014JC009834, 2014.

Tozuka, T., Qu, T., and Yamagata, T.: Dramatic impact of the South China Sea on the Indonesian Throughflow, Geophys. Res. Lett., 34, L12612, doi:10.1029/2007GL030420, 2007.

Ueki, I., Kashino, Y., and Kuroda, Y.: Observation of the current variations off the New Guinea coast including the 1997–1998 El Nino period and their relationship with Sverdrup transport, J. Geophys. Res., 108, 3243, doi:10.1029/2002JC001611, 2003.

Umlauf, L. and Burchard, H.,: A generic length-scale equation for geophysical turbulence models, J. Marine Res. 61, 235–265, doi:10.1357/002224003322005087, 2003.

Van Aken, H. M. and Brodjonegoro, I. S.: IndraJaya, the deep-water motion through the Lifamatola passage and its contribution to the Indonesian throughflow, Deep-Sea Res. Pt. I, 56, 1203–1216, 2009.

Van Aken, H. M., Punjanan, J., and Saimima, S.: Physical aspects of the flushing of east Indonesian seas, Neth. J. Sea. Res., 22, 315–339, 1988.

Van Sebille, E., Sprintall J., Schwarzkopf, F. U., Sen Gupta, A., Santoso, A., England, M. H., Biastoch, A., and Böning, C. W.: Pacific-to-Indian Ocean connectivity: Tasman leakage, Indonesian Throughflow, and the role of ENSO, J. Geophys. Res.-Oceans, 119, 1365–1382, doi:10.1002/2013JC009525, 2014.

Zeng, L., Liu, W. T., Xue, H., Xiu, P., and Wang, D.: Freshening in the South China Sea during 2012 revealed by Aquarius and in situ data, J. Geophys. Res.-Oceans, 119, 8296–8314, doi:10.1002/2014JC010108, 2014.

Zhao, W., Zhou, C., Tian, J., Yang, Q., Wang, B., Xie, L., and Qu, T.: Deep water circulation in the Luzon Strait, J. Geophys. Res.-Oceans, 119, 790–804, doi:10.1002/2013JC009587, 2014.

Chapter 4

Modelling Explicit tides in the Indonesian seas: an important process for surface sea water properties (accepted article)

4.1 Introduction

In the previous chapter we showed that the INDO12 model was able to provide a realistic simulation of the ocean circulation and water mass transformation through the Indonesian Archipelago. The vertical mixing induced by internal tides is taken into account by INDO12. This model explicitly solves the barotropic tides and uses the vertical mixing parameterisation of Koch-Larrouy et al. (2007) which artificially enhances the vertical viscosity and the diffusion coefficient.

The inclusion of barotropic tides in the model can create strong internal waves at the tidal frequency, called internal tides. These internal tides are generated on the slope of sharp topography and eventually will propagate in the interior of the ocean. When an internal tide gets unstable it will break, resulting in a strong mixing. This mixing upwells cold, salty water and nutrients richer water from bllow and downwells warmer and fresher water from the surface at deeper depth. This upwelling of cold nutrient-richer water at the surface, could prove to be critic for climate system and for marine resources.

The objective of this chapter, and the following submitted paper, is thus to study the impact of the internal tides produced by the model on the surface properties and, in particular, the sea surface temperature.

To this aim, we conducted three simulations in order to examine the impact of tides on surface properties. The EXPL run includes explicit tidal forcing and the reference configuration (CTRL) doesn't. The PARAM simulation is forced by the Koch-Larrouy et al. (2007) parameterisation. All of them are forced by the same buoyancy and wind forcing.The results of the three simulations are compared in order to understand exactly how, when and where tidal mixing influences surface temperature.

The tides induce a cooling at the surface is of 0.3 °C with maxima of 0.8°C at the location of internal tides energy. The cycle of spring tides and neap tides produces modulate this impact by 0.1°C to 0.3°C. These results suggest that this mixing might also upwell nutrients at the surface, which in turn influence the survival rate of most planktonic organisms at the base of the whole marine ecosystem.

4.2 Scientific paper :

Modelling Explicit tides in the Indonesian seas: an important process for surface sea water properties

Dwiyoga Nugroho[1,2], *Ariane Koch-larrouy*[1,3], *Philippe Gaspar*[4], *Florent Lyard*[1], *Guillaume Reffray*[3] and *Benoit Tranchant*[4]

1. Laboratoire d'Etudes en Géophysique et Océanographie Spatiales (LEGOS)
Université de Toulouse, CNRS, IRD, CNES, UPS, 14 avenue Edouard -Belin, 31400 Toulouse, France
2. Agency of Research and Development for Marine And Fisheries, MMAF, Jakarta, Indonesia
3. Mercator-Ocean, 10 Rue Hermès, 31520 Ramonville-Saint-Agne, France
4. Collecte Localisation Spatiale, CLS, 11 Rue Hermès, 31520 Ramonville-Saint-Agne, France

Accepted in Marine Pollution Bulletin, 20 Avril 2016

ARTICLE IN PRESS

Marine Pollution Bulletin xxx (xxxx) xxx–xxx

Contents lists available at ScienceDirect

Marine Pollution Bulletin

journal homepage: www.elsevier.com/locate/marpolbul

Modelling explicit tides in the Indonesian seas: An important process for surface sea water properties

Dwiyoga Nugroho[a,b,*], Ariane Koch-Larrouy[a,c], Philippe Gaspar[d], Florent Lyard[a], Guillaume Reffray[c], Benoit Tranchant[d]

[a] Laboratoire d'Etudes en Géophysique et Océanographie Spatiales (LEGOS), Université de Toulouse, CNRS, IRD, CNES, UPS, 14 avenue Edouard-Belin, 31400 Toulouse, France
[b] Agency of Research and Development for Marine and Fisheries, MMAF, Jakarta, Indonesia
[c] Mercator-Ocean, 10 Rue Hermès, 31520 Ramonville-Saint-Agne, France
[d] Collecte Localisation Spatiale, CLS, 11 Rue Hermès, 31520 Ramonville-Saint-Agne, France

ARTICLE INFO

Keywords:
INDESO
ITF
Internal tides
Vertical mixing
Explicit tides
Ocean Physical General Circulation Model (OGCM)

ABSTRACT

Very intense internal tides take place in Indonesian seas. They dissipate and affect the vertical distribution of temperature and currents, which in turn influence the survival rates and transports of most planktonic organisms at the base of the whole marine ecosystem. This study uses the INDESO physical model to characterize the internal tides spatio-temporal patterns in the Indonesian Seas. The model reproduced internal tide dissipation in agreement with previous fine structure and microstructure observed in-situ in the sites of generation. The model also produced similar water mass transformation as the previous parameterization of Koch-Larrouy et al. (2007), and show good agreement with observations. The resulting cooling at the surface is 0.3 °C, with maxima of 0.8 °C at the location of internal tides energy, with stronger cooling in austral winter. The cycle of spring tides and neap tides modulates this impact by 0.1 °C to 0.3 °C. These results suggest that mixing due to internal tides might also upwell nutrients at the surface at a frequency similar to the tidal frequencies. Implications for biogeochemical modelling are important.

1. Introduction

The Indonesian archipelago, with its estimated 17,000 islands is a unique region in the world. It contains much of the world's marine biodiversity and is part of the “Coral Triangle”, the global hotspot of marine biodiversity (Allen and Werner, 2002; Mora et al., 2003; Allen, 2007; Veron et al., 2009). In addition to biodiversity, the physical oceanography of this region is remarkable by several aspects. Among them, the large tidal currents coming either from the Indian Ocean or the Pacific Oceans interact with the rough topography and create strong internal wave at the tidal frequency, called internal tides (Fig. 1). These internal tides are generated on the slope of sharp topography and eventually propagate in the interior of the ocean. When an internal tide gets instable, it breaks, resulting in a strong mixing. This mixing upwells cold, salty and nutrient-rich water from below and downwells warm and fresh water from the surface to deeper depth. This mixing, and the upwelling of cold nutrient-rich waters at the surface, could be critical for the climate system and for marine resources. Second, Indonesia also has the warmest oceanic waters on earth. These waters feed the most powerful atmospheric convective activity. The resulting large tropical atmospheric circulation affects, via teleconnexion, the global system. In such an energetic atmospheric region, any modulation of the ocean heat surface content by oceanic processes can have a large impact on local and tropical climate (Koch-Larrouy et al., 2010; Sprintall et al., 2014). Lastly, the Indonesian seas offer the only low latitude passage in the world for water flowing from the Pacific Ocean to the Indian Ocean, which is referred to as the Indonesian throughflow (ITF) (Murray and Arief, 1988; Fieux et al., 1994; Gordon and Fine, 1996; Hautala et al., 2001; Molcard et al., 2001).

In fine, Indonesian islands and their surrounding waters provide several billion dollars of annual revenue through fisheries, aquaculture and tourism. Tuna fisheries are a major economical sector in Indonesia, and fishing and aquaculture employ almost 6.4 million people (source from Fisheries and Aquaculture Department, http://www.fao.org/fishery/facp/IDN/en#CountrySector-Overview).

An accurate monitoring and forecasting system for the ocean is certainly vital to manage Indonesia waters and its resources. To help meeting these challenging objectives the INDESO (Infrastructure

---

[*] Corresponding author at: Laboratoire d'Etudes en Géophysique et Océanographie Spatiales (LEGOS), Université de Toulouse, CNRS, IRD, CNES, UPS, 14 avenue Edouard-Belin, 31400 Toulouse, France.
E-mail address: dwi.yoga.nogroho@legos.obs-mip.fr (D. Nugroho).

http://dx.doi.org/10.1016/j.marpolbul.2017.06.033
Received 16 December 2016; Received in revised form 7 June 2017; Accepted 9 June 2017
0025-326X/

Please cite this article as: Nugroho, D., Marine Pollution Bulletin (2017), http://dx.doi.org/10.1016/j.marpolbul.2017.06.033

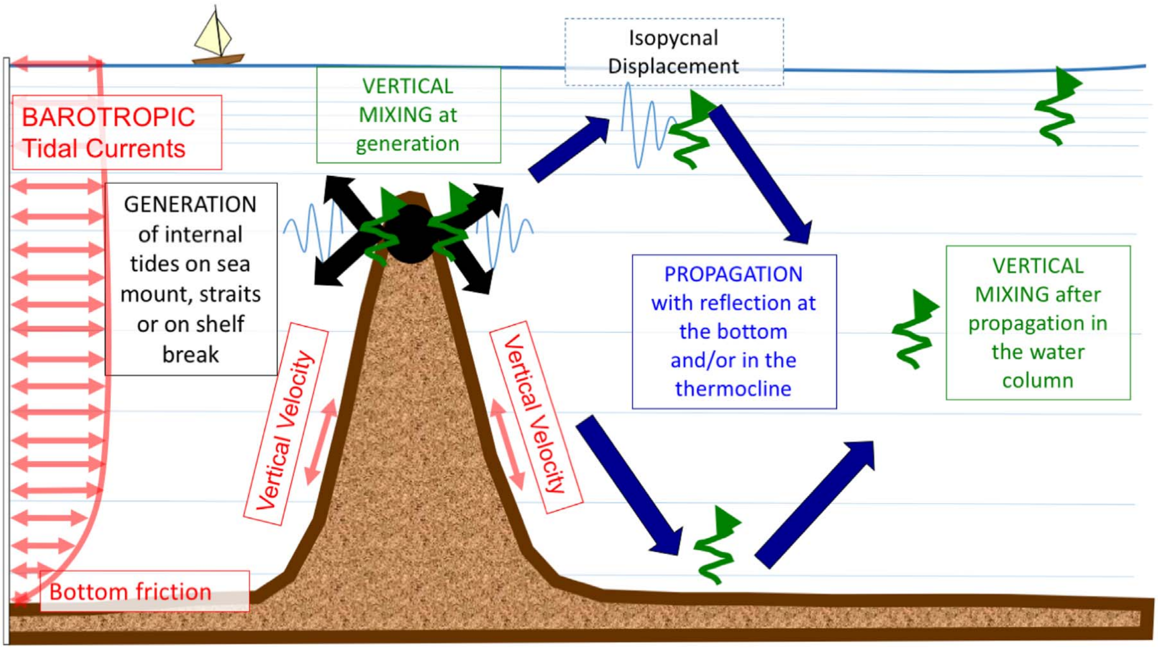

Fig. 1. Schematic of internal tides generation, propagation and dissipation. The barotropic (or surface) tides oscillate horizontally in the plain ocean (red arrow). It loses part of its energy at the bottom due to bottom friction (red arrow) or when internal tides are generated (black arrow). When the tidal currents encounter the topography feature (brown) it creates vertical currents on its sides (red arrows). This vertical motion in a stratified ocean acts as a vertical generator of waves at tidal frequency. Part of internal tides will dissipate and produce vertical mixing (green arrow) locally just after generation, or later after propagation. When internal tides propagate it can be seen isopycnal displacements (blue line) in the interior sea, and if the internal tides are very strong vertical displacement signature can also be seen at the surface. (For interpretation of the references to colour in this figure legend, the reader is referred to the web version of this article.)

Development of Space Oceanography) project was developed for the Government of Indonesia. With this project, Indonesia has implemented a new system for the monitoring and management of its tuna resources. Within INDESO, physical and biogeochemical coupled models are used to constrain a dynamical tuna population model SEAPODYM (Lehodey et al., 2008). In this study, we use for the first time the physical model to study the impact on surface properties of internal tides mixing and discuss the spatio-temporal patterns in the Indonesia Seas.

1.1. Background information on internal tides in the Indonesian region.

Internal tides are generated when barotropic (or surface) tides oscillate over a topography feature (Fig. 1). Barotropic horizontal motions are converted into vertical velocities (red arrow, Fig. 1) over the topography. As the ocean is a stratified fluid (thin horizontal blue line representing the isopycnal layers, Fig. 1), the vertical velocity will act as a vertical generator of wave at the tidal frequency. Part of the internal tides can dissipate and produce vertical mixing (green arrow, Fig. 1) locally just after generation, or later after propagation. The fate of internal tides can be traced using satellite and Radar images as it has been done in the Lombok strait for example (Mitnik et al., 2000; Sari Ningsih, 2008; Aiki et al., 2011; Matthews et al., 2011; Astawa Karang et al., 2012; Ray and Susanto, 2016) or in the Sulawesi Sea (Nagai and Hibiya, 2015). Signature of internal tides are also found in in-situ data. For instance, direct yo-yo station measurement in Lifamatola (Ffield and Gordon, 1996) and in Labani channel (Purwandana, 2014) shows the oscillation of isopycnal in the thermocline over the tidal period.

The Indonesian archipelago is the only region of the world with strong internal tides generation in a semi-enclosed area. Therefore, all of the internal (or baroclinic) tidal energy remains trapped locally inside the archipelago and is available for dissipation, and the archipelago has the largest internal tide generation value (10% of the global value). As a result, water mass is transformed when entering the archipelago, producing colder and fresher thermocline water and saltier and cooler surface water (Ffield and Gordon, 1996; Hautala et al., 2001; Koch-Larrouy et al., 2007). A vertical diffusivity of $1\text{–}2 \cdot 10^{-4}\ \mathrm{m^2/s}$ has been estimated from observations in order to explain the water mass transformation in the archipelago (Ffield and Gordon, 1992).

Recently, the INDOMIX cruise (Koch-Larrouy et al., 2015) provided direct estimates of internal tide mixing with higher values ($10^{-2}\ \mathrm{m^2/s}$) in the shallow and narrow passage between Ombai Strait and Halmahera, in comparison to lower values in the inner Halmahera Sea ($10^{-4}\ \mathrm{m^2/s}$) or further away from generation sites ($10^{-6}\ \mathrm{m^2/s}$) in the Banda Sea. These new results showed that the mixing induced by internal tides in the Indonesian archipelago is highly heterogeneous in space, with high values within straits. In addition, it demonstrated that internal tide mixing is also strong at the surface.

Modelling in the region is quite challenging because of the numerous processes at play and the very complex bathymetry. Koch-Larrouy et al. (2007), implemented a tidal parameterization adapted to the specificities of the Indonesian archipelago. Introduced in an Oceanic General Circulation Model (OGCM), this parameterization allowed the model to better represent the properties of the water mass evolution in each sub-basin, in good agreement with the observations (Koch-Larrouy et al., 2007). This model produced heterogeneous vertical diffusivity as large as $10 \cdot 10^{-4}\ \mathrm{m^2/s}$, with an average of $1.5 \cdot 10^{-4}\ \mathrm{m^2/s}$. This suggested that the total energy input provided by the tidal parameterization had the right order of magnitude. The tidal mixing parameterization resulted in the cooling of the sea surface by 0.5 °C in annual average, which reduced the deep convection, and the rain activity (by ~20%) (Koch-Larrouy et al., 2010; Sprintall et al., 2014). The impact on biological activity has not yet been studied, but it could be guessed from these results that the vertical mixing would have a significant impact on blooms of phytoplankton by upwelling water richer in nutrients at the surface. However this tidal mixing parameterization did not take into account the propagation of internal tides and thus the mixing that could occur further away from generation sites. It also does not take into account the upwelling of the base of the mixed layer associated to the isopycnal displacement of the wave when it propagates away from generation zones (Fig. 1).

Recently, with the increase of model resolution, a larger number of studies now includes the explicit forcing by the tides (Castruccio et al., 2013; Nagai and Hibiya, 2015; Tranchant et al., 2016). However, internal tides cover horizontal scales of several 100 km for their propagation to 1 cm/mm for their dissipation. It is thus impossible for any kind of model to accurately reproduce at the same time all the processes related to the internal tides. (Niwa and Hibiya, 2011) showed that with a 1/12° resolution, a model is able to reproduce only 75% of the internal tides generation. With a 1/36° resolution model, the score rises to 90%. However, specific parameterization for their dissipation must be used and it does not yet exist such specific parameterization for OGCM in the literature. The dissipation of internal tides in OGCM is under active research and is beyond the scope of the present study. We emphasize that we did not expect the model to dissipate the internal tides exactly as observed, but we expected that part of the modelled internal tides behaviour would be similar to the observations.

2. Method and data

2.1. Model and simulations

This study used the INDESO configuration detailed in Tranchant et al. (2016). The horizontal resolution is 1/12° and the domain covers all Indonesian seas, the South China Sea, as well as the Luzon strait, known as one of the strongest internal tides generator in the region. In the southern part it covers the Northern Australian Shelf (Fig. 2). Vertical grid uses *Z*-partial steps with 50 variable layers going from few meters resolution at the surface and 250 m at the bottom. Initial and open boundary conditions (OBCs) are forced by the Mercator-Ocean Global Ocean Forecasting System at 1/4° (PSY3V3R3). These conditions include temperature, salinity, currents and Sea Surface Height (SSH). Open boundary conditions (OBCs) are located on a relaxation band of 10 grid points (~1°).

Atmospheric forcing fields came from the European center (ECMWF) and had a high frequency (3 h). "Bulk" formulae from CORE were used to model the atmosphere-ocean interface (Large and Yeager, 2004). The surface atmospheric pressure forcing was also explicitly considered. There was no restoring tem in SST nor in SSS.

Tracer advection scheme is an upstream biased third order scheme (Tranchant et al., 2016) and is diffusive. Horizontal diffusion is done by a bilaplacian formulation with a K_h coefficient of $1.25 \cdot 10^{10}\ \mathrm{m}^2/\mathrm{s}$. Vertical diffusivity, K_z, is calculated through the turbulence vertical closure GLS (generic length scale) (Umlauf and Burchard, 2003) including wave impact and logarithmic bottom friction.

This configuration included explicit tidal forcing, with 11 tidal constituents. As in Shriver et al. (2012), INDESO configuration had geopotential tidal forcing for M2, S2, N2 and K2 (the four largest semidiurnal constituents) and for K1, O1, P1 and Q1 (the four largest diurnal constituents). As in Maraldi et al. (2013), two long-period tides Mf and Mm and one non-linear constituent (compound tides) M4 were also added. Explicit tides were resolved non-linearly in the model using explicit free surface (Madec, 2008). These 11 tidal constituents coming from the astronomical forcing TPX0.7 (Egbert and Erofeeva, 2002) were used to force open boundaries. More details about the configuration can be found in Tranchant et al. (2016).

2.2. Numerical experiments

We used three main simulations.

1) The CTRL simulation did not include any effect of the tides,

2) The EXPL simulation included explicit tidal forcing, as explained above.

3) The PARAM simulation was forced by the Koch-Larrouy et al. (2007) parameterisation.

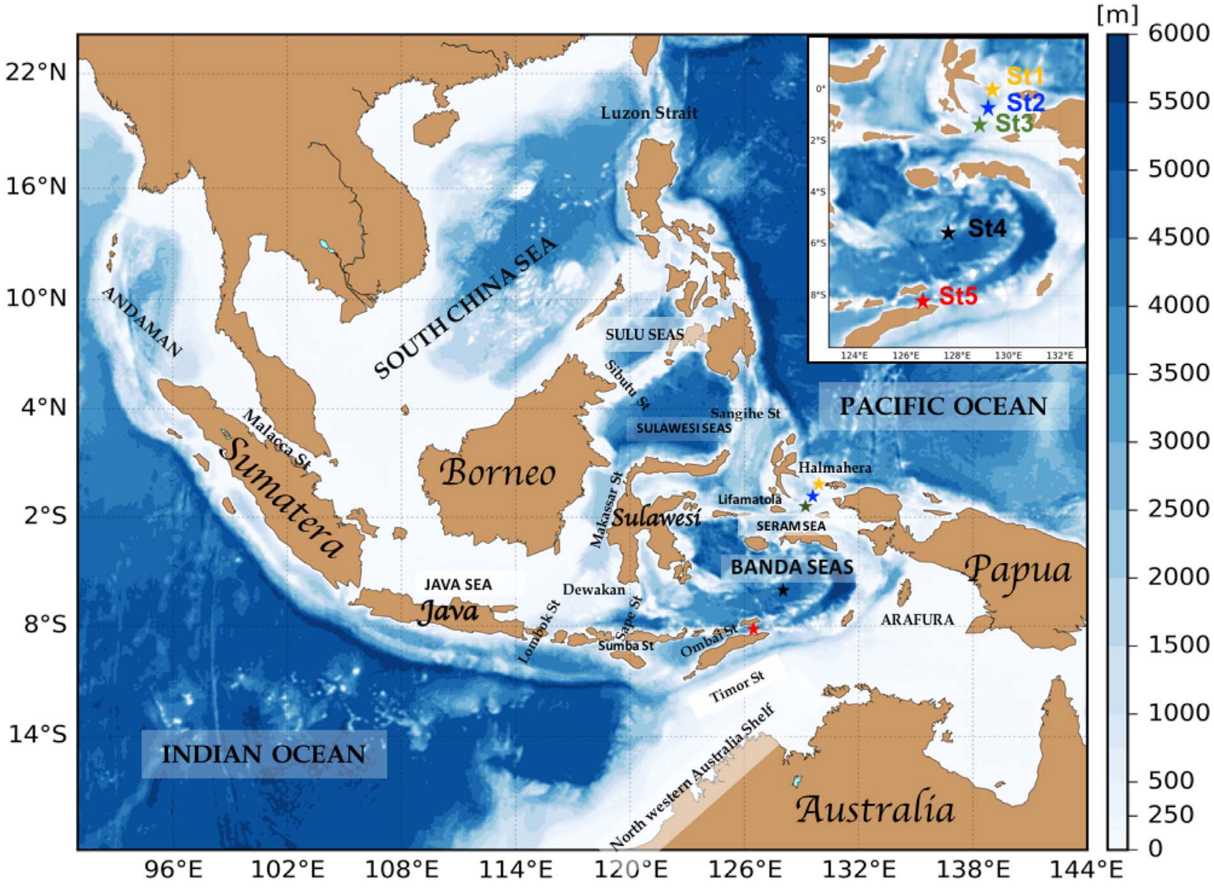

Fig. 2. Bottom topography over the model domain and names of the main seas and straits described in this paper. Coloured stars represent the 5 stations of the INDOMIX cruise. (For interpretation of the references to colour in this figure legend, the reader is referred to the web version of this article.)

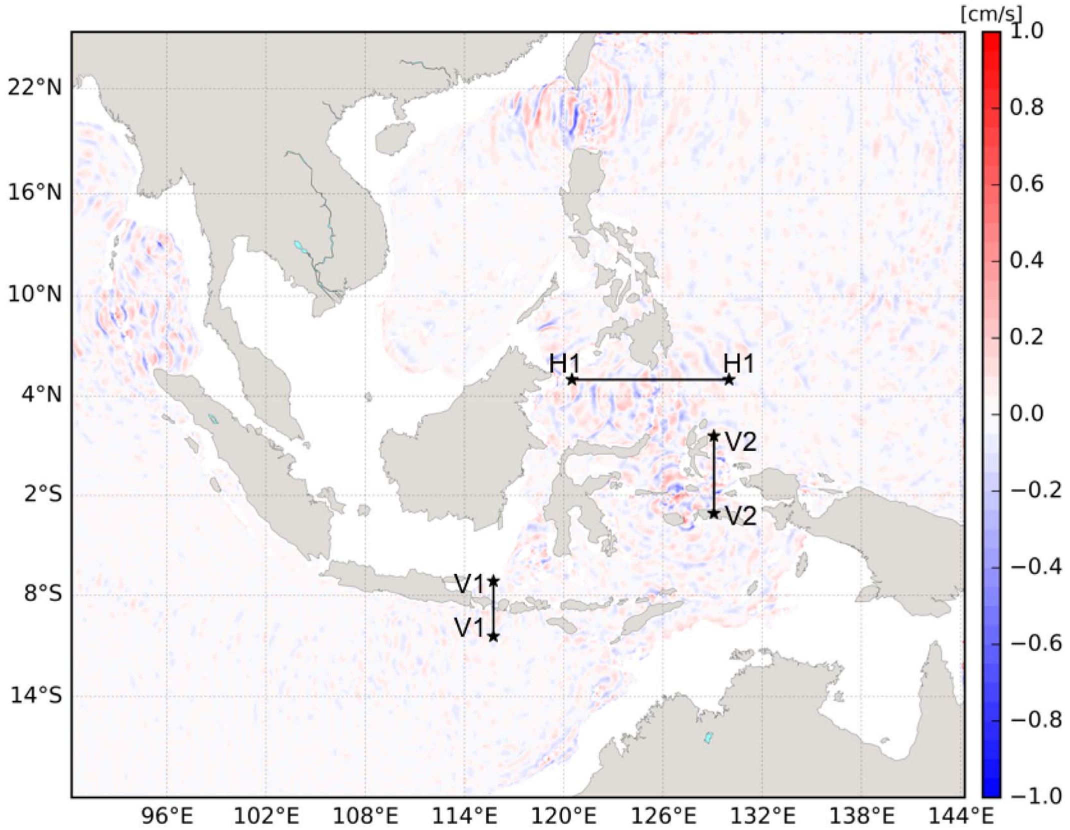

Fig. 3. Instantaneous vertical velocity at 142 m depth on 07th of June 2010, 16:00 UTC for the EXPL simulation.

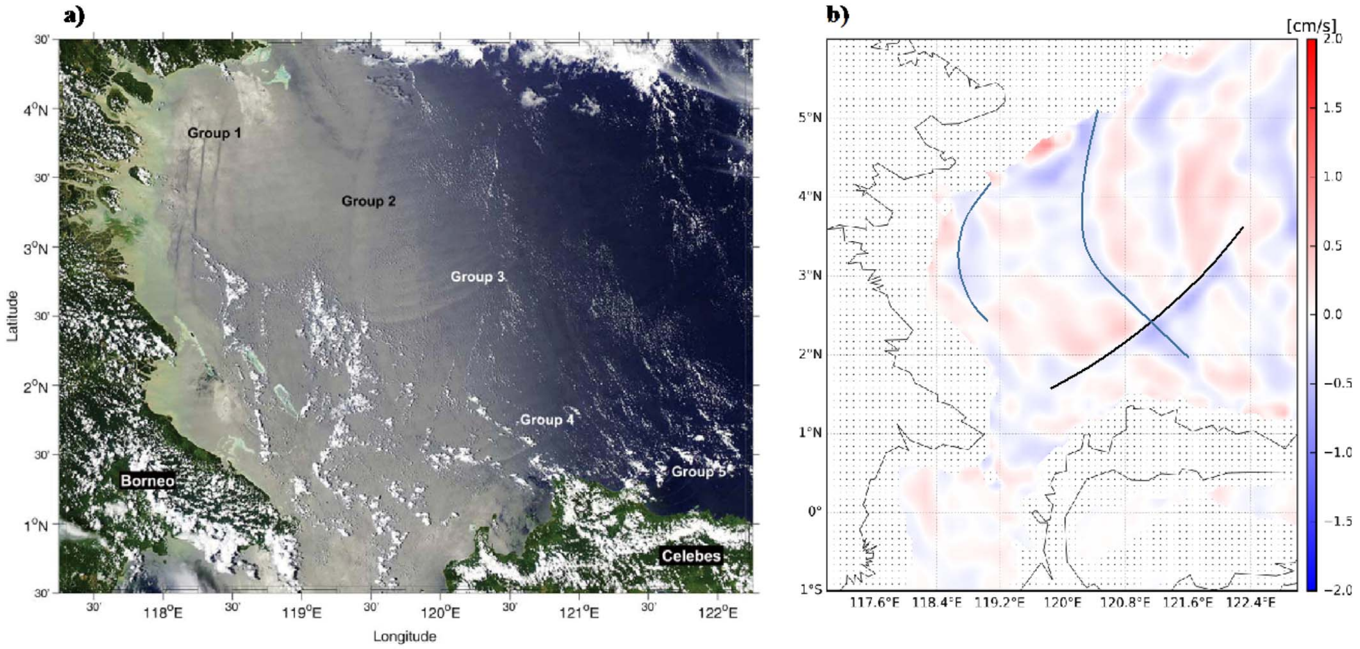

Fig. 4. True-colour MODIS image of the Sulawesi Sea acquired on 6 March 2006 at 5:25 UTC. Five groups of internal waves are visible in western half of the sea, two propagating west toward Borneo, two wave groups propagating southeast toward Celebes (or Sulawesi), and the partial signature of a fifth group visible immediately adjacent to the coast of Sulawesi (adapted from Figure 5 of Jackson (2007). Copyright (2007) American Geophysical Union). (b) Instantaneous model vertical velocity at 1000 m depth on 10 July 2010 at 15:30 UTC.

All of the simulations were forced by the same buoyancy and wind forcing. Simulations started January 3rd 2007 until December 31st 2011. Outputs are daily average and the four last years are analysed after spin up. Shorter run (1–31 July 2010) with instantaneous hourly output were also performed in order to calculate the vertical dissipation from the model and compare it to the INDOMIX 2010 cruise described below (Koch-Larrouy et al., 2015).

2.3. Dissipation rates.

Energy diagnostics and precise evaluations of the energy dissipation in the model are essential elements of our study. They are detailed

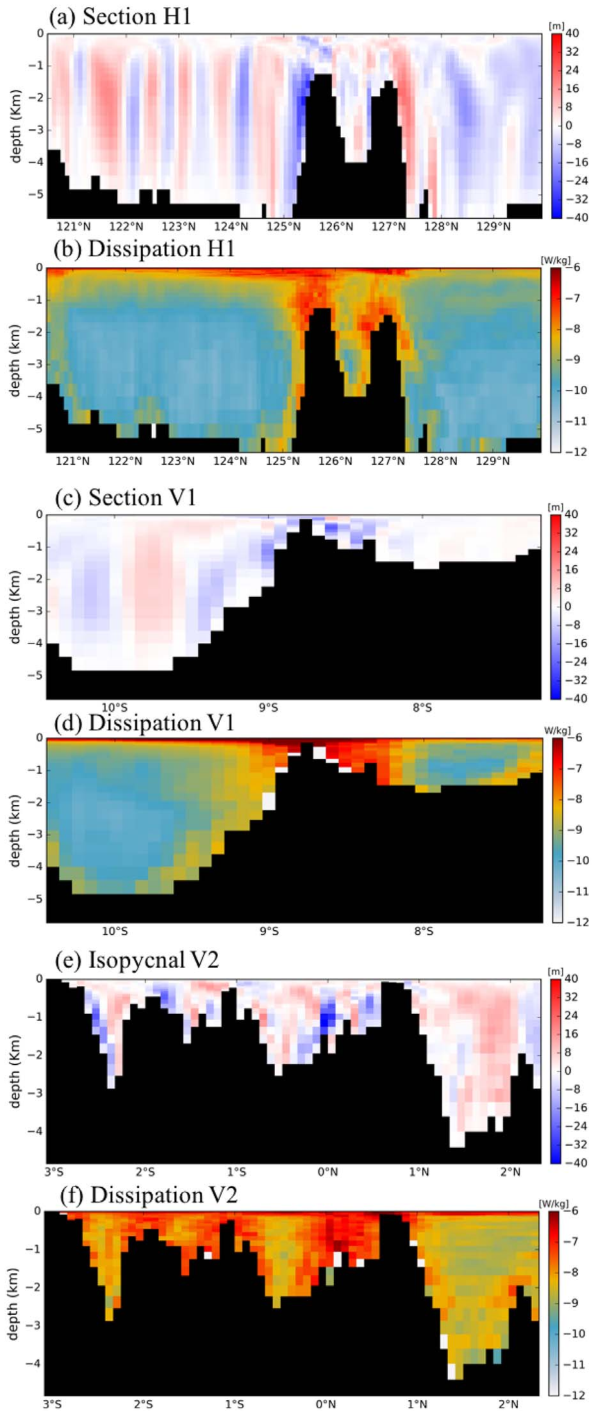

Fig. 5. Snapshopt of Isopycnal displacement (m) for July 07, 2010 at 16:00 UTC and kinetic energy dissipation (log10 E_{diss}, Eq. (2), W/kg) averaged over July 2010 for vertical sections H1, V1 and V2 defined Fig. 3.

below. The model kinetic energy (KE) equation can be written as follows:

$$\underbrace{\frac{1}{2}\rho_0\partial_t u_h^2}_{\text{KE}} = -\underbrace{\rho_0 u_h(\overrightarrow{u_h}.\ \overrightarrow{\nabla_h})u_h - \rho_0\ \overrightarrow{u_h}.\ \vec{w}\partial_z u_h}_{\text{ADV}} - \underbrace{\overrightarrow{u_h}.\ \overrightarrow{\nabla_h}p}_{\text{PRESS}} + \underbrace{\rho_0 u_h.\ D_h}_{\varepsilon_h} + \underbrace{\rho_0 u_h.\ \nabla_z(\kappa_z\nabla_h u_h)}_{\varepsilon_v} + D_{time} \tag{1}$$

where the subscript u is the velocity, p the pression and ρ_0 the ocean density (1020 kg/m^3), “h” denotes a horizontal vector, κ_z is the vertical viscosity, D_h the contribution of lateral diffusion processes and D_{time} the dissipation of kinetic energy by the time stepping scheme. The dissipation of kinetic energy by diffusive processes (E_{diss}) is computed as the spatial integral of the diffusive terms ε_h and ε_v in Eq. (1) (Nikurashin et al., 2012; Jouanno et al., 2016):

$$E_{diss} = \iiint(\varepsilon_h + \varepsilon_v)dxdydz \tag{2}$$

2.4. INDOMIX data.

We compared the dissipation of the model forced by explicit tides to the recent INDOMIX results (Koch-Larrouy et al., 2015). The cruise was held in July 2015 and measurements were done at five 24 h-yoyo-stations. The strategy of measurement was done such as different regions of internal tides energy could be sampled. Three sites above straits have been sampled: Station St1 was located at the entrance of the Halmahera Sea, St3 at the exit of the Halmahera sea and St5 at the Ombai strait (Fig. 2). Further away from generation site but still under the possible influence of propagating internal tides, St2 was located in the middle of Halmahera Sea. Finally, St4, in the Banda Sea (Fig. 1) was very far away from any generation site so that it could be verify that there was no influence of the tides. For each station, a microstructure profiler able to measure turbulence at scale of 1 mm/1 cm provides direct estimates of dissipation (Koch-Larrouy et al., 2015).

3. Results

3.1. Internal tidal mixing in the INDESO model

Vertical instantaneous velocities at 142 m depth of the EXPL simulation (Fig. 3) show evidences of internal tides propagation from several locations such as Luzon strait, Sangihe chain (H1), Lifamatola strait, Sibutu Chanel, Halmahera Sea (V2) and Lombok Strait (V1). Propagation from Luzon strait occurs toward both sides of the seamount, to the eastern and the western directions. In the western direction, after 2 reflexions, i.e., 2 positive vertical velocity signals, the signal is much weaker and we conclude that it must have been dissipated during the propagation. Signal toward the eastern direction is stronger and three significant reflexions at the surface can be seen before complete dissipation. Similarly, the Sangihe islands, the Sibutu Chanel and Lifamatola strait create strong propagating internal tides in the model (Fig. 3). The interaction with the inner seas may stop the internal tides from further propagation as seen in the Sulu Sea and in the Seram Sea. Also, in this inner part of the archipelago, the interaction between several generation sources make the signal noisier, as seen for example for the Sulawesi Sea that exhibits internal tides coming from either Sangihe Island (H1) or Sibutu Chanel.

Satellite true colour image from MODIS (in Nagai and Hibiya, 2015) Fig. 4) reveals five groups of internal waves, visible in the western half of the sea: two propagating west toward Borneo, two wave groups propagating southeast toward Sulawesi, and the partial signature of a fifth group visible immediately adjacent to the coast of Sulawesi. The model compares well to this image as we clearly see internal waves corresponding to groups 1, 2 and 4 (green lines) validating qualitatively the direction of propagation from Sangihe islands and from Sibutu channel.

Vertical sections of the isopycnal displacement (vertical velocity × time) show for Sangihe Islands (section H2 on Fig. 3) strong signal on the eastern side of the ridge (Fig. 5a). The internal tides propagate toward the east and the signal is quite coherent, although, the positive isopycnal displacement at 123 and 122°E might come from Sibutu channel at the northern part of the Sulawesi Sea. In addition, internal tides that generate on the eastern side of the western part of the ridge and propagating to the east are also seen. They reach the surface just above the eastern part of the ridge. Part of the internal tides generating

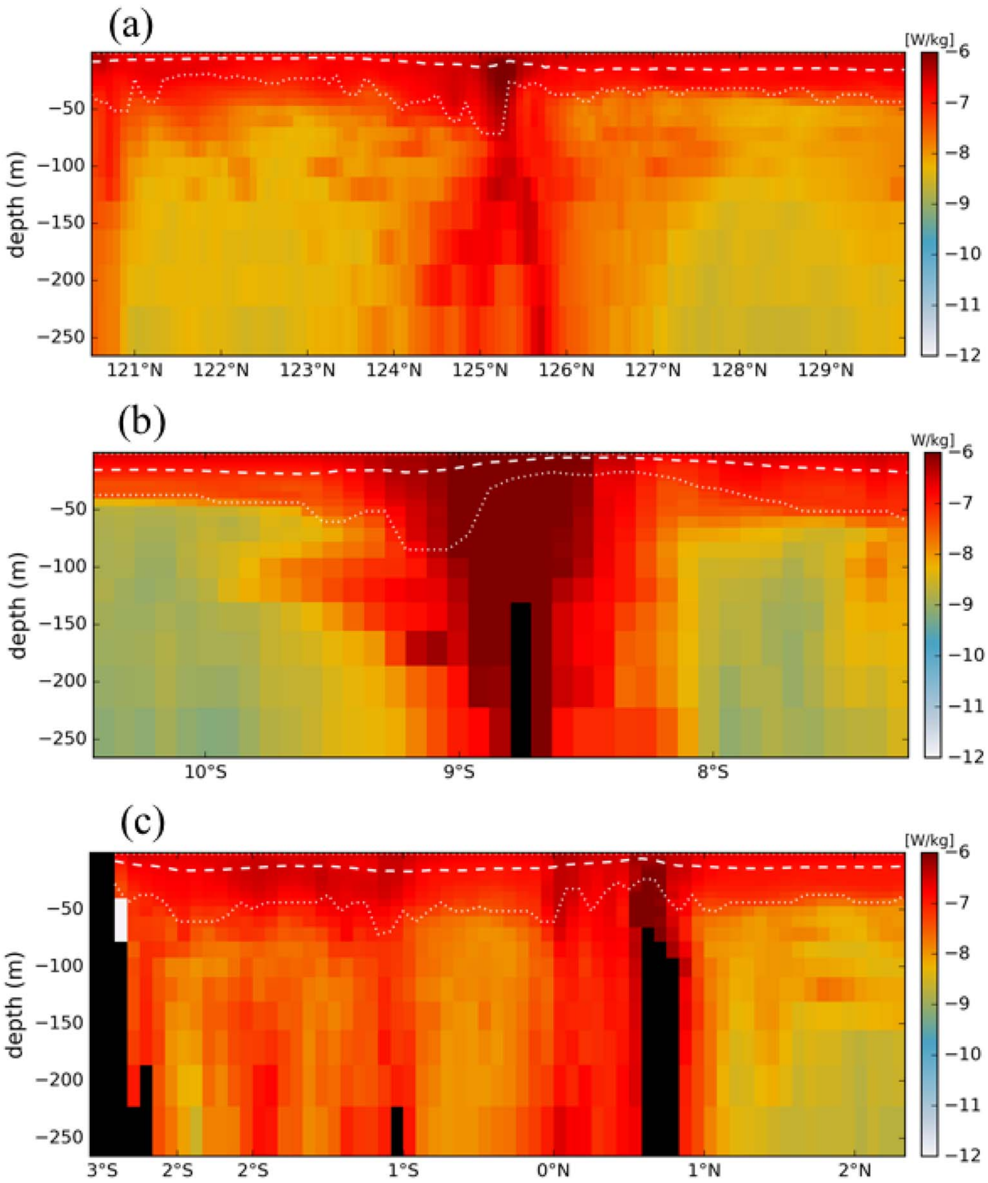

Fig. 6. Zoom from surface to 300 m depth in Fig. 5. (a), (b) and (c) are kinetic energy dissipation (log10, Eq. (2), W/kg) for vertical sections H1, V1 and V2 in Fig. 3 respectively. The minimum and maximum of mixed layer depth (MLD) over one month (July 2010) is overplot on each vertical section (min: dashed, and max: plain white lines).

on the same location are also propagating to the west, but the signal is weaker and rapidly damped.

Dissipation associated to the internal tides has been calculated following eq. 2. The model produces strong dissipation right above the eastern part of the ridge from the bottom until the surface (Fig. 5b). The surface strong mixing is also found between 124°E and 125°E as part of the reflexion of the internal tides generated at 125°E.

In the shallower Lombok strait (section V1 on Fig. 3), internal tides are also generated on both side of the slope and the isopycnal displacement is very strong in the first 500 m (Fig. 5c). This leads to a dissipation of 10^{-6} W/kg in the thermocline and close to the surface (Fig. 5d). The northern side of the strait exhibits stronger displacement and mixing. The model reproduces propagation toward the south although it concerns small part of the internal tides.

In the Halmahera and Seram Seas (section V2 on Fig. 3), the succession of the shallow passages and the semi-enclosed Seas favour multi sites of generation and interference of wave activity, and thus a strong vertical mixing background (10^{-8} W/kg) is found, although it is far away from the generation sites (Fig. 5e and f). A surface intensified mixing induced by internal tides is found above the three passages and also in the northern part of Halmahera Sea, reaching a dissipation of 10^{-6} W/kg. The Fig. 6 shows a zoom in the surface and sub-surface layers of the dissipation and the mixed layer depth. It is clearly seen that the additional tidal mixing is surface intensified and below the mixed layers, and thus capable of upwelling cold and nutrients rich water at the surface as shown in Luzon (Jan and Chen, 2009).

The spatially integrated dissipation of the tides (Eq. 2) is shown Fig. 7. The model shows intensified dissipation close to the generation sites such as Sangihe Chain, Luzon, Sibutu, Lombok, Lifamatola and Dewakang Straits or Halmahera portals with values close to 10^{-1} W/m^2. In the big Sulawesi, Banda seas and South China Sea as well as in the smaller Halmahera and Molluca Seas, we clearly see intensified dissipation further away from generation sites with smaller values of 10^{-2} W/m^2. Finally, on the Australian shelf, in the southern South China Sea and Java Sea as well as in the Southern part of the Andaman Sea, bottom friction due to the tides produce large dissipation between 10^{-2} and 10^{-1} W/m^2.

3.2. Comparison of model mixing with observations

The INDESO model (Fig. 7) agrees well with the Ffield and Robertson (2008) fine structure estimates, which indicate intensified tidal mixing in Ombai, Lifamatola and Dewakang Straits, in Molucca Sea, in the Banda Sea offshore the Muna and Buton Island (125°E, 6°S),

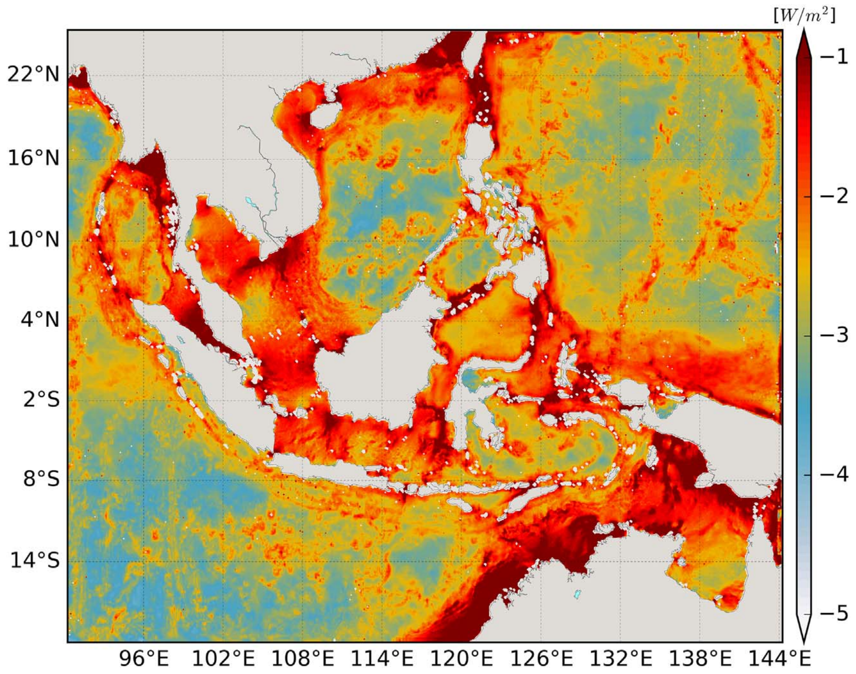

Fig. 7. Spatially integrated dissipation (log10 E_{diss}, Eq. (2)) below mixed layer depth.

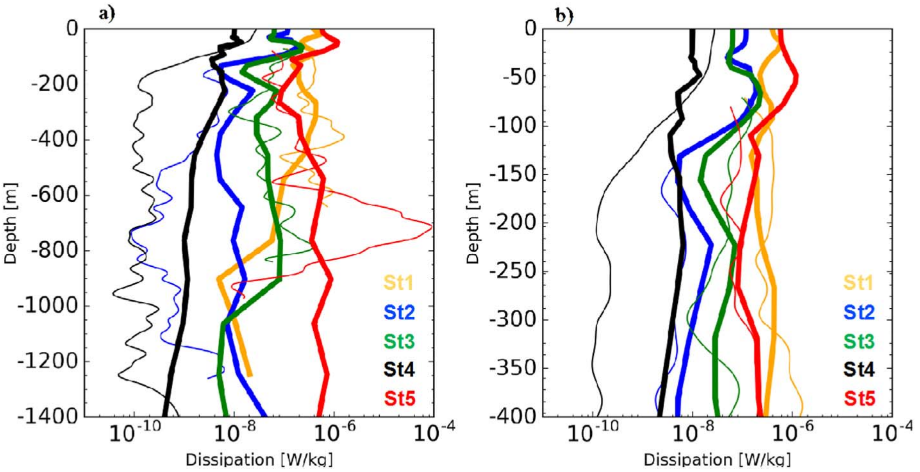

Fig. 8. (a) Dissipation (in W/kg) from INDOMIX station (Koch-Larrouy et al. 2015), using microstructure direct estimates (thin line) compared to horizontal kinetic energy dissipation (in W/kg) from EXPL calculated following from Eq. (2). Colours refer to the 5 different stations (see Fig. 2 for location). The length of the box shows the uncertainties of the method. (b) Zoom between 0 and 400 m.

in the Flores Sea, and in the eastern part of the Australian shelf.

During the INDOMIX cruise in July 2015, direct estimates of dissipation from microstructure in Halmahera Sea, Banda Sea and Ombai Strait have been obtained (Fig. 8a). Vertical dissipation estimates over the three main straits Ombai Strait (St5, red), Northern Halmahera (St1, yellow) and southern Halmahera (St3, green) portals show very good agreement between INDOMIX and EXPL, with values between 10^{-7} and 10^{-6} W/kg for both model and microstructure measurements. In contrast, region further away from generation sites (st2) are overestimated by the model, which shows value of 10^{-8} W/kg in comparison smaller dissipations between 10^{-9} and 10^{-10} W/kg below 200 m. In the Banda Sea, far away from the generation sites, there is no evidence in the observation of internal tides activity (10^{-10} W/kg) the model still produce 10^{-9} W/kg of dissipation.

If we look more closely in the first 400 m (Fig. 8b), the agreement between the model forced by explicit tides and the observation is closer than elsewhere in the water column, apart for St4. This station still overestimates the dissipation by one or two order of magnitude, while there is no evidence of additional mixing in the observations. It is striking that both for the model (EXPL) and for the observations, the mixing is very strong at the base of the mixed layer and in the thermocline with similar value for both of them, between 10^{-8} and 10^{-7} W/kg.

3.3. *Impact of mixing on water mass and sea surface temperature: spatio-temporal patterns*

Impact of the mixing on water masses is illustrated by a temperature-salinity diagram from the Banda Sea (Fig. 9). CTRL presents a large bias in salinity, with a maximum in the thermocline of 35 psu while in the observation, the value is closer to 34.5 psu. The simulations that included the effect of the tides, either PARAM or EXPL, show better agreement with the observations, including a salinity maximum in the thermocline of 34.55 psu. We remark that both PARAM and EXPL produce almost the same water mass transformation when the forcing terms and the method of taking into account the internal tides are very different.

For the whole Indonesia, the impact of mixing on the sea surface temperature (SST) is shown Fig. 10. Both PARAM and EXPL induce an annual cooling that ranged between 0.2 and 0.8 °C (Fig. 8a), in good agreement with previous studies (Koch-Larrouy et al., 2007, 2010; Kida and Wijffels, 2012). In the region where the parameterization is applied (inner seas of the archipelago, see Koch-Larrouy et al., 2007) the SST cooling obtained with PARAM and with EXPL is very similar, and

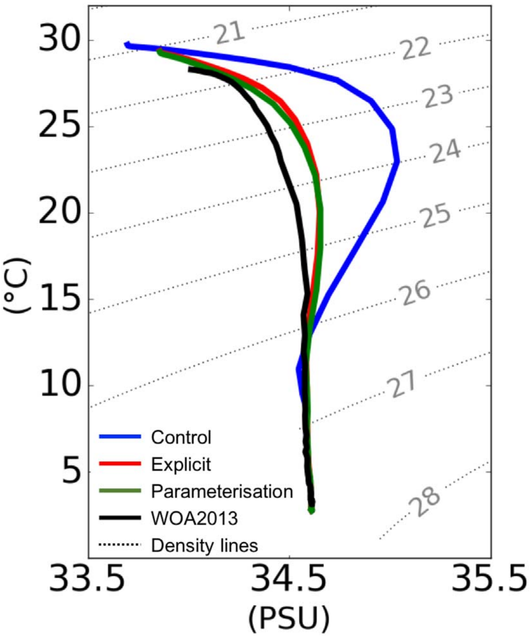

Fig. 9. Temperature-salinity diagram in the Banda Sea from CTRL simulation (blue line), EXPL simulation (red line), PARAM simulation (green line) and climatologies WOA 2013 (www.nodc.noaa.gov). Plot shows horizontally averaged properties on a box (124.75°E–130.83°E; 6.65°S–4.41°S). (For interpretation of the references to colour in this figure legend, the reader is referred to the web version of this article.)

slightly stronger for PARAM than for EXPL. For both simulations, the cooling is heterogeneous in space and stronger above topographic features such as Sibutu, Lifamatola, Lombok and Dewakang Straits, where internal tides are generated (about 0.7 °C for EXPL-CTRL and 0.8–0.9 °C for PARAM). This agrees well with the total dissipation produced by the tides in the model (Fig. 7).

In the Indonesian interior seas the residual mean cooling is between 0.2 and 0.4 °C and is advected by the ITF toward the Indian Ocean, in both simulations. EXPL presents additional cooling compare to PARAM above the Australian shelf, in South China Sea, in Andaman Sea and in Luzon Strait. The cooling in the Luzon strait comes from internal tides generated in Luzon that were not taking into account in the previous PARAM study of Koch-Larrouy et al. (2007). Conversely, the warming in the South China Sea is the result of exchanges intensified by high tidal currents in Malacca Strait, between the colder South China Sea and the warmer Andaman Sea. Finally, the cooling over Australian shelf comes from the strong surface tidal currents that, on the shallow shelf, produce intense mixing (Fig. 7).

Temporally, the impact of tidal mixing on the SST is observed with a distinct seasonal cycle in EXPL (Fig. 10c, d, e and f). On basin average, tidal mixing cools the SST during South East Monsoon the most, as previously showed by Kida and Wijffels (2012). A decrease in cooling is observed during spring and autumn, when the Monsoonal winds are weaker, also in good agreement with Kida and Wijffels (2012).

During austral winter, which corresponds to South East Monsoon, strong cooling is found in region of intensified mixing such as in the Island chain between Sulu and Sulawesi Seas, or downstream of the Lombok, Ombai and Lifamatola Straits. In this season, cooling is found to cover large area from the southern side of the Nusa Tenggara toward the Indian Ocean and from the Seram and Halmahera Seas and the Lifamatola passage to the northern part and norther-eastern part of the Banda Sea. The vertical mixing induced by the tides during austral winter is more efficient because the strong monsoonal winds upwell the thermocline. Colder waters are closer to the surface and thus mixing is more efficient to cool the surface. This spatially large cooling of the SST found during South East Monsoon suggests that tidal mixing is likely capable of affecting the atmosphere during the season of deep atmospheric convection over the Indonesian Seas.

Cooling of the SST is found to occur more locally in other seasons. In North West Monsoon, cooling is observed along the shelf-break of the Australian shelf and in the northern part of the Lifamatola Passage as well as in Sibutu Chanel and the southern part of Sulu Sea (Fig. 7b). Strong cooling is also found in the Island chain between Sulu and Sulawesi Seas. The winds are reversed and create at this season a downwelling, which do not favour a surface cooling due to mixing by the tides.

The M2 and S2 semidiurnal tides combine to produce a fortnightly (14.8 days, spring tides-neap tides) modulation, firstly documented in the observations of the Indonesian archipelago by Ffield and Gordon (1996). Over a fortnight the SST range is between 0.1 and 0.15 °C in the main regions of intensified mixing induced by internal tides, such as Luzon, Dewakang, Makassar, Ombai and Lifamatola Straits as well as in the Islands chain between Sulu and Sulawesi Seas, at the entrance of the Halmahera Sea or in the Sangihe Islands (Fig. 11). In Lombok and Sibutu straits, it is even larger than 0.3 °C (not shown). Also in the shelf-break of the Australian shelf the signal is quite strong, as well as in the northern part of China Sea. In addition the internal tides propagating away from the Luzon Strait or from Sangihe Islands show intensified signal at the Msf frequency. In the northern part of the domain, the signal is noisy and this might be due to the presence of open boundary conditions.

These results compare fairly well in the Nusantarra Islands, in Seram Sea and in the Sibutu Islands to the recent results of Ray and Susanto (2016) (Fig. 1 in their paper) using satellite data. However, the model produces more energy in Dewakang, Makassar, Lifamatola and Malacca Straits and in the entrance of Halmahera Sea, which are regions of intense tidal activity. In contrast, the model does not exhibit any Msf tidal signal in the in Sumba Strait, which does not agree with the study of Ray and Susanto (2016). This might be due to lack of resolution in Sape Strait, connecting Flores Sea and Sumba strait, that prevents semidiurnal tides to generate and passes through the strait. The signal away from the Australian shelf covers a large area where it has been shown that the coupling between ocean and atmosphere is quite efficient (Koch-Larrouy et al., 2010). Also the South China Sea and the Luzon Strait show strong variability at the Msf frequency over basin large domain. Modulation at the Msf (14.8 days) frequency might be of some importance for the intraseasonal variability of the SST at large scale and thus for the convective activity as shown for the Gulf of California (Martinez-Diaz-de-Leon et al., 2013). This could be one of the sources of modulation of the rain activity in the region that would interfere with the passing Madden Julian Oscillation (MJO) (Madden and Julian, 1994; Zhang, 2008).

4. Summary, discussion and perspective

INDESO physical model was forced by explicit tides and was able to reproduce part of the internal tides. They were generated by the interaction of the tidal currents on the topography in the stratified ocean. As observed, part of them radiated away from generation sites. The model is able to reproduce quite well the direction of propagation, as in the Sulawesi Sea. Mixing is found in the model right after generation close to the seamount, but also in the whole water column above the seamount, and in particular close to the surface. In addition, some mixing is also found at the surface further away from the topography feature.

The model shows intensified dissipation close to the generation sites such as Sangihe, Lombok, Lifamatola, Dewakang Straits or Halmahera portals. In Sulawesi and Banda Seas, we also clearly see intensified dissipation further away from generation sites. The model dissipation agrees well with the spatial fine structure obtained by Ffield and Robertson (2008) for Ombai, Dewakang and Lifamatola Straits, and Molucca and Flores seas.

The model and the recent INDOMIX cruise (Koch-Larrouy et al.,

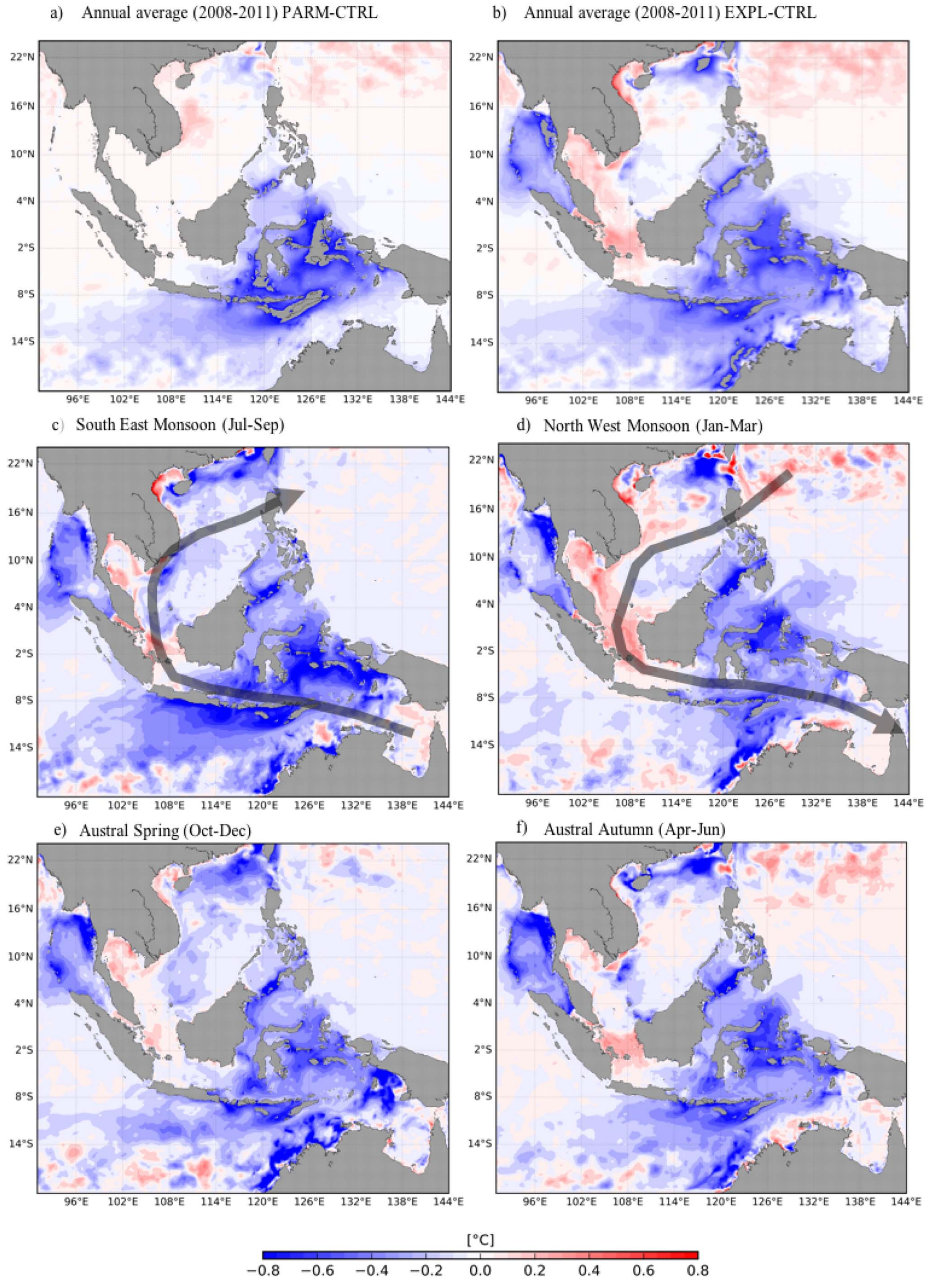

a) Annual average (2008-2011) PARM-CTRL

b) Annual average (2008-2011) EXPL-CTRL

c) South East Monsoon (Jul-Sep)

d) North West Monsoon (Jan-Mar)

e) Austral Spring (Oct-Dec)

f) Austral Autumn (Apr-Jun)

Fig. 10. Sea surface temperature (SST) annual anomaly for (a) PARAM-CTRL and (b) EXPL-CTRL. Sea surface temperature (SST) seasonal anomaly for EXPL-CTRL averaged over: (c) July–August–September (JAS), (d) January–February–March (JFM) (e) April–May–June (AMJ) and (f) October–November–December (OND).

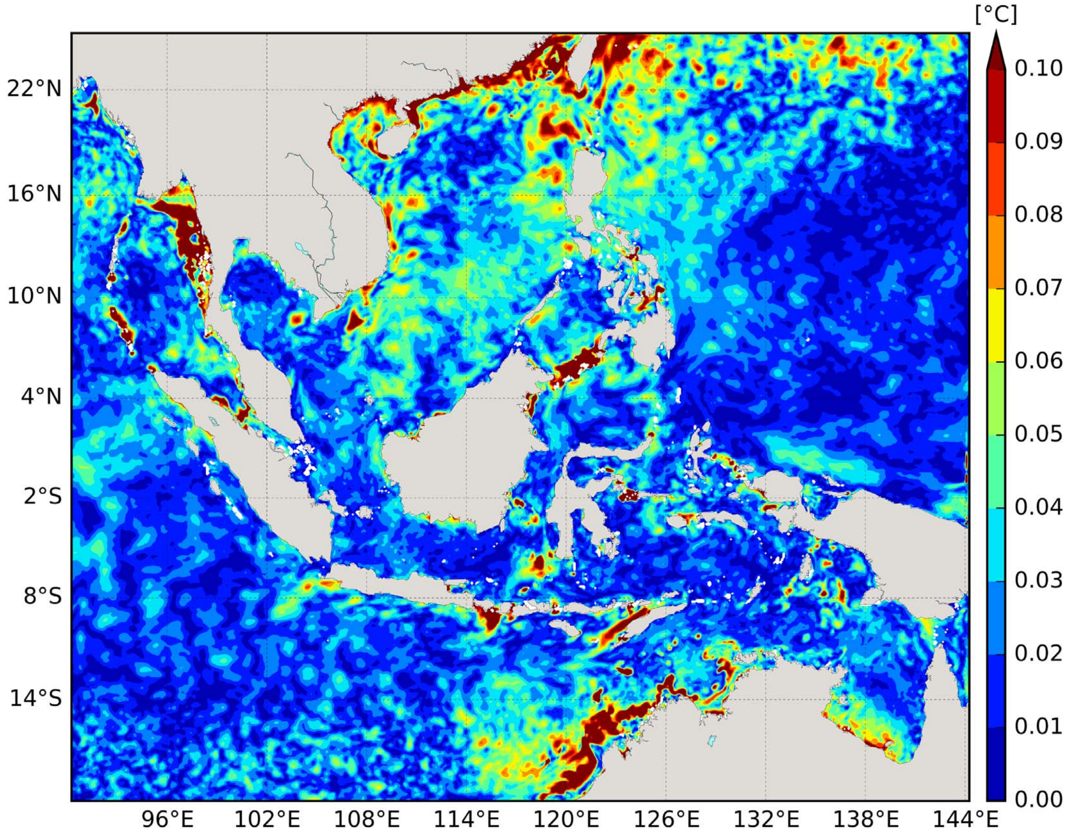

Fig. 11. Amplitude of the harmonic analysis of the SST at the Msf (M2-S2, 14.8 days) frequency (in °C) for EXPL.

2015), which provided direct estimates of the mixing, are in good agreement mainly above straits (station St1, St3 and St5 of INDOMIX). However, in regions far away from any generation sites (Banda Sea) where INDOMIX and also Alford et al. (1999) found no evidence of intensified mixing, the model produced a too strong mixing. Also, below 200 m, in station St2 the model produced stronger mixing compared to the observation.

Both parameterization and explicit tides produced similar water transformation and allowed reproducing the homohaline Indonesian water, whereas in the simulation without tides (CTRL) the model produced large salinity bias.

In basin average, the intensified surface mixing is able to cool the sea surface between 0.3 and 0.7 °C. EXPL and PARAM produce similar SST cooling structure above generation sites, which is slightly stronger for PARAM (0.8 °C). The EXPL simulation produced also cooling due to strait exchange of water mass properties (Malacca strait) and due to dissipation at the bottom above the Australian shelf that were not reproduce in PARAM.

Temporally, the cooling is stronger during South East Monsoon (austral winter), when the winds favour upwelling along the Java coast and in the northern eastern part of the archipelago. Whereas for the other seasons the cooling is localised in small regions of intensified mixing. During South East Monsoon (austral winter) the cooling covers basin scale regions and thus might be of some importance for modulating the above convection and rain in the atmosphere, as shown in Koch-Larrouy et al. (2010).

In addition, the fortnightly (14.8 days) modulation of the cooling due to the tides (spring tides-neap tides) is strong over all straits of intense internal tides generation, such as Luzon, Dewakang, Lifamatola, Ombai, Lombok Straits, Halmahera entrance and Sibutu Islands, as well as in the shelf break of the Australian Shelf and in the South China Sea. The large-scale signal at Msf frequency in the Australian shelf and in the South China Sea might inprints tidal modulation of the atmosphere convective system as found in California for example (Martinez-Diaz-de-Leon et al., 2013). Further research need to be done at sea to investigate if tidal frequency is found in the rain and convective data.

The first limitation of this study is the spatial resolution of the model, which does not allow reproducing correctly the internal tides. As shown in Niwa and Hibiya (2011) a model with 1/12° resolution is able of reproducing only 75% of the internal tides generation due to both insufficient resolution of the bathymetry slopes and of the tidal currents. Furthermore, once generated, the internal tides are dissipated by the model by parameterisation or numerical set ups that are not specifically adapted to the physics of the tides, but rather to larger scale processes or to eddy diffusivity. Thus, the model might not dissipate tides as observed and produces unrealistic mixing. Indeed, when comparing the model to the recent INDOMIX cruise, the model produces higher background mixing in Banda Sea, region where in reality no mixing as been found (Alford et al., 1999; Koch-Larrouy et al., 2015), as well as below 200 m in the inner Halmahera Sea. These shortcomings likely come from the lack of specific set up to dissipate the internal tides once generated. More work is required to solve this problem.

Knowing these limitations, we also show that the model reproduced part of the internal tides in qualitatively good agreement with INDOMIX for their propagation (in Sulawesi) or their intensity in region of high mixing (at St1, St3 and St5 of INDOMIX stations). The model is worth using as a first step to predict the influence of internal tidal mixing to surface properties. However, in future studies it will be important to quantify the exact dissipation produced by the model when adding explicit tides and improve both the resolution and the physics of the model, to take into better account the special behaviour of internal tides.

This study has focused on the impact of mixing on sea surface temperature. The results can be easily transposable for nutrients and biomass as shown in previous studies (e.g. Franks and Chen, 1996; Souza and Pineda, 2001; da Silva et al., 2002; Jan and Chen, 2009) since the vertical mixing would upwell deeper layer richer in nutrients at the surface. Microscale turbulence maintains well-mixed biomass and nutrients within the turbulent surface boundary layer as well as driving nutrient fluxes into the mixed layer (e.g. Lewis et al., 1976). Also, when the internal tides propagate, it can generate vertical displacement of the base of the mixed layer (as shown in Fig. 1) and trigger phytoplankton blooms, by periodically heaving biomass into the euphotic zone (Holloway and Denman, 1989; da Silva et al., 2002). Finally, tidal fronts can also produce phytoplankton blooms (Franks and Chen, 1996). We can thus assume that where the mixing is intensified and there is a surface cooling, this mixing would also modulate at annual, seasonal and intraseasonal timescale the nutrients enrichment of the surface layers. Finally, we can also assume from Fig. 3 that the propagation of the internal tides can produce blooms of phytoplankton along their route.

This study has shown that it would be worth improving the resolution and the representation of the dissipation of the internal tides in the model, as it may improve the realism of the tides. This may also be of some importance for generating better the submesoscales fronts as shown in Lévy et al. (2012). The tides are important for nutrients upwelling at mixing site, on propagation route of internal tides or at tidal front, as well as for connectivity (larvae transport) and maintenance of ecological diversity. Their behaviors could influence the trophic chain of the Indonesian Seas ecosystems, and we hope this study provides the foundation for future enhanced biophysical modelling (Lehodey et al., 2017).

Acknowledgments

This work is part of the INDESO project funded by the Indonesian Ministry of Marine Affairs and Fisheries (01/Balitbang KP.3/INDESO/11/2012). Turbulence dissipation rate data provided by INDOMIX cruise (Koch-Larrouy et al., 2015) using RV Marion Dufresne, http://dx.doi.org/10.17600/10200020.

References

Aiki, H., Matthews, J.P., Lamb, K.G., 2011. Modeling and energetics of tidally generated wave trains in the Lombok Strait: impact of the Indonesian Throughflow. J. Geophys. Res. Oceans 116 (3), 1–17. http://dx.doi.org/10.1029/2010JC006589.

Alford, M.H., Gregg, M.C., Ilyas, M., 1999. Diapycnal mixing in the Banda Sea: results of the first microstructure measurements in the Indonesian Throughflow. Geophys. Res. Lett. 26 (17), 2741. http://dx.doi.org/10.1029/1999GL002337.

Allen, G.R., 2007. Subtidal macrobenthic structure in the lower Lima estuary, NW of Iberian Peninsula. Aquat. Conserv. Mar. Freshwat. Ecosyst. 44 (August), 303–313. http://dx.doi.org/10.1002/aqc.

Allen, G.R., Werner, T.B., 2002. Coral reef fish assessment in the “Coral Triangle” of Southeastern Asia. Environ. Biol. Fish 65, 209–214. http://dx.doi.org/10.1023/A:1020093012502.

Astawa Karang, I.W.G., Nishio, F., Mitnik, L., Osawa, T., 2012. Spatial-temporal distribution and characteristics of internal waves in the Lombok Strait area studied by Alos-Palsar images. Earth Sci. Res. 1 (2), 11–22. http://dx.doi.org/10.5539/esr.v1n2p11.

Castruccio, F.S., Curchitser, E.N., Kleypas, J.A., 2013. A model for quantifying oceanic transport and mesoscale variability in the Coral Triangle of the Indonesian/Philippines Archipelago. J. Geophys. Res. Ocean. 118 (11), 6123–6144. http://dx.doi.org/10.1002/2013JC009196.

Egbert, G.D., Erofeeva, S.Y., 2002. Efficient inverse modeling of barotropic ocean tides. J. Atmos. Ocean. Technol. 19 (2), 183–204. http://dx.doi.org/10.1175/1520-0426(2002)019<0183:EIMOBO>2.0.CO;2.

Ffield, A., Gordon, A.L., 1992. Vertical mixing in the Indonesian thermocline. J. Phys. Oceanogr. 22 (2), 184–195. http://dx.doi.org/10.1175/1520-0485(1992)022<0184:VMITIT>2.0.CO;2.

Ffield, A., Gordon, A.L., 1996. Tidal mixing signatures in the Indonesian seas. J. Phys. Oceanogr. 26 (9), 1924–1937. http://dx.doi.org/10.1175/1520-0485(1996)026<1924:TMSITI>2.0.CO;2.

Ffield, A., Robertson, R., 2008. Temperature fine structure in the Indonesian seas. J. Geophys. Res. Ocean. 113 (9), 1–19. http://dx.doi.org/10.1029/2006JC003864.

Fieux, M., Andrié, C., Delecluse, P., Ilahude, A.G., Kartavtseff, A., Mantisi, F., Molcard, R., Swallow, J.C., 1994. Measurements within the Pacific-Indian oceans throughflow region. Deep. Res. Part I 41 (7), 1091–1130. http://dx.doi.org/10.1016/0967-0637(94)90020-5.

Franks, P.J.S., Chen, C., 1996. Plankton production in tidal fronts: a model of Georges Bank in summer. J. Mar. Res. 54 (4), 631–651. http://dx.doi.org/10.1357/0022240963213718.

Gordon, A.L., Fine, R.A., 1996. Pathways of water between the Pacific and Indian oceans in the Indonesian seas. Nature 379 (6561), 146–149. http://dx.doi.org/10.1038/379146a0.

Hautala, S. L., J. Sprintall, J. T. Potemra, J. C. Chong, W. Pandoe, N. Bray, and a. G. Ilahude (2001), Velocity structure and transport of the Indonesian throughflow in the major straits restricting flow into the Indian Ocean, J. Geophys. Res., 106(C9), 19527, doi:http://dx.doi.org/10.1029/2000JC000577.

Holloway, G., Denman, K., 1989. Influence of internal waves on primary production. J. Plankton Res. 11 (2), 409–413.

Jan, S., Chen, C.T.A., 2009. Potential biogeochemical effects from vigorous internal tides generated in Luzon Strait: a case study at the southernmost coast of Taiwan. J. Geophys. Res. Oceans 114 (4), 1–14. http://dx.doi.org/10.1029/2008JC004887.

Jouanno, J., Capet, X., Madec, G., Roullet, G., Klein, P., Masson, S., 2016. Dissipation of the energy imparted by mid-latitude storms in the Southern Ocean. Ocean Sci. Discuss. 1–49. http://dx.doi.org/10.5194/os-2016-3.

Kida, S., Wijffels, S., 2012. The impact of the Indonesian Throughflow and tidal mixing on the summertime sea surface temperature in the western Indonesian seas. J. Geophys. Res. Ocean. 117 (9), 1–14. http://dx.doi.org/10.1029/2012JC008162.

Koch-Larrouy, A., Madec, G., Bouruet-Aubertot, P., Gerkema, T., Bessières, L., Molcard, R., 2007. On the transformation of Pacific water into Indonesian throughflow water by internal tidal mixing. Geophys. Res. Lett. 34 (4), 1–6. http://dx.doi.org/10.1029/2006GL028405.

Koch-Larrouy, A., Lengaigne, M., Terray, P., Madec, G., Masson, S., 2010. Tidal mixing in the Indonesian seas and its effect on the tropical climate system. Clim. Dyn. 34 (6), 891–904. http://dx.doi.org/10.1007/s00382-009-0642-4.

Koch-Larrouy, A., Atmadipoera, A., van Beek, P., Madec, G., Aucan, J., Lyard, F., Grelet, J., Souhaut, M., 2015. Estimates of tidal mixing in the Indonesian archipelago from multidisciplinary INDOMIX in-situ data. Deep. Res. Part I Oceanogr. Res. Pap. 106, 136–153. http://dx.doi.org/10.1016/j.dsr.2015.09.007.

Large, W., Yeager, S., 2004. Diurnal to decadal global forcing for ocean and sea-ice models: the data sets and ux climatologies. In: CGD Division of the National Center for Atmospheric Research, NCAR Technical Note, NCAR/TN-460 + STR.

Lehodey, P., Senina, I., Murtugudde, R., 2008. A spatial ecosystem and populations dynamics model (SEAPODYM) — modeling of tuna and tuna-like populations. Prog. Oceanogr. 78 (4), 304–318. http://dx.doi.org/10.1016/j.pocean.2008.06.004.

Lehodey, P., Senina, I., Wibawa, T., Titaud, O., Calmettes, B., Conchon, A., Tranchant, B., Gaspar, P., 2017. Operational modeling of bigeye tuna (*Thunnus obesus*) in the Indian Ocean and the Indonesian region. Mar. Pollut. Bull (submitted).

Lévy, M., Ferrari, R., Franks, P.J.S., Martin, A.P., Rivière, P., 2012. Bringing physics to life at the submesoscale. Geophys. Res. Lett. 39 (14). http://dx.doi.org/10.1029/2012GL052756.

Lewis, M.R., Glen Harrison, W., Oakey, S., Neil, D.H., Platt, T., 1976. Vertical nitrate fluxes in the oligotrophic ocean. Science 234 (80), 870–873.

Madden, R.a., Julian, P.R., 1994. Observations of the 40–50-day tropical oscillation—a review. Mon. Weather Rev. 122, 814–837. http://dx.doi.org/10.1175/1520-0493(1994)122<0814:OOTDTO>2.0.CO;2.

Madec, G., 2008. NEMO Ocean Engine. (27).

Maraldi, C., et al., 2013. NEMO on the shelf: assessment of the Iberia-Biscay-Ireland configuration. Ocean Sci. 9 (4), 745–771. http://dx.doi.org/10.5194/os-9-745-2013.

Martinez-Diaz-de-Leon, A., Castro, R., Santamaria-del-angel, E., Pacheco-Ruiz, I., Blanco-Betancourt, R., 2013. Sea surface heat fluxes and fortnightly modulation of the surface temperature within the Ballenas Channel, Gulf of California. J. Coast. Res. 29 (6), 1400–1412. http://dx.doi.org/10.2112/JCOASTRES-D-12-00189.1.

Matthews, J.P., Aiki, H., Masuda, S., Awaji, T., Ishikawa, Y., 2011. Monsoon regulation of Lombok Strait internal waves. J. Geophys. Res. Oceans 116 (5), 1–14. http://dx.doi.org/10.1029/2010JC006403.

Mitnik, L., Alpers, W., Hock, L., 2000. Thermal plumes and internal solitary waves generated in the Lombok strait studied by ERS SAR. Eur. Sp. Agency (Special Publ. ESA SP) 461, 1834–1842.

Molcard, R., Fieux, M., Syamsudin, F., 2001. The throughflow within Ombai Strait. Deep. Res. Part I Oceanogr. Res. Pap. 48 (5), 1237–1253. http://dx.doi.org/10.1016/S0967-0637(00)00084-4.

Mora, C., Chittaro, P.M., Sale, P.F., Kritzer, J.P., Ludsin, S.A., Africa, S., 2003. Patterns and processes in reef fish diversity. Nature 421 (February), 933–936. http://dx.doi.org/10.1038/nature01421.1.

Murray, S.P., Arief, D., 1988. Throughflow into the Indian Ocean through the Lombok Strait, January 1985–January 1986. Nature 333 (6172), 444–447. http://dx.doi.org/10.1038/333444a0.

Nagai, T., Hibiya, T., 2015. Internal tides and associated vertical mixing in the Indonesian Archipelago. J. Geophys. Res. C Oceans Atmos. 3373–3390. http://dx.doi.org/10.1002/2014JC010592.

Nikurashin, M., Vallis, G.K., Adcroft, A., 2012. Routes to energy dissipation for geostrophic flows in the Southern Ocean. Nat. Geosci. 6 (1), 48–51. http://dx.doi.org/10.1038/ngeo1657.

Niwa, Y., Hibiya, T., 2011. Estimation of baroclinic tide energy available for deep ocean mixing based on three-dimensional global numerical simulations. North 1–15. http://dx.doi.org/10.1007/s10872-011-0052-1.

Purwandana, A., 2014. Turbulent mixing in Labani Channel, Makassar Strait. Oseanol. Limnol. Indones. 40 (2), 155–169.

Ray, R.D., Susanto, R.D., 2016. Tidal mixing signatures in the Indonesian seas from high-resolution sea surface temperature data. Geophys. Res. Lett. 43 (15), 8115–8123. http://dx.doi.org/10.1002/2016GL069485.

Sari Ningsih, N., 2008. Internal waves dynamics in the Lombok strait studied by a numerical model. Int. J. Remote Sens. Earth Sci. 5.

Shriver, J.F., Arbic, B.K., Richman, J.G., Ray, R.D., Metzger, E.J., Wallcraft, A.J., Timko, P.G., 2012. An evaluation of the barotropic and internal tides in a high-resolution global ocean circulation model. J. Geophys. Res. Oceans 117 (10), 1–14. http://dx.doi.org/10.1029/2012JC008170.

da Silva, J.C.B., New, A.L., Srokosz, M.A., Smyth, T.J., 2002. On the observability of internal tidal waves in remotely-sensed ocean colour data. Geophys. Res. Lett. 29 (12), 10–13. http://dx.doi.org/10.1029/2001GL013888.

Souza, A.J., Pineda, J., 2001. Tidal mixing modulation of sea-surface temperature and diatom abundance in Southern California. Cont. Shelf Res. 21 (6–7), 651–666. http://dx.doi.org/10.1016/S0278-4343(00)00105-9.

Sprintall, J., Gordon, A.L., Koch-Larrouy, A., Lee, T., Potemra, J.T., Pujiana, K., Wijffels, S.E., Wij, S.E., 2014. The Indonesian seas and their role in the coupled ocean–climate system. Nat. Geosci. 7 (7), 487–492. http://dx.doi.org/10.1038/ngeo2188.

Tranchant, B., Reffray, G., Greiner, E., Nugroho, D., Koch-Larrouy, A., Gaspar, P., 2016. Evaluation of an operational ocean model configuration at 1/12° spatial resolution for the Indonesian seas (NEMO2.3/INDO12) — part 1: ocean physics. Geosci. Model Dev. 9 (3). http://dx.doi.org/10.5194/gmd-9-1037-2016.

Umlauf, L., Burchard, H., 2003. A generic length-scale equation for geophysical. J. Mar. Res. 61 (2), 235–265. http://dx.doi.org/10.1357/002224003322005087.

Veron, J.E.N., Devantier, L.M., Turak, E., Green, A.L., Kininmonth, S., Stafford-Smith, M., Peterson, N., 2009. Delineating the Coral Triangle, *Galaxea*. J. Coral Reef Stud. 11 (2), 91–100. http://dx.doi.org/10.3755/galaxea.11.91.

Zhang, C., 2008. Madden Julian oscillation impacts. Rev. Geophys. 43 (2005), 4. http://dx.doi.org/10.1029/2004RG000158.

Chapter 5

Mixing induced by explicit tides in a realistic simulation of the Indonesian Seas. (Paper to be submitted)

contents

5.1 Mixing induced by explicit tides in a realistic simulation of the Indonesian Seas

5.1.1 Introduction

Context

Internal tides in the Indonesian archipelago are very active and produce intense mixing. As a result, the salinity maximum of the North and the South Pacific Subtropical Water (NPSW and SPSW) is strongly eroded to produce a nearly homohaline water when exiting the Indonesian archipelago [Gordon (1986); Hautala et al. (2001); Ffield and Gordon (1992); Gordon (2005); Sprintall et al. (2014)] .

A vertical diffusivity 10 times higher than in the open ocean ($1.10^{-4} m^2/s$) is necessary to reproduce the water masses as observed [Ffield and Gordon (1992)]. Actually, the mixing is non-heterogeneous and higher values reaching $1.10^{-2} m^2/s$ can be observed above straits as shown in the recent INDOMIX cruise [Koch-Larrouy et al. (2015)]. Models who do not take into account this additional mixing induced by the tides produce large biases (see Koch-Larrouy et al.; Sasaki et al.).

However, in order to take into account this mixing several scientific challenges are to overpass. Internal tides are generated by the barotropic surface tides that create vertical velocity in the stratified ocean above seamount or self break at tidal frequency. The length scale of the generation is thus of the scale of the bathymetry. Once generated the internal tides propagate eventually far away from the generation site as for example in Luzon (eg: Zhao et al.; Xu and Yin; Chao et al.; Alford et al.; Johnston et al.; Rainville et al.) where the internal tides could propagate for several 100 km. Finally, they would eventually dissipate with a scale of turbulence of cm/mm. A model capable of resolving all processes involved in the life of an internal tide (from cm to 1000 km) does not exist. Until now scientists either parameterised the additional mixing Koch-Larrouy et al. (2007) hereinafter KL07 or forced their model by explicit tides and partly resolved the internal tides [Kartadikaria et al. (2011); Castruccio et al. (2013); Nagai and Hibiya (2015)].

Our study began with this statement and our intention is to properly quantify the energy of the dissipation when adding of explicit forcing in the model and compare it to the one induced by the parameterization.

5.1.2 The internal tides in the Indonesian Seas

In the Indonesian seas, the strong surface tidal currents [Egbert and Erofeeva (2002); Ray et al. (2005)] interact with the very complex topography composed by numerous narrow straits, shallow passages and abrupt shelf breaks [Gordon et al. (2003); Gordon (2005); van Aken et al. (2009)] and generate very strong internal tides. The generation of internal tides in the Indonesian archipelago represents 10% of the global value, between 110 GW in KL07 and 85 GW in Nagai and Hibiya (2015) (calculation in smaller domain than KL07 excluding Luzon Strait). Luzon strait generation estimates vary depending on the region and number of tidal component used : 14 GW for M2 [Niwa (2004)],12.4 GW for K1 [Jan et al. (2007)], 30 GW for M2+K1 [Jan et al. (2008)], 18.8 GW [Kerry et al. (2013)], 24.1 GW for M2+K1 [Alford et al. (2011)], 24 GW for M2+K1 [Alford et al. (2015)], 24.9-41.1 GW for M2+S2+K1+O1 [Wang et al. (2016)], or 17.3 GW [Xu and Yin (2016)]. South China Sea, Lifamatola, Dewakang, Ombai, Buru straits, Halmahera portails and Sangihe islands 5.1 also allow strong generation of internal tides [Robertson and Ffield (2008); Koch-Larrouy et al. (2007); Hatayama (2004)].

In the interior of the archipelago, the numerous and small seas do not allow propagation over a large region and it is reasonable to assume that the internal tides will dissipate in the sea where they have been generated. Using this assumption, Koch-Larrouy et al.(2007) adapted the parameterisation developed for open ocean by St. Laurent and Garrett (2002) to the small and semi enclosed seas of the Indonesian archipelago. It prescribes an additional vertical diffusivity, calculated knowing the sites and energy of generation (FES2004, Lyard et al. (2006)), with an idealized vertical profile, maximum in the thermocline, under the assumption that 100% of the energy will dissipate locally. This parametrisation improve the water mass representation in all seas of the domain, with a very good agreement with observations [Koch-Larrouy et al. (2007, 2008, 2010); Tranchant et al. (2016)] and allow reproducing the homohaline water at the outflow portals. The averaged vertical diffusivity (Kz) generated is of $1.5x10^{-4}m/s$, which is the same order of magnitude as the one predicted by Ffield and Gordon (1992). Above straits of generation vertical diffusivity of $10^{-2}m/s$ are found in Koch-Larrouy et al. (2015).

When tested in a coupled model this parameterization reduces the Sea Surface Temperature (SST) by 0.5degC in annual average, which reduces in turn the precipitation by 20%, leading to a more realistic representation of the atmospheric convection [Koch-Larrouy et al. (2010);

Sprintall et al. (2014)]. This impact is larger in austral winter, when the thermocline is shallower due to the monsoonal winds [Kida and Richards (2009); Kida and Wijffels (2012); Nugroho et al. (2017)]. However, this parameterisation was a first step towards taking into account the mixing induced by the internal tides, as in reality, the dissipation may not occurs exclusively locally but some fraction could dissipate in the far field. Also this dissipation may vary in time following the cycles of variability of the surface tides. Such limitations and the increase of resolution encourage scientists to force their Ocean General Circulation Models (OGCMs) by the explicit tidal forcing (eg: in Indonesian seas : Castruccio et al.; Kartadikaria et al.; Nagai and Hibiya, in Luzon : Niwa and Hibiya, in Global : Niwa and Hibiya (2014); Arbic et al. (2012); Simmons et al. (2004); Shriver et al. (2012). The resolution of these models is between 5 to 10 km. Niwa and Hibiya. 2011 show that using a 9km ($\sim 1/12\,\mathrm{deg}$) resolution the model is able to generate only 75% of the internal tides. With a 4km ($\sim 1/36\,\mathrm{deg}$) resolution, the model generates 90% of the internal tides. With such relatively coarse resolution the processes involved in the dissipation of the internal tides can not be resolved. However, studies in the Indonesian archipelago [Castruccio et al. (2013); Nagai and Hibiya (2015); Kartadikaria et al. (2011)] show that the addition of explicit tidal forcing produces mixing that improves the water mass, reproducing the homohaline Indonesian Water.

The question rises then of how much mixing is introduced when forcing by explicit tides? How the model dissipates it, horizontally vertically? In our study we want to answer these questions. We will quantify the generation, propagation and dissipation done by the model and compare it with recent observations [Koch-Larrouy et al. (2015)], with the parameterisation KL07, and with a tidal hydrodynamic model with data assimilation [Lyard et al. (2017)]. We will also quantify the near field and far field dissipation and the spring vs. neap tides dissipation. In this study we perform a set of numerical experiments to answer these questions: with the parameterisation of KL07, PARAM, with explicit tidal forcing, EXPL, and without any additional forcing, CTRL. Simulations are conducted for 5 years and the last 4 years are analysed. We also performed simulation with hourly output during july 2010, as in INDOMIX cruise.

The paper is organized as follow. Section 2 describes the model, the numerical set up and the INDOMIX observations we use in this study, as well as the calculation of energy dissipation we perform. Then section 3 describes the results that are organized as follow. First we describe rapidly the tides reproduced by the model and compare it to observations. We then show the impact of the tidal mixing on water mass, parameterized or explicitly forced in the model. Then we calculate the energy generation and dissipation in the different simulation and compare it for EXPL and PARAM. Finally, we compare this energy dissipation to the recent in-situ INDOMIX cruise.

5.2 Methods and Data

5.2.1 Model and Simulations

This study uses the INDESO configuration detailed in Tranchant et al. (2016). The horizontal resolution is 1/12 deg and the domain covers all Indonesian seas, the South China Sea, as well as the Luzon strait, known as one of the strongest internal tides generation in the region and in the southern part it covers the Northern Australian Shelf (figure 1). Vertical grid uses Z-partial steps with 50 variable layers going from few meters resolution at the surface and 250 m at the bottom. Initial and open boundary conditions (OBCs) are forced by the Mercator-Ocean Global Ocean Forecasting System at 1/4 deg (PSY3V3R3). These conditions include temperature, salinity, currents and Sea Surface Height (SSH). Open boundary onditions (OBCs) are located on a relaxation band of 10 grid points (~ 1 deg). Atmospheric forcing fields come from the European center (ECMWF) and have a high frequency (3 hours). "Bulk" formulae from CORE are used to model the atmosphere-ocean interface [Large and Yeager (2004)]. The surface atmospheric pressure forcing is also explicitly considered. There is NO restoring tem in SST nor in SSS. This configuration includes explicit tidal forcing, with 11 tidal constituents. As in Shriver et al. (2012), INDESO configuration has geopotential tidal forcing for M2 , S2 , N2 and K2 (the four largest semidiurnal constituents) and for K1 , O1 , P1 and Q1 (the four largest diurnal constituents). As in Maraldi et al. (2011), two long-period tides Mf and Mm and one non-linear constituent (compound tides) M4 are also added. These 11 tidal constituents coming from the astronomical forcing TPX0.7 [Egbert and Erofeeva (2002)] are used to force open boundaries. More details about the configuration can be found in [Tranchant et al. (2016)]. Specific physical parameterisations for regional modelling are used such as the GLS (generic length scale) turbulence model [Umlauf and Burchard (2003)] including wave impact and logarithmic bottom friction.

5.2.2 Numerical experiments

We present in this paper three main simulations. The EXPL run includes explicit tidal forcing and the reference configuration (CTRL) doesn't, while the PARAM simulation is forced by the Koch-Larrouy et al. (2007) parameterisation. All of them are forced by the same buoyancy and wind forcing. Simulations start January 3rd 2007 until December 31th 2011. Outputs are sets as daily average and the four last years are analysed after spin up. Shorter run (1 – 31 July 2010) with instantaneous hourly output are also performed in order to calculate the vertical dissipation from the model and compare it to the INDOMIX cruise [Koch-Larrouy et al., 2015] held in July 2010.

5.2.3 FES2014 numerical simulation

In this paper, we compare the modelled tides to the barotropic model FES2014 [Carrere et al. (2016); Lyard et al. (2017)]. FES2014 is the last version of the FES (Finite Element Solution) tide model developed in 2014-2016. It is an improved version of the FES2012 model [Carrere (2012)]. FES2014 takes advantage of longer altimeter time series and better altimeter standards, improved modelling and data assimilation techniques, a more accurate ocean bathymetry and a refined mesh in most of shallow water regions. Special efforts have been dedicated to address the major non-linear tides issue and to the determination of accurate tidal currents. FES2014 is based on the resolution of the tidal barotropic equations (T-UGO model) in a spectral configuration. This configuration is used by AVISO to remove tides from altimetry data, as it has proven to given very good prediction of barotropic tides. It has a finite element grid (2.9 million nodes). The 'free' solution (independent of in situ and remote-sensing data assimilation) gives already very good tidal prediction, which is improved by assimilating long-term altimetry data (Topex/ Poseidon, Jason-1, Jason-2, TPN-J1N, and ERS-1, ERS-2, ENVISAT) and tidal gauges through an improved representer assimilation method. It resolved 34 tidal components (2N2, EPS2, J1, K1, K2, L2, La2, M2, M3, M4, M6, M8, Mf, MKS2, Mm, MN4, MS4, MSf, MSqm, Mtm, Mu2, N2, N4, Nu2, O1, P1, Q1, R2, S1, S2, S4, Sa, Ssa, T2). In addition, it includes geocentric (elastic) tide and also loading tides. Internal tides is parameterized as a sink of energy of barotropic tides. This has been shown to be an essential step towards improvement of the tidal predictions [Le Provost (2003)], as the sink of energy due to internal tides generation, improves the barotropic tides, which compares weel with independent altimetry data. The global conversion rate is of 1.1 TW, in good agreement with independent estimates [Egbert and Ray (2001)], which gives confidence on the estimate of internal tides generation.

5.2.4 INDOMIX in-situ data

In this study we compare the dissipation of the model forced by explicit tides to the recent INDOMIX results [Koch-Larrouy et al. (2015)]. The cruise was held in July 2015 and measurements were done at 5 24h-yoyo-stations. The strategy of measurement is done such as region of different internal tides energy is sampled. Three sites above straits have been sampled: Station St1 is located at the entrance of the Halmahera Sea (figure 1), St3 at the exit of the Halmahera sea and St5 at the Ombai strait. Further away from generation site but still under the possible influence of propagating internal tides, St2 is located in the middle of Halmahera Sea. Finally, St4, in the Banda Sea (figure 1) is very far away from any generation site so that it could be verify that there was no influence of the tides. For each station, estimates of dissipation are done using direct estimate of dissipation provided by a microstructure profiler able to measure the dissipation at scale of 1mm/1cm.

5.2.5 Generation rate

In the general circulation model forced by explicit tides, we calculate the generation rate of internal tides for each tidal components following Kelly et al. (2010):

$$Ct = \langle \bar{u_h} P'|_{z=H} . \nabla H \rangle \tag{5.1}$$

P' and u_h are the perturbation hydrostatic pressure associated to internal tides and horizontal barotropic flow analysed for four main components (M2, K1 S2 and O1) and formed in complex tidal frequency. The angle brackets are a time average over a wave period.This formulation has similar interpretation as previous one from Niwa and Hibiya (2001a)

$$Ct_{niwa} = g \int \rho' \bar{w} \tag{5.2}$$

For the hydrodynamical 2D model FES2014, a parameterization is prescribe to retrieve energy to the barotropic field. The energy transfer from the barotropic to the baroclinic modes(internal tides generation rates) is parameterized as follows:

$$\vec{D} = C \rho \kappa^{-1} N \left(\vec{\nabla} H \vec{u} \right) \vec{\nabla} H \tag{5.3}$$

where κ is the typical topography horizontal wave number, H is the ocean mean depth, N is a depth-weighted average buoyancy frequency, with weights decreasing linearly from the ocean bottom up to the surface to account for the vertical velocity upward linear profile Lyard et al. (2006) and C = 200 (dimensionless) is an empirical tuning coefficient.

5.2.6 Dissipation rate

In PARAM

The Koch-Larrouy et al.,(2007) parameterization of tidal mixing follows the general formulation for the vertical eddy diffusivity proposed by St. Laurent and Garrett,(2002). In this formulation the vertical diffusivity resulting from internal tide breaking, *ktides* is expressed as a function of the energy transfer from barotropic tides to baroclinic tides which is a function of space and stratification :

$$k_{tides} = \frac{q\Gamma E(x,y)F(z)}{\rho N^2} \tag{5.4}$$

where Γ=0.2 is the mixing efficiency, N the Brunt-Vaisala frequency, ρ the density, q the tidal dissipation efficiency, $E(x,y)$ the energy transfer per unit of area from barotropic tides to baroclinic tides and $F(z)$ its vertical structure. Koch-Larrouy et al. propose that $q = 1$, assuming that all the energy will dissipated locally, and proposed $F(z)$ maximum in the thermocline. The associated dissipation introduced in the model can be calculated as:

$$\epsilon_{pot} = \int \rho k_{tides} N^2 \tag{5.5}$$

In EXPL and CTRL

Energy diagnostics and precise evaluations of the energy dissipation in the model are essential elements of our study. They are detailed below. The model kinetic energy (KE) equation can be written as follows [Jouanno et al. (2016)]:

$$\underbrace{\frac{1}{2}\rho_0 \nabla_t u_h^2}_{\text{KE}} = -\underbrace{\rho_0 u_h \left(\vec{u_h}.\vec{\nabla}_h\right) - \rho_0 \vec{u_h}.\vec{w}\nabla_z u_h}_{\text{ADV}} - \underbrace{\vec{u_h}.\vec{\nabla}_h p}_{\text{PRESS}} + \underbrace{\rho_0 u_h.D_h}_{\epsilon_h} + \underbrace{\rho_0 u_h.\nabla_z\left(\kappa_v \nabla_h u_h\right)}_{\epsilon_v} + D_{time} \tag{5.6}$$

where the subscript "h" denotes a horizontal vector,u_h is horizontal velocity vector where w is vertical velocity vector, ρ_0 is the background density, p is hydrostatic pressure, κ_v is the vertical viscosity, Dh is the contribution of lateral diffusion processes and D_{time} the dissipation of kinetic energy by the time stepping scheme. The two first part of right hand side (RHS) in eq.5.6 are the horizontal and vertical advection terms. Third part in RHS is pressure works. Fourth and fifth terms in RHS are horizontal and vertical diffusion, while the last term is the dissipation of kinetic energy by the time stepping scheme. We use bilaplacian operator for horizontal(geopotential) lateral diffusion on momentum with a constant value $1.25.10^{10} m^2/s$.

$$\epsilon_v^{kin} = \iiint \left(\rho_0 \kappa_v \frac{\partial u_h}{\partial_z} . \frac{\partial u_h}{\partial_z} \right) dxdydz + \iint \left(u_h.\tau_s - u_h.\tau_b \right) dxdy \tag{5.7}$$

where $(u_h.\tau_s)$ is the wind stress and $(u_h.\tau_b)$ is bottom stress, i.e the friction

$$\epsilon_h^{kin} = \iiint \rho_0 \sqrt{\kappa_h} \left[\left(\frac{\partial^2 u_h}{\partial x} \right) . \left(\frac{\partial^2 u_h}{\partial x} \right) + \left(\frac{\partial^2 u_h}{\partial y} \right) . \left(\frac{\partial^2 u_h}{\partial y} \right) \right] dxdydz \tag{5.8}$$

The total dissipation of kinetic energy by spatial diffusive processes (E_{diss}) is computed as the total spatial integral of diffusive terms ($\epsilon_h^{kin} + \epsilon_v^{kin}$) Jouanno et al. (2016). The model potential energy (PE) equation can be written as follows:

$$\left(\frac{\partial \rho}{\partial t} + \nabla(\rho u_h) \right) gz = \frac{\partial \rho}{\partial z} gz + \underbrace{\frac{\partial \left(\kappa_z \frac{\partial \rho}{\partial z} \right)}{\partial z} gz}_{\epsilon_v^{pot}} + F_{surface} \tag{5.9}$$

Where $F_{surface}$ are all the forcing terms at the surface. The dissipation of internal tides is not resolved explicitly in the model and may happen through various terms: horizontal or vertical diffusion due to the shear (ϵ_h^{kin},ϵ_v^{kin},friction($u_h.\tau_b$) or vertical destruction of buoyancy (ϵ_v^{pot}). In this paper we calculate these terms (ϵ_h^{kin},ϵ_v^{kin},friction,ϵ_v^{pot}) for both the EXPL and the CTRL simulations and make the difference for each term between the two simulations to assess the tidal contribution. Indeed, in simulation including thermodynamical forcing such as ours, it is not trivial to calculate dissipation terms of the tides only as dissipation is non linear, which make it difficult to separate dissipation of the tides from the rest of the circulation. The calculation we propose here is unperfected as it assumes that the rest of the physic apart from the tides will produce the same dissipation with or without tides, which may not be entirely true. However we believe that these effects are smaller than the first order that we are looking for, and that as a first step it will give coherent results. Note also that the tides may also dissipate through numerical dissipation such as the asselin filter or the barotropic filter, etc. In this study we do not calculate these terms, as they may be of second order.

5.3 Results

5.3.1 Impact on water mass

As previously shown by other modelling studies [Castruccio et al. (2013); Kartadikaria et al. (2011); Nagai and Hibiya (2015)] the explicit tidal forcing significantly modifies the water mass in the Indonesian Throughflow (figure 5.2). The salinity maximum of the South Pacific Subtropical Water (SPSW) at the entrance (box e1) in the CTRL simulation (blue line) is of about 35.6 psu. It remains almost unchanged in Halmahera and Seram seas while the observations (black line) show water in Seram Sea almost homohaline water due to strong vertical mixing in the Halmahera seas. The simulation including the explicit tidal forcing (EXPL) reproduces better this salty erosion at the eastern entrance than CTRL. Actually, it produces a water mass transformation as the one observed in PARAM. Along the western route, the model (CTRL, PARAM and EXPL) has a salinity bias at the entrance (box w1) and the salinity maximum is of 34.55 psu when in the observations it is 34.5 psu. This bias remains all along the western route until Banda and Flores seas. The simulation with explicit tidal forcing does a better job in reproducing the salinity erosion. As for the eastern route, the EXPL simulation reproduces a very similar water mass transformation as in PARAM for the western route. The question is then how the mixing produced by the parameterisation compares to the one produced by the model when introducing the explicit tidal forcing. In section 5.3.5 we will compare the energy dissipation for both PARAM and EXPL.

5.3.2 Semidiurnal and diurnal tides

We present the two primary tidal components, M2 and K1, resolved by the EXPL simulation, as both of them form the largest amplitude of the semidiurnal and diurnal tides in the Indonesian seas [Robertson and Ffield (2008); Kartadikaria et al. (2011)]. In figure 5.3, they are compared with the FES2014 simulation [Carrere et al. (2016); Lyard et al. (2017)]. EXPL show internal tides signature that are not explicitly calculated in FES2014. The general value of phase and amplitude for both M2 and K1 reproduced by EXPL are in quite good agreement with the FES2014 simulation. They both show that the semidiurnal tides enter from both the Pacific and

Indian oceans converging in Makassar Strait and in the Seram Sea with an amphidromic point forming above the Australian shelf. Diurnal tides were dominated by the Pacific Ocean tide. The amplitude of the semi-diurnal tide presents maxima on the Australian shelf, in the Adaman Sea both in quite good agreement with the FES2014 simulation. However, EXPL exhibits too large amplitude from Sulawesi Sea to Makassar Strait between 70 and 80 cm when in FES2014 it is about 10 cm less. On the contrary M2 amplitude in South China Sea is underestimated in comparison to the FES2014 model. K1 show better agreement to the FES2014 simulation in the South China Sea, however it underestimates the amplitude in the Eastern edge of Banda Sea. When comparing to the tidal elevation estimated from TOPEX/Jason1/Jason2 crossovers (See Tranchant et al.(2016), fig 5 right panels), the model successfully replicates them with better agreement for the diurnal constituents - RMS differences of 1 to 3 cm in the domain except in the South China Sea, RMS differences of 6 to 7 cm – and for the semidiurnal constituents – RMS differences of 2 to 4 cm in the domain except over the Asutralian shelf and southward of Lombok Strait, RMS differences of 7 to 10 cm. In addition, a power Spectrum of the model SSH is compared to several tide gauges at the coast and show very good agreement with observations (Tranchant et al.,(2016), fig 6). The spectral analysis shows that SSH fluctuations depict the same peaks at the dominant tidal frequencies, the diurnal (O1 and K1) and semidiurnal (M2 and S2). The same intensity is found in the model and in the observations (see Tranchant et al.,(2016) for more details). The barotropic field is in quite good agreement with previous model study the tides in the Indonesian seas [Castruccio et al. (2013); Kartadikaria et al. (2011); Robertson and Ffield (2008)].

5.3.3 Generation of baroclinic tides

Internal tides generation are calculated for EXPL following eq. (1) for the four primary tidal components, namely M2, S2 K1 and O1, which are found to be the major components that drive tidal forcing in the Indonesian seas [Robertson and Ffield (2005, 2008); Kartadikaria et al. (2011)]. As previously shown in earlier studies [Castruccio et al. (2013); Hatayama (2004); Robertson and Ffield (2005); Nagai and Hibiya (2015)] strong internal tides generate above main straits and shallow passage in the EXPL simulation. It is compared to the internal tides generation in FES2014 [Carrere et al. (2016); Lyard et al. (2017)] calculated as a wave drag coefficient wave drag has the direction of the topography gradient (eq.30 in Lyard et al. (2006)). FES2014 with its high finite element resolution gives a good estimate of internal tides conversation rate, helping barotropic tides to loose energy and compares better to the altimetry data [Le Provost (2003)]. Both models exhibit strong generation energy ($10^{-0} W/kg$) at Luzon strait, Sangihe chain, Lifamatola strait, Sibutu Chanel, Halmahera Sea, Buru, Ombai and Lombok Straits (figure5.4). Also the inner arc of the western part of Banda as well as the Dewakang, Timor and Makassar Straits and the Buton and Muna Islands present smaller energy of generation ($10^{-1} W/kg$) in good agreement for both simulations. Note that in our model the conversion term is not strictly positive and similar results are found in other studies [Niwa (2004); Carter et al. (2008); Zilberman et al. (2009); Kang and Fringer (2012b); Nagai and Hibiya (2015)]. The latest study explain the negative values from the average operation of the complex variable (eq.5.1), when p' and are not at the same phase, the cosinus could be negative. We propose possible scenario when it could happened: (1) when the baroclinic tides propagates and encounter a bathymetry feature where there is another internal tides generation, most probably the recent internal tides may not have the same phase as the ancient one as barotropic tides do not propagate at the same phase; (2) if dissipation occurs (through friction and/or horizontal or vertical dissipation) this will change the phase of baroclinic tides in comparison to the barotropic tides, and may product negative values. Table 5.1 compares the integrated values of generation energy for both models on the total domain, on the inner seas and Luzon strait. For the entire domain, INDESO configuration produces about 215 GW of internal tides for the four main components (M2+K1+S2+O1). FES2014 gives a total of 295 GW for the four main components. For the Inner seas, along the ITF region, INDESO configuration produces about 123 GW of internal tides, while, for FES2014 it is 165 GW. The model with a 1/12ˆ0 resolution, in the global domain, produces about 73% of the internal tides estimated by the higher resolution FES2014 and 74% in the inner seas. This result is in very good agreement with the previous estimate of Niwa and Hibiya (2011), who predicted that a model with 1/12ˆ0 resolution would reproduces only 75% of the internal tides energy for the four main components (M2+K1+S2+O1). Surprisingly, for Luzon the model produces more internal tides (50GW) than the FES2014 simulation (48GW), when we would have expected smaller value of about 36GW, if the model had respected the same rule of 75% of generation of the tides of FES2014. This might be due to a too large incoming barotropic flux across the slope, and/or poor resolution of bathymetry features. In addition, energy input for the parameterization is calculated in the inner seas (where the parameterization is enhanced). It uses only two components with the ratio: 1.25*M2 + K1. The values are smaller than for FES2014 with 122.7 GW in comparison to 165.5 GW due to poorer resolution, which accidentally is closer to INDESO simulation (123 GW).

5.3.4 Propagation of baroclinic tides

Figure 5.5 show the signature of propagating internal tides generated by EXPL. Propagation from Luzon strait occurs towards both sides of the seamount, ie to the eastern and the western directions. In the western direction, the baroclinic tide propagates southwestward. After 5 reflexions at the surface (positive anomaly) the signal is much weaker. We can still see three more reflexions but very weak. We conclude that it must dissipate during the propagation. Signal towards the eastern direction is seen on a larger distance. Similarly, the Sangihe islands, the Sibutu and Lifamatola straits create strong propagating internal tides in the model. The interaction with the inner seas may stop the internal tides from further propagation as seen in the Sulu Sea and in the Seram Sea. Also in this inner part of the archipelago the interaction between several generation sources make the signal more noisy as for example in Sulawesi sea that exhibit internal tides coming from either Sangihe Island or Sibutu Strait.

Satellite true color image from MODIS [Jackson (2007), figure 3 and 5 of his paper] provide a qualitative validation when comparing to the model isopycnal displacement (figure 5.5a) and show for both of them clear propagation of internal tides from Sulawesi Sea (figure 5.5b) and within Ombai Strait (figure 5.5c). In Sulawesi Sea, the MODIS image reveals five groups of internal waves, visible in western half of the sea, two propagating west toward Borneo, two wave groups propagating southeast toward Sulawesi, and the partial signature of a fifth group visible immediately adjacent to the coast of Sulawesi. The model compares well to this image as we clearly see internal waves corresponding to group 1, 2 and 4 (green lines) validating qualitatively the direction of propagation from Sangihe islands and from Sibutu channel. Generated in the Ombai Strait, internal tides propagate northward towards Buru Island.

The model represent fairly well this propagation both in terms of direction and distance of propagation. Wang et al.,(2011) , using more than 2500 images from several satellite instruments (ENVISAT ASAR, ERS-2 SAR, MODIS and HJ-1A/1B), show that internal waves propagation from Luzon can reach the Hainan Island (see figure 5.1), and few of them propagate further south in the South China Sea. However, in the model, internal tides are strongly dissipated after 400 km and do not propagate as far as observed. This first step comparison with available observations gives confidence in the model, at least for direction of propagation but a more quantitative validation would be needed with other type of in-situ observation. In the next sub-section, we will compare the diffusion of the model to recent INDOMIX cruise.

5.3.5 Dissipation

In this paper we are looking at the sink of both potential and kinetic energy associated to the tides following equations 5.7,5.8 and 5.9. Assessing the dissipation of the tides only in our simulation that includes also thermodynamical forcing is not obvious. In this study, we choose to run twin experiments with and without tides to retrieve the tidal energy. Doing that we assume that the non-tidal physic will be the same in CTRL and EXPL, which may be not entirely true as non-linear exchanges may occur between the mean flow and the tides, but we assume that at first order it is correct. In a following study, we plan to compare this results to other simulations forced only by the tides to validate this hypothesis. In addition, in this paper, we compare the dissipation rates calculated as mentioned above to the one obtained by the parameterisation of Koch-Larrouy et al.,(2007).

Friction

The friction of EXPL-CTRL is shown figure 5.6. It may correspond to the friction due to barotropic or baroclinic tides. Separate them is not possible with our simulation only as friction is a non linear process. Above all internal tides generation sites friction is quite strong with values of $1.10^{-1}W/m^2$, such as Luzon strait Sibuttu, Sangihe chain, Lifamatola Dewakang, Makassar and Ombai, straits as well as Halmahera portals. In addition, the friction is intensified over the shallow Seas such as Java Sea, northern part of South China Sea and over the Australian shelf with values between 10^{-2} and $10^{-1}W/m^2$, which may be attributed to the barotropic tides. In the deeper but small sea such as Malukku and Seram Seas and Timor passage the friction is between 10^{-3} and $10^{-3}W/m^2$. The integrated values for the whole domain is 316.35 GW, out of which 61 GW is lost in the inner seas and 26.52 GW in the Luzon box (figure 5.6). The remaining energy is lost in the Admaman Sea and in the southern part of the South China Sea and Java Sea as well as in the southern part of the Australian shelf (not shown).

Horizontal Vs vertical dissipation

Figure 5.7 and 5.8 show vertical distribution of dissipation rate for PARAM, EXPL and CTRL. For PARAM the enhanced dissipation due to the tides comes from the additional vertical diffusivity, K_{tides} (eq. 5.4), prescribed locally above generation sites [Koch-Larrouy et al. (2007)]. In figure 5.7a, we show the equivalent dissipation rate for PARAM computed following eq 5.5. Intensified dissipation is found above generation sites of $10^{-6} W/kg$: in Sulawesi Sea (section H1, see figure 5.5 for localization), both above Sangihe Chain and on the Sibuttu strait slope, above Lombok strait (section V1), in section V2, on the slope of the Ombai strait and close to the Buton and Muna islands at 5^0S in the Banda Sea, and finally along section V3, within the entire Halmahera Sea. For all section, vertical profile of enhanced dissipation is maximum in the thermocline as prescribed in Koch-Larrouy et al. (2007). Figure 5.7 (b and c) show ϵ_h^{kin} for EXPL and CTRL respectively. The tidal forcing in EXPL produces stronger horizontal dissipation compared to CTRL on both sides of the Sangihe chain (H1, see figure 5.5 for localisation) above the 1500 m sill with values of $10^{-7} W/kg$ and also on the slope of Sibutu Strait ($10^{-8} W/kg$). We also note smaller additional energy in the inner Sulawesi Sea below the mixed layer with hot spot between 10^{-9} and $10^{-8} W/kg$. For Lombok strait (Section V1), strong dissipation due to the tides is found in EXPL above the strait and on the northern part of it, with values as high as $10^{-6} W/kg$, and also on the southern slope with values of $10^{-8} W/kg$, that does not appear in CTRL. On the Ombai northern edge (section V2) strong energy is dissipated above the slope between 4000m and the surface, with values between 10^{-7} and $10^{-6} W/kg$. We also see clearly hot spot of intensified dissipation in EXPL of $10^{-8} W/Kg$ all along the section, that are associated to the tides since we don't see them in CTRL. The region of intensified mixing between 8^0S until 4000m and 6.5^0S concerning the first 500m is the signature of northward propagating internal tides generated in the Ombai slope. We note another point of generation over the seamount at 6^0S. Signature of intensified mixing further north may also come from the generation site in the Buton and Muna Islands. Finally within the Halmahera Sea, several points of generation are seen at 2^0 S, 1^0S and 0.5^0N, with higher dissipation of $10^{-8} W/kg$. Once generated the internal tides remain trapped in the Halmahera semi enclosed sea and explain higher value than for the other sections further away from the generation site, with values between 10^{-8} and $10^{-7} W/kg$. We also note that the generation is stronger in the northern part of the Halmahera Sea than in the southern part with more hot spot of mixing with values close to $10^{-6} W/kg$. In contrast, the vertical dissipation ϵ_v^{kin} and ϵ_v^{pot} of EXPL (figure 6) does not exhibit significant tidal signature, as they are very similar to CTRL. We still note a small increase of mixing in ϵ_v^{kin} above straits of the order of $10^{-10} W/kg$, with rare hot spot of mixing between 10^{-8} and $10^{-7} W/kg$ mainly at the bottom in Lombok and Halmahera. As for ϵ_v^{pot}, we do not see on these sections significant differences between CTRL and EXPL. When calculating the integrated value of these dissipation rates below the mixed layer (table 5.2), we found the same result. The internal tides in the model when forced by explicit tides (EXPL) are dissipated mainly by the kinetic horizontal dissipation (hkin), with rate of 19.9 GW in the inner seas. Another 3 GW comes from the vertical kinetic dissipation (ϵ_v^{kin}). While vertical potential dissipation does not show significant value. Similar results are found for Luzon strait, with horizontal dissipation of 10.5 GW and vertical dissipation is 3 GW and 0.4 GW, for kinetic and potential energy respectively. We conclude that the main term that dissipates the additional energy from the tidal forcing is done by the horizontal dissipation, and in the following sections we will concentrate on the (ϵ_h^{kin}) to study the spatial and temporal distribution of the dissipation of the tides.

The tidal energy dissipation obtained in EXPL compares well with the one added by the parameterization. For PARAM, the dissipation of the tides is 16.8 GW. In addition, PARAM produces less vertical dissipation, in comparison with CTRL, ϵ_v^{kin}= -3 W/kg, which can be understood as follow: the additional mixing induced by the parameterization of the tides destroys the stratification and the fronts, reducing the global instability of the ocean, thus the turbulent kinetic scheme (tke) work less in PARAM than in CTRL.

Local, near field and farfield dissipation

The integrated horizontal distribution of dissipation of the tides is shown for the Luzon and ITF regions (figure 5.9). The model, as previously discussed, shows intensified dissipation close to the generation sites such as Sangihe, Lombok, Lifamatola, Dewakang Straits or Halmahera portals. In Sulawesi and Banda seas, we clearly see intensified dissipation further away from generation sites. In section 5.3.4, we have seen that the model is able to create propagative internal tides, from Ombai, from Sangihe or from Luzon. The next step is now to quantify how much energy is dissipated far from the generation site. In this sub-section, we try to quantify the dissipation at the generation site, near to it and far from it. Of course, the limit between local, near field and far field is arbitrary and we make several sensitivity tests of the distance from generation site to document it. We construct a mask for generation sites using the conversion rate from barotrope to baroclinic tides of both FES2014 and our model (figure 5.4). When generation rate for both simulations reach significant values ($1.10^{-2} W/m^2$), we defined the region as a generation site. Note, that using our simulation only to construct this mask is not satisfactory because it produces some noise (positive/negative values) far away from generation sites in open sea (see section 5.3.3 for possible explaination), which are not related to internal tides generation. We verify that generation terms match for each region for both models, and that what we remove from our model is only associated to this noise of the conversion term (not shown). When applying this mask to the horizontal dissipation produced by EXPL due to the tides (figure 5.7b), we obtain figure (5.9a-d) and (5.9e-h) for the Luzon and ITF regions respectively. The total dissipation above generation site is 10.8 GW in the inner archipelago, i.e. 56% of the total dissipation over this region. For Luzon, the local dissipation is of 6 GW, which represent also 56% of the total dissipation this strait. Dissipation in the near field is defined within a distance of 6 points from the generation source, i.e. approximately 54km (figure 5.9c and g). About 25% (5 GW) is dissipated near the generation sites. We perform tests for this distance within the range of 1 to 6 points (see table 5.3 and 5.4) from the generation point, and the near field dissipation ranges between approximately 2.6 to 5 GW, when changing the distance from 36 km to 54 km, which correspond to 15 to 25% of the total dissipation in the inner seas. The semi enclosed Seram, Halmahera and Malukku seas are so small that almost all the energy remains in the near field. Similarly, the Flores, Savu and Timor seas are almost entirely concerned by the near-field dissipation. What remain for the far field dissipation is the Sulawesi sea, part of the inner Banda Sea and the Indian and Pacific Ocean. The total of far field dissipation vary from 4 to 6 GW, depending on the distance chosen between 36 and 54 km respectively, which represents between 20 and 30% of the total dissipation (table 5.3). The main signal comes from dissipation in the southern Sulawesi Sea, with values of 10 -2 W/m2, with internal tides coming either from Sibuttu Strait or Sangihe Islands. We verify that this signal is not the signature generation of internal tides (not shown). Also in the inner Sulawesi Sea, coming from Sangihe Chain signature of the propagative tides is seen. The signal is stronger closer to the Sangihe chain and decrease progressively from 10-2 to 10-3 W/m2. For Luzon strait, near field represents between 25 and 29% of the total, when varying the distance from 36 to 54 km, and the far field between 15 and 20%. For both the inner seas and the Luzon strait the proportion of far, vs. near field is very similar 19 and 15% for the far field and 25 or 29% for near field respectively.

5.3.6 Comparison to in-situ estimates

The model agree well with the Ffield and Robertson (2008) finestructure estimates, which indicate intensified tidal mixing in Ombai, Lifamatola and Dewakang straits, in Molucca Sea, in the Banda Sea offshore the Muna and Buton Island (125^0E, 6^0S), and in the Flores Sea, as well as in the eastern part of the Australian shelf. However, this estimates only give spatial structure but not quantitative estimate. During the INDOMIX cruise (July 2010), direct estimates of dissipation from microstructure in Halmahera Sea, Banda Sea and Ombai Strait have been obtained (figure 5.10). Vertical dissipation estimates over the three main straits Ombai Strait

(St5, red), Northern Halmahera (St1, yellow) and southern Halmahera (St3, green) portals show very good agreement between INDOMIX and EXPL, with values between 10^{-7} and 10^{-6} W/kg for both model and microstructure measurements. In contrast, region further away from generation sites (st2) showing in the observation smaller mixing between 10^{-9} and 10^{-10} W/kg below 200m are overestimated by the model, which show value of 10^{-8} W/kg. Also in the Banda Sea, far away from generation sites, in the observation there is no evidence of internal tides activity ($10^{-10}-$W/kg) the model still produce 10^{-9} W/kg of dissipation. In the first 400m (figure 5.10b), the agreement between the model forced by explicit tides and the observations is better than for the entire water column, apart for St4, which still overestimate the dissipation by one or two order of magnitude when in the observation there is no evidence of additional mixing. What is striking is that both for the model (EXPL) and for the observations, the mixing is very strong at the base of the mixed layer and in the thermocline with similar value for both of them between 10^{-8} and 10^{-7} W/kg. The surface intensified mixing cools and modulates the surface water properties at tidal frequencies [Koch-Larrouy et al. (2007, 2008, 2010); Kida and Wijffels (2012); Nugroho et al. (2017)].

5.3.7 Spring tides and neap tides

The M2 and S2 semidiurnal tides combine to produce a fortnightly (14.8 days, spring tides-neap tides) modulation, firstly documented in the observations of the Indonesian archipelago by Ffield and Gordon (1996). There is about a seven-day interval between spring and neap tides. Figure 5.11 show horizontal kinetic dissipation (ϵ_h^{kin}) for four regions for both neap tides and spring tides: Luzon strait (B1), Sulawesi sea and Sangihe chain (B2), the eastern archipelago including, Halmahera Sea and Lifamatola Strait (B3) and the Ombai Strait with the Southern Banda Sea (B4).

Table 5.5 show the integrated values of ϵ_h^{kin} for both spring and neap tides. Note that these values are calculated by removing CTRL from EXPL. We verify that values for CTRL are the same between spring and neap tides (not shown). So the difference between spring and neap tides obtained in table 5.5 are only due to the tides.

For Luzon strait (B1), dissipation for spring tides is of 16 GW when it is only 8.8 GW for neap tides, which correspond to an increase of 60 % in comparison to the mean value. This increase of dissipation during spring tides is seen above the seamount, but also downstream in the interior of the Sulawesi Sea. For Sulawesi region (B2), dissipation is larger both at generation site of Sangihe and Sibuttu Strait and in the Sulawesi sea interior in spring tides than in neap tides. Spring tides generate double dissipation than neap tides (7.6 GW, 1.7 GW), which correspond to 125% more energy in spring tides than in the mean. For the Eastern entrance of the archipelago (B3), the dissipation over a fortnight cycle varies by only 25% from the mean (7.6 GW for spring vs. 6 GW for Neap tides). Spring and Neap tides, in contrast to the two previous regions, are of the same order of magnitude. We still note smaller increase during spring tides above all main straits of generation such as Buru and Lifamatola straits and Halmahera portals and in the interior Halmahera Sea. Finally for Southern Banda region (B4), spring tides produce two times more dissipation than neap tides, but both of them are relatively small (2 GW vs. 1.1 GW).

As previously shown in this study, the horizontal dissipation ϵ_h^{kin} described above exhibits the largest signal of the tides in comparison to the vertical terms (eq. 5.6 to 5.9). However, we still note a small increase of vertical kinetic dissipation ϵ_v^{kin} due to the tides between spring and Neap tides in Luzon strait (B1) and in Sangihe chain (B2) (table 5.5). No significant changes are seen for vertical dissipation of potential energy (ϵ_v^{pot}) (table 5.5).

5.4 Summary

More and more studies are including explicit tides to their simulation in the Indonesian seas, as it has shown to improve water mass properties [Castruccio et al. (2013); Kartadikaria et al. (2011); Nagai and Hibiya (2015); Tranchant et al. (2016)]. However, General Circulation Models are not able to resolve internal tides properly. Firstly, with 1/12° resolution it has been shown that only 75% of generation could be retrieve [Niwa and Hibiya (2014)]. But more importantly, how the model will dissipate the additional tidal energy is a big unknown. Our study aims at quantifying how much and how mixing is reproduced by the model when forced by explicit tides.

In this paper, we show, as previous studies [Castruccio et al. (2013); Kartadikaria et al. (2011); Nagai and Hibiya (2015); Tranchant et al. (2016)] that introducing internal tides improve the water mass transformation in the Indonesian Through Flow. In fact, we show that it produces very similar response than the dedicated parameterization constructed by Koch-Larrouy et al.,(2007). The maximum of salinity of the Pacific Subtropical Water is eroded at almost the same rate for both PARAM and EXPL, and the model is able to reproduce at the exit of the archipelago the homohaline water characteristic of the Indonesian Water.

The barotropic tides main features are well reproduced by the model. M2 enters from the Indian and Pacific oceans while K1 enters mainly from the Pacific Ocean. Amplitude and Phase compares well with the hydrodynamic assimilated model FES2014 [Lyard et al. (2017)]. We note some biases for M2 over the Australian shelf and in the Pacific before entering Luzon Strait, as well as in Flores and Makassar strait, while for K1, the larger bias is mainly in the south china sea. These biases are comparable to the one obtain by other study [Kartadikaria et al. (2011)] at such resolution.

Also, the model reproduces qualitatively well the direction of propagation coming from Luzon, Sangihe and Sibuttu in Sulawesi Sea and Ombai strait when comparing to previous study Wang et al. (2011, 2016); Jackson (2007) using SAR images. This validation is only qualitative and validation using in-situ data, such as gliders or current meters or dedicated analysis of altimetry data, would be needed to properly validate the propagation of the internal tides in the model.

Generation of internal tides is 215 GW, upon which 123 GW is generated in the inner seas while 50 GW is converted over Luzon Strait. The model reproduces 74% of the conversion rate (295 GW) calculated by the hydrodynamical model FES2014 for the entire domain, which provides a good estimate of internal tides generation thanks to its high resolution finite element grid [Carrere et al. (2016); Lyard et al. (2017)]. This result is in good agreement with the previous study of Niwa and Hibiya,(2014), who predicted that model, with such resolution, would reproduce 75% of the total internal tides conversion. In addition, the previous parameterization Koch-Larrouy et al.,(2007), using an older version of FES2004, has an energy input for internal tides of 195GW over the total domain and 123 GW over the inner seas. The good agreement with previous studies, give us confidence to study the becoming of dissipation in the model, as it should offers food for thought not only for our model but for all general circulation models.

We thus calculate dissipation as sinks of energy of potential and Kinetic energy as described in equations 5.7 to 5.9. Since dissipation is highly non linear it is not possible to separate the friction due to the barotropic and due to the baroclinic. The total friction induced by the tides is 316 GW, out of which 61 GW is lost in the inner seas, while 26 GW in Luzon Strait. In the total domain, the horizontal and vertical dissipation done by the tides is 48.3 GW, while in the inner seas it is 22.4 GW and in Luzon 13.7 GW. In the inner seas, where the parameterization (Koch-Larrouy et al. (2007)) is added, PARAM exhibits 16.3 GW, which is of the same order of magnitude as the 22.4 GW for the simulation forced by explicit tides. The good agreement for dissipation due to the internal tides for both EXPL and PARAM may explain the very similar water mass transformation along the ITF path of both simulations.

About 85% of the dissipation in the inner seas, is dissipated by the horizontal shear (19GW), while in the total domain and in Luzon domain 60% is dissipated horizontally. The rest is dissipated (15% in the inner seas and 30% in Luzon) is dissipated through vertical shear. Vertical dissipation via potential energy is not significant. This result is anti-intuitive, since we would have expected that internal tides would dissipate through vertical shear [Eden et al. (2014)].

Most of the dissipation occurs at the generation sites (55%) or close to it (25%). 20% remain for the far field dissipation, in the inner seas. For Luzon strait, the proportions are similar with slightly less dissipation in the far field. The model dissipation agrees well with the spatial finestructure obtained by Ffield and Robertson (2008) for Ombai, Dewakang and Lifamatola straits, and Molucca and Flores seas. And it is in very good agreement with the recent INDOMIX microstructure estimates [Koch-Larrouy et al. (2015)], above the three straits measured (station St1, St3 and St5 of INDOMIX). However, in regions far away from any generation sites (Banda Sea) where INDOMIX and also Alford et al. (1999) found NO evidence of intensified mixing, the model produces too strong mixing. Also, below 200m, in station St2 the model produces stronger mixing compare to the observation. These biases might come from the fact that the model doesn't have any specific set up to dissipate the internal tides once generated. More work has to be done in order to solve this problem.

Another key point when dealing with dissipation of internal tides is to look at vertical distribution. EXPL produces intensified dissipation at the bottom, which is in good agreement with the profiles obtained in the INDOMIX cruise. The previous parameterisation made the assumption maximum in the thermocline, which is not what is reproduced by the model nor the observations. However, all three methods found very strong and comparable dissipation at the surface and in the thermocline. This surface mixing explain surface cooling of 0.2 to 0.8°C [Nugroho et al. (2017); Koch-Larrouy et al. (2008, 2010)] which is very important for local atmospheric convection and global tropical climate [Koch-Larrouy et al. (2010); Sprintall et al. (2014); Jochum and Potemra (2008)]. Over Spring tides, dissipation is 60 to 125% larger than the mean in the Luzon strait and Sulawesi Sea, whereas it has a smaller variation in the eastern part of the archipelago. Dissipation is stronger above straits for spring tides than neap tides. In fact, in the interior seas signal is also stronger during spring tides as propagation seems more efficient during spring tides than neap tides.

5.5 Discussion/perspective

The first limitation of this study is the resolution of the model, which does not allow reproducing correctly the internal tides. As shown in Niwa and Hibiya (2011) and also found in this study, the model with 1/12° resolution is able of reproducing only 75 % of the internal tides generation due to both insufficient resolution of the bathymetry slopes and of the tidal currents. Furthermore, once generated, the internal tides are dissipated by the model by parameterisations or numerical set up that are NOT specifically adapted to the physics of the tides, but rather to the larger scale processes or to eddy diffusivity. Thus it might not dissipate them as observed and produces unrealistic mixing. Indeed, when comparing the model to the recent INDOMIX cruise, the model produces higher background mixing in Banda Sea, region where in reality no mixing as been found Alford et al. (2015); Koch-Larrouy et al. (2015), and below 200m in the inner Halmahera Sea. In reality, where internal waves dissipate and cause mixing is not really known. It is thought that non-linear wave-wave interactions and scattering when internal waves reflect off the ocean floor cause low vertical wavenumber modes to cascade to higher wavenumbers. At higher vertical wavenumbers, there is increased vertical shear and eventually a shear instability, and hence mixing, results. Of course OGCM are not able to correctly resolve this energy cascade. Our results show that most of the dissipation in the model occurs through horizontal shear. This result is anti-intuitive, since we would have expected that internal tides would dissipate through vertical shear. We thus identify a significant bias of this model that may also be found in all general circulation models since actually there is no special care to take into account internal tides in such models. Our study offers a new clew of how to improve internal tides dissipation. In future research, work has to be done so that the dissipation occurs through vertical processes. Maybe need to established new parameterisation for the partially resolved internal tides.

5.6 Figures

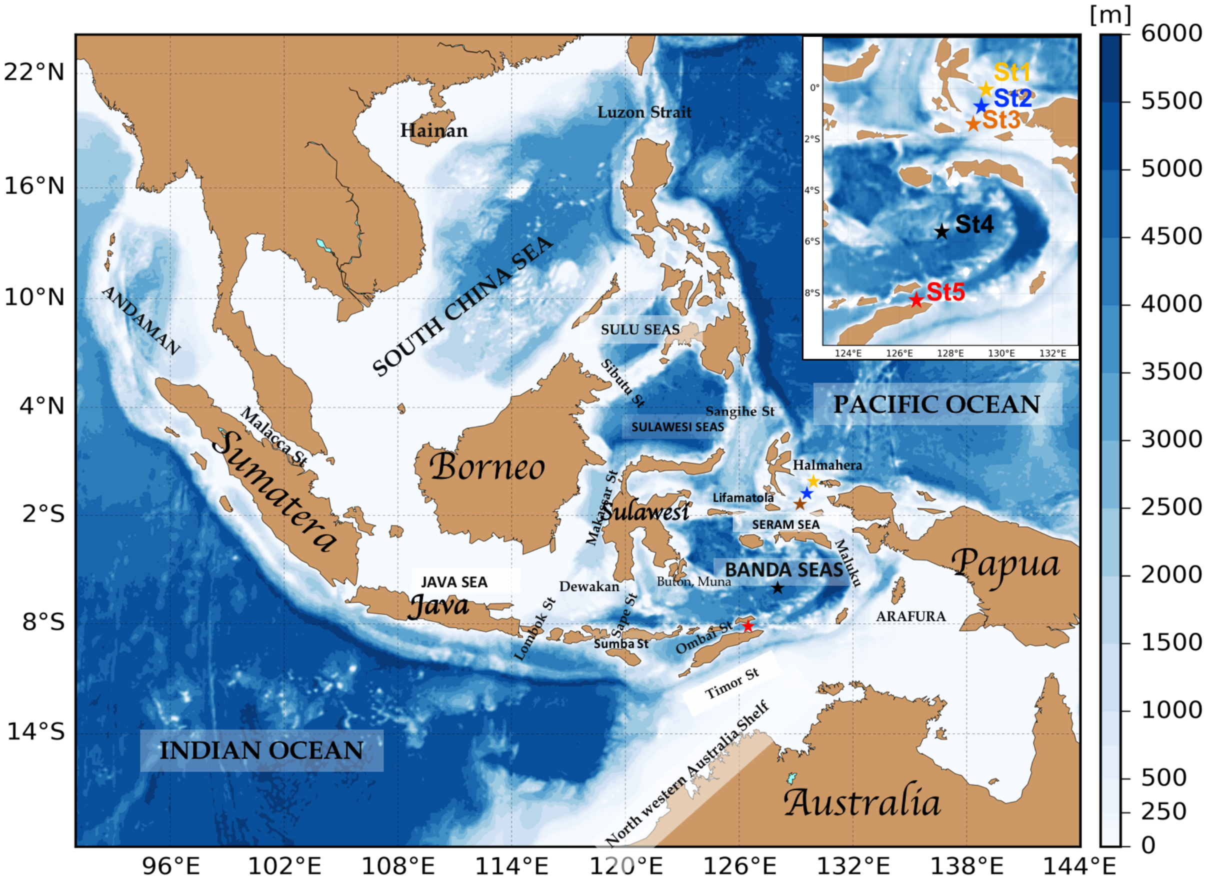

Figure 5.1: Model Domain with geographic names used in the study. INDOMIX station is shown in Upper right inset figure

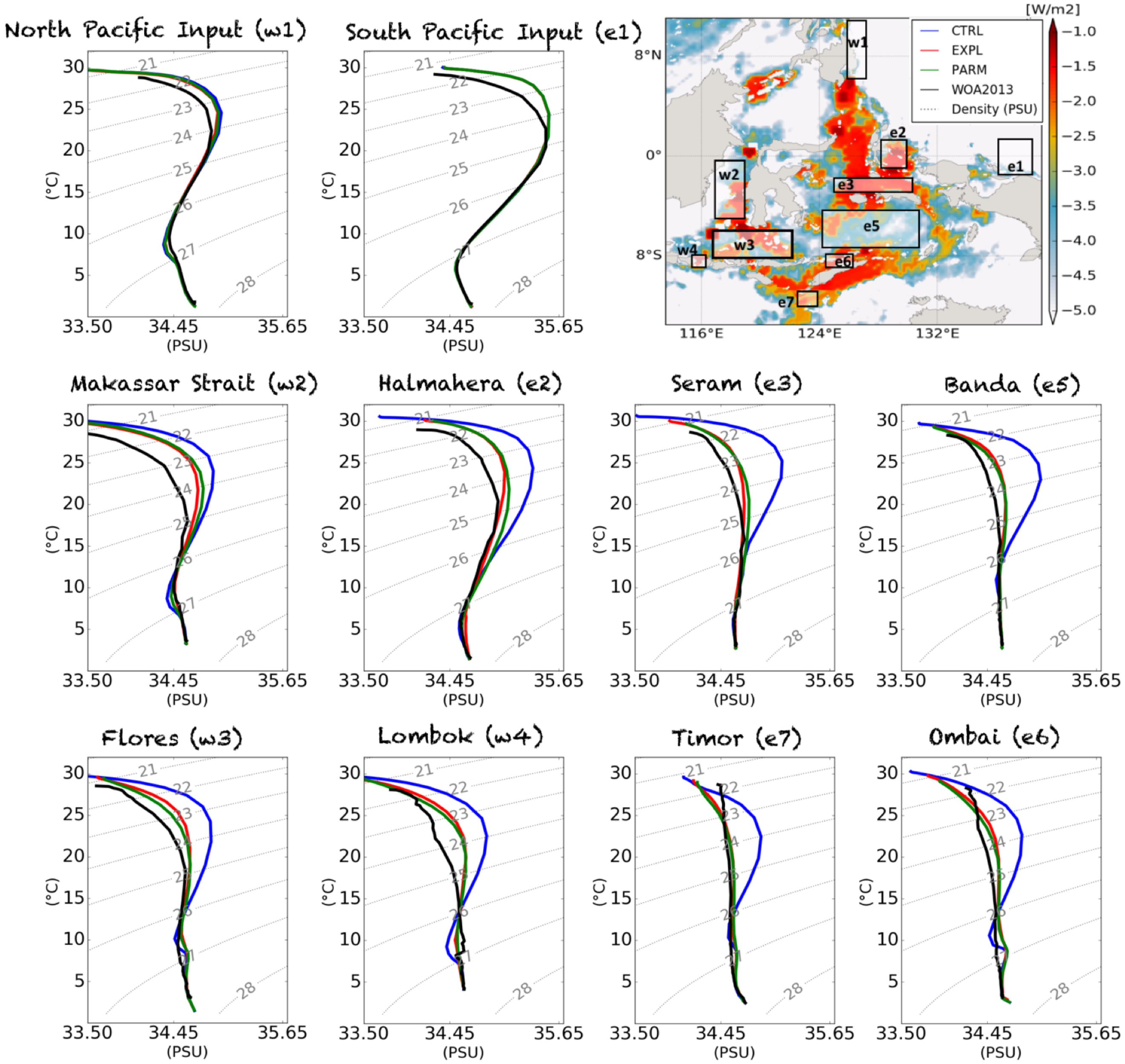

Figure 5.2: Figure of water mass transformation shown in TS diagram

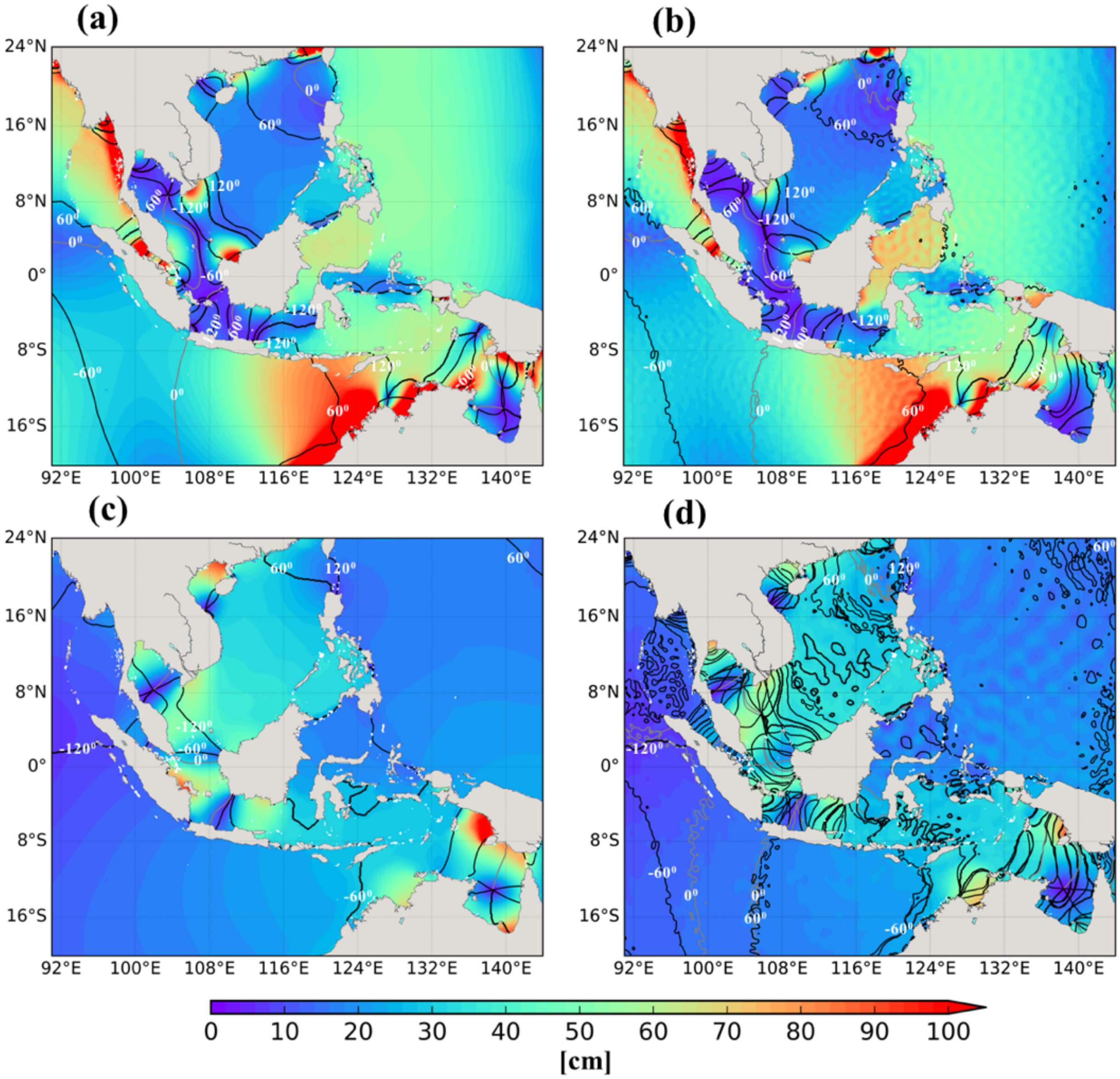

Figure 5.3: Amplitude and Phase of the M2 and K1 tide components (a and c) FES2014 and (b and d) M2 and K1 tide components in EXPL simulation. Amplitude is indicated with a shaded color in centimeters. Co-phase is plotted every 60^0 indicated with the contoured line in degree

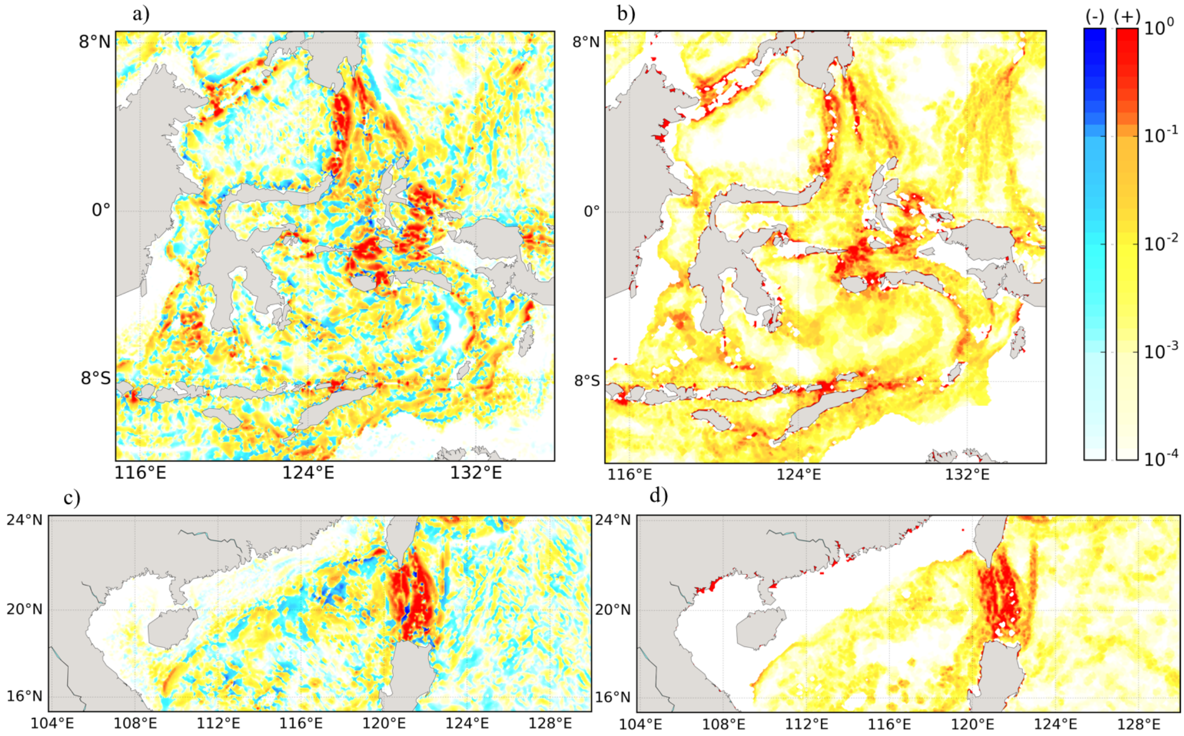

Figure 5.4: Barotropic to internal tides conversion rate for inner Indonesian sea (a and b) and Luzon (c and d) in EXPL simulation (left side) and wave drag in FES2014 (right side). The units are W/m^2.

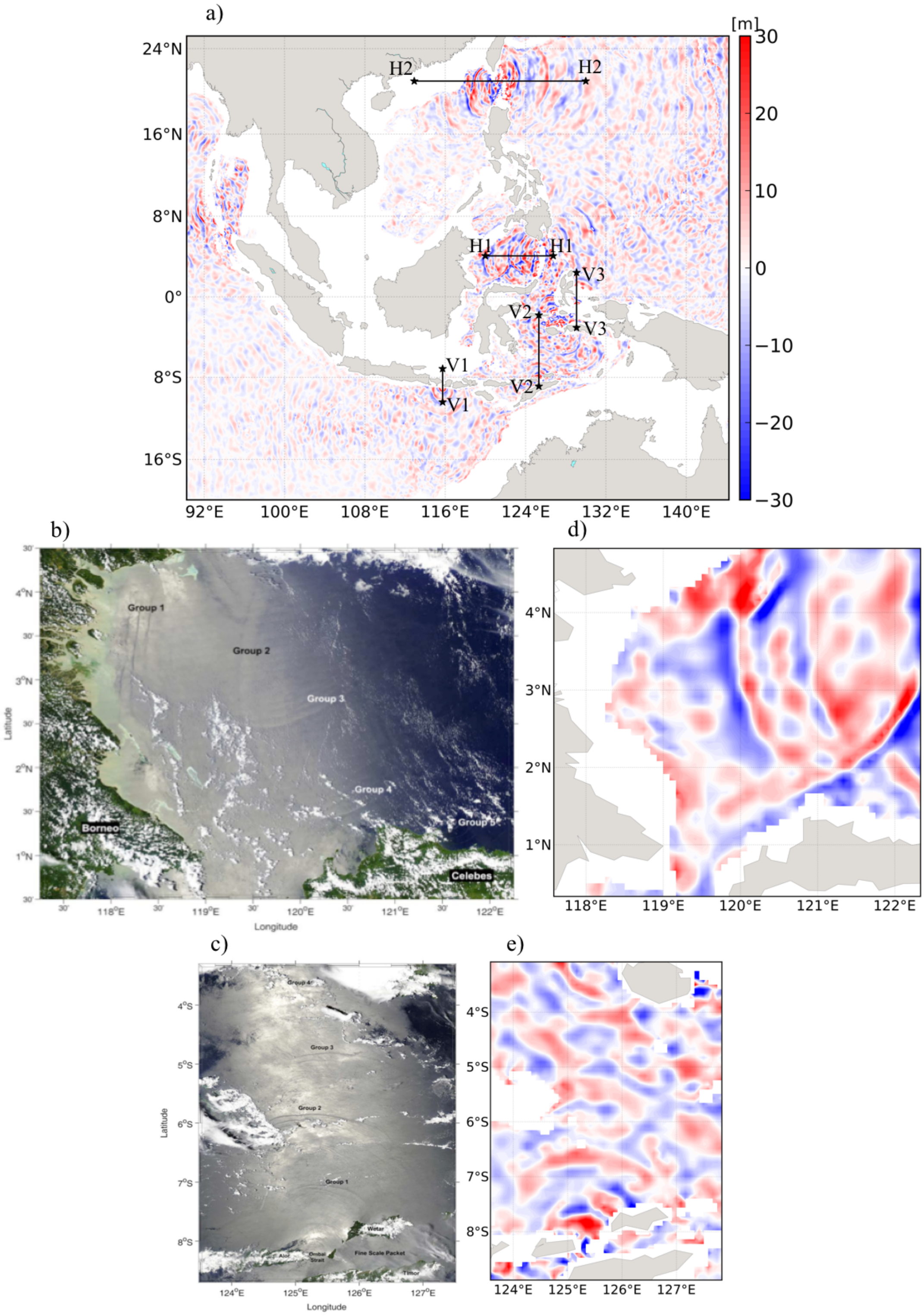

Figure 5.5: Snapshot of the model- predicted isopycnal displacement at 1150 m on 12th of July 2010, 11:00 UTC from EXPL simulation (a,d and e). True-color MODIS image of the Sulawesi Sea acquired on 6 March 2006 at 5:25 UTC and for Banda sea acquired on 24 February 2004 at 5:05 UTC (b and c) from Jackson (2007) compared with EXPL simulation on the same region

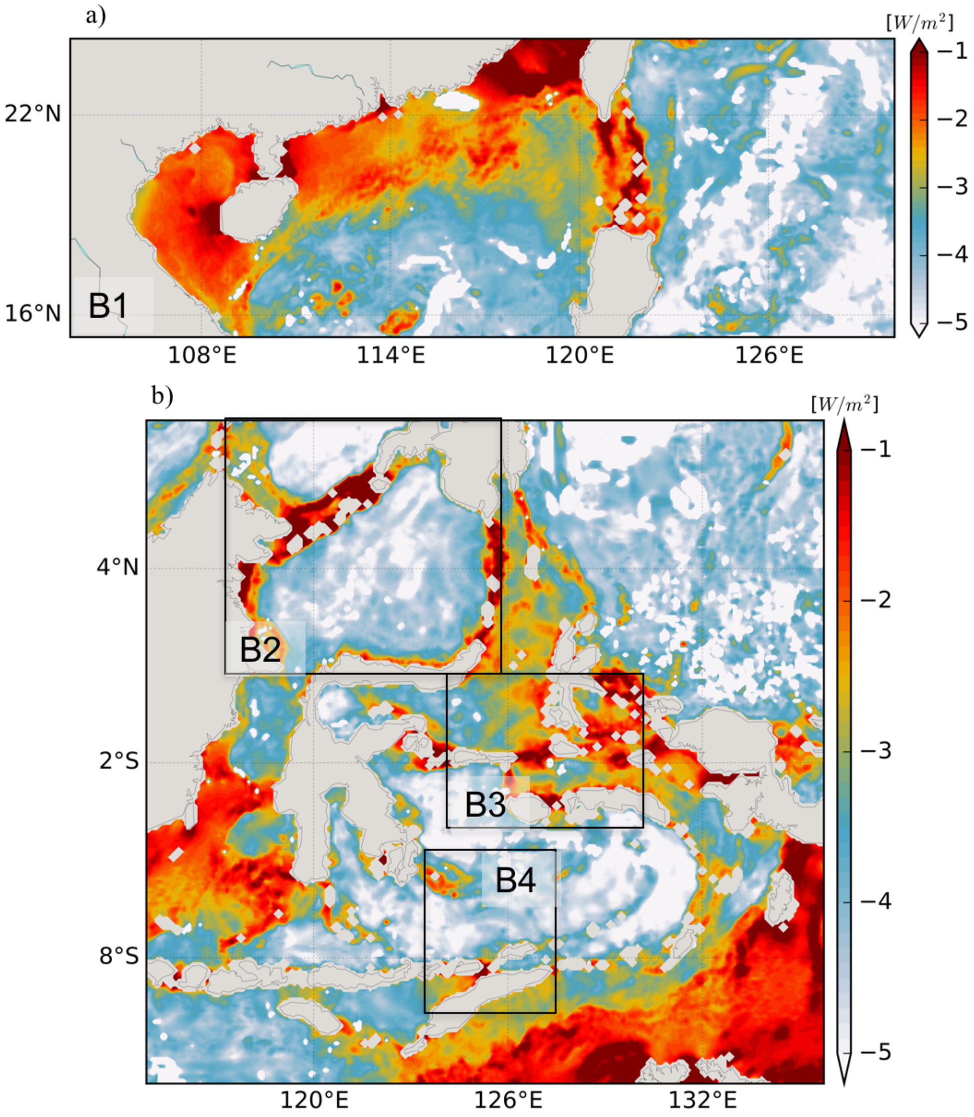

Figure 5.6: Bottom friction dissipation from EXPL-CTRL in Luzon strait (a) and inner Indonesian sea(b)

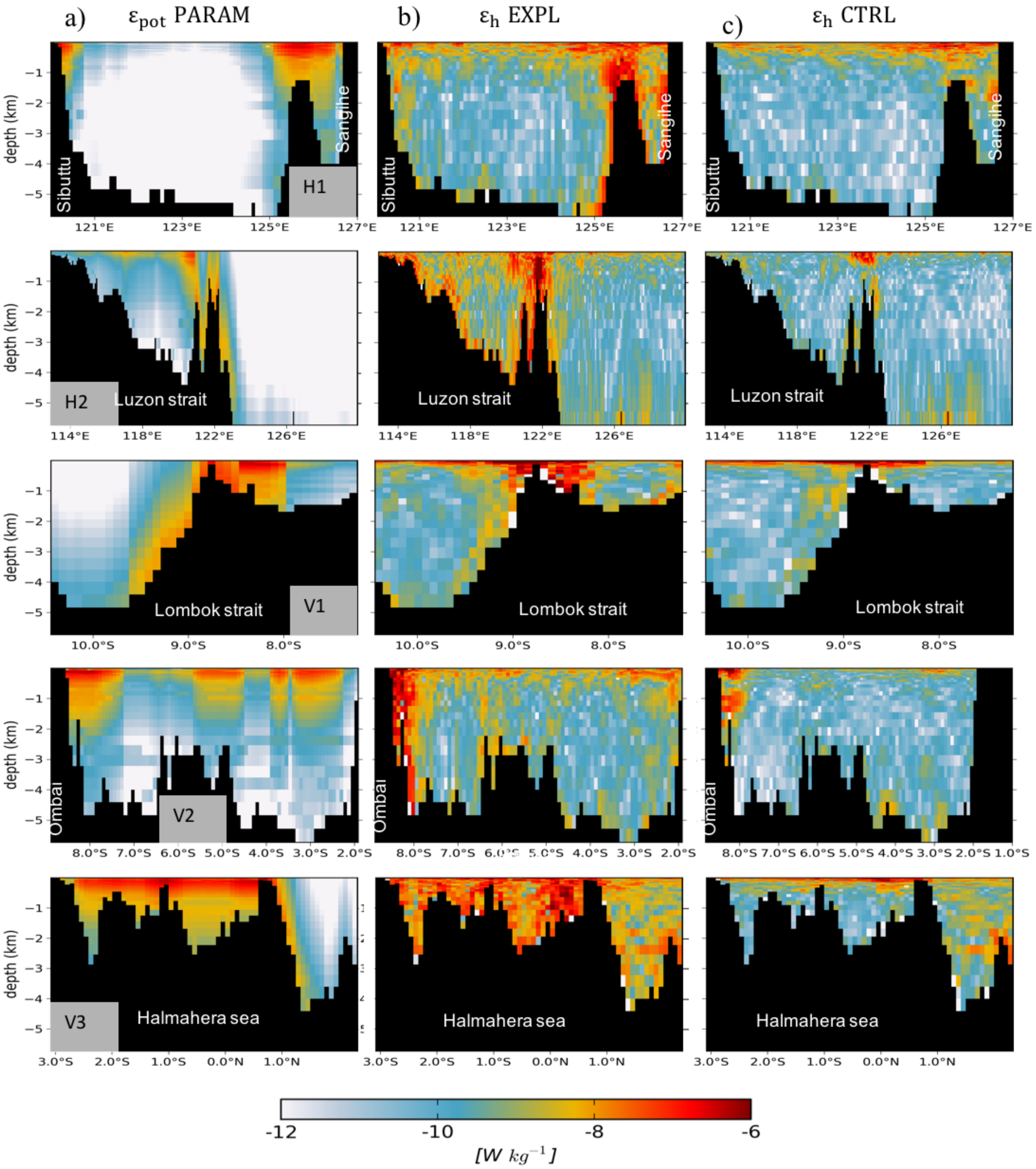

Figure 5.7: Instantaneous vertical distribution of dissipation rate during spring tide on 12 July 2010: 00:00 UTC for ϵ_v PARAM (left),ϵ_h EXPL (middle) and ϵ_h CTRL (left) along the lines H1, H2,V1,V2 in figure 5.5a respectively.The units are in W/kg

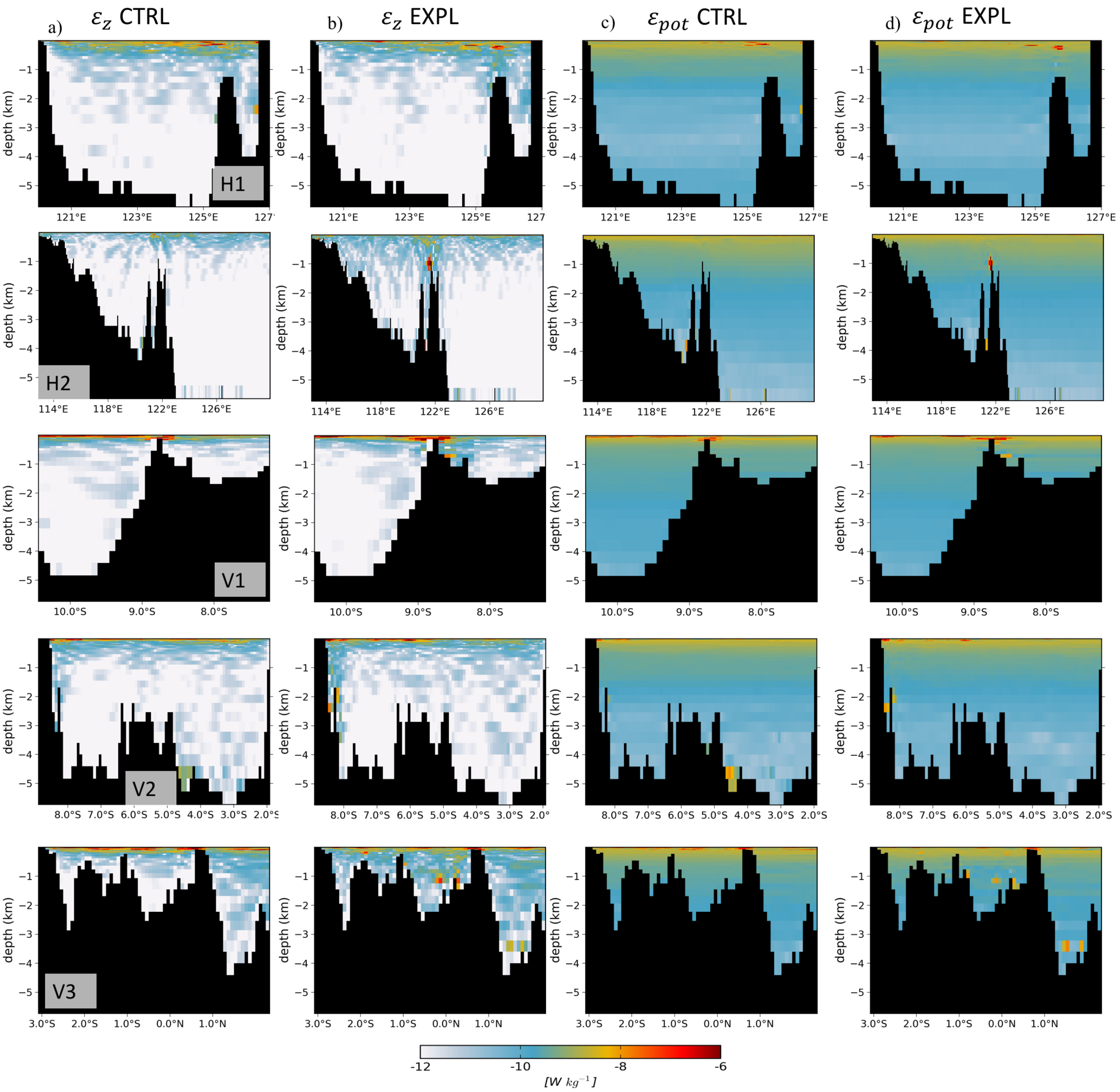

Figure 5.8: Instantaneous vertical distribution of dissipation rate during spring tide on 12 July 2010: 00:00 UTC for ϵ_z CTRL (a),ϵ_z EXPL (b), ϵ_{pot} CTRL (c), ϵ_{pot} EXPL (d) (along the lines H1,V1,V2 in figure 5.5a respectively). The units are in W/kg

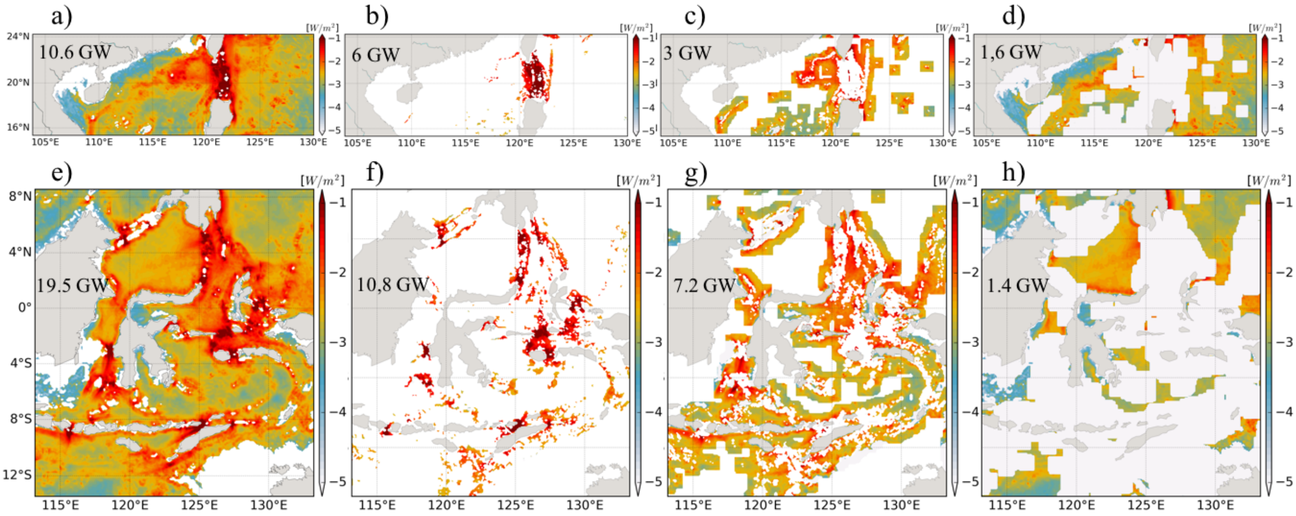

Figure 5.9: Horizontal dissipation rate in Luzon strait (a-d) and in inner indonesian sea (e-h). Total dissipation (a,e) is localized above area of internal tides generation (b,f), near field dissipation(c,g) and far field dissipation (d-h) for Luzon and Inner indonesian sea respectively. Total dissipation shown as number inside each figures. The units are in *Gigawatt*

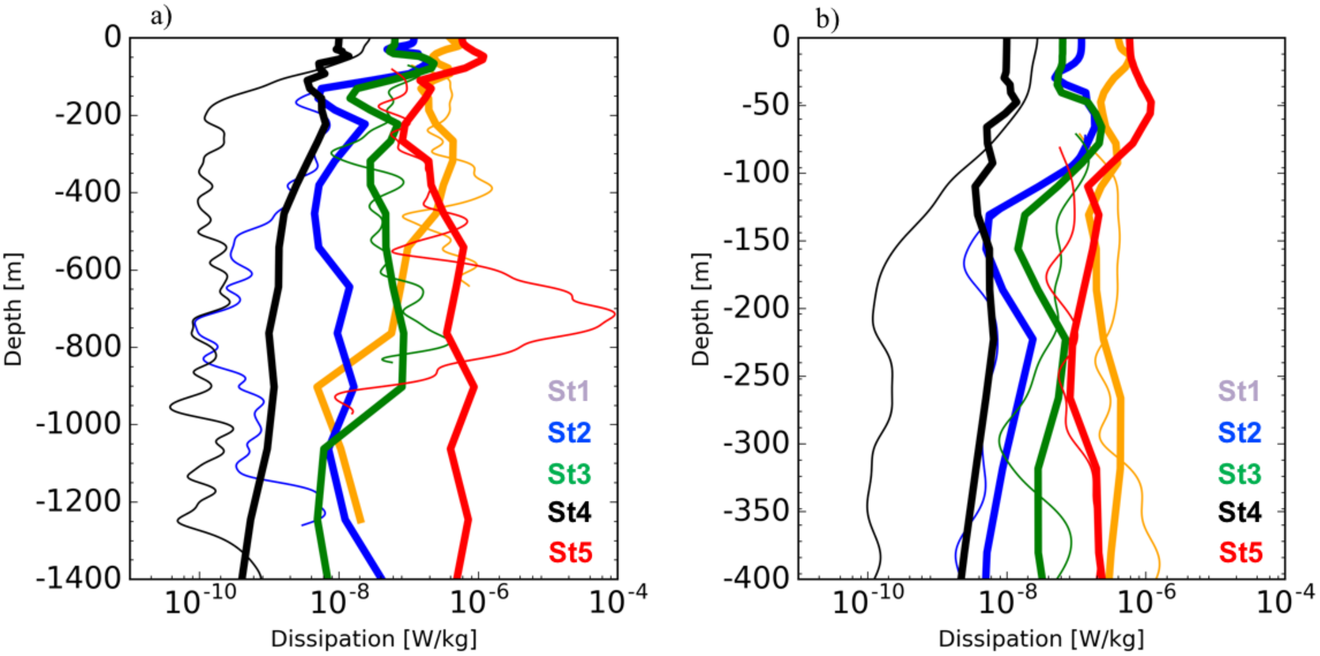

Figure 5.10: (a) dissipation (in W/kg) from INDOMIX station (Koch-Larrouy et al. 2015), using microstructure direct estimates (thin line) compared to horizontal kinetic energy dissipation (in W/kg) from EXPL calculated following from equation (2). Colours refer to the 5 different stations (see figure 2 for location). The length of the box shows the uncertainties of the method. (b) zoom between 0-400m

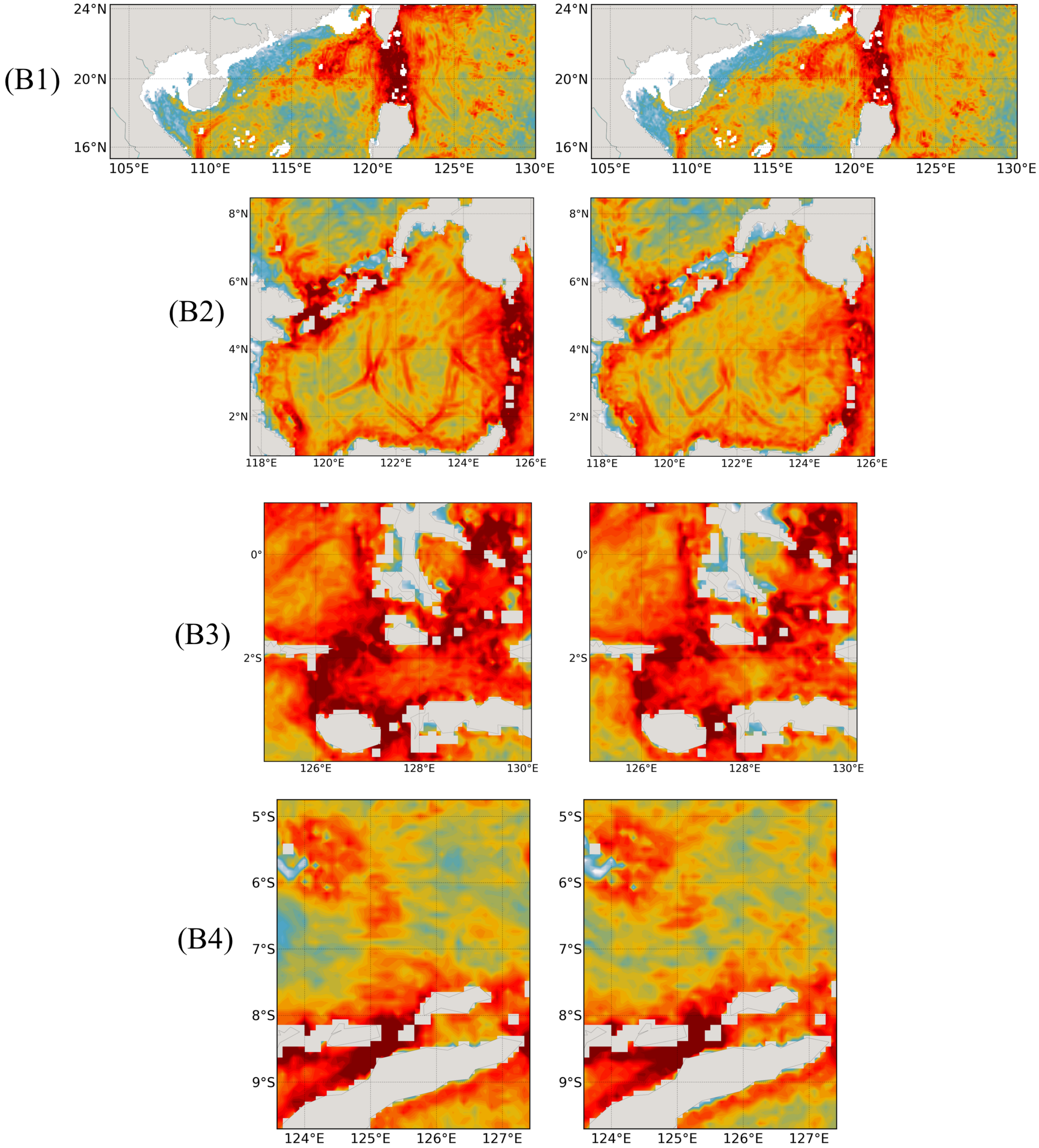

Figure 5.11: Horizontal dissipation rate (ϵ_h) for each box area in figure 5.6 for region B1 during spring tide (12/07/2010,21:00 UTC) and neap tide(20/07/2010,03:00 UTC) ,region B2 during spring tide (13/07/2010,01:00 UTC) and neap tide(20/07/2010,03:00 UTC), region B3 during spring tide (12/07/2010,01:00 UTC) and neap tide(20/07/2010,01:00 UTC), region B4 during spring tide (12/07/2010,05:00 UTC) and neap tide(20/07/2010,01:00 UTC). The units are in W/kg

5.7 Tables

	Total Domain	Inner seas	Luzon
FES2014	295	165.5	42.85
INDESO	215	123	50

Table 5.1: Total internal tides energy generation in FES2014 and INDESO. The units are in Gigawatt

	EXPL-CTRL(Inner seas)	PARM-CTRL(Inner seas)	EXPL-CTRL(Luzon)
ϵ_h	19.9	0	10.5
ϵ_v	3	-3	3
ϵ_{pot}	0.4	16.8	0.4

Table 5.2: Total energy dissipation following equation 5.7 - 5.9 under mixed layer depth(MLD). The units are in Gigawatt

Distance (in Km)	9	18	27	36	45	54
Local	10.8	10.8	10.8	10.8	10.8	10.8
Far	4.8	3.5	2.6	2.1	1.8	1.4
Near	3.9	5.2	6.1	6.5	6.9	7.2
Total	19.5	19.5	19.5	19.5	19.5	19.5

Table 5.3: Total local, near and far field horizontal dissipation energy away from generation site (9,18,27,36,45,54 Km) in inner seas. The units are in Gigawatt

Distance (in Km)	9	18	27	36	45	54
Local	6.0	6.0	6.0	6.0	6.0	6.0
Far	3.3	2.9	2.4	2.1	1.8	1.6
Near	1.3	1.8	2.2	2.5	2.8	3.0
Total	10.6	10.6	10.6	10.6	10.6	10.6

Table 5.4: Total local, near and far field horizontal dissipation energy away from generation site (9,18,27,36,45,54 Km) in Luzon strait. The units are in Gigawatt

	B1(Spring)	B1(Neap)	B2(Spring)	B2(neap)
ϵ_h^{kin}	16	8.8	7.6	1.7
ϵ_v^{kin}	3.2	0.8	2.5	0.0
ϵ_v^{pot}	0.3	0.1	0.4	0.0

	B3(Spring)	B3(Neap)	B4(Spring)	B4(neap)
ϵ_h^{kin}	7.6	6	2.0	1.1
ϵ_v^{kin}	0.5	0.0	0.0	0.0
ϵ_v^{pot}	0.0	0.1	0.0	0.0

Table 5.5: Total dissipation (EXPL-CTRL) obtained during spring tides and neap tides for each box area in figure 5.6. The units are in Gigawatt

Bibliography

Aiki, H., Matthews, J. P., and Lamb, K. G. (2011). Modeling and energetics of tidally generated wave trains in the Lombok Strait: Impact of the Indonesian Throughflow. *Journal of Geophysical Research: Oceans*, 116(3):1–17.

Aldrian, E. and Dwi Susanto, R. (2003). Identification of three dominant rainfall regions within Indonesia and their relationship to sea surface temperature. *International Journal of Climatology*, 23(12):1435–1452.

Alford, M. H., Gregg, M. C., and Ilyas, M. (1999). Diapycnal mixing in the Banda Sea: Results of the first microstructure measurements in the Indonesian Throughflow. *Geophysical Research Letters*, 26(17):2741.

Alford, M. H., MacKinnon, J. a., Nash, J. D., Simmons, H., Pickering, A., Klymak, J. M., Pinkel, R., Sun, O., Rainville, L., Musgrave, R., Beitzel, T., Fu, K.-H., and Lu, C.-W. (2011). Energy Flux and Dissipation in Luzon Strait: Two Tales of Two Ridges. *Journal of Physical Oceanography*, 41(11):2211–2222.

Alford, M. H., Peacock, T., MacKinnon, J. a., Nash, J. D., Buijsman, M. C., Centuroni, L. R., Chao, S.-Y., Chang, M.-H., Farmer, D. M., Fringer, O. B., Fu, K.-H., Gallacher, P. C., Graber, H. C., Helfrich, K. R., Jachec, S. M., Jackson, C. R., Klymak, J. M., Ko, D. S., Jan, S., Johnston, T. M. S., Legg, S., Lee, I.-H., Lien, R.-C., Mercier, M. J., Moum, J. N., Musgrave, R., Park, J.-H., Pickering, A. I., Pinkel, R., Rainville, L., Ramp, S. R., Rudnick, D. L., Sarkar, S., Scotti, A., Simmons, H. L., St Laurent, L. C., Venayagamoorthy, S. K., Wang, Y.-H., Wang, J., Yang, Y. J., Paluszkiewicz, T., and (David) Tang, T.-Y. (2015). The formation and fate of internal waves in the South China Sea. *Nature*, 521(7550):65–69.

Allen, G. R. and Werner, T. B. (2002). Coral reef fish assessment in the 'coral traingle' of Southeastern Asia. *Environmental Biology of Fishes*, 65:209–214.

Arbic, B. K., Richman, J. G., Shriver, J. F., Timko, P. G., Metzger, E. J., and Wallcraft, A. J. (2012). Global modeling of internal tides within an eddying ocean general circulation model. *Oceanography*, 25(2):20–29.

Arbic, B. K., Wallcraft, A. J., and Metzger, E. J. (2010). Concurrent simulation of the eddying general circulation and tides in a global ocean model. *Ocean Modelling*, 32(3-4):175–187.

Aumont, O. (2004). PISCES biogeochemical model WARNING : This document is not intended to be an exhaustive description of PISCES and is still incomplete. pages 1–16.

Baines, P. (1982). On internal tide generation models. *Deep Sea Research Part A. Oceanographic Research Papers*, 29(3):307–338.

Baines, P. G. (1973). The generation of internal tides by fiat-bump topography. 20(February 1972):179–205.

Buijsman, M., Arbic, B., Green, J., Helber, R., Richman, J., Shriver, J., Timko, P., and Wallcraft, a. (2015). Optimizing internal wave drag in a forward barotropic model with semidiurnal tides. *Ocean Modelling*, 85:42–55.

Carrere, L. (2012). A new global tidal model taking taking advantage of nearly 20 years of altimetry. *Proceedings of meeting "20 Years of Altimetry"*.

Carrere, L., Lyard, F., Cancet, M., Guillot, A., and Picot, N. (2016). FES 2014, a new tidal model - Validation results and perspectives for improvements, presentation to ESA Living Planet Conference. Technical report, Prague.

Carter, G., Fringer, O., and Zaron, E. (2012). Regional Models of Internal Tides. *Oceanography*, 25(2):56–65.

Carter, G. S., Merrifield, M. a., Becker, J., and Gregg, M. C. (2008). Energetics of M 2 Barotropic to Baroclinic tidal conversion at the Hawaiian Islands. *Journal of Physical Oceanography*, 38:2205–2223.

Castruccio, F. S., Curchitser, E. N., and Kleypas, J. a. (2013). A model for quantifying oceanic transport and mesoscale variability in the Coral Triangle of the Indonesian/Philippines Archipelago. *Journal of Geophysical Research: Oceans*, 118(11):6123–6144.

Chang, C. P., Wang, Z., McBride, J., and Liu, C. H. (2005). Annual cycle of Southeast Asia - Maritime continent rainfall and the asymmetric monsoon transition. *Journal of Climate*, 18(2):287–301.

Chao, S.-Y., Ko, D. S., Lien, R.-C., and Shaw, P. T. (2007). Assessing the West Ridge of Luzon Strait as an Internal. *Journal of Oceanography*, 63(2004):897–911.

Clement, A. C., Seager, R., and Murtugudde, R. (2005). Why are there tropical warm pools? *Journal of Climate*, 18(24):5294–5311.

da Silva, J., New, A., Srokosz, M., and Smyth, T. (2002). On the observability of internal tidal waves in remotely-sensed ocean colour data. *Geophysical Research Letters*, 29(12):10–13.

Eden, C., Czeschel, L., and Olbers, D. (2014). Toward Energetically Consistent Ocean Models. *Journal of Physical Oceanography*, 44(12):3160–3184.

Egbert, G. D. and Erofeeva, S. Y. (2002). Efficient inverse modeling of barotropic ocean tides. *Journal of Atmospheric and Oceanic Technology*, 19(2):183–204.

Egbert, G. D. and Ray, R. D. (2001). Estimates of \mathrm{M_2} tidal energy dissipation from {TOPEX/Poseidon} altimeter data. *J. Geophys. Res.*, 106(C10):22,422–475,502.

Ffield, A. and Gordon, A. L. (1992). Vertical Mixing in the Indonesian Thermocline.

Ffield, A. and Gordon, A. L. (1996). Tidal Mixing Signatures in the Indonesian Seas.

Ffield, A. and Robertson, R. (2008). Temperature finestructure in the Indonesian seas. *Journal of Geophysical Research: Oceans*, 113(9):1–19.

Fieux, M., Andrié, C., Delecluse, P., Ilahude, A. G., Kartavtseff, A., Mantisi, F., Molcard, R., and Swallow, J. C. (1994). Measurements within the Pacific-Indian oceans throughflow region. *Deep-Sea Research Part I*, 41(7):1091–1130.

Franks, P. J. and Chen, C. (1996). Plankton production in tidal fronts: A model of Georges Bank in summer. *Journal of Marine Research*, 54(4):631–651.

Gerkema, T. and van Haren, H. (2007). Internal tides and energy fluxes over Great Meteor Seamount. *Ocean Science Discussions*, 4:371–398.

Godfrey, J. S. (1996). The effect of the Indonesian throughflow on ocean circulation and heat exchange with the atmosphere: A review. *Journal of Geophysical Research*, 101(C5):12217.

Gordon, A. (2005). Oceanography of the Indonesian Seas. *Oceanography*, 18(4):13–13.

Gordon, A. L. (1986). Interocean exchange of thermocline water. *J. Geophys. Res.*, 91(6):5037–5046.

Gordon, A. L. and Fine, R. a. (1996). Pathways of water between the Pacific and Indian oceans in the Indonesian seas.

Gordon, A. L., Giulivi, C. F., and Ilahude, A. G. (2003). Deep topographic barriers within the Indonesian seas. *Deep-Sea Research Part II: Topical Studies in Oceanography*, 50(12-13):2205–2228.

Gordon, a. L., Sprintall, J., Van Aken, H. M., Susanto, D., Wijffels, S., Molcard, R., Ffield, a., Pranowo, W., and Wirasantosa, S. (2010). The Indonesian throughflow during 2004-2006 as observed by the INSTANT program. *Dynamics of Atmospheres and Oceans*, 50(2):115–128.

Hatayama, T. (2004). Transformation of the Indonesian throughflow water by vertical mixing and its relation to tidally generated internal waves. *Journal of Oceanography*, 60(3):569–585.

Hautala, S. L., Sprintall, J., Potemra, J. T., Chong, J. C., Pandoe, W., Bray, N., and Ilahude, a. G. (2001). Velocity structure and transport of the Indonesian Throughflow in the major straits restricting flow into the Indian Ocean. *Journal of Geophysical Research*, 106(C9):19527.

Holloway, G. and Denman, K. (1989). Influence of internal waves on primary production. *Journal of Plankton Research*, 11(2):409–413.

Holloway, P. E. (1996). A Numerical Model of Internal Tides with Application to the Australian North West Shelf.

Jackson, C. (2007). Internal wave detection using the Moderate Resolution Imaging Spectroradiometer MODIS. *Journal of Geophysical Research*, 112(C11):C11012.

Jan, S. and Chen, C. T. A. (2009). Potential biogeochemical effects from vigorous internal tides generated in Luzon Strait: A case study at the southernmost coast of Taiwan. *Journal of Geophysical Research: Oceans*, 114(4):1–14.

Jan, S., Chern, C. S., Wang, J., and Chao, S. Y. (2007). Generation of diurnal K1 internal tide in the Luzon Strait and its influence on surface tide in the South China Sea. *Journal of Geophysical Research: Oceans*, 112(6):1–13.

Jan, S., Lien, R. C., and Ting, C. H. (2008). Numerical study of baroclinic tides in Luzon Strait. *Journal of Oceanography*, 64(5):789–802.

Jeon, C., Park, J.-h., Varlamov, S. M., Yoon, J.-h., Kim, Y. H., Seo, S., Park, Y.-g., Min, H. S., Lee, J. H., and Kim, C.-h. (2014). Journal of Geophysical Research : Oceans. *Journal of Geophysical Research: Oceans*, 119:2843–2859.

Jochum, M. and Potemra, J. (2008). Sensitivity of tropical rainfall to Banda Sea diffusivity in the Community Climate System Model. *Journal of Climate*, 21(23):6445–6454.

Johnston, T. M. S., Rudnick, D. L., Alford, M. H., Pickering, A., and Simmons, H. L. (2013). Internal tidal energy fluxes in the South China Sea from density and velocity measurements by gliders. *JOURNAL OF GEOPHYSICAL RESEARCH: OCEANS*, 118:3939–3949.

Jouanno, J., Capet, X., Madec, G., Roullet, G., Klein, P., and Masson, S. (2016). Dissipation of the energy imparted by mid-latitude storms in the\r\nSouthern Ocean. *Ocean Science Discussions*, pages 1–49.

Kang, D. (2010). Energetics and Dynamics of Internal Tides in Monterey Bay Using Numerical Simulations a Dissertation Submitted To the Department of Civil and Environmental Engineering and the Committee on Graduate Studies of Stanford University in Partial Fulfillment of. (November):170.

Kang, D. and Fringer, O. (2012a). Energetics of Barotropic and Baroclinic Tides in the Monterey Bay Area. *Journal of Physical Oceanography*, 42(2):272–290.

Kang, D. and Fringer, O. (2012b). Energetics of Barotropic and Baroclinic Tides in the Monterey Bay Area. *Journal of Physical Oceanography*, 42(2):272–290.

Kartadikaria, a. R., Miyazawa, Y., Varlamov, S. M., and Nadaoka, K. (2011). Ocean circulation for the Indonesian seas driven by tides and atmospheric forcings: Comparison to observational data. *Journal of Geophysical Research: Oceans*, 116(9):1–21.

Kawamura, R. and Matsuura, T. (2003). A mechanism of the onset of the South Asian summer monsoon. 81:563–580.

Kelly, S. M. and Nash, J. D. (2010). Internal-tide generation and destruction by shoaling internal tides. *Geophysical Research Letters*, 37(23):1–5.

Kelly, S. M. and Nash, J. D. (2011). Reply to comment by T. Gerkema on “Internal-tide energy over topography”. *Journal of Geophysical Research*, 116(C9):2010–2012.

Kelly, S. M., Nash, J. D., and Kunze, E. (2010). Internal-tide energy over topography. *Journal of Geophysical Research: Oceans*, 115(6):1–13.

Kelly, S. M., Nash, J. D., Martini, K. I., Alford, M. H., and Kunze, E. (2012). The Cascade of Tidal Energy from Low to High Modes on a Continental Slope. *Journal of Physical Oceanography*, 42(7):1217–1232.

Kerry, C. G., Powel, B. S., and Carter, G. S. (2013). Effects of Remote Generation Sites on Model Estimates of M 2 Internal Tides in the Philippine Sea *. pages 187–204.

Khatiwala, S. (2003). Generation of internal tides in an ocean of finite depth: Analytical and numerical calculations. *Deep-Sea Research Part I: Oceanographic Research Papers*, 50(1):3–21.

Kida, S. and Richards, K. J. (2009). Seasonal sea surface temperature variability in the Indonesian Seas. *Journal of Geophysical Research: Oceans*, 114(6):1–17.

Kida, S. and Wijffels, S. (2012). The impact of the Indonesian Throughflow and tidal mixing on the summertime sea surface temperature in the western Indonesian Seas. *Journal of Geophysical Research: Oceans*, 117(9):1–14.

Koch-Larrouy, A., Atmadipoera, A., van Beek, P., Madec, G., Aucan, J., Lyard, F., Grelet, J., and Souhaut, M. (2015). Estimates of tidal mixing in the Indonesian archipelago from multidisciplinary INDOMIX in-situ data. *Deep-Sea Research Part I: Oceanographic Research Papers*, 106:136–153.

Koch-Larrouy, A., Lengaigne, M., Terray, P., Madec, G., and Masson, S. (2010). Tidal mixing in the Indonesian seas and its effect on the tropical climate system. *Climate Dynamics*, 34(6):891–904.

Koch-Larrouy, A., Madec, G., Bouruet-Aubertot, P., Gerkema, T., Bessières, L., and Molcard, R. (2007). On the transformation of Pacific Water into Indonesian Throughflow Water by internal tidal mixing. *Geophysical Research Letters*, 34(4):1–6.

Koch-Larrouy, A., Madec, G., Iudicone, D., Atmadipoera, A., and Molcard, R. (2008). Physical processes contributing to the water mass transformation of the Indonesian throughflow. *Ocean Dynamics*, 58(3-4):275–288.

Kundu, P., Cohen, M. I., and Hu, H. H. (2004). *Fluid mechanics*. Elsevier Academic Press, Amsterdam.

Kunze, E., Rosenfeld, L. K., Carter, G. S., and Gregg, M. C. (2002). Internal Waves in Monterey Submarine Canyon. *Journal of Physical Oceanography*, 32(6):1890–1913.

Kurapov, A. L., Egbert, G. D., Allen, J. S., Miller, R. N., Erofeeva, S. Y., and Kosro, P. M. (2003). The M 2 Internal Tide off Oregon: Inferences from Data Assimilation. *Journal of Physical Oceanography*, 33(8):1733–1757.

Large, W. G. and Yeager, S. G. (2004). Diurnal to decadal global forcing for ocean and sea–ice models: {The} data sets and flux climatologies. *NCAR Tech. Note*, TN–460+ST(May):105pp.

Le Provost, C. (2003). Ocean tides after a decade of high precision satellite altimetry. *Presentation in Swt JASON 1, Arles November 18-21.*

Lee, T., Fukumori, I., Menemenlis, D., Xing, Z., and Fu, L.-L. (2002). Effects of the Indonesian Throughflow on the Pacific and Indian Oceans. *Journal of Physical Oceanography*, 32(5):1404–1429.

Lehodey, P., Senina, I., and Murtugudde, R. (2008). A spatial ecosystem and populations dynamics model (SEAPODYM) - Modeling of tuna and tuna-like populations. *Progress in Oceanography*, 78(4):304–318.

Lévy, M., Ferrari, R., Franks, P. J. S., Martin, A. P., and Rivière, P. (2012). Bringing physics to life at the submesoscale. *Geophysical Research Letters*, 39(14).

Lewis, M. R., Glen Harrison, W., Oakey, Neil, S., Hebert, D., and Platt, T. (1976). Vertical Nitrate Fluxes in the Oligotrophic Ocean. *Science*, 234:870–873.

Lorenzo, E. D. (2006). Numerical and analytical estimates of M 2 tidal conversion at steep oceanic ridges. *Journal of physical . . .* , (2001):1072–1084.

Lu, Y., Wright, D. G., and Brickman, D. (2001). Internal tide generation over topography: Experiments with a free-surface z-level ocean model. *Journal of Atmospheric and Oceanic Technology*, 18(6):1076–1091.

Lukas, R., Yamagata, T., and McCreary, J. (1996). Pacific low-latitude western boundary currents and the Indonesian throughflow. *Journal of Geophysical Research C: Oceans*, 101(5):12209–12216.

Lyard, F., Carrere, L., Cancet, M., and Guillot, A. (2017). FES2014, a new finite elements tidal model for global ocean. *Ocean Dynamics,in preparation.*

Lyard, F., Lefevre, F., Letellier, T., and Francis, O. (2006). Modelling the global ocean tides: Modern insights from FES2004. *Ocean Dynamics*, 56(5-6):394–415.

Lyard, F., Roblou, L., and Allain, D. (2012). FES 2012, 4th PROJECT MEETING. Technical report, LEGOS, Toulouse.

Madec, G. (2008). NEMO ocean engine. (27).

Maraldi, C., Lyard, F., Testut, L., and Coleman, R. (2011). Energetics of internal tides around the Kerguelen Plateau from modeling and altimetry. *Journal of Geophysical Research: Oceans*, 116(6):1–10.

Matthews, J. P., Aiki, H., Masuda, S., Awaji, T., and Ishikawa, Y. (2011). Monsoon regulation of Lombok Strait internal waves. *Journal of Geophysical Research: Oceans*, 116(5):1–14.

Mattias Green, J. a. and Nycander, J. (2012). A comparison of tidal conversion parameterizations for tidal models. *Journal of Physical Oceanography*, (2004):121015111501009.

Melet, A., Nikurashin, M., Muller, C., Falahat, S., Nycander, J., Timko, P. G., Arbic, B. K., and Goff, J. a. (2013). Internal tide generation by abyssal hills using analytical theory. *Journal of Geophysical Research: Oceans*, 118(11):6303–6318.

Meyers, G. (1996). Variation of Indonesian throughflow and the El Niño-Southern Oscillation. *Journal of Geophysical Research: Oceans*, 101(C5):12255–12263.

Mitnik, L., Alpers, W., and Hock, L. (2000). Thermal plumes and internal solitary waves generated in the Lombok strait studied by ERS SAR. *European Space Agency, (Special Publication) ESA SP*, (461):1834–1842.

Molcard, R., Fieux, M., and Syamsudin, F. (2001). The throughflow within Ombai Strait. *Deep-Sea Research Part I: Oceanographic Research Papers*, 48(5):1237–1253.

Moore, S. E. and Lien, R.-C. (2007). Pilot Whales Follow Internal Solitary Waves. *Marine Mammal Science*, 23(January):193–196.

Mora, C., Chittaro, P. M., Sale, P. F., Kritzer, J. P., Ludsin, S. a., and Africa, S. (2003). Patterns and processes in reef fish diversity. *Nature*, 421(February):933–936.

Muller, M., Cherniawsky, J. Y., Foreman, M. G. G., and Von Storch, J. S. (2012a). Global M 2 internal tide and its seasonal variability from high resolution ocean circulation and tide modeling. *Geophysical Research Letters*, 39(19):L19607.

Muller, M., Cherniawsky, J. Y., Foreman, M. G. G., and Von Storch, J. S. (2012b). Global M 2 internal tide and its seasonal variability from high resolution ocean circulation and tide modeling. *Geophysical Research Letters*, 39(19):1–6.

Murray, S. P. and Arief, D. (1988). Throughflow into the Indian Ocean through the Lombok Strait, January 1985–January 1986. *Nature*, 333(6172):444–447.

Nagai, T. and Hibiya, T. (2015). Internal tides and associated vertical mixing in the Indonesian Archipelago. *Journal of Geophysical Research C: Oceans*, pages 3373–3390.

Neale, R. and Slingo, J. (2003). The Maritime Continent and its role in the global climate: A GCM study. *Journal of Climate*, 16(5):834–848.

Niwa, Y. (2004). internal tides in the East China Sea. *Journal of Geophysical Research*, 109(C4):1–14.

Niwa, Y. and Hibiya, T. (2001a). Numerical study of the spatial distribution of the M 2 internal tide in the Pacific Ocean. 106.

Niwa, Y. and Hibiya, T. (2001b). Numerical study of the spatial distribution of the M2 internal tide in the Pacific Ocean. *Journal of Geophysical Research*, 106:22441–22449.

Niwa, Y. and Hibiya, T. (2011). Estimation of baroclinic tide energy available for deep ocean mixing based on three-dimensional global numerical simulations. *Journal of Oceanography*, 67(4):493–502.

Niwa, Y. and Hibiya, T. (2014). Generation of baroclinic tide energy in a global three-dimensional numerical model with different spatial grid resolutions. *Ocean Modelling*, 80:59–73.

Nugroho, D., Koch-Larrouy, A., Gaspar, P., Lyard, F., Reffray, G., and Tranchant, B. (2017). Modelling Explicit tides in the Indonesian seas : an important process for surface sea water properties, in revision. *Submitted to Marine Pollution Bulletin.*

Park, J.-h. and Watts, D. R. (2005). Internal Tides in the Southwestern Japan / East Sea. pages 1–37.

Pichon, A. and Maze, R. (1990). Internal Tides over a Shelf Break: Analytical Model And Observations. *American Meteorological Society*, pages 657–671.

Potemra, J. T. (1999). Seasonal Variations of Upper Ocean Transport from the Pacific to the Indian Ocean via Indonesian Straits*. *Journal of Physical Oceanography*, 29(11):2930–2944.

Rainville, L., Lee, C. M., Rudnick, D. L., and Yang, K. C. (2013). Propagation of internal tides generated near Luzon Strait: Observations from autonomous gliders. *Journal of Geophysical Research: Oceans*, 118(9):4125–4138.

Ramp, S. R., Tang, T. Y., Duda, T. F., Lynch, J. F., Liu, A. K., Chiu, C. S., Bahr, F. L., Kim, H. R., and Yang, Y. J. (2004). Internal solitons in the northeastern South China Sea Part I: Sources and deep water propagation. *IEEE Journal of Oceanic Engineering*, 29(4):1157–1181.

Ray, R., Egbert, G., and Erofeeva, S. (2005). A Brief Overview of Tides in the Indonesian Seas. *Oceanography*, 18(4):74–79.

Robertson, R. (2010). Tidal currents and mixing at the INSTANT mooring locations. *Dynamics of Atmospheres and Oceans*, 50(2):331–373.

Robertson, R. and Ffield, A. (2005). M2 Baroclinic Tides in the Indonesian Seas. *Oceanography*, 18(4):62–73.

Robertson, R. and Ffield, A. (2008). Baroclinic tides in the Indonesian seas: Tidal fields and comparisons to observations. *Journal of Geophysical Research: Oceans*, 113(7):1–22.

Sari Ningsih, N. (2008). INTERNAL WAVES DYNAMICS IN THE LOMBOK STRAIT STUDIED BY A NUMERICAL MODEL. *International Journal Of Remote Sensing And Earth Sciences*, 5.

Sasaki, H., Sasai, Y., Nonaka, M., Masumoto, Y., and Kawahara, S. (2006). An Eddy-Resolving Simulation of the Quasi-Global Ocean Driven by Satellite-Observed Wind Field – Preliminary Outcomes from Physical and Biological Fields –. *Journal of the Earth Simulator*, 6(October):35–49.

Schiller, A. (2004). Effects of explicit tidal forcing in an OGCM on the water-mass structure and circulation in the Indonesian throughflow region. *Ocean Modelling*, 6(1):31–49.

Shang, X., Liu, Q., Xie, X., Chen, G., and Chen, R. (2015). Deep-Sea Research I Characteristics and seasonal variability of internal tides in the southern South China Sea. *Deep-Sea Research Part I*, 98:43–52.

Shriver, J. F., Arbic, B. K., Richman, J. G., Ray, R. D., Metzger, E. J., Wallcraft, a. J., and Timko, P. G. (2012). An evaluation of the barotropic and internal tides in a high-resolution global ocean circulation model. *Journal of Geophysical Research: Oceans*, 117(10):1–14.

Simmons, H. L., Hallberg, R. W., and Arbic, B. K. (2004). Internal wave generation in a global baroclinic tide model. *Deep-Sea Research Part II: Topical Studies in Oceanography*, 51(25-26 SPEC. ISS.):3043–3068.

Song, Q. and Gordon, A. L. (2004). Significance of the vertical profile of the Indonesian Throughflow transport to the Indian Ocean. *Geophysical Research Letters*, 31(16).

Souza, A. J. and Pineda, J. (2001). Tidal mixing modulation of sea-surface temperature and diatom abundance in Southern California. *Continental Shelf Research*, 21(6-7):651–666.

Sprintall, J., Gordon, A. L., Koch-Larrouy, A., Lee, T., Potemra, J. T., Pujiana, K., Wijffels, S. E., and Wij, S. E. (2014). The Indonesian seas and their role in the coupled ocean–climate system. *Nature Geoscience*, 7(7):487–492.

Sprintall, J., Wijffels, S. E., Molcard, R., and Jaya, I. (2009). Direct estimates of the indonesian throughflow entering the indian ocean: 2004-2006. *Journal of Geophysical Research: Oceans*, 114(7):2004–2006.

St. Laurent, L. and Garrett, C. (2002). The Role of Internal Tides in Mixing the Deep Ocean. *Journal of Physical Oceanography*, 32(10):2882–2899.

Susanto, R. D. and Gordon, A. L. (2005). Velocity and transport of the Makassar Strait throughflow. *Journal of Geophysical Research: Oceans*, 110(1):1–10.

Susanto, R. D., Mitnik, L., and Zheng, Q. (2005). Ocean Internal Waves Observed in the Lombok Strait. *Oceanography*, 18(4):80–87.

Talley, L. D. and Sprintall, J. (2005). Deep expression of the Indonesian Throughflow: Indonesian Intermediate Water in the South Equatorial Current. *Journal of Geophysical Research C: Oceans*, 110(10):1–30.

Tranchant, B., Reffray, G., Greiner, E., Nugroho, D., Koch-Larrouy, A., and Gaspar, P. (2016). Evaluation of an operational ocean model configuration at 1/12 spatial resolution for the Indonesian seas . Part I : ocean physics. pages 1–49.

Umlauf, L. and Burchard, H. (2003). A generic length-scale equation for geophysical. *Journal of Marine Research*, 61(2):235–265.

van Aken, H. M., Brodjonegoro, I. S., and Jaya, I. (2009). The deep-water motion through the Lifamatola Passage and its contribution to the Indonesian throughflow. *Deep-Sea Research Part I: Oceanographic Research Papers*, 56(8):1203–1216.

Veron, J., Devantier, L. M., Turak, E., Green, A. L., Kininmonth, S., Stafford-Smith, M., and Peterson, N. (2009). Delineating the Coral Triangle. *Galaxea, Journal of Coral Reef Studies*, 11(2):91–100.

Vranes, K., Gordon, A. L., and Ffield, A. (2002). The heat transport of the Indonesian throughflow and implications for the Indian Ocean heat budget. *Deep-Sea Research Part II: Topical Studies in Oceanography*, 49(7-8):1391–1410.

Wang, J., Huang, W., Yang, J., and Zhang, H. (2011). The internal waves' distribution of whole South China Sea extracted from ENVISAT and ERS-2 SAR images. *Proceedings of SPIE - The International Society for Optical Engineering*, 8175:1–7.

Wang, X., Peng, S., Liu, Z., Huang, R. X., Qian, Y.-K., and Li, Y. (2016). Tidal Mixing in the South China Sea: An Estimate Based on the Internal Tide Energetics. *Journal of Physical Oceanography*, 46(1):107–124.

Wijffels, S. (2012). The impact of the Indonesian Throughflow and tidal mixing on the Seasonal Cycle of the Sea Surface Temperature in the Indonesian Seas Why Study the SST in the Indonesian Seas ? The role of Tidal mixing The role of the Indonesian Throughflow (ITF). (July 2012):6016.

Wijffels, S. E., Meyers, G., and stuart Godfrey, J. (2008). A 20-Yr Average of the Indonesian Throughflow: Regional Currents and the Interbasin Exchange. *Journal of Physical Oceanography*, 38:1965–1978.

Wunsch, C. and Ferrari, R. (2004). Vertical Mixing, Energy, and the General Circulation of the Oceans. *Annual Review of Fluid Mechanics*, 36(1):281–314.

Xu, Z. and Yin, B. (2016). Long - range propagation and associated variability of internal tides in the South China LR. *Journal Of Geophysical Research*, (November).

Zhao, Z., Alford, M., and Girton, J. (2012). Mapping Low-Mode Internal Tides from Multisatellite Altimetry. *Oceanography*, 25(2):42–51.

Zilberman, N. V., Becker, J. M., Merrifield, M. a., and Carter, G. S. (2009). Internal Tide Generation over Mid-Atlantic Ridge Topography. *Journal of Physical Oceanography*, 39(10):2635–2651.

Chapter 6

Tidal Energy Budget Controversy. (Paper to be submitted)

contents

6.1 Introduction

The wind stress and the ocean tides are believed to be the only significant sources of mechanical energy driving the deep ocean mixing necessary to sustain the global overturning circulation [Wunsch and Ferrari (2004)]. The overall tidal energy budget (time-averaged) is estimated to be about 3.5 TW. Tidal energy is provided by the astronomic bodies (Earth, Moon and Sun) through gravitational forces work. 2.6 TW of this (mostly barotropic) energy is dissipated through to bottom friction and 0.9 TW are converted into internal tides which will further dissipate locally or after propagation. The mechanism of internal tides dissipation is still highly controversial, however it is usually admitted that a great parts of the energy get finally converted into ocean mixing.

The proportion of barotropic tides energy converted into baroclinic tides has been discussed for a long time. Tidal hydrodynamic model with data assimilation [Lyard et al. (2006)] and through inverse calculation using altimeter data [Egbert and Ray (2001)] indicates that 0.7 TW or roughly 25% – 35% of the barotropic M2 tidal energy is converted through internal tides generation. Barotropic hydrodynamical models are not capable to resolve explicitly internal tides, hence energy conversion is parameterized as a wave drag based on bottom topography slope and barotropic currents, acting as a barotropic energy sink [Lyard et al. (2006); Shriver et al. (2012); Buijsman et al. (2015)]. In the recent years, OGCMs have been used to estimate internal tides energy in realistic stratification [Jan et al. (2007, 2008); Jan and Chen (2009); Carter et al. (2008); Kang and Fringer (2012a); Lorenzo (2006); Muller et al. (2012b); Nagai and Hibiya (2015); Niwa (2004); Niwa and Hibiya (2001a, 2014); Shang et al. (2015); Zilberman et al. (2009); Wang et al. (2016)]. In that case, internal tides are explicitly solved by the model, with more or less accuracy. More recently, the linear theory estimate of the abyssal hills contribution to the conversion of the M2 barotropic tides into internal tide represents of the 10% of the 0.6–0.8 TW conversion in regions deeper than 500 m by larger topographic scales [Mattias Green and Nycander (2012); Melet et al. (2013)].

The internal tides generation occurs in the area where barotropic flows interact with strong topographic gradient and create isopycnal heaving at tidal frequency. Because the across-slope velocity (hence vertical velocity as prescribed by the bottom impermeability condition) increases as depth diminishes, isopycnal heaving tends to be stronger in the upper slope region. In addition, the enhanced stratification found in the upper ocean will increase isopycnal heaving effects in those regions. For those reasons, most of internal tides generation is expected to occur at the upper part of continental slopes and ocean ridges.

Today, the precise quantification of internal tide generation (through energy budget computation) and the fate of internal tide energy remains open questions.

The central issue in calculating tidal energy budget is the separation of barotropic and baroclinic precesses, in terms of velocity and pressure. Although intuitive, this issue is nothing but trivial and needs to define precisely the meaning of ”barotropic dynamics” and ”baroclinic dynamics” terms. A universal, precise definition does not exist and still trigger some controversy among researchers. The most common definitions can be summarized as follow: 1, barotropic tides are the ones that would be present in absence of ocean stratification (uniform density ocean), and baroclinic tides the departure from those barotropic tides when stratification is taken into account; 2, barotropic tides are the depth-averaged part of the tidal dynamics in a stratified ocean, baroclinic tides being then the residual between the full 3D tides and the barotropic tides; 3, barotropic tides are the fast mode (in the vertical modes theory frame, see [Gill.,1982]), and baroclinic tides the slow modes. This variety of definitions not only creates different types of tidal energy calculation but also lead to different understanding of how the barotropic tides contribute in the global mechanical energy budget.

First definition has been widely adopted by many authors [Kunze et al. (2002)] and proved to be useful to some extents (rigid-lid assumption). However it is strongly deemed by the fact that internal tide generation will take energy from the barotropic motion, hence barotropic tides in a non-stratified ocean will significantly differs from barotropic tides in a stratified ocean. As a consequence, the ”baroclinic” tides obtained by differencing non-stratified ocean tides and stratified ocean tides will contain parasite barotropic residuals.

Second definition is quite conventional and popular, and mostly acceptable for first order analysis. It reflects the idea that baroclinic quantities vanish when integrated with depth (also called baroclinicity condition). This assumption has some consistency with the vertical modes vision when making the rigid lid approximation, which eliminate the fast mode (this approximation is however inappropriate in the internal tide case, as the gradient of barotropic tides and internal tides sea surface displacements, hence current, can have the same order of magnitude, the shorter wavelength of internal tides compensating for the smaller sea surface displacement amplitude). Still, it remains controversial for various reasons. One is that it can not be valid in region where the barotropic velocity profile is non-uniform because of bottom friction effects, typically in macro-tidal shelfs seas. More importantly, it is much too simplified when assessing energy budget that are sensitive to second order details and tends to lead to quite unphysical energy budget computation.

Third definition has a much better physical meaning, a stronger formal and theoretical background, and has attracted much attention in the tidal community. However vertical modes theory is usually seen as valid in a flat bottom context, but failing in a sloping topography case. However, they are some empirical and analytical indications that vertical modes theory will hold even in uneven topography conditions.

Starting from the second approach, some attempts have been made to tackle the spurious energy budget issue. As clearly mentionned in [Kelly et al. (2010)], the various attempts found in literature can be written in the general form:

$$p^s(x,z) = P + \bar{p} \tag{6.1}$$

$$p^i(x,z) = p - P - \hat{p} \tag{6.2}$$

where p, P, p^s, p^i are total, depth averaged, surface tide, internal tide pressure respectively. $\hat{p}$ is an arbitrary pressure adjustment term which definition will vary following the various approaches. No special treatment is deployed for velocities, keeping intact the usual splitting based on depth averaging. interestingly enough, the authors derive a new and more physical pressure adjustment term by making analogy between classical energy budget formulation and its expression in the vertical modes framework. But interestingly enough, the best empirical arbitrary correction leads to a formulation similar to the one that can be straight-forwardly obtained from vertical modes approach.

In consequence, for this study, we propose to make a more formal use of vertical modes decomposition to define and separate barotropic and baroclinic dynamics. The derivations will be illustrated by the COMODO internal test case, with simulations performed using 2 different models. First one is the time-stepping, finite difference, C-grid coordinates, 3D NEMO model [Madec (2008)]. The second model is the frequency-domain, un-structured finite element T-UGOm model [Lyard et al. (2012)],(https://www5.obs-mip.fr/sirocco/ocean-models/tugo/).

Both model are implemented on the same domain (made of a flat abyssal plain, a continental slope and a flat shelf, with transverse periodic boundary conditions), and make the hydrostatic assumption. Test case prescribes null bottom friction, and horizontal/vertical diffusion kept as small as permitted by model stability. This chapter is organized as follows:

- The assessment of the barotropic and baroclinic definition will be reviewed in section 2.
- Section 3 presents a derivation of vertical modes decomposition equations.
- Section 4 discusses the model description for NEMO model and TUGO model.
- Section 5 covers the complete separation technique for barotropic and baroclinic.
- Section 6 Provides a detailed derivation of the tidal energy diagnostic.
- Section 7 focuses on results on numerical Internal tides case using COMODO test case

The conclusion is given in section 8

6.2 Barotropic and baroclinic tides definition

Over decades, depth averaging methods have been used to separate barotropic and baroclinic dynamics. Depth-averaged quantities are considered as related to barotropic motion, and the vertically varying part as related to the baroclinic motion. This view has been widely accepted and carried out in physical oceanography, including internal tides studies. However, this straight forward separation, and further variants, has been debated by many researcher because it leads to unsatisfactory tidal energy budget [Gerkema and van Haren (2007); Holloway (1996); Kelly and Nash (2010); Kunze et al. (2002); Niwa and Hibiya (2001a); Baines (1973)].

As mentioned in introduction, three class of definitions (and subsequent separation techniques) can be found in litterature. The first one, proposed by Baines (1973) (P'_A) defines internal tides motion as a perturbation term obtained by removing the barotropic motion that would exist in a unstratified ocean. Internal tides represents as density perturbation (ρ') and has been adapted to calculate tidal energy budget by [Niwa and Hibiya (2001a); Niwa (2004); Khatiwala (2003)]. Lu et al. (2001) follows this approach over a simple steep slope bottom topography consisting deep and shallow region and found large amplitude periodic variations over the flat regions. These anomalous periodic variations indicate that the internal tides mode is not properly separated from barotropic parts. Moreover Lorenzo (2006) found that barotropic parts produce by unstratified simulation is slightly different with stratified simulations. This is because the internal tide acts as a drag mechanism on the barotropic tide that resulting in weaker barotropic currents and eventually creates error in internal tides pressure. In practice Lorenzo (2006) propose to define internal tides by using pressure fluid at rest (not including free surface contribution) instead of using pressure from unstratified simulations. The barotropic pressure define as the calculation of pressure in the external-mode(depth average) of their model. The internal tides pressure from this methods is :

$$p'_A(x,y,z,t) = p(x,y,z,t) - P_0(z) \tag{6.1}$$

where $P_0(z)$ is the pressure at rest. This definition of internal tides pressure has been widely used to calculate the tidal energy budget by Niwa and Hibiya (2001a); Jan et al. (2007); Niwa and Hibiya (2011); Park and Watts (2005); Nagai and Hibiya (2015); Jan et al. (2007). Again, this approach fails to account for pressure variations due to isopycnal heaving linked with purely barotropic dynamics.

Second definition was introduced by Kunze et al. (2002) (P'_B). Internal tides is define as isopycnal heaving that can be obtained from both model and observations. This technique practically calculates the internal tides pressure from buoyancy terms after substracting the depth averaged buoyancy. The equations from this methods are:

$$p'_B(z) = \int_z^0 \tilde{b}\left(z'\right) dz' - \frac{1}{d}\int_d^0 \int_z^0 \tilde{b}\left(z'\right) dz' dz \tag{6.2}$$

where $\tilde{b} = -N^2\xi$. N is buoyancy frequency ξ is isopycnal displacement and d is total depth. Isopycnal displacement can be derived by observation data (e.g mooring data) or by extracting vertical velocity components associate to internal tides frequency [Holloway (1996)]. Kurapov et al. (2003) found spurious barotropic to internal tides energy generation by using this technique. Spurious terms is found as positive and negative value in the energy conversion. Zilberman et al. (2009) and Carter et al. (2012) argued that the spurious energy conversion terms produce from phase difference between the vertical velocity of barotropic tides and the perturbation pressure of the internal tides. On the other hand Kelly et al. (2010) propose technique to eliminate spurious conversion by changing the isopycnal displacement by movement of free surface. I prevent to use this technique because its complicity adapted. Moreover, this technique propose that the barotropic and internal tides is independently terated. Thus the concisten terms in the calculation of closed energy budget can not be achieved from this definition.

A variant of the second approach comes from the study of Kelly et al. (2010). Barotropic tides pressure is expressed as the depth average of total pressure plus a new depth dependent profile of pressure, which is due to isopycnal heaving by movement of the free surface. Internal tide velocity and pressure are defined as total variables minus the barotropic tide components. By using analogy with energy budget written under the modal decomposition formalism, this technique solved all inconsistency that comes from surface pressure due to isopycnal displacement. Energy diagnostics computed from idealised, steep slope simulations show no spurious energy flux after remofing pressure surface due to isopycnal heaving. From the idealized bottom slope, the energy cascade from barotropic to internal tides show a reasonable structure. Another test using realistic stratification by Kelly et al. (2012) gives a consistent barotropic energy flux with energy conversion and has good agreement with observations.

The decomposition techniques by Kelly et al. (2010) can reasonably accepted, but more importantly suggests us to directly operate the barotropic and baroclinic dynamics separation by using the vertical modes approach. This techniques had not fully proven before to be adequate in a realistic forcing and complex bottom topography model configuration such as the NEMO's Indonesian seas configuration. Here, I propose develop and assess the definition of barotropic tides as "fast mode" and internal tides as "slow modes" and to examine the vertical modes separation capabilities to address qualitatively and quantitatively the energy budget diagnostics issue.

6.3 Vertical Modes Decomposition

6.3.1 Momentum and continuity equation in vertical modes

We are seeking for the **dynamical perturbation of a stratified ocean** under the internal wave excitation. Starting from three dimensional conservative form of momentum, continuity equation and mass conservation by using hydrostatic approximation:

$$\rho_0 \frac{\partial u}{\partial t} - \rho_0 f v = -\frac{\partial p}{\partial x} \tag{6.1}$$

$$\rho_0 \frac{\partial v}{\partial t} - \rho_0 f u = -\frac{\partial p}{\partial y} \tag{6.2}$$

$$\rho_0 \frac{\partial w}{\partial t} = -\frac{\partial p}{\partial z} - \rho g \tag{6.3}$$

The continuity equation, **under Boussinesq approximation**, yields:

$$\nabla.\mathbf{u} = \frac{\partial u}{\partial x} + \frac{\partial v}{\partial y} + \frac{\partial w}{\partial z} = 0 \tag{6.4}$$

where $u = u(x,y,z,t)$, $v = v(x,y,z,t)$, $w = w(x,y,z,t)$ are perturbation velocities in x-,y- and z- direction. and $\mathbf{u} = (u,v,w)$ is the perturbation velocity vector. ρ is insitu density perturbation from state equation and p=$p(x,y,z,t)$ is hydrostatic pressure. Continuity and momentum equations are combined to eliminate horizontal velocities and obtain a system of equations by where w and ρ are the only variables.

Comment: elimination of horizontal advection would be natural if treating a purely periodic case, as advection would project into higher harmonics.

First step consists in modifying the horizontal momentum equation. The primitive momentum equations (eq.6.1 and eq.6.2) are differentiated with respect to time and rearranged as:

for u velocity (x-direction):

$$\frac{\partial^2 u}{\partial t^2} - f\frac{\partial v}{\partial t} = -\frac{1}{\rho_0}\frac{\partial^2 p}{\partial x \partial t} \tag{6.5}$$

Replacing $\frac{\partial v}{\partial t}$ from primitive equations (eq.6.2) yields:

$$\frac{\partial^2 u}{\partial t^2} + f^2 u = \left(\frac{\partial^2}{\partial t^2} + f^2\right) u = -\frac{1}{\rho_0}\frac{\partial^2 p}{\partial x \partial t} - f\frac{1}{\rho_0}\frac{\partial p}{\partial y} \tag{6.6}$$

Operating similarly for v velocity (y-direction):

$$\frac{\partial^2 v}{\partial t^2} + f^2 v = \left(\frac{\partial^2}{\partial t^2} + f^2\right) v = -\frac{1}{\rho_0}\frac{\partial^2 p}{\partial y \partial t} + f\frac{1}{\rho_0}\frac{\partial p}{\partial x} \tag{6.7}$$

By **ignoring changes of f with latitude**, differentiated equation 6.6 and equation 6.7 with respect to x,y and z respectively, the transform momentum equations are:

$$\frac{\partial}{\partial x}\left(\frac{\partial^2}{\partial t^2} + f^2\right) u = \frac{\partial u}{\partial x}\left(\frac{\partial^2}{\partial t^2} + f^2\right) = -\frac{1}{\rho_0}\frac{\partial^2 p}{\partial^2 x \partial t} - f\frac{1}{\rho_0}\frac{\partial^2 p}{\partial x \partial y} \tag{6.8}$$

$$\frac{\partial}{\partial y}\left(\frac{\partial^2}{\partial t^2} + f^2\right) v = \frac{\partial v}{\partial y}\left(\frac{\partial^2}{\partial t^2} + f^2\right) = -\frac{1}{\rho_0}\frac{\partial^2 p}{\partial^2 y \partial t} + f\frac{1}{\rho_0}\frac{\partial^2 p}{\partial x \partial y} \tag{6.9}$$

Transforming Boussinesq continuity equation yields:

$$\left(\frac{\partial^2}{\partial t^2}+f^2\right)\frac{\partial w}{\partial z}=-\left(\frac{\partial^2}{\partial t^2}+f^2\right)\frac{\partial u}{\partial x}-\left(\frac{\partial^2}{\partial t^2}+f^2\right)\frac{\partial v}{\partial y} \tag{6.10}$$

Then **forming the internal wave equation** by combining equation 6.8 and equation 6.9 to equation 6.10 yields:

$$\left(\frac{\partial^2}{\partial t^2}+f^2\right)\frac{\partial w}{\partial z}=\frac{1}{\rho_0}\frac{\partial}{\partial t}\left(\nabla_h^2 p\right) \tag{6.11}$$

in non rotating fluid (ignoring coriolis effect), the above equation simplifies into:

$$\frac{\partial^2 w}{\partial z \partial t}=\frac{1}{\rho_0}\nabla_h^2 p \tag{6.12}$$

At this point, we need an additional equation for w, p variables closure by re-arranging vertical velocity equation:

Hydrostatic pressure:

$$\frac{\partial p_0(z)}{\partial z}=-\rho_0(z)g \tag{6.13}$$

$$\frac{\partial p(z)}{\partial z}=-\rho(z)g \tag{6.14}$$

Density advection:

$$\frac{d\rho}{dt}=\frac{\partial \rho}{\partial t}+\mathbf{u}.\nabla\rho=\frac{\partial \rho}{\partial t}+w\frac{\partial \rho}{\partial z}=0 \tag{6.15}$$

Discarding horizontal advection, the evolution of density perturbations is given by:

$$\frac{\partial \rho}{\partial t}=-w\frac{\partial \rho_0}{\partial z} \tag{6.16}$$

This a central equation in vertical modes derivation, that assumes change in density is solely due to vertical heaving of background density.

Differentiating eq. 6.3 with time yields:

$$\rho_0\frac{\partial^2 w}{\partial t^2}=-\frac{\partial^2 p}{\partial t \partial z}-g\frac{\partial \rho}{\partial t} \tag{6.17}$$

Combining the equation 6.17 and equation 6.16 yields:

$$\rho_0 \frac{\partial^2 w}{\partial t^2} = -\frac{\partial^2 p}{\partial t \partial z} + g\frac{d\rho_0}{dz} w \tag{6.18}$$

introducing Brunt-Vaissala frequency

$$N^2 = -g\frac{1}{\rho_0}\frac{d\rho_0}{dz} \tag{6.19}$$

By combining equations 6.18 and 6.19, **the second base equation** yields:

$$\frac{\partial^2 w}{\partial t^2} + N^2 w = -\frac{1}{\rho_0}\frac{\partial^2 p'}{\partial t \partial z} \tag{6.20}$$

Comment: density heaving is sometimes express directly as isopycnal displacement "s":

$$\frac{\partial s}{\partial t} = w \tag{6.21}$$

or after reformulation

$$\frac{\partial \rho}{\partial t} = -g\rho_0 N^2 \frac{\partial s}{\partial t} \tag{6.22}$$

As pressure pertubation is null when displacement is null:

$$\rho = -\frac{1}{g\rho_0} N^2 s \tag{6.23}$$

This approach has been followed for instance in Kunze et al. (2002) and Zilberman et al. (2009). It allows to exchange vertical w with vertical displacement s in vertical modes derivation.However, it must be noticed that the vertical structure will be identical.

6.3.2 Pressure and vertical velocity modes

We have obtained a coupled system of two equations and two unknowns (vertical velocity and pressure anomaly). This system can then solved **by separation of variables method**, i.e. by seeking the solution of equations 6.11 and 6.20 by separation of variables of the form:

$$p' = \hat{p}(z)\,\tilde{p}(x,y,t) \tag{6.24}$$

$$w = \hat{w}(z)\,\tilde{w}(x,y,t) \tag{6.25}$$

Treating first base equation

Rewriting equation 6.11 by virtue of 6.24 and 6.25 yields:

$$\left(\frac{\partial^2}{\partial t^2}+f^2\right)\frac{\partial w}{\partial z} = \left(\frac{\partial^2 \tilde{w}}{\partial t^2}(x,y,t)+f^2\tilde{w}(x,y,t)\right)\frac{\partial \hat{w}}{\partial z}(z) \tag{6.26}$$

$$\frac{1}{\rho_0(z)}\frac{\partial\left(\nabla_h^2 p'\right)}{\partial t} = \frac{1}{\rho_0(z)}\hat{p}(z)\frac{\partial}{\partial t}\left(\nabla_h^2\tilde{p}(x,y,t)\right) \tag{6.27}$$

finally :

$$\left(\frac{\partial^2 \tilde{w}}{\partial t^2}(x,y,t)+f^2\tilde{w}(x,y,t)\right)\frac{\partial \hat{w}}{\partial z}(z) = \frac{1}{\rho_0(z)}\hat{p}(z)\frac{\partial}{\partial t}\left(\nabla_h^2\tilde{p}(x,y,t)\right) \tag{6.28}$$

Separating (x,y,t) and (z) terms, 6.28 yields:

$$\left(\frac{\partial^2 \tilde{w}}{\partial t^2}+f^2\tilde{w}\right)\left[\frac{\partial}{\partial t}\left(\nabla_h^2\tilde{p}\right)\right]^{-1}(x,y,t) = \frac{1}{\rho_0}\hat{p}\left[\frac{\partial \hat{w}}{\partial z}\right]^{-1}(z) = cste = c_e^2 \tag{6.29}$$

Equation 6.28 can then be splitted into separate w vertical and horizontal mode equations:

w velocity for vertical mode:

$$c_e^2\frac{\partial \hat{w}}{\partial z}(z) = \frac{1}{\rho_0(z)}\hat{p}(z) \tag{6.30}$$

w velocity for for horizontal mode:

$$\left(\frac{\partial^2 \tilde{w}}{\partial t^2}(x,y,t)+f^2\tilde{w}(x,y,t)\right) = c_e^2\frac{\partial}{\partial t}\left(\nabla_h^2\tilde{p}(x,y,t)\right) \tag{6.31}$$

Here c_e is the phase velocity of the different modes and acts as a separation constant and can be obtained from the eigen value problem : $c_e^2 = \frac{1}{\lambda}$

Treating second base equation

Equation 6.30 and equation 6.31 is re-arrange to introduce buoyancy. By inserting equation 6.24 and 6.25 to buoyancy terms in equation 6.19, and neglecting w time derivatives (as usual in hydrostatic approximation) :

$$N^2 w = N^2 \hat{w}(z)\hat{w}(x,y,t) = -\frac{1}{\rho_0}\frac{\partial^2 p}{\partial t \partial z} = -\frac{1}{\rho_0}\frac{\partial p}{\partial z}(z)\frac{\partial \hat{\eta}}{\partial t}(x,y,t) \tag{6.32}$$

Two equations can be deduced (for vertical and horizontal modes)from the previous equality:

$$N^2 \hat{w}(z) = \frac{1}{\rho_0}\frac{\partial \hat{p}}{\partial z}(z) \tag{6.33}$$

$$\tilde{w}(x,y,t) = \frac{\partial \tilde{p}}{\partial t}(x,y,t) \tag{6.34}$$

Comment: if assuming periodic perturbation, there is no necessity to neglect w time derivatives, and eq. 6.35 would rewrite:

$$(N^2 - \omega^2)\hat{w}(z) = \frac{1}{\rho_0}\frac{\partial \hat{p}}{\partial z}(z) \tag{6.35}$$

However, this is equivalent to reconsider the hydrostatic approximation. In case where vertical modes are used to analyze hydrostatic simulations, it might ne be consistent.

Vertical velocity modal equations

Replacing p in 6.35 from 6.30 We get the final form of vertical mode of w :

$$\frac{1}{\rho_0(z)}\frac{\partial}{\partial z}\left(\rho_0(z)\frac{\partial \hat{w}}{\partial z}(z)\right) + \frac{N^2(z)}{c_e^2}\hat{w}(z) \tag{6.36}$$

Replacing w in 6.34 from 6.31 We get the final form of horizontal mode w:

$$\left(\frac{\partial^2 \tilde{w}}{\partial t^2}(x,y,t) + f^2 \tilde{w}(x,y,t)\right) = c_e^2\left(\nabla_h^2 \tilde{w}(x,y,t)\right) \tag{6.37}$$

This equation is the equivalent to wave equation of barotropic gravity waves.

Pressure modal equation

Vertical modes for pressure is obtained by replacing h in equation 6.30 with equation 6.35 yields:

$$\rho_0(z)\frac{\partial}{\partial z}\left(\frac{1}{N^2(z)\rho_0(z)}\frac{\partial \hat{p}(z)}{\partial z}+\frac{1}{c_e^2}\hat{p}(z)\right)=0 \tag{6.38}$$

and horizontal mode for pressure is

$$\tilde{w}(x,y,t)=\frac{\partial \tilde{p}}{\partial t}(x,y,t) \tag{6.39}$$

Both vertical velocity (eq. 6.36) and pressure (eq. 6.38) vertical equations are Sturm-Liouville equations. Solutions are then obtained by prescribing boundary conditions, described in next section.

Comment: In mathematics and its applications, a classical Sturm–Liouville theory, named after Jacques Charles François Sturm (1803–1855) and Joseph Liouville (1809–1882), is the theory of a real second-order linear differential equation of the form:

$$\frac{d}{dx}p(x)\frac{d}{dx}y+q(x)y+\lambda w(x)y=0 \tag{6.40}$$

where y is a function of the free variable x. Here the functions $p(x)$, $q(x)$, and $w(x)>0$ are specified at the outset. In the simplest of cases all coefficients are continuous on the finite closed interval [a,b], and p has continuous derivative. In this simplest of all cases, this function y is called a solution if it is continuously differentiable on (a,b) and satisfies the equation ('1') at every point in (a,b). In addition, the unknown function y is typically required to satisfy some boundary conditions at a and b. The function w(x), which is sometimes called r(x), is called the "weight" or "density" function.

The value of λ is not specified in the equation; finding the values of λ for which there exists a non-trivial solution of ('1') satisfying the boundary conditions is part of the problem called the Sturm–Liouville (S–L) problem.

Such values of λ, when they exist, are called the eigenvalues of the boundary value problem defined by eq. 6.40 and the prescribed set of boundary conditions. The corresponding solutions (for such a λ) are the eigenfunctions of this problem. Under normal assumptions on the coefficient functions p(x), q(x), and w(x) above, they induce a Hermitian differential operator in some function space defined by boundary conditions. The resulting theory of the existence and asymptotic behavior of the eigenvalues, the corresponding qualitative theory of the eigenfunctions and their completeness in a suitable function space became known as Sturm–Liouville theory. This theory is important in applied mathematics, where S–L problems occur very commonly, particularly when dealing with linear partial differential equations that are separable.

A Sturm–Liouville (S–L) problem is said to be regular if $p(x), w(x) > 0$, and $p(x)$, $p'(x)$, $q(x)$, and $w(x)$ are continuous functions over the finite interval [a, b], and has separated boundary conditions of the form

$$\alpha_1 y(a) + \alpha_2 y'(a) = 0 \tag{6.41}$$

$$\beta_1 y(b) + \beta_2 y'(b) = 0 \tag{6.42}$$

Under the assumption that the S–L problem is regular, the main tenet of Sturm–Liouville theory states that:

The eigenvalues λ_1, λ_2, λ_3, ... of the regular Sturm–Liouville problem eq. 6.40, 6.41, 6.42 are real and can be ordered such that

$$\lambda_1 < \lambda_2 < \lambda_3 < \cdots < \lambda_n < \cdots \to \infty \tag{6.43}$$

Corresponding to each eigenvalue λ_n is a unique (up to a normalization constant) eigenfunction $y_n(x)$ which has exactly $n-1$ zeros in (a, b). The eigenfunction $y_n(x)$ is called the n-th fundamental solution satisfying the regular Sturm–Liouville problem eq. 6.40, 6.41, 6.42. Providing that coefficients in 6.41, 6.42 are not dependent upon λ, the normalized eigenfunctions form an orthonormal basis

$$\int_a^b y_n(x) y_m(x) w(x) \, \mathrm{d}x = \delta_{mn} \tag{6.44}$$

in the Hilbert space $L2([a,b], w(x)dx)$. Here δ_{mn} is the Kronecker delta. As it will be seen in next sections, it will not be the case for vertical velocity modes.

Primary boundary conditions

The usual boundary conditions are set at surface for pressure (free surface or rigid lid) and null vertical velocity at bottom. As it will be needed in the following, let's recall the impermeability condition

$$w = \omega + \mathbf{v}.\nabla s + \frac{\partial s}{\partial t} \tag{6.45}$$

where ω is velocity across s, $\mathbf{v}$ horizontal velocity.

Vertical velocity boundary condition:
Considering ocean bottom (i.e. s(x,y,t)=-h) as an impermeable (i.e. $\omega = 0$) and non-moving interface (i.e. $\frac{\partial s}{\partial t} = 0$):

$$w_{(z=-h)} = -\mathbf{v}_{(z=-h)}.\nabla d \tag{6.46}$$

Imposing null vertical velocity at bottom (Dirichlet-type boundary condition):

$$\hat{w}_{(z=-h)}\tilde{w}(x,y,t) = 0 \Longrightarrow \hat{w}_{(z=-h)} = 0 \tag{6.47}$$

It can be easily seen from eq. 6.46 that this conditions hold naturally in flat bottom case, and is disputable in sloping bottom case.

Surface pressure condition: in free surface case, it is obtained by the fact that pressure must vanish a the free surface. Free surface (i.e. $s = \eta$) impermeability condition ($\omega = 0$) is given by:

$$w_{(z=\eta)} = \mathbf{v}_{(z=\eta)}.\nabla \eta + \frac{\partial \eta}{\partial t} \tag{6.48}$$

The usual approximation consists then in neglecting $\mathbf{v}_{(z=\eta)}.\nabla \eta$ (small perturbation approximation). Impermeability condition then becomes:

$$w_{(z=\eta)} = \frac{\partial \eta}{\partial t} \tag{6.49}$$

Writing hydrostatic condition:

$$p_{(z=0)} = \rho_0 g \eta \tag{6.50}$$

Combining the two above equations yields:

$$\frac{\partial p}{\partial t} = \rho_0 g w \tag{6.51}$$

By virtue of variable separation, it gives:

$$\hat{p}_{(z=0)} = \rho_0 g \hat{w} \tag{6.52}$$

Eliminating $\hat{w}$ by using eq. 6.35 finally yields:

$$g \frac{\partial \hat{p}}{\partial z}(z) + N^2 \hat{p}(z) = 0 \tag{6.53}$$

Comment: use of rigid-lid surface condition can be abundantly found in literature (see for instance Kunze et al. (2002),Zilberman et al. (2009)). It would lead to have vertical derivative of pressure and vertical velocity to vanish at $z = 0$. It seems to us as being not convenient with respect to the use of vertical modes decompositions of free-surface simulations. Actually, the rigid-lid surface condition will remove the fast (barotropic) mode from the st of modes solution of the Sturm-Liouville problem. As a consequence, barotropic/baroclinic separation of tidal dynamics can not be performed by modal decomposition, and must be performed by other means such as depth-averaging.

Secondary boundary conditions

Secondary boundary conditions are deduced from primary boundary conditions. Combining w bottom boundary condition 6.46 with equations 6.35 yields the Neuman-type boundary condition:

$$\frac{\partial \hat{p}}{\partial z}(z = -h) = 0 \tag{6.54}$$

Combining p surface boundary condition 6.52 with equations 6.30 yields Neuman-type boundary condition:

$$c_e^2 \frac{\partial \hat{w}}{\partial z}(z) - g \hat{w}(z) = 0 \tag{6.55}$$

Final boundary conditions

The final set of modal boundary conditions for vertical velocity is:

$$c_e^2 \frac{\partial \hat{w}}{\partial z}(z) - g\hat{w}(z) = 0 \quad \text{at} \quad z = 0 \tag{6.56}$$

$$\hat{w}(z) = 0 \quad \text{at} \quad z = -h \tag{6.57}$$

and for pressure:

$$g\frac{\partial \hat{p}}{\partial z}(z) + N^2 \hat{p}(z) = 0 \quad \text{at} \quad z = 0 \tag{6.58}$$

$$\frac{\partial \hat{p}}{\partial z}(z) = 0 \quad \text{at} \quad z = -h \tag{6.59}$$

It must be noticed that w surface boundary condition depends upon the separation constant (i.e. introducing a mode dependance), which as some consequences on modes orthogonality.

6.3.3 Horizontal velocity modes

Horizontal velocity in -x and -y direction is decompose similar way. Starting by using equation 6.6 and equation 6.7 and introducing $u_h = u, v$

$$\frac{\partial^2 u}{\partial t^2} + f^2 u = \left(\frac{\partial^2}{\partial t^2} + f^2\right) u = -\frac{1}{\rho_0}\frac{\partial^2 p}{\partial x \partial t} - f\frac{1}{\rho_0}\frac{\partial p}{\partial y} \tag{6.60}$$

by virtue of variable separation, it yields:

$$u = \hat{u}(z)\tilde{u}(x, y, t) \tag{6.61}$$

$$\rho_0(z)\frac{\hat{u}(z)}{\hat{p}(z)} = constant \tag{6.62}$$

The constant can arbritrary chosen, from Gill,1982

$$\rho_0(z)\frac{\hat{u}(z)}{\hat{p}(z)} = \frac{1}{g} \tag{6.63}$$

Barotropic mode is define by the mode-0 (fast mode) in the solutions. higher modes (mode ≥ 1)is slow (baroclinic modes)

6.3.4 Internal tides special case

In case where dealing with period dynamics, for instance tides, some simplifications automatically arise in time derivative terms. Because modal equations are linear, it is possible to project those equations in the complex space. For any periodic variable u, we can write:

$$u(x,y,z,t) = \hat{u}(z)\tilde{u}(x,y,t) = \hat{u}(z)\Re(\tilde{u}_c(x,y,\omega)e^{j\omega t}) \tag{6.64}$$

where $\tilde{u}_c$ is the complex-valued function associated with $\tilde{u}$. Similarly:

$$u_c(x,y,z,t) = \hat{u}(z)\tilde{u}(x,y,t) = \hat{u}(z)\tilde{u}(x,y,\omega)e^{j\omega t} \tag{6.65}$$

where u_c is the complex-valued function associated with u. Time first and second derivatives take the simple expression:

$$\frac{\partial \tilde{u}}{\partial t} = j\omega\tilde{u} \tag{6.66}$$

$$\frac{\partial^2 \tilde{u}}{\partial t^2} = -\omega^2\tilde{u} \tag{6.67}$$

Then the horizontal modal equation for w (eq. 6.37) in the complex space yields:

$$\left(f^2 - \omega^2\right)\tilde{w} = c_e^2\nabla_h^2\tilde{w} \tag{6.68}$$

This is an harmonic equation, also called wave equation. It is similar to the wave equation that would be obtained from the barotropic, shallow-water equations of tides, replacing $\tilde{w}$ with free surface η and c_e with barotropic phase celerity $(gh)^{\frac{1}{2}}$. To some extent, at least in linearized, flat bottom conditions where modes do not interact together, modal separation leads to a solution being the linear superposition of horizontally propagating "shallow-water" waves with specific vertical phase celerity. This is even more easy to understand for special cases such 2 density-layer problem.

Plane wave (particular) solutions can be easily derived from the wave equation, and this property is widely exploited in internal waves literature. Assuming propagation follows the x axis, and amplitude and horizontal wave number are constant, solution takes the form:

$$\tilde{w} = \tilde{w}_a e^{-jkx} \tag{6.69}$$

Space first and second derivatives take the simple expression:

$$\frac{\partial \tilde{u}}{\partial x} = jk\tilde{u} \tag{6.70}$$

$$\frac{\partial^2 \tilde{u}}{\partial x^2} = -k^2\tilde{u} \tag{6.71}$$

Replacing $\tilde{u}$ in Eq. 6.68 yields the simple dispersion relationship:

$$\left(\omega^2 - f^2\right) = c_e^2 k^2 \tag{6.72}$$

Comment : the academic internal tides test case discussed in the following sections will enforce solutions to be of plane waves nature in flat bottom sections of the domain. This is the reason why introducing them here. However, one should remember that plane waves are extremely particular gravity waves, that are barely observed in true oceanic conditions when considering barotropic or internal tides. In the case of barotropic tides, most tidal structures can be identified as coastal Kelvin waves or rotating waves (around amphidromic points). Both are particular solutions of the wave equation, but contrary to the plane wave solutions, they are not limited inside regions bounded by the north and south critical latitudes. Similarly, ocean internal tides, as observed in altimetry or in numerical model simulations, do not appear to be of plane wave nature, as they often display along-propagation and across-propragation horizontal length scales of similar order (plane waves would require to have across-propragation length scales to be one order larger thant the along-propagation). Unfortunately, the overwehlming simplicity of the plane wave approximation has made it extremily popular, and probably misused in many studies dedicated to real ocean internal tides.

6.3.5 Practical decomposition on vertical modes

Vertical modes numerical computation:

The vertical modes are computed by forming the linear system based on vertical velocity (respectively pressure) modal equation and boundary conditions at each horizontal grid's nodes. Mathematical libraries provide solvers to solve for eigenvectors and associated eigenvalues. It must be noticed that some solvers have scope restriction (such as limitation to symetric matrix, readily broken by free-surface boundary condition, or non-even spaced model levels). In practice, vertical modes computation and simulations decomposition has been performed by using the SIROCCO tools, which make use of the DGGEV LAPACK routine to solve the generalized eigenvector/eigenvalue problem. It must be emphasized that the formulation of the discrete Sturm-Liouville problem must be as closed as feasible to the dynamical model discretisation, first in the vertical grid level/layer setting (for instance vertical level/layer remapping should be avoid), but ideally also in term of vertical numerical schemes.

The internal tide propagation is sensitive to potential density vertical contrast, as compressibility effects are neutral with respect to vertical restoring forces. Therefore Brunt-Väisälä frequency N must be computed either by using potential density or by using in situ density with pressure taken at density layers mid-position (i.e. levels). In case of unstable stratification (i.e. $\frac{\partial \rho}{\partial z} > 0$), a null value is assigned to N.

For a given grid point, with L valid levels, the maximum number of acceptable eigenvalues λ (i.e. strictly real, positive valued) for vertical velocity w will be theoretically L, but will in fact reduce to $L-1$. At same grid point, with $L-1$ valid layers, the maximum number of acceptable eigenvalues λ for pressure perturbation p is $L-1$. Maximum number of eigenvalues may not be reached, in particular when the Brunt-Väisälä frequency N is null at a given level (this will rarely happen in realistic cases, namely in unstable conditions, but can be frequently found in academic cases such two-layers stratification case).
In practice, there is no necessity to solve both for w and p Sturm-Liouville problem, as the latter can be numerically deduced from eq. 6.35.

Vertical modes orthgonality and normalization:

Reformulating pressure vertical mode equation 6.38 under eq. 6.40 formulation, and applying eq. 6.44, orthogonality of $\hat{p}$ is expressed by:

$$\int_{-h}^{0} \frac{1}{\rho_0(z)} \hat{p}_m(z) \hat{p}_n(z) dz = 0 \quad m \neq n \tag{6.73}$$

Using $\hat{p}$ and $\hat{u}$ relationship (eq. 6.62), orthogonality of $\hat{u}$ can be deduced from orthogonality of $\hat{p}$:

$$\int_{-h}^{0} \rho_0(z) \hat{u}_m(z) \hat{u}_n(z) dz = 0 \quad m \neq n \tag{6.74}$$

The vertical and horizontal components of variable separation are defined modulus a multiplying factor. Before performing modal decomposition (i.e. decomposing a given 3D field upon related vertical modes), it is necessary to define a practical normalization. We make the choice of making the vertical mode profile dimensionless by using:

$$\frac{1}{h}\int_{-h}^{0} \hat{u}^2(z)dz = 1 \tag{6.75}$$

This normalization has the advantage to keep close to the vertical average operator. As the vertical profile is dimensionless, the horizontal mode component hold the variable units.

Vertical modes decomposition:

Let's take 3D x-velocity u example. Once the vertical modes set $\{\hat{u}_n\}$ numerically computed, decomposition consists in seeking for the horizontal mode $\tilde{u}_n$ such that:

$$u(x,y,z,t) = \sum_{0}^{M-1} \hat{u}_m(z)\tilde{u}_m(x,y,t) + \epsilon(x,y,z,t) \tag{6.76}$$

where M is the number of available modes, i.e. modes having an acceptable phase celerity c_e, and ϵ the part of the field u that does not project on modes. This residual can be seen as the dynamical residuals not compatible with the physics and assumptions sustaining the modal derivation. However, if vertical modes forms a vector basis which rank equal the number of model valid layers (i.e. typically non-masked layers in z-coordinates grids), the residuals will automatically be zero, so of no signification on vertical modes derivation consistency. To some extent, it is the similar issue of decomposing non-periodic signal with Fourier discrete transform, the recomposed Fourier series will always fit the original signal. Actually this will be the case in most realistic ocean fields cases (remember p, u modes are orthogonal, hence linearly independent, and number of modes will generally fit the number of discrete grid layers).

In the case of analyzing internal waves fields, first step will be to perform an harmonic analysis and decomposes the the so-obtained complex-valued field:

$$u(x,y,z,\omega) = \sum_{0}^{M-1} \hat{u}_m(z)\tilde{u}_m(x,y,\omega) + \epsilon(x,y,z,\omega) \tag{6.77}$$

As $\{\hat{u}_m\}$ modes are orthonormal (in the sense of normalization defined in eq. 6.75), scalar product of field u with a given vertical mode $\hat{u}_n$ will simplify in:

$$\frac{1}{h}\int_{-h}^{0} \hat{u}_m u dz = \frac{1}{h}\int_{-h}^{0} \hat{u}_n \left(\sum_{0}^{M-1} \hat{u}_m \tilde{u}_m + \epsilon\right) dz = \tilde{u}_m + \frac{1}{h}\int_{-h}^{0} \hat{u}_m \epsilon dz \tag{6.78}$$

In case where residual is zero, decomposition could be obtained by:

$$\tilde{u}_m = \frac{1}{h}\int_{-h}^{0} \hat{u}_m u dz \tag{6.79}$$

This method cannot be used in w mode case, as they are not orthogonal (because of surface boundary condition). In that case we compute horizontal mode component by minimizing for each horizontal grid node (x,y):

$$J = \left\| u(x,y,z,\omega) - \sum_{0}^{M-1} \hat{u}_m(z)\tilde{u}_m(x,y,\omega) \right\|^2 \tag{6.80}$$

where:

$$\phi \cdot \psi = \frac{1}{h}\int_{-h}^{0} \phi \psi^* dz \tag{6.81}$$

$$\|\phi\|^2 = \phi \cdot \phi \tag{6.82}$$

The equivalent discrete formulation is then given by:

$$J = \sum_{1}^{K} \left\| u_k - \sum_{0}^{M-1} \hat{u}_{m,k}\tilde{u}_m \right\|^2 \tag{6.83}$$

6.4 Models description

Discussion on barotropic and baroclinic dynamics separation and subsequent energy derivation will be illustrated in following sections by its application to the COMODO internal tide test case using the NEMO time-stepping model and the frequency-domain solver available in T-UGOm model. A brief description of those two hydrodynamical models is given in the next subsections.

6.4.1 Primitive equations in NEMO Model

Time-stepping numerical internal tides simulation is conducted using NEMO (ver 3.6 STABLE) model Madec (2008). NEMO is a non linear, non hydrostatic model using C grid in the horizontal and has a variable grid in the vertical. We partly detail the derivation of the energy equations which are given by sets of equations in NEMO model. The equations consist of primitive momentum and tracer equation,the continuity equation, the equation of pressure gradient and density equation. The primitive momentum equations and the continuity equation in NEMO are:

$$\frac{\partial u_h}{\partial t} = -\left(u_h.\nabla_h\right)u_h - w\frac{\partial u_h}{\partial z} - \frac{1}{\rho_0}\nabla_h P - fk\times u_h + D^u + F_h \tag{6.1}$$

$$\overrightarrow{\nabla}.\mathbf{u} = 0 \tag{6.2}$$

subscript "h" denotes a horizontal vector and t is time. P is hydrostatic total pressure, f is coriolis terms.D^h_u, D^h_v, D^T, D^S are the parameterisations of small-scale physics for momentum, temperature and salinity. F^h_u, F^h_v, F^T, F^S are surface forcing terms. g is potential gravity. ρ_0 is the background density, $\rho = \rho\left(T,S,P\right)$ is insitu density calculated from equation of state(not shown). Laplace operator is define as $\nabla = \frac{\partial}{\partial x} + \frac{\partial}{\partial y} + \frac{\partial}{\partial z}$ where $\nabla_h = \frac{\partial}{\partial x} + \frac{\partial}{\partial y}$

The equation of tracer is: .

$$\frac{\partial T}{\partial t} = -\nabla.\left(T\mathbf{U}\right) + D^T + F^T \tag{6.3}$$

where T and S is the tracer of temperature and salinity respectively.

$$\frac{\partial S}{\partial t} = -\nabla.\left(S\mathbf{U}\right) + D^S + F^S \tag{6.4}$$

Total pressure is given by:

$$P = \frac{P_s + P_{hyd}}{\rho_0} \tag{6.5}$$

Where P_s and P_{hyd} are surface and hydrostatic pressure respectively.

$$P_s = \rho g \eta \tag{6.6}$$

The hydrostatic pressure is diagnosed from hydrostatic pressure gradient.

$$\frac{\partial P_{hyd}}{\partial z} = -\rho g z \tag{6.7}$$

Boundary Condition

An ocean is bounded by complex coastlines, bottom topography at its base and an air-sea or ice-sea interface at its top. These boundaries can be defined by two surfaces, $z = d(x,y)$ and $z = \eta(x,y,z,t)$, where d is the depth of the ocean bottom and η is the height of the sea surface. Both d and η are usually referenced to a given surface, $z = 0$. the velocity normal to the ocean bottom and coastlines is zero (in other words, the bottom velocity is parallel to solid boundaries). The kinematic boundary condition in the surface can be expressed as :

$$w = \frac{\partial \eta}{\partial t} + \mathbf{u}.\nabla_h \eta \quad at \quad z = \eta \tag{6.8}$$

$$w = \mathbf{u}.\nabla_h H \quad at \quad z = -h \tag{6.9}$$

Non-linear variable volume is choosen in free surface treatment where water surface elevation (η) is is defined by means of an equation of motion of the sea surface height, and the ocean surface is generally permeable to fresh water flux. (q_w):

$$\frac{\partial \eta}{\partial t} = w_{(at\ z=\eta)} - q_w \tag{6.10}$$

The stress at the bottom is parameterised as :

$$(\tau_x, \tau_y) = \rho C_d \sqrt{u^2 + v^2}\,(u,v) \quad at \quad z = -h \tag{6.11}$$

where $C_d = 0.0025$ is the friction coeeficient.

Total kinetic energy equation is obtained by multiplying eq.(6.1) by $\rho_0 U_h$ and the kinetic energy equation can be written as follows:

$$\underbrace{\frac{1}{2}\frac{\partial u_h^2}{\partial t}}_{\text{Ek}} = -\rho_0 u_h (u_h.\nabla_h) u_h - \rho_0 u_h.w\frac{\partial u_h}{\partial z} - \rho_0 u_h.\frac{1}{\rho_0}\nabla_h P + u_h.D^u + u_h.F_h \tag{6.12}$$

6.4.2 T-UGOm frequency-domain 3D model equations

In the following we do an intensive use og Leibniz rule:

$$\frac{\mathrm{d}}{\mathrm{d}x}\left(\int_{a(x)}^{b(x)} f(x,t)\,\mathrm{d}t\right) = f(x,b(x))\cdot\frac{\mathrm{d}}{\mathrm{d}x}b(x) - f(x,a(x))\cdot\frac{\mathrm{d}}{\mathrm{d}x}a(x) + \int_{a(x)}^{b(x)} \frac{\partial}{\partial x} f(x,t)\,\mathrm{d}t \quad (6.13)$$

Idem for the Stokes formula:

$$\nabla\cdot p\mathbf{u} = p\nabla\cdot\mathbf{u} + \nabla p\cdot\mathbf{u} \quad (6.14)$$

Base equations, hydrostatic and Boussinesq approximations

In the following, we describe the main ingredients of the 3D frequency-domain T-UGOm solver.

Momentum equation:

$$\frac{\partial u}{\partial t} + \nabla\cdot(u\mathbf{u}) - fv = -\frac{1}{\rho}\frac{\partial p}{\partial x} + D_x + \frac{\partial}{\partial z}\left(\kappa_v\frac{\partial u}{\partial z}\right) + g\frac{\partial \Pi}{\partial x} \quad (6.15)$$

$$\frac{\partial v}{\partial t} + \nabla\cdot(v\mathbf{u}) + fu = -\frac{1}{\rho}\frac{\partial p}{\partial y} + D_y + \frac{\partial}{\partial z}\left(\kappa_v\frac{\partial v}{\partial z}\right) + g\frac{\partial \Pi}{\partial y} \quad (6.16)$$

where u,v are horizontal velocity component, $\mathbf{u} = (u,v,w)$ is the 3D velocity vector, κ_v is the vertical viscosity coefficient, (D_x, D_y) the horizontal diffusion and Π is the astronomical and self-attraction potential (expressed in length unit). Horizontal diffusion rarely reflects any molecular viscosity effects in numerical models, but is usually used to parametrize sub-grid scale's effects and stabilize the numerical advection schemes. In fine, we want to build a frequency-domain solver, where no stabilization at all is needed, so it is traditionnally omitted and for simplicity this term will not be discussed here. Also, the test case illustration has no tidal potential forcing and again we also not discuss it here.

Continuity equation, under Boussinesq approximation, reads:

$$\nabla\cdot\mathbf{u} = 0 \quad (6.17)$$

Density advection:

$$\frac{d\rho}{dt} = \frac{\partial \rho}{\partial t} + \mathbf{u}.\nabla\rho = 0 \tag{6.18}$$

Density advection, conservative form:

$$\frac{d\rho}{dt} = \frac{\partial \rho}{\partial t} + \nabla \cdot \rho\mathbf{u} - \rho\nabla \cdot \mathbf{u} = \frac{\partial \rho}{\partial t} + \nabla \cdot \rho\mathbf{u} = 0 \tag{6.19}$$

Layer-integrated equations

Vertical discretisation is achieved by defining model variables to be layer-integrated velocity and layer-averaged density. Actually, a more sophisticated density vertical discretisation is needed over slopping topography where isopycnals do intersect model levels (therefore T-UGOm uses a piecewise linear vertical discretisation), but the former allows to derive the model equation at greater simplicity without loss of generality. Equations of model variables are then obtained by integrating primitive equations between discrete model levels σ.

Horizontal momentum equation

Horizontal momentum equation, acceleration term:

$$\int_{\sigma_0}^{\sigma_1} \frac{\partial u}{\partial t} + \nabla \cdot (u\mathbf{u}) = \frac{\partial}{\partial t}\int_{\sigma_0}^{\sigma_1} u + \nabla_h \cdot \int_{\sigma_0}^{\sigma_1} u\mathbf{v} + [\varpi u]_{\sigma_0}^{\sigma_1} \tag{6.20}$$

$$\int_{\sigma_0}^{\sigma_1} \frac{\partial v}{\partial t} + \nabla \cdot (v\mathbf{u}) = \frac{\partial}{\partial t}\int_{\sigma_0}^{\sigma_1} v + \nabla_h \cdot \int_{\sigma_0}^{\sigma_1} v\mathbf{v} + [\varpi v]_{\sigma_0}^{\sigma_1} \tag{6.21}$$

where $\mathbf{v} = (u,v)$ is the horizontal velocity vector. Horizontal momentum equation, pressure gradient term:

$$\int_{\sigma_0}^{\sigma_1} \frac{\partial p}{\partial x} = \frac{\partial}{\partial x}\int_{\sigma_0}^{\sigma_1} p + \left[p\frac{\partial \sigma}{\partial x}\right]_{\sigma_0}^{\sigma_1} \tag{6.22}$$

Further development in the pressure gradient term will be dependent upon denisty discretisation choices on the vertical, and will not be displayed here. Horizontal momentum equation, vertical diffusion term:

$$\int_{\sigma_0}^{\sigma_1} \frac{\partial}{\partial z}\left(\kappa_v \frac{\partial u}{\partial z}\right) = \left[\kappa_v \frac{\partial u}{\partial z}\right]_{\sigma_0}^{\sigma_1} \tag{6.23}$$

with the classical boundary conditions. At ocean bottom, it reads:

$$\kappa_v \frac{\partial u}{\partial z} = -\|\mathbf{u}^*\| u^* \tag{6.24}$$

$$\kappa_v \frac{\partial v}{\partial z} = -\|\mathbf{u}^*\| v^* \tag{6.25}$$

where $\mathbf{u}^* = (u^*, v^*, w^*)$ is the frictional velocity. It is approximated by the usual parametrization:

$$\mathbf{u}^* = C_D \mathbf{u}_{z=-h} \tag{6.26}$$

with C_D a friction coefficient that can be either directly prescribed or deduced from the logarithmic parametrization. At ocean free surface, in absence of surface wind stress (dismissed here, for simplicity), it reads:

$$\kappa_v \frac{\partial u}{\partial z} = \kappa_v \frac{\partial v}{\partial z} = 0 \tag{6.27}$$

Density advection equation

$$\int_{\sigma_0}^{\sigma_1} \frac{\partial \rho}{\partial t} + \nabla \cdot (\rho \mathbf{u}) = \frac{\partial}{\partial t} \int_{\sigma_0}^{\sigma_1} \rho + \nabla_h \cdot \int_{\sigma_0}^{\sigma_1} \rho \mathbf{v} + [\varpi \rho]_{\sigma_0}^{\sigma_1} = 0 \tag{6.28}$$

Continuity equation

$$\int_{\sigma_0}^{\sigma_1} \nabla \cdot \mathbf{u} = \nabla_h \cdot \int_{\sigma_0}^{\sigma_1} \mathbf{v} + [w - \mathbf{v} \cdot \nabla_h s]_{\sigma_0}^{\sigma_1} = \nabla_h \cdot \int_{\sigma_0}^{\sigma_1} \mathbf{v} + \left[\varpi + \frac{\partial s}{\partial t}\right]_{\sigma_0}^{\sigma_1} = 0 \tag{6.29}$$

Finally we define model levels as impermeable, moving levels (i.e.$\varpi = 0$), making T-UGOm semi-Lagrangian on the vertical. Continuity equation then reads:

$$\nabla_h \cdot \int_{\sigma_0}^{\sigma_1} \mathbf{v} + \frac{\partial \Delta \sigma}{\partial t} = 0 \tag{6.30}$$

Layer-integrated, frequency-domain equations

Last step consists in writting first order, quasi-linearized frequency domain equation.The technique to transform time-domain equation toward frequency-domain can be summarized as follow. Let a dynamical system writes such as:

$$L(u,p) = 0 \tag{6.31}$$

and complex-valued variable as:

$$u(x,y,z,t) = \Re\left(u_c(x,y,z)e^{i\omega t}\right) \tag{6.32}$$

where u_c is a complex-valued function. Frequency-domain equation are obtained by applying the convolution operator:

$$\frac{1}{T}\int_0^T L(u,p)e^{i\omega t}dt = L_c(u_c,p_c) = 0 \tag{6.33}$$

Let' define the complex-valued k^{th} level position σ_k:

$$\sigma_k = s_k + \eta_k \tag{6.34}$$

where s is vertical level position at rest, and η level vertical displacement from s. Uppermost level is ocean free surface, and lowermost is ocean bottom.

Let' define the complex-valued density ρ':

$$\rho(\mathbf{x},\omega) = \rho_0(\mathbf{x}) + \rho'(\mathbf{x},\omega) \tag{6.35}$$

where $\mathbf{x} = (x,y,z)$. Let' define the complex-valued pressure, under hydrostatic approximation:

$$p(x,y,\sigma_{k+1}) = p(x,y,\sigma_k) + \int_{\sigma_k}^{\sigma_{k+1}} \rho_0 dz + + \int_{s_k}^{s_{k+1}} \rho' dz \tag{6.36}$$

In practice, it is equivalent to retain only terms at ω frequency, hence eliminating periodic terms cross-products such as advection terms (that in fact will be part of higher or sub-harmonics equations). Let's define complex-valued transport variables U and V :

$$U = \int_{\sigma_0}^{\sigma_1} u \qquad\qquad V = \int_{\sigma_0}^{\sigma_1} v \tag{6.37}$$

Spectral (frequency-domain) momentum equations, in hydrostatic and Boussinesq approximations yield:

$$j\omega U - fV = -\frac{1}{\rho_0}\int_{\sigma_0}^{\sigma_1} \frac{\partial p}{\partial x} dz + \left[\kappa_v \frac{\partial u}{\partial z}\right]_{\sigma_0}^{\sigma_1} \tag{6.38}$$

$$j\omega V + fU = -\frac{1}{\rho_0}\int_{\sigma_0}^{\sigma_1}\frac{\partial p}{\partial y}dz + \left[\kappa_v\frac{\partial v}{\partial z}\right]_{\sigma_0}^{\sigma_1} \tag{6.39}$$

Frequency-domain continuity equation yields:

$$\frac{\partial \Delta\sigma}{\partial t} + \nabla_h \cdot \mathbf{V} = j\omega\Delta\eta + \nabla_h \cdot \mathbf{V} = 0 \tag{6.40}$$

Density advection (under impermeable level condition yields):

$$\frac{\partial}{\partial t}\int_{\sigma_0}^{\sigma_1}\rho + \nabla_h \cdot \int_{\sigma_0}^{\sigma_1}\rho\mathbf{v} = \frac{\partial \rho'}{\partial t}\Delta s + \rho_0\frac{\partial \Delta\eta}{\partial t} + \nabla_h \cdot \rho_0\mathbf{V} = 0 \tag{6.41}$$

Using Eq. 6.40 in the previous equation, it yields

$$j\omega\rho'\Delta s + \nabla_h\rho_0 \cdot \mathbf{V} = 0 \tag{6.42}$$

3D wave equation

The 3D wave equation is obtained by eliminating velocity variables in continuity and density perturbation equations. Using lumped transport equations (hence blockwise diagonal transport matrices), transport vector can be expressed has a non-trivial matrix product of level excursion and density perturbation:

$$\mathbf{MV} = \mathbf{G}_1\eta + \mathbf{G}_2\rho' \tag{6.43}$$

Replacing its expression in continuity and density perturbation equations leads to a sparse linear system where level excursion η and density perturbation ρ' remain the only (but coupled) unknowns:

$$j\omega\Delta\eta + \nabla_h \cdot \mathbf{M}^{-1}\left(\mathbf{G}_1\eta + \mathbf{G}_2\rho'\right) = 0 \tag{6.44}$$

$$j\omega\Delta s\rho' + \nabla_h \cdot \rho_0\mathbf{M}^{-1}\left(\mathbf{G}_1\eta + \mathbf{G}_2\rho'\right) = 0 \tag{6.45}$$

Level excursion η and density perturbation ρ' coupled equations are solved by using usual finite element (Galerkin) technique. Then solutions are replaced in eq. 6.43 to obtain the 3D tidal velocities/transport.

Numerical settings

T-UGOm can use triangle and quadrangles unstructured meshes. At the moment, 3D equations have been implemented only for triangle domain partition.Various numerical discretisation can be implemented on the finite element grid. For horizontal discretisation, the most commonly used is defined by P_0 horizontal transport (i.e. uniform in the triangle) and P_1 level displacement and density. On the vertical, we use layer-uniform transport and piece-wise (in layer) linear density.

6.5 Barotropic/baroclinic separation

The two main aspects of barotropic/baroclinic separation is first to operate separation for state vector variables such as **u**, p, etc... but also to provide the corresponding momentum equations. Usual approach consist in defing the barotropic quantities, and then to obtain the baroclinic one by difference with the original quantities. It must be reminded in the following that **u**, ρ, p are perturbation quantities. However, in the frame of internal tides, **u** represent the full tidal velocities as they can be seen as perturbation of a given state at rest.

A critical quantity to define is the perturbation pressure. Let start from density split up:

$$\rho(x,y,z,t) = \rho_0(z) + \rho'(x,y,z,t) = \bar{\rho} + \rho'_0(z) + \rho'(x,y,z,t) \tag{6.1}$$

Examination of pressure term gives:

$$\nabla_h p = \nabla \int_z^\eta \rho g dz' = \int_z^\eta \nabla_h \rho' g dz' + [\rho \nabla_h s]_z^\eta = \int_z^\eta \nabla_h \rho' g dz' + \rho|_{z=\eta} g \nabla_h \eta \tag{6.2}$$

Let's reformulate this equation:

$$\nabla_h p = \int_z^0 \nabla_h \rho' g dz' + \int_0^\eta \nabla_h \rho' g dz' + \rho|_{z=\eta} g \nabla_h \eta \tag{6.3}$$

As change in density is considered to be due to vertical advection only:

$$\rho'(z=\eta) = \rho_0(z=0) \tag{6.4}$$

By writing the impermeability condition at first order ($w(z=0)=\frac{\partial \eta}{\partial t}$):

$$\frac{\partial \rho'}{\partial t}(z=0) = -\frac{\partial \rho_0}{\partial z}(z=0)\frac{\partial \eta}{\partial t} \tag{6.5}$$

As $\rho'=0$ when $\eta=0$, it yields:

$$\rho'(z=0) = -\frac{\partial \rho_0}{\partial z}(z=0)\eta \tag{6.6}$$

At first order:

$$\int_0^\eta \nabla_h \rho' g dz' = -\frac{\partial \rho_0}{\partial z}(z=0) g\eta \nabla_h \eta \tag{6.7}$$

It is of second oder compared to other terms in eq. 6.3. Moreover, in tidal applications, this term will project in to permanent and sub-harmonics of the considered wave. Reversely, when dealing with non-linear or compound tides, it will be necessary to taken into account the contribution of the generating tides to the non-linear tide pressure.

$$\nabla_h p = \nabla_h p' = \nabla_h \left(\int_z^0 \rho' g dz' + \rho_0|_{z=0} g\eta \right) \tag{6.8}$$

where

$$p' = \int_z^0 \rho' g dz' + \rho_0|_{z=0} g\eta \tag{6.9}$$

Again, when dealing with internal tide, the complex-valued perturbation pressure p' is obtained from the (harmonically analyzed) complex-valued density perturbation ρ' and sea surface elevation η.

6.5.1 Principles

Classical variable separation can be unified in the following way. First let's define depth-averaging operator notation:

$$\langle u \rangle = \frac{1}{h}\int_{-h}^0 u dz \tag{6.10}$$

Then let's define the following vertical, normalized convolution operator:

$$\langle u \rangle_{\psi} = \langle u\psi \rangle = \frac{1}{h}\int_{-h}^{0} u\psi(z)dz, \quad \frac{1}{h}\int_{-h}^{0} \psi^2(z)dz = 1 \tag{6.11}$$

In case where we choose $\psi \equiv 1$, I operator is the depth-averaging operator:

$$\langle u \rangle_1 = \langle u \rangle = \frac{1}{h}\int_{-h}^{0} udz \tag{6.12}$$

Let's formulate the momentum equation as:

$$L(u,p) = 0 \tag{6.13}$$

Then dynamical separation is obtained by selecting an appropriate ψ profile so that:

$$u_{bt}(x,y,z,t) = \langle u \rangle_{\psi}(x,y,t)\psi(z), \quad u_{bc}(x,y,z,t) = u - u_{bt} \tag{6.14}$$

Corresponding barotropic 3D equation is obtained by:

$$\langle L(u,p) \rangle_{\psi} \psi(z) = 0 \tag{6.15}$$

(equivalent to shallow-water ψ-equation)

$$\langle L(u,p) \rangle_{\psi} = 0 \tag{6.16}$$

and corresponding 3D baroclinic equation is obtained by:

$$L(u,p) - \langle L(u,p) \rangle_{\psi} \psi(z) = 0 \tag{6.17}$$

Again, in case where $\psi \equiv 1$, this would lead to the usual shallow-water momentum equation. It is worthy to notice that:

$$\langle u_{bc} \rangle_{\psi} = 0 \tag{6.18}$$

Let's take a closer look at 3D-equivalent Laplace's tidal momentum equations:

$$\rho\frac{\partial u}{\partial t} - \rho f v = -\frac{\partial p}{\partial x} \tag{6.19}$$

It is quite clear that the pressure gradient term will need some transformation. First let's derive the so-called modified Leibniz rule, obtained from combining the usual Leibniz rule with product derivation rule :

$$\frac{\partial}{\partial x}\int_{-h}^{0}\phi dz = \int_{-h}^{0}\frac{\partial \phi}{\partial x}dz + \left[\phi\frac{\partial s}{\partial x}\right]_{-h}^{0} = \int_{-h}^{0}\frac{\partial \phi}{\partial x}dz + \phi_{(z=-h)}\frac{\partial h}{\partial x} \tag{6.20}$$

$$\frac{\partial}{\partial x}\left(\frac{1}{h}\int_{-h}^{0}\phi dz\right) = \frac{1}{h}\frac{\partial}{\partial x}\int_{-h}^{0}\phi dz - \frac{1}{h^2}\frac{\partial h}{\partial x}\int_{-h}^{0}\phi dz \tag{6.21}$$

Combining the two above equations yields:

$$\frac{\partial}{\partial x}\left(\frac{1}{h}\int_{-h}^{0}\phi dz\right) = \frac{1}{h}\int_{-h}^{0}\frac{\partial \phi}{\partial x}dz - \frac{1}{h}\frac{\partial h}{\partial x}\left(\frac{1}{h}\int_{-h}^{0}\phi dz - \phi_{(z=-h)}\right) \tag{6.22}$$

It can straight-forward reformulated as:

$$\frac{\partial}{\partial x}\langle\phi\rangle = \left\langle\frac{\partial \phi}{\partial x}\right\rangle - \frac{1}{h}\frac{\partial h}{\partial x}\left(\langle\phi\rangle - \phi_{(z=-h)}\right) \tag{6.23}$$

Applied to pressure term in eq. 6.16, it yields:

$$\left\langle\frac{\partial p\psi}{\partial x}\right\rangle = \frac{\partial}{\partial x}\langle p\psi\rangle + \frac{1}{h}\frac{\partial h}{\partial x}\left(\langle p\psi\rangle - p\psi_{(z=-h)}\right) \tag{6.24}$$

Separating barotropic and baroclinic terms yields:

$$\left\langle\frac{\partial p\psi}{\partial x}\right\rangle = \frac{\partial}{\partial x}\langle p_{bt}\psi\rangle + \frac{1}{h}\frac{\partial h}{\partial x}\left(\langle p_{bt}\psi\rangle - p_{bt}\psi_{(z=-h)}\right) - \frac{1}{h}\frac{\partial h}{\partial x}p_{bc}\psi_{(z=-h)} \tag{6.25}$$

This relation establishes the partition between barotropic and baroclinic terms in the momentum equation and allows for defining the barotropic/baroclinic coupling term (also called production term):

$$\tau_{iw} = -\frac{1}{h} p_{bc} \psi_{(z=-h)} \nabla d \tag{6.26}$$

Comment: using 0 *as surface level is an acceptable approximation for the horizontal momentum equation, it is no more the case for the continuity and hydrostatic equations.*

6.5.2 Depth-averaging separation approach

As above-mentioned, depth-averaging separation approach is equivalent to choose $\psi \equiv 1$. Using a uniform profile function ψ makes barotropic variables independent upon z:

$$\mathbf{v}_{bt}(x,y,t) = \frac{1}{h+\eta} \int_{-h}^{\eta} \mathbf{v} dz \tag{6.27}$$

$$p_{bt}(x,y,t) = \frac{1}{h+\eta} \int_{-h}^{\eta} p dz \tag{6.28}$$

At first order for horizontal momentum equation case:

$$\mathbf{v}_{bt} = \frac{1}{h} \int_{-h}^{0} \mathbf{v} dz \tag{6.29}$$

$$p_{bt} = \frac{1}{h} \int_{-h}^{0} p dz \tag{6.30}$$

Barotropic equations are obtained by convolution of 3D equation with the (vertical) scalar product based operator. Looking at pressure term from eq. 6.25, we first notice that:

$$\langle p_{bt} \rangle - p_{bt(z=-h)} = 0 \tag{6.31}$$

Finally horizontal pressure gradient term yields:

$$\left\langle \frac{\partial p}{\partial x} \right\rangle = \frac{\partial}{\partial x} \langle p_{bt} \rangle - \frac{1}{h} \frac{\partial h}{\partial x} p_{bc(z=-h)} \tag{6.32}$$

6.5.3 Vertical modes separation approach

Notations:

$$u(x,y,z,t) = \hat{u}_0(z)\tilde{u}_0(x,y,t) + \sum_{1}^{M-1} \hat{u}_m(z)\tilde{u}_m(x,y,t) = u_{bt} + u_{bc} \tag{6.33}$$

$$p(x,y,z,t) = \hat{p}_0(z)\tilde{p}_0(x,y,t) + \sum_{1}^{M-1} \hat{p}_m(z)\tilde{p}_m(x,y,t) = p_{bt} + p_{bc} \tag{6.34}$$

Let's start with 3D-equivalent Laplace's tidal equations:

$$\rho\frac{\partial u}{\partial t} - \rho f v = -\frac{\partial p}{\partial x} \tag{6.35}$$

Barotropic equations are obtained by convolution of 3D equation with the (vertical) scalar product based operator:

$$\frac{1}{h}\int_{-h}^{0} \rho u(x,y,z,t)\hat{u}_0(z)dz = \tilde{u}_0(x,y,t) \tag{6.36}$$

Let's start with time acceleration. Ignoring change with time of vertical modes, and invoking vertical modes orthonormal properties:

$$\frac{1}{h}\int_{-h}^{0} \rho\frac{\partial u}{\partial t}\hat{u}_0 dz = \frac{\partial \tilde{u}_0}{\partial t} \tag{6.37}$$

Coriolis term:

$$\frac{1}{h}\int_{-h}^{0} \rho f v \hat{u}_0 dz = f\tilde{v}_0 \tag{6.38}$$

Transormation of the pressure gradient requires some more sophisticated manipulations. As vertical modes do depend upon z only:

$$\int_{-h}^{0} \frac{\partial p}{\partial x}\hat{u}_0 dz = \int_{-h}^{0} \frac{\partial p\hat{u}_0}{\partial x} dz \tag{6.39}$$

Finally:

$$\frac{1}{h}\int_{-h}^{0}\frac{\partial p}{\partial x}\hat{u}_0 dz = \frac{\partial \tilde{p}_0}{\partial x} + \frac{1}{h}\frac{\partial h}{\partial x}(\tilde{p}_0 - (p_0\hat{u}_0)_{z=-h}) - \frac{1}{h}\frac{\partial h}{\partial x}(p_{bc}\hat{u}_0)_{z=-h} \tag{6.40}$$

Vector notation:

$$\frac{1}{h}\int_{-h}^{0}\hat{u}_0\nabla_h p dz = \nabla_h\tilde{p}_0 - [p\hat{u}_0\cdot\nabla s]_{-h}^{0} \tag{6.41}$$

$$\tau_{iw} = -\frac{1}{h}p_{bc}\hat{u}_{0(z=-h)}\nabla d \tag{6.42}$$

It is interesting to emphasize first order similarity with depth-averaging derivation. Noting that:

$$\hat{u}_0 \simeq 1 \tag{6.43}$$

and consequently that:

$$\tilde{p}_0 - (p_0\hat{u}_0)_{z=-h} = \tilde{p}_0\left(1 - \hat{u}_0^2(z-h)\right) \simeq 0 \tag{6.44}$$

then:

$$\frac{1}{h}\int_{-h}^{0}\frac{\partial p}{\partial x}\hat{u}_0 dz \approx \frac{\partial \tilde{p}_0}{\partial x} - \frac{1}{h}\frac{\partial h}{\partial x}p_{bcz=-h} \tag{6.45}$$

In other words, the internal tide coupling term is similar in vertical modes approach and depth-averaging approach. To some extent, differences will mostly arise from state vector separation.

6.6 Tidal energy diagnostics

6.6.1 Time-average energy budget

Energy fluxes formulation

In tidal studies, the examination of time-averaged energy budget is a powerful approach to depict tidal mechanisms. In a permanent regime (i.e. time-invariant amplitude and phase of tidal variables), kinetic energy variation over a period is zero:

$$\frac{1}{T}\int_0^T -\nabla p\cdot \mathbf{u}dt + \frac{1}{T}\int_0^T \mathbf{F}\cdot\mathbf{u}dt = 0 \tag{6.1}$$

where $\mathbf{u} = (u, v, w)$ is the 3D velocity vector and $\mathbf{F}$ the resultant forces at the exception of pressure gradient. The above equation clearly depicts that pressure forces rate of work equilibrates all other forces rate of work. Making use of Stokes formula and Boussinesq continuity equation, it yields:

$$\nabla p\cdot\mathbf{u} = (\nabla\cdot p\mathbf{u} - p\nabla\cdot\mathbf{u}) = \nabla\cdot p\mathbf{u} \tag{6.2}$$

Finally:

$$\int_0^T \nabla\cdot p\mathbf{u}dt = \int_0^T \mathbf{F}\cdot\mathbf{u}dt \tag{6.3}$$

In other words, pressure forces rate of work can be written as the divergence of $p\mathbf{u}$, usually named as energy flux divergence. Despite valuable, 3D budget estimates are rather difficult to interpret, and looking at the depth-integrated budget is a much more synthetic approach. Let us examine the pressure term:

$$\int_{-h}^{\eta} \nabla\cdot p\mathbf{u}dz = \int_{-h}^{\eta} \nabla_h\cdot p\mathbf{v}dz + [pw]_{-h}^{\eta} \tag{6.4}$$

where $\mathbf{v} = (u, v)$ is the horizontal velocity vector. Let examine those two right terms. First by using Leibniz rule, it yields:

$$\int_{-h}^{\eta} \nabla\cdot p\mathbf{v}dz = \nabla_h\cdot\int_{-h}^{\eta} p\mathbf{v}dz - [p\mathbf{v}\cdot\nabla s]_{s=-h}^{s=\eta} \tag{6.5}$$

As pressure vanishes at sea surface (i.e. neglecting atmospheric pressure loading), they simplify in:

$$\int_{-h}^{\eta} \nabla_h\cdot p\mathbf{v}dz = \nabla_h\cdot\int_{-h}^{\eta} p\mathbf{v}dz - p\mathbf{v}_{(z=-h)}\cdot\nabla d \tag{6.6}$$

and

$$[pw]_{-h}^{\eta} = -pw_{(z=-h)} \tag{6.7}$$

From ocean bottom impermeability equation, w is given by:

$$w_{(z=-h)} = -\mathbf{v}_{(z=-h)} \cdot \nabla d \tag{6.8}$$

Therefore:

$$[pw]_{-h}^{\eta} = -pw_{(z=-h)} = p\mathbf{v}_{(z=-h)} \cdot \nabla d \tag{6.9}$$

Finally we obtain the classical relationship for depth-integrated pressure rate of work:

$$\int_{-h}^{\eta} \nabla p \cdot \mathbf{u} dz = \nabla_h \cdot \int_{-h}^{\eta} p\mathbf{v} dz \tag{6.10}$$

where the depth-integrated pressure work is equal to the divergence of the horizontal energy flux vector. Formulating time-integrated equation yields:

$$\frac{1}{T}\int_0^T \nabla_h \cdot \int_{-h}^{\eta} p\mathbf{v} dz dt = \frac{1}{T}\int_0^T \int_{-h}^{\eta} \mathbf{F} \cdot \mathbf{u} dz dt \tag{6.11}$$

Practical application

$$\int_0^T \nabla_h \cdot \int_{-h}^{\eta} p\mathbf{v} dz dt = \int_0^T \nabla_h \cdot \int_{-h}^{0} p\mathbf{v} dz dt + \int_0^T \nabla_h \cdot \int_{0}^{\eta} p\mathbf{v} dz dt \tag{6.12}$$

As integration limits are independant, first right-hand side term yields:

$$\int_0^T \nabla_h \cdot \int_{-h}^{0} p\mathbf{v} dz dt = \nabla_h \cdot \int_{-h}^{0}\int_0^T p\mathbf{v} dt dz \tag{6.13}$$

Formulated for u and v components of horizontal velocity:

$$\int_0^T \nabla_h \cdot \int_{-h}^{0} pu dz dt = \nabla_h \cdot \int_{-h}^{0}\int_0^T pu dt dz = \frac{1}{2}T\nabla_h \cdot \int_{-h}^{0} a_p a_u \cos(G_p - G_u) dz \tag{6.14}$$

where a_p, G_p is amplitude and phase lag of pressure, and a_u, G_u is amplitude and phase lag of u-component. Similarly:

$$\int_0^T \nabla_h \cdot \int_{-h}^{0} pv dz dt = \nabla_h \cdot \int_{-h}^{0}\int_0^T pv dt dz = \frac{1}{2}T\nabla_h \cdot \int_{-h}^{0} a_p a_v \cos(G_p - G_v) dz \tag{6.15}$$

Time-averaged, depth-integrated energy fluxes are maximum for in-phase u and p (propagating wave) and null for in-quadrature u and p (stationary wave). Let examin the second right-hand side term:

$$\int_0^\eta p\mathbf{v}dz \approx \int_0^\eta \rho_s g\,(\eta - z)dz\mathbf{v}_s = -\frac{1}{2}\rho_s g\left[(\eta - z)^2\right]_0^\eta \mathbf{v}_s = -\frac{1}{2}\rho_s g\eta^2\mathbf{v}_s \tag{6.16}$$

It is of null average over one tidal period. Finally:

$$\frac{1}{T}\int_0^T \nabla_h \cdot \int_{-h}^\eta p\mathbf{v}dzdt = \frac{1}{T}\int_0^T \int_{-h}^\eta \mathbf{F}\cdot\mathbf{u}dzdt = \nabla_h \cdot \int_{-h}^0 \phi dz \tag{6.17}$$

where $\phi = (a_p a_u \cos(G_p - G_u), a_p a_v \cos(G_p - G_v)$.

Comment on pressure rate of work calculation

The derivation of pressure forces (time-averaged, depth-integrated) rate of work from the horizontal divergence of (time-averaged, depth-integrated) energy fluxes offers the great advantage to enable separate barotropic and baroclinic estimates (actually separate modes estimates), but is usually sensitive to residual pollution by numerical defects. In particular, in the case of staggered grid such as the NEMO's C-grid, normal fluxes need to be computed at velocity nodes, and then average divergence on the tracer cell can be more safely estimated by flux budget at cell sides (this is in fact a finite volume derivation, equivalent to the semi-empirical finite difference derivation). Similarly, space-integrated rate of work computed from flux budget at boundaries is also highly sensitive to numerical details (and defects). An alternative consists in directly estimating pressure gradient rate of work (but losing barotropic/baroclinic nice orthogonality and separation properties):

$$\int_{-h}^\eta \nabla p\cdot\mathbf{u}dz = \int_{-h}^\eta \nabla_h p\cdot\mathbf{v}dz + \int_{-h}^\eta \frac{\partial p}{\partial z}wdz \tag{6.18}$$

Using hydrostatic approximation:

$$\int_{-h}^\eta \nabla p\cdot\mathbf{u}dz = \int_{-h}^\eta \nabla_h p\cdot\mathbf{v}dz - g\int_{-h}^\eta \rho wdz = \int_{-h}^\eta \nabla_h p\cdot\mathbf{v}dz - g\int_{-h}^\eta (\rho_0 + \rho')wdz \tag{6.19}$$

$$\int_{-h}^\eta (\rho_0 + \rho')wdz = \int_{-h}^0 (\rho_0 + \rho')wdz + \int_0^\eta (\rho_0 + \rho')wdz \tag{6.20}$$

ρ_0 contribution to first right-hand term side is null:

$$\frac{1}{T}\int_0^T \left(\int_{-h}^0 \rho_0 wdz\right)dt = \frac{1}{T}\int_{-h}^0 \left(\int_0^T \rho_0 wdt\right)dz = 0 \tag{6.21}$$

as w is periodic and ρ_0 is constant with time. Let's examine ρ_0 contribution to second right-hand term. Making the approximation $w \approx \frac{\partial \eta}{\partial t}$ near ocean sea surface:

$$\int_0^{\eta} \rho_0 w dz \approx \int_0^{\eta} \rho_{0,s} \frac{\partial \eta}{\partial t} dz \tag{6.22}$$

where $\rho_{0,s}$ is surface average density. Then:

$$\frac{1}{T}\int_0^T \left(\int_0^{\eta} \rho_0 w dz\right) dt \approx \frac{1}{T}\int_0^T \rho_{0,s} \frac{1}{2}\frac{\partial \eta^2}{\partial t} dt = \frac{1}{T}\rho_{0,s}\left[\frac{\eta^2}{2}\right]_0^T = 0 \tag{6.23}$$

ρ_0 contribution to right-hand side is approximately null. Let's examine ρ' contribution to the first right-hand term. Using vertical modes approximation:

$$\frac{\partial \rho'}{\partial t} = \frac{\partial \rho_0}{\partial z} w = -\frac{\rho_0}{g} N^2 w \tag{6.24}$$

Then:

$$\int_{-h}^0 \rho' w dz = \int_{-h}^0 \rho' \frac{\partial \rho'}{\partial t} dz = \frac{1}{2}\int_{-h}^0 \frac{\partial \rho'^2}{\partial t} dz \tag{6.25}$$

$$\frac{1}{T}\int_0^T \left(\int_h^0 \frac{\partial \rho'^2}{\partial t} dz\right) dt = \frac{1}{T}\int_h^0 \left(\int_0^T \frac{\partial \rho'^2}{\partial t} dt\right) dz = \frac{1}{T}\int_h^0 \left[\rho'^2\right]_0^T dz = 0 \tag{6.26}$$

Let's examine ρ' contribution to the second right-hand term:

$$\frac{1}{T}\int_0^T \left(\int_0^{\eta} \rho' w dz\right) dt \approx \frac{1}{T}\int_0^T \rho_{0,s} \frac{1}{2}\frac{\partial \eta^2}{\partial t} dt = \frac{1}{T}\rho_{0,s}\left[\frac{\eta^2}{2}\right]_0^T = 0 \tag{6.27}$$

Finally, the vertical velocity term contribution to the time-averaged, depth-integrated pressure rate of work can be considered as negligible, hence allowing for limiting computation to horizontal terms.

6.6.2 Depth-averaging separation approach

Barotropic Tidal Energy

In order to obtain barotropic tidal kinetic energy equation, all dynamic variables in 6.12 are projected into tidal complex amplitude where variables U,V,V and $\tilde{\rho}$ represent all velocity in -u,-v,-w direction and density in tidal complex amplitude respectively.

Tidal kinetic energy is integrated in one tidal cycle, thus the avection, coriolis and surface forcing terms is negligable. The barotropic/depth averaged (denoted by overbar sign) tidal energy kinetic average in one tidal cycle is given by :

$$\frac{1}{2}\frac{\partial \overline{U}}{\partial t} = -\frac{1}{\rho_0 d} U_h \overline{\nabla_h P} \tag{6.28}$$

where $d{=}h{+}\eta$ is total depth

The dissipation terms by the viscosity and diffusivity as well as forcing terms can be expressed as barotropic tidal equation. In this study all dissipation terms related to tidal kinetoc energy is neglected.

Over sloping topography, taking the depth average of a horizontal gradient requires the use of Leibniz's theorem [i.e., Kundu et al. (2004) and Kelly and Nash (2010)]. The resulting Leibnitz rule of integration where φ can be u,v velocities,pression(P) or Energy (E). and m is either in $x-$ or $y-$ direction. :

$$\frac{\partial}{\partial m}\int_{\alpha(m)}^{\beta(m)} \frac{\partial \varphi}{\partial m}\partial z = \int_{\alpha(m)}^{\beta(m)} \frac{\partial \varphi}{\partial m}\partial z + \varphi\left(m,\beta\left(m\right)\right)\frac{\partial \beta}{\partial m} - \varphi\left(m,\alpha\left(m\right)\right)\frac{\partial \alpha}{\partial m} \tag{6.29}$$

the developed leibnitz rule is written as :

$$\nabla_h \int_{\alpha}^{\beta} \varphi = \int_{\alpha}^{\beta} \nabla_h \varphi + \left[\varphi \nabla_h\right]_{\alpha}^{\beta} \tag{6.30}$$

Employing leibnitz rule in 6.29 to equation 6.28 resulting the barotropic kinetic energy equation as :

$$\int_{d}^{\eta} \mathbf{u}.\nabla_h p = \nabla_h \int_{d}^{\eta} \overline{\mathbf{u}} p - [\overline{\mathbf{u}} p \nabla S]_{d}^{\eta} - \int_{d}^{\eta} p \nabla_h \overline{\mathbf{u}} \tag{6.31}$$

where S is surface. Using modified leibnitz rule in equation 6.30 by using $\varphi = \overline{\mathbf{u}} p$ yields:

$$\nabla_h \int_{d}^{\eta} \overline{\mathbf{u}} p = \int_{d}^{\eta} \nabla_h . \overline{\mathbf{u}}\,\overline{p} + [\overline{\mathbf{u}}\,\overline{p} \nabla_S]^{\eta}_{-h} \tag{6.32}$$

by inserting equation 6.32 to equation 6.31 gives,

$$\int_{h}^{\eta} \mathbf{u}.\nabla_h p = \int_{d}^{\eta} \nabla_h \overline{\mathbf{u}}\,\overline{p} + [\overline{\mathbf{u}}\,\overline{p} \nabla_S]^{\eta}_{-h} - [\overline{\mathbf{u}} p \nabla S]^{\eta}_{-h} - \int_{-h}^{\eta} p \nabla_h \overline{\mathbf{u}} \tag{6.33}$$

and resulting :

$$\int_{d}^{\eta} \mathbf{u}.\nabla_h P = \int_{-h}^{\eta} \nabla_h \overline{\mathbf{u}p} - \left(\overline{\mathbf{u}}p'\right)_{z=-h} \nabla_h d - \int_{-h}^{\eta} p \nabla_h \overline{\mathbf{u}} \tag{6.34}$$

Equation of barotropic energy is :

$$\overline{Ek} = \frac{1}{2}\rho_0 \overline{\mathbf{u}} \left(\overline{\mathbf{u}}.\nabla_h\right) + \rho_0 \overline{\mathbf{u}}^2.w - \int_{d}^{\eta} \nabla_h \overline{\mathbf{u}p} - \left(\overline{\mathbf{u}}p'\right)_{z=-h} \nabla_h d - \int_{d}^{\eta} p \nabla_h \overline{\mathbf{u}} \tag{6.35}$$

the last term in equation 6.35 its physical interpretation is not entirely intuitive Kurapov et al. (2003).The final barotropic tidal energy average in one tidal cycle yields:

$$\overline{Ek} = \int_{d}^{\eta} \nabla_h \overline{\mathbf{u}p} - \left(\overline{\mathbf{u}}p'\right)_{z=-h} \nabla_h d \tag{6.36}$$

Baroclinic Tidal Energy

Baroclinic tidal energy is derived by substracting barotropic momentum in equation 6.28 from total momentum equation 6.1 gives :

$$\frac{\partial U_{it}}{\partial t} = -\frac{1}{\rho_0 h} U_h \overline{\nabla_h P_{it}} \tag{6.37}$$

where "it" sign denotes the internal tides as perturbation parts derived from total - depth average. Employing leibnitz rule in equation 6.30 and integrated in one tidal cycle, the baroclinic depth integrated energy equation is :

$$Ek_{it} = \left(\overline{\mathbf{u}}p'\right)_{z=-h} \nabla_h + \int_{d}^{\eta} p' \nabla_h \mathbf{u'} \tag{6.38}$$

The final baroclinic tidal energy yields:

$$Ek_{it} = \int_{d}^{\eta} \nabla_h \mathbf{u'}p' + \left(\overline{\mathbf{u}}p'\right)_{z=-h} \nabla_h d \tag{6.39}$$

First part RHS and second part in THS from both equation 6.36 and equation 6.39 is divergence of barotropic/baroclinic flux energythe energy conversion terms from barotropic to baroclinic respectively.

Both barotropic and baroclinic kinetic energy has flux divergence terms and conversion terms. The conversion terms in equation 6.36 has different sign with conversion terms in equation 6.39. The conversion term represent topographic internal tide generation and also the energy transfer from both barotropic and baroclinic. This is interesting because we can approach the conversion terms in such barotropic or in baroclinic equation.

6.6.3 Vertical modes separation approach

Depth integrated kinetic energy

As vertical modes are orthonormals:

$$\int_{-h}^{\eta} \rho_0 \mathbf{u}^2 dz = \rho_0 \sum_{0}^{M-1} \tilde{u}_m^2 \tag{6.40}$$

Energy fluxes

Let's expand eq. 6.10 by using vertical modes decomposition:

$$\int_{-h}^{\eta} p\mathbf{v}dz = \int_{-h}^{\eta} \left(\sum_{n=0}^{M-1} \hat{p}_n(z)\tilde{p}_n(x,y,t) \sum_{m=0}^{M-1} \hat{u}_m(z)\tilde{\mathbf{v}}_m(x,y,t) \right) dz \tag{6.41}$$

For a given m,n term:

$$\int_{-h}^{\eta} \hat{p}_n(z)\tilde{p}_n(x,y,t)\hat{u}_m(z)\tilde{\mathbf{v}}_m(x,y,t)dz = \left(\int_{-h}^{\eta} \hat{u}_m(z)\hat{p}_n(z)dz \right) \tilde{p}_m(x,y,t)\tilde{\mathbf{v}}_m(x,y,t) \tag{6.42}$$

As vertical modes are orthonormals:

$$\int_{-h}^{\eta} \hat{u}_m(z)\hat{p}_n(z)dz = \delta_{m,n} \tag{6.43}$$

Then the total energy flux vector can be expressed as the sum of modal energy vectors:

$$\int_{-h}^{\eta} p\mathbf{v}dz = \sum_{0}^{M-1} \tilde{p}_m(x,y,t)\tilde{\mathbf{v}}_m(x,y,t) \tag{6.44}$$

In internal tide applications, time -varying variables are replaced by complex-valued variables:

$$\tilde{p}_m(x,y,t) = \Re\left(a_{p,m} e^{-G_{p,m}} e^{j\omega t} \right) \tag{6.45}$$

$$\tilde{u}_m(x,y,t) = \Re\left(a_{u,m} e^{-G_{u,m}} e^{j\omega t} \right) \tag{6.46}$$

$$\tilde{v}_m(x,y,t) = \Re\left(a_{v,m} e^{-G_{v,m}} e^{j\omega t} \right) \tag{6.47}$$

Finally the two components of the time-averaged, depth-integrated energy flux are given by:

$$\int_0^T \tilde{p}_m(x,y,t)\tilde{u}_m(x,y,t)dz = \frac{1}{2}a_{p,m}a_{u,m}\cos\left(G_{u,m} - G_{p,m}\right) \tag{6.48}$$

$$\int_0^T \tilde{p}_m(x,y,t)\tilde{v}_m(x,y,t)dz = \frac{1}{2}a_{p,m}a_{v,m}\cos\left(G_{v,m} - G_{p,m}\right) \tag{6.49}$$

Internal tides production term

From eq. 6.42, depth-integrated internal wave drag rate of work yields:

$$\int_{-h}^0 \tau_{iw}\cdot \mathbf{v}_0 dz = (p_{bc}\hat{u}_0)_{z=-h}\nabla h\cdot\tilde{\mathbf{v}}\left(\frac{1}{h}\int_{-h}^0 \hat{u}_0^2 dz\right) = (p_{bc}\hat{u}_0)_{z=-h}\nabla h\cdot\mathbf{v} \tag{6.50}$$

as modes are normalized so that $\frac{1}{h}\int_{-h}^0 \hat{u}_m^2 dz = 1$.

6.7 Numerical COMODO internal tide test case

This section implement the definition of barotropic and internal tides on the calculation of tidal energy budget using idealised numerical case. This test case has objectives to study the generation of internal tides and model study about the energetics of internal tides.

6.7.1 Test case description

The simulation on COMODO internal waves test case (http://www.comodo-ocean.fr/) is a vertically stratified field forced by a barotropic flow interacting over an idealized abyssal plain/slope/shelf topography and without bottom friction (figure 6.1). The configuration was set up by Pichon and Maze (1990). COMODO test case has a linear stratification ($N2 = 0.002s^{-2}$). The domain is 880 km wide and has 40 vertical levels. Model runs for 30 days. It is set long enough to limit undesirable effects of the open boundaries. The domain consists of three parts. Deep water (4000m) region found in west-side of the domain followed by steep continental slope (about 20 %) until shallow water part in east-side (200m). The idealized bathymetry consists of:

- an abyssal plain at 4000m between x = 0 and x = 430km
- a continental slope between x ∼ 430 km and x ∼ 480 km with initial slope is (sin(x)/x).

The horizontal grid resolution is 1 km in all domain. There is no grid refinement above the slope. The Coriolis parameter is set to f = $1.04510x10^{-4}s^{-1}$ (corresponding to a latitude of

46.95N). Density is based on linear equation of state by using

$$\rho = \rho_0 - rn\_a_0 * (\theta_0 - 10) \tag{6.1}$$

With $rn\_a_0 = 1.6550x10^{-1}kg.m^{-3}.C^{-1}$

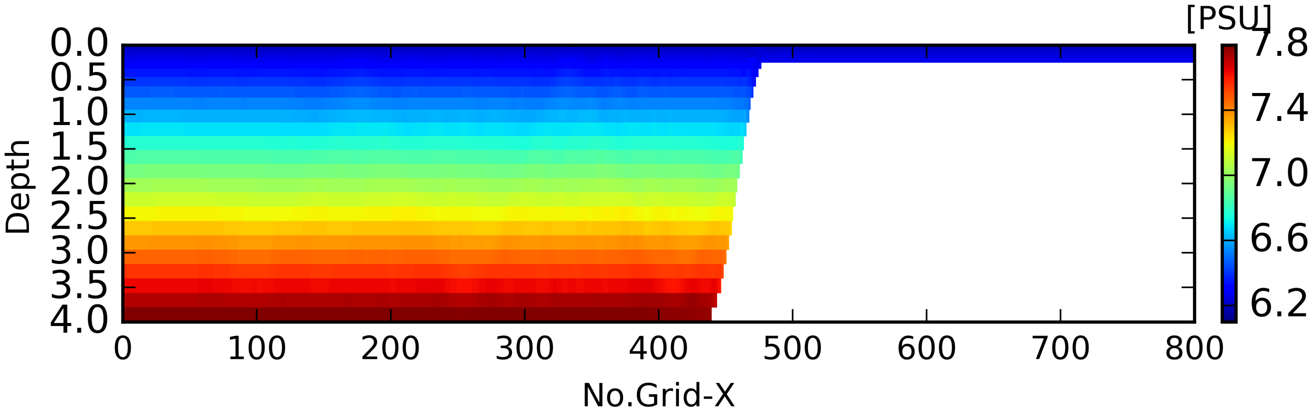

Figure 6.1: Model domain in COMODO test case. Color is density

Boundary conditions:

Purely barotropic open boundary conditions are set at both extremities. To avoid internal tides generated at the continental slope to reach domain limits (and get reflected there), solution is damped toward barotropic solution in boundary buffer zone through a relaxation coefficient of the form:

$$\kappa = \frac{e^{-\frac{d}{\lambda}}}{\tau} \tag{6.2}$$

with the time scale $\tau = 0.05 * 86400s$ and the space scale $\lambda = 20000m$. The relaxation is switched to 0 when the relaxation time scale is greater than 120 days (i.e. $\kappa < 1/(120 * 86400)$, corresponding to $d \approx 156km$).

Comment: in the test configuration used here (uniform N), the expected horizontal wavelength of the first baroclinic mode is about 160 km, i.e. the buffer zones extent compare with the longest expected horizontal wavelength. Empirically, it has been observed that internal tides first mode is not fully damped before reaching the open limits, thus moderatly triggering some wave reflection. Ideally, it would be necessary to slightly extend the buffer zone.by increasing the horizontal scale λ. *However, to keep consistent with existing COMODO experiments, the test case original setting has been kept unchanged.*

Modal decomposition:

Despite an analytical solution is not available for the test case, periodicity condition and vertical modes framework allows us for inferring some properties of the theoretical solution(actually the shallow-water problem, that could be seen as a one-layer 3D problem, has theoretical solution that is also of plane wave nature on flat bottom and Bessel functions-based nature above the continental slope). At first order (i.e. making rigid lid approximation), in case where N is uniform, dispersion relationship reads:

$$m_n c_n = N \tag{6.3}$$

where $m = \frac{n\pi}{h}$ is the vertical wavenumber, and $c_n = \frac{Nh}{n\pi}$ the vertical phase celerity. The theoretical vertical mode profile are sinusoidal functions, and applying boundary conditions yields:

$$\hat{w_n}(z) = \sin(m_n z) \tag{6.4}$$

$$\hat{p_n}(z) = \cos(m_n z) \tag{6.5}$$

In practice, especially for vertical modes decomposition computations, **it is not only unnecessary but also inconvenient to make the rigid lid approximation**. However, the main characteristics of vertical modes are captured in this approximation. Following eq. 6.72, in flat bottom regions, plane wave horizontal wavenumber is given by:

$$k_n = \frac{\left(\omega^2 - f^2\right)^{\frac{1}{2}}}{c_n} \tag{6.6}$$

First order validation of modes computation can consist in comparing the numerical modal celerities with theoretical values. However, it must be noticed that the discrete nature of the numerically-solved Sturm-Liouville problem will be responsible for numerical dispersion, and agreement between theoretical and numerical vertical celerities will decrease when the mode number increases. Also, horizontal resolution can be not sufficient to solve for higher modes horizontal structure, hence leading to dispersed or unsolved modes (in our test case, this will mainly occur on the shelf section of the domain). Consequently it is necessary to first solve vertical modes on the model vertical grid, and to operate the verification of modes vertical and horizontal wavenumbers in numerical solution with numerical but not theoretical vertical modes predicates.

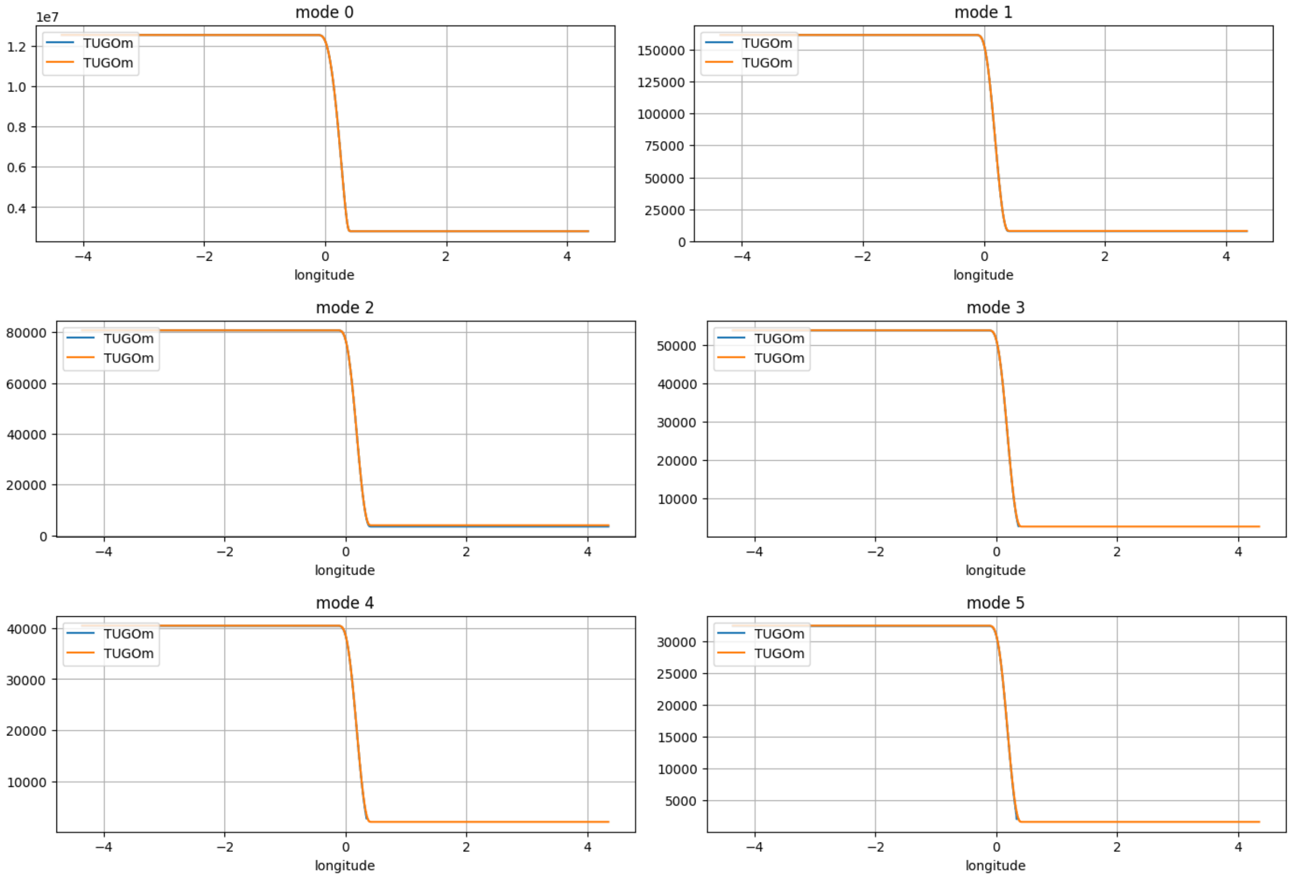

Figure 6.2: modes horizontal wavelengths in meters (for a standard σ-layer vertical grid as in T-UGOm simulations)

In the T-UGOm and NEMO COMODO simulations presented in the next sections, the vertical grids differs (T-UGOM has be run a standard 40 σ-layers vertical grid, and NEMO on a 40 layers z-grid with vertical resolution increasing near the surface). This will trigger some differences in vertical modes, especially for the higher ones. However, both solve the full set of modes over the abyssal plain, as the highest mode wavelength is larger than twice the horizontal grid resolution. Reversely, both will solve only the first 6 modes (barotropic one included) as the horizontal grid resolution is not sufficient to capture the higher modes horizontal wavelength. This strongly suggests to use flexible grids, where the resolution coupling between vertical and horizontal grids could be set more consistent. The main difficulty in doing so lies in that it is necessary to take a kind of climatological stratification (if this makes any sense) into account to determine the optimal grid setting.

6.7.2 Numerical model configuration

NEMO configuration

The bathymetry is chosen to represent the continental slope. The barotropic tide S2 is introduced at the eastern and western boundaries. The residual tide current across the boundaries is set to 0.

Calculation of tidal/internal tides kinetic energy is depending the condition on the bottom grid. The non-uniform bottom thickness variation in Z-partial steps leading to complexity in depth dependent vertical grid calculation. In order to examine the bottom sensitivity, I compare different simulation using Z-partial steps grid and S-coordinates grid.

Grid size is set to 880 x 1, with cell size of 1 kilometer. Only one cell in the y-coordinates grid thus periodic boundary condition is used in order to treat flux in y- direction. UBS scheme is used for momentum and TVD advection scheme for tracer. There is no explicit horizontal diffusivity. Vertical viscosity is constant = $1x10-4m^2.s^{-1}$, and vertical diffusivity is zero. All simulation runs for 30 days with instantaneous hourly outputs. Harmonic analysis for barotropic tides S2 calculated on last twenty days of simulation. Hydrostatic pressure (p) in the tracer points grid is calculated by:

$$p[n] = g\ \rho_0\ \eta + (0.5\ \rho\ g\ z[n])\,;\ for\ n = 1\,[layer1] \tag{6.7}$$

$$p[n+1] = p[n-1] + (0.5\ \rho\ g\ z[n])\,;\ for\ \ [n > 1] \tag{6.8}$$

T-UGOm configuration

T-UGO is used in its hydrostatic, spectral (i.e. frequency domain) mode, solving layer integrated spectral equations in the three dimensional spectral form of wave continuity equations. T-UGOm grid is evenly spaced in the horizontal dimensions at a 1 kilometer resolution, and uses terrain following coordinates in vertical. In spectral simulation, there are no temporal derivation, hence no implicit diffusion linked with the time derivation/advection scheme. This is the advantage by using T-UGO model in COMODO test case so we can compare the propagation of internal tides in the spectral model without influence of physical nor numerical dissipation (as found in NEMO simulation).

In a realistic configuration, one would take profit of the flexibility of finite element grids in

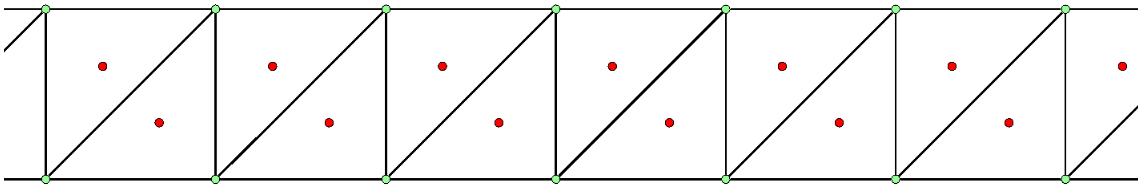

Figure 6.3: T-UGOm horizontal grid and LGP0xLGP1 discretion nodes. Pressure/elevation (continuous) linear discretisation is LGP1 (green nodes), velocity (discontinuous) discretisation is LGP0 (red nodes). x-direction resolution is 1 kilometer.

horizontal to increase resolution above the continental slope and shelf, where dynamics length scales get much shorter than above the abyssal plain. In particular, the horizontal modes wavelengths are not resolved on the shelf except for the very first ones. However, to keep the twin experiments (NEMO/T-UGOm) as much similar as possible, the T-UGOm horizontal grid is set to mimic the NEMO structured grid.

6.7.3 Internal tides simulations

In the following, we will describe the internal tides simulation results both for the NEMO and T-UGOm model. For the present, no 3D analytical solution, exact nor approximated, is known for the COMODO test case. To some extents, the comparisons between both model solutions gives us an estimate for modeling errors and uncertainties.

Horizontal and vertical velocities snapshots are displayed in figures 6.4 and 6.5. Both components are dominated by the internal tides dynamics, except for the u velocity component on the shelf where barotropic and baroclinic velocities can be of similar order, at least in T-UGOm solution (this point will be discussed in next sections).

As it could be expected, NEMO solutions are much smoother than T-UGOm solutions. First NEMO numerical schemes are known to have implicit diffusion, and vertical viscosity was not set to zero for numerical stability reasons. In contrast, T-UGOm are absolutely diffusionless, leaving noisy, short wavelength dynamics to propagate without damping. In addition, T-UGOm display respects the discontinuous discretization of velocity, where NEMO display is partially smoothed by usual C-grid interpolation.

The main internal tides characteristics are similar in both simulations, showing however some significant differences in the details. The internal tides beam is generated at the upper part of the shelf slope, and the beam slope fits the expected value. This can be easily explained by the fact that, in uniform N conditions, isopycnal heaving is directly proportional to vertical velocity, which reaches its maximum above the slope where barotropic horizontal motion is accelerated by water column constriction. In real ocean, uniform N conditions are rarely met,

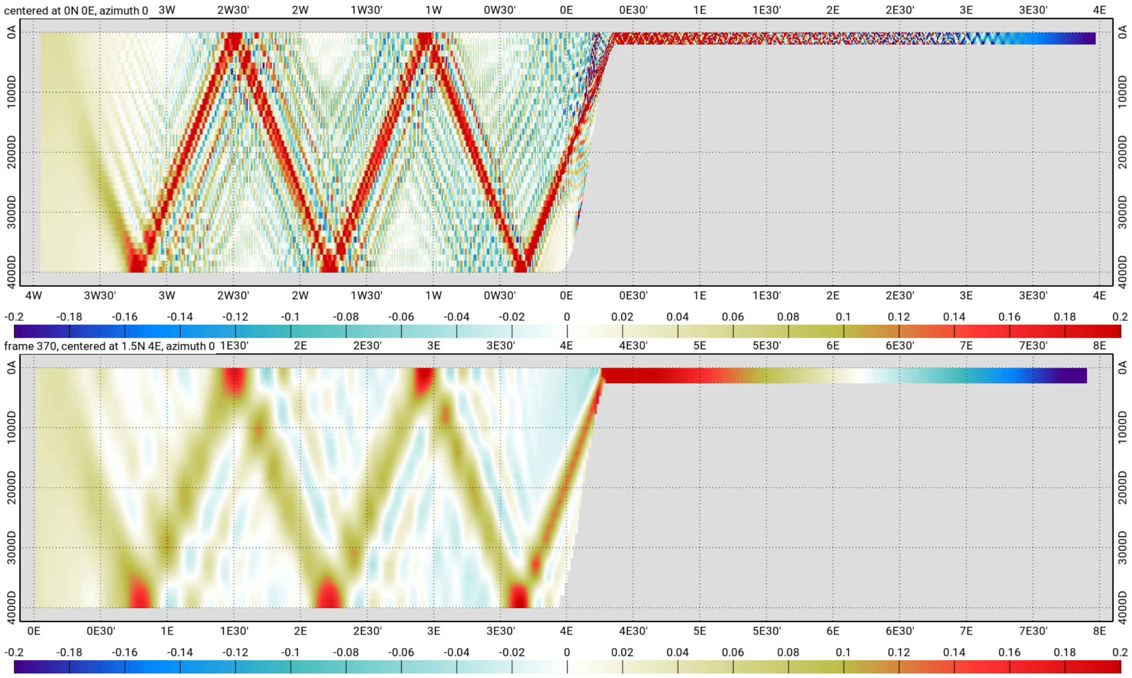

Figure 6.4: Instantaneous horizontal velocity for T-UGOm non diffusive (top) and NEMO (bottom)). Units are m/s

but again maximum N values are reached in permanent/seasonal thermoclines or at mixed layer bottom, in any cases in the upper part of the oceans. Internal tides get damped when reaching the relaxation buffer zone at both domain extremities. In T-UGOm solution, the beam is more focused, while in NEMO solution it get wider and smoother after about 100km propagation toward the western open boundary. In the abyssal plain, intensity of velocity is of similar order of magnitude. In T-UGOm solution, the beam is unchanged and of higher intensity until it reaches the relaxation buffer, while NEMO beam has smaller intensity and is also slightly damped during propagation. Contrary to T-UGOM, NEMO's solution shows no internal tides signature on the continental shelf. As discussed earlier, this might be due to the fact that the internal tides propagating toward the shelf are much less energetic than the one propagating toward the abyssal plain, and then can be easily damped by numerical diffusion or dissipation (NEMO). It might also be due to the fact that the wave speed on shelf is comparable to the barotropic physical velocity, hence is capable of de-structuring the wave propagation over the shelf (Doppler effect). This mechanism is not reproduced in the frequency-domain solution of T-UGOm (unless iterative processing being used, which was not the case here).

To illustrate effect of vertical viscosity, u and w velocity components obtained from T-UGOm with a $k_v = 5e^{-2}$) viscosity coefficient are displayed in figure 6.6. On one hand, short wavelength patterns are no more visible, but on the other hand, amplitudes are reduced compared to T-UGOm non-viscous simulations, and continuously damped along propagation from the shelf

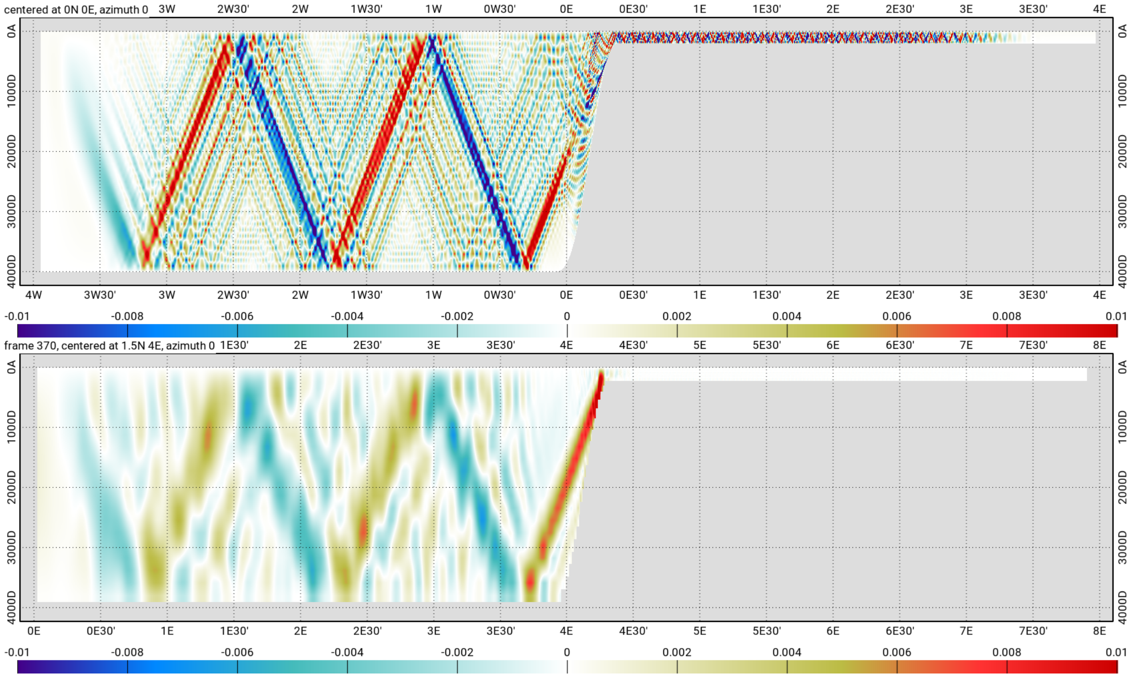

Figure 6.5: Instantaneous vertical velocity for T-UGOm non diffusive (top) and NEMO (bottom). Units are m/s

edge (generation site) toward open boundaries. In addition, internal tides are rapidly damped on the shelf. The internal tide beam keeps quite focused (more than the one in NEMO solution), and most of extra-beam internal tide signature has vanished. To some extent, it shows that NEMO solution is not affected by diffusion-related mechanism, and that more complex numerical aterfacts must be at work.

A more detailled diagnostics can be obtained by examining the modal decomposition of solutions. In Figure 6.7, we display the modal decomposition coefficients for the u component (lower modes only). Mode 0 (barotropic) coefficients are similar for the two models. Baroclinic mode coefficients show some interesting differences. The main discrepancies between T-UGOm and NEMO are first, the point that the NEMO's coefficients decrease from generation site toward the western open boundary (abyssal plain) indicating a partial internal tide dissipation along propagation, and second, the quick and total dissipation of internal tides over the shelf in NEMO's solution. The rate of decrease over the abyssal plain of NEMO's modal coefficient seems to be higher when mode number increases, suggesting a scale-dependent mechanism such as momentum diffusion. When looking at phase lag, T-UGOm and NEMO solution are quite similar for the lowest modes, with wavelength consistent with theoritical, expected values. However, in mode 4 and 5, it is quite clear that NEMO wavelengths are shorter that the ones from T-UGOm simulations. This is of some surprise, as diffusion could alter the horizontal

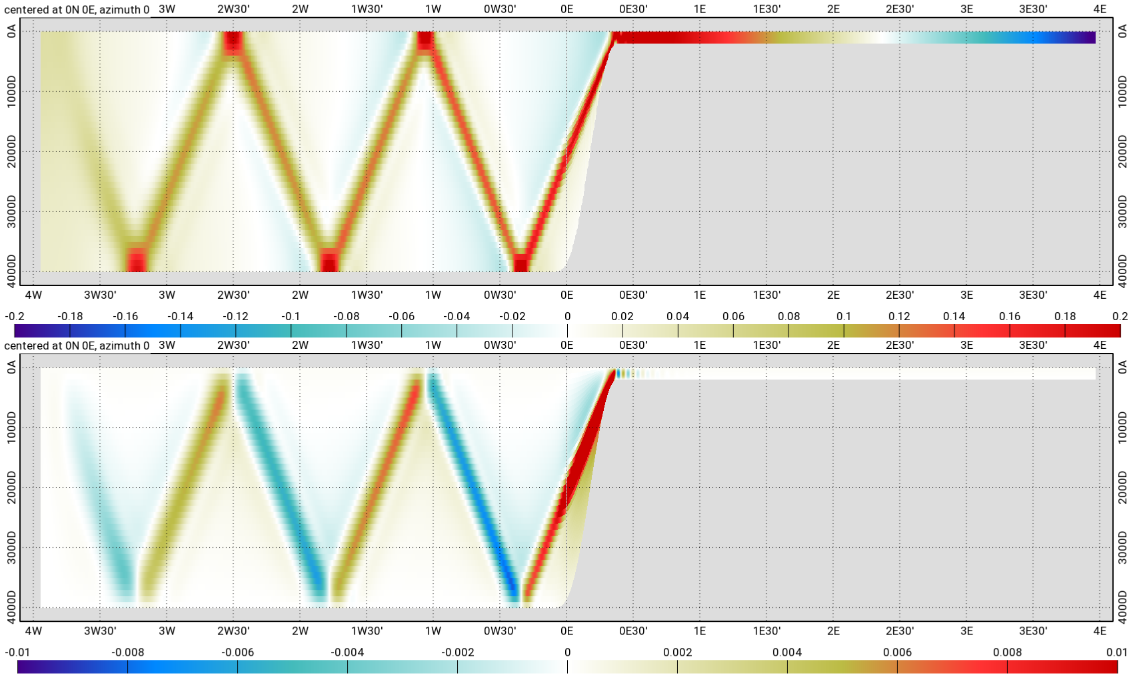

Figure 6.6: Viscous ($k_v = 5e^{-2}$) T-UGOm instantaneous horizontal velocity (top) vertical velocity(bottom). Units are m/s

wave-number, but not by increasing it (i.e. by shortening the horizontal wavelengths) but the reverse. This is an issue that would need further investigations in NEMO simulations.

Mode 1 coefficient amplitude show some oscillation above the abyssal plain, in NEMO and T-UGOm solution. It is due to the combination of a (strong) westward propagating wave with a (weak) eastward propagating wave. In absence of internal tide generation at the western boundary, the eastward component must arise from a reflection of the westward component. Actually, mode 1 horizontal wavelength is about 160 kilometers, comparable to the relaxation buffer zone, and therefore is not fully damped before reaching the domain limit. Mode 2 wave, which horizontal wavelength is half of the one of mode 1, shows much reduced reflection effect, and higher modes are clearly free of wave reflecting effects. This is also the case for all modes traveling onto the shelf part of the domain, because their horizontal wave length are about 20 times lower than over the abyssal plain, hence the ratio wavelength/buffer zone extent is much smaller, and damping is consequently much more efficient.

Reconstitution (i.e. multiplicative combination of modal coefficient with vertical modes profiles) of 3D modal harmonic velocity u, from T-UGOm solution, is shown in Figures 6.8. The barotropic mode is close to what would be expected from a uniform density simulation, with velocity amplitude being of a few centimeters per seconds on the abyssal plain and then increasing to reach about 50 cm/s on the shelf part of the domain. Baroclinic modes show

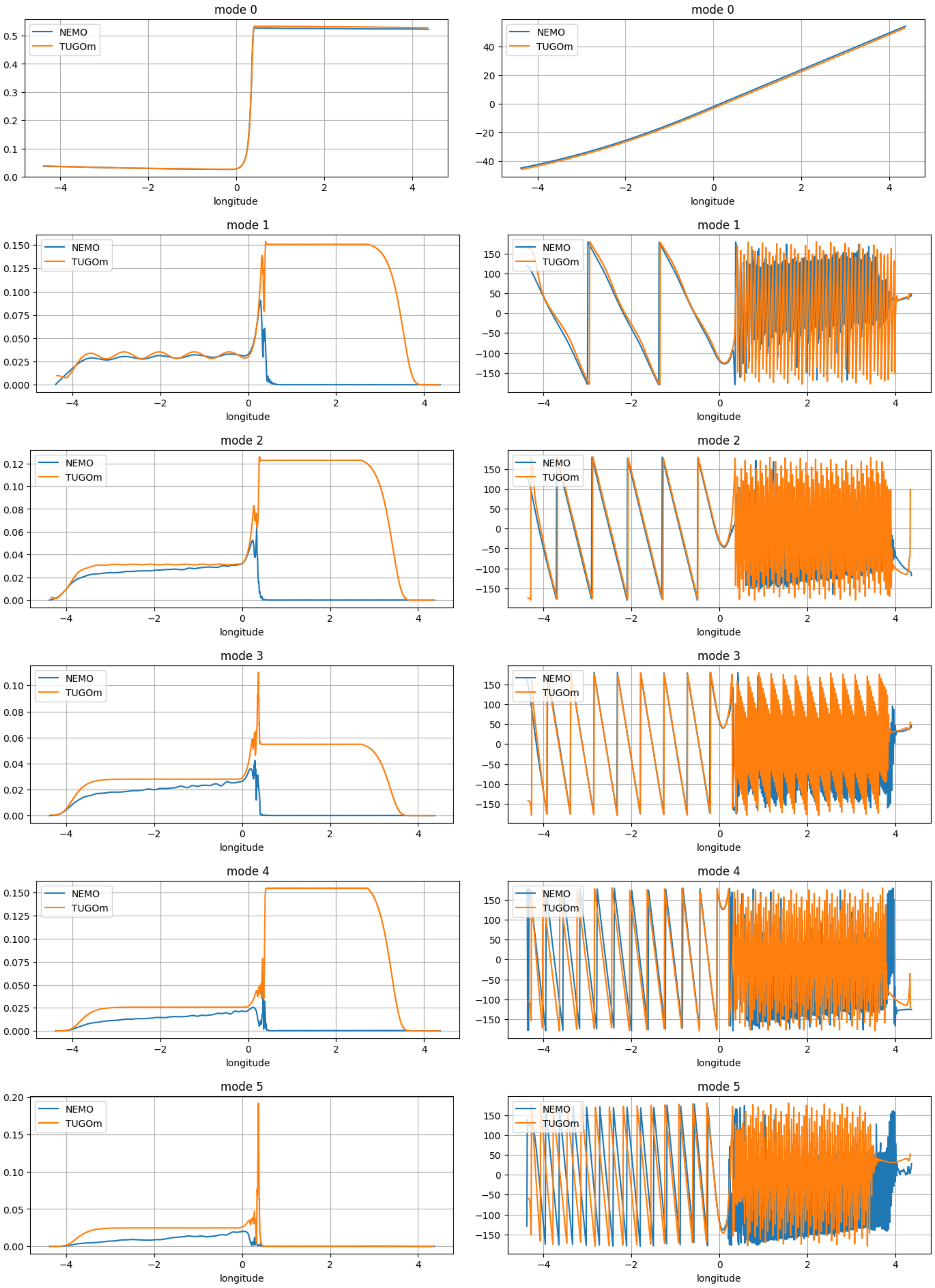

Figure 6.7: Modal decomposition coefficients for NEMO and T-UGOm horizontal velocity. Amplitude (m/s) on the left, phase lag (degrees) on the right.

amplitude ranging from a few cm/s up to 5 cm/s on the abyssal plain (hence greater than the barotropic one) and also show amplification on the shelf. The strong decrease close to the western and eastern boundaries are due to the relaxation term. As mentioned in earlier sections, first baroclinic mode amplitude shows some variations from the generation spot toward the western boundary, and its amplitude not totally vanishing there, showing insufficient damping and wave reflection effects.

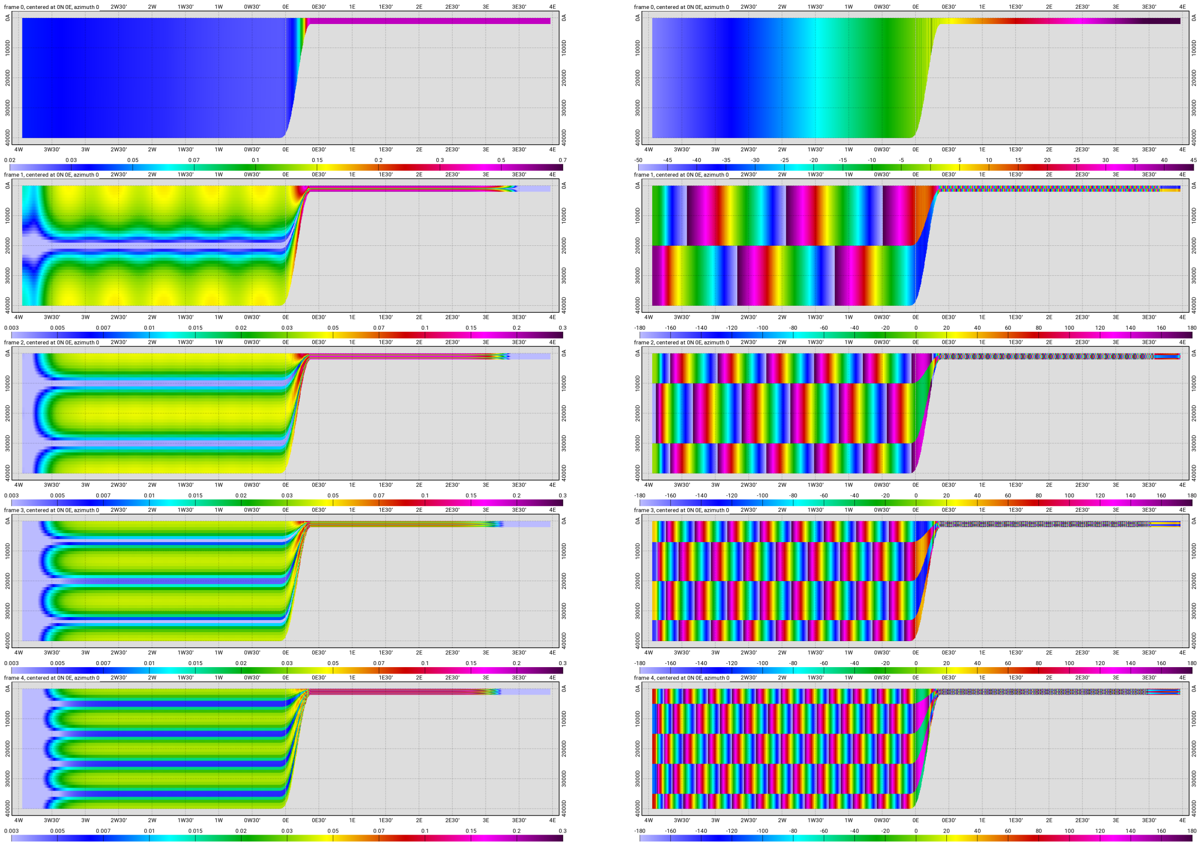

Figure 6.8: S2 horizontal velocity modal decomposition for NEMO solutions, (left) amplitude (m/s), (right) phase lag (degrees). From mode 0 (top) to mode 4 (bottom)

6.7.4 Energy budget

As internal tide beams have the same angle independently of mode number, the global beam will show a focused beam, at least if diffusion is not at work. Most of the internal tide generation clearly takes place in the upper part of the continental slope. As N and slope being uniform, highest generation will occur where barotropic vertical velocity is maximum, i.e. where horizontal velocity get accelerated by topography constriction.

Time averaged energy budget provides a synthetic view of the tidal dynamics. It can be used to highlight physical processes, such as the internal tide generation mechanisms, but also can reveal some numerical properties of the models. The first step consists in separating the tidal solutions into barotropic and baroclinic components, using vertical modes decomposition. The COMODO test case is frictionless, and most of the present numerical models can easily reproduce this constraint. It is also aimed to be diffusion-less, this condition being more difficult to respect as first numerical schemes can be implicitly diffusive, and some minimal vertical diffusion might be necessary to guarantee the numerical stability.

In the ideal conditions, total energy fluxes, which is the sum of the barotropic and baroclinic energy fluxes by virtue of modes orthogonality (see Eq. 6.44), and which divergence do balance dissipation terms, hence being null, should be preserved untouched in the whole domain. Consequently, barotropic and baroclinic energy fluxes should remain constant along the wave propagation, except at the continental slope (where barotropic energy is converted into baroclinic energy) and inside the relaxation buffer zone, where baroclinic energy fluxes must decrease vanish. At internal tide generation site, the barotropic energy conversion (Eq. 6.42) must match the divergence of barotropic energy flux and hence be the inverse of baroclinic energy divergence.

Let us examine NEMO solution. The amplitude of depth-integrated barotropic and baroclinic energy fluxes are shown on Figure 6.9 (bottom topography has been added to localize energy conversion). Looking at baroclinic energy fluxes, it is negative over the abyssal plain (hence energy is traveling from the generation site toward the western boundary where it is disspated by the relaxation term) and uniformly zero above the shelf (consistently with NEMO snapshots displayed in earlier section). The baroclinic energy flux is created at the upper part of the slope and reaches $7.1 W m^{-1}$. Barotropic energy flux is positive (hence energy is traveling from the western boundary toward the eastern boundary), with a sudden drop of $8.3 W m^{-1}$ above internal tide generation site. Both numbers (internal tide energy gain and barotropic energy loss) should match in a dissipation-less simulation, but they do not match exactly in the case of NEMO, indicating that some numerical and/or physical dissipation occurs. This is confirmed as one can observe a significant energy fluxes decrease from slope toward the abyssal limit in NEMO's solution. More worrying, one can also notice a significant and continuous decrease of the barotropic energy flux travelling from the western boundary toward the eastern boundary. As no bottom friction applies, this loss of energy, notably on the shelf part of the domain, must be linked with numerical dissipation. Horizontal or vertical diffusion can be at work, but this seems quite unlikely, especially as conditions for significant diffusion are physi-

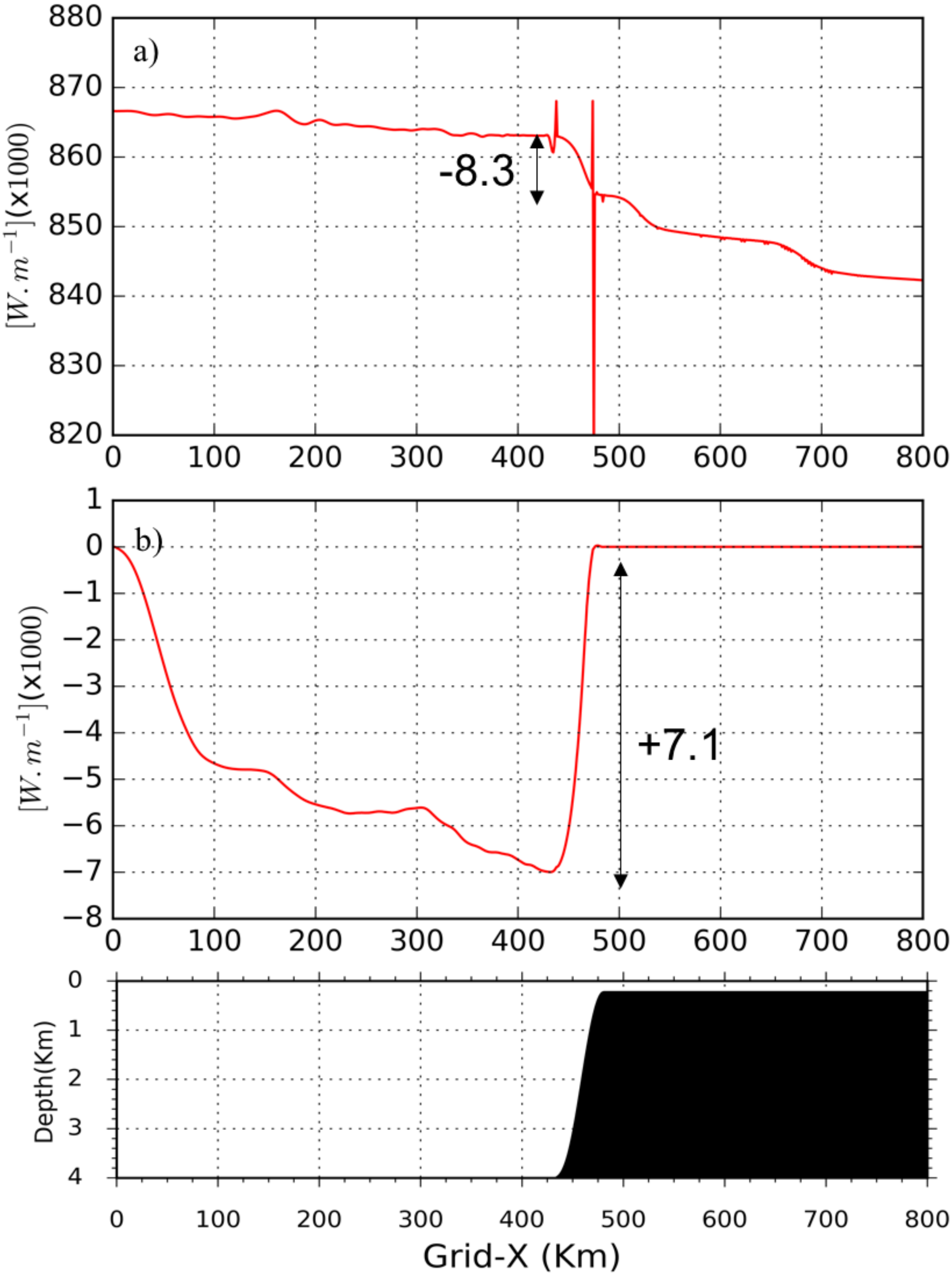

Figure 6.9: Tidally averaged, depth integrated energy flux in x-direction. (a) Barotropic flux, (b) internal tides flux. Units are Wm^{-1}

cally not met on flat bottom portions of the domain for barotropic dynamics. The best suspect might be the 2D/3D coupling scheme implied by the NEMO's time splitting.

Fig. 6.10 shows the spatial distribution of internal tide (baroclinic) energy production term and the divergence of depth-integrated barotropic and baroclinic energy fluxes. Again both shoud match exactly except in relaxation buffer zones. It is nearly the case, which capture slightly less energy than barotropic mode are producing at peak generation location. Negative divergence on the abyssal plain is due to baroclinic energy loss mentioned in the above paragraph. A schematic view of the energy budget, computed from the NEMO solution, is summarized in Figure 6.11.

On Fig. 6.12, we compare energy diagnostics of both T-UGOm and NEMO. Both are comparable, however the T-UGOm solution does not show barotropic nor baroclinic energy erosion along propagation, at no surprise as it can be solved in a true diffusion-less mode. To illustrate of what would be the effects of vertical diffusion, the diffusive T-UGOm solution diagnostics has been also plotted. It is interesting to notice that, first T-UGOm diffusive and non-diffusive barotropic fluxes are indistinguishable for barotropic fluxes, and second that T-UGOm diffusive baroclinic fluxes tends to resemble NEMO's fluxes.

To complete the discussion upon energy budget, it is interesting to examine the barotropic energy sink effect on the barotropic sea surface elevation. Fig. 6.13 displays the sea surface amplitude for the homogeneous density solution and the uniform Brünt-Vaissala solution. In the first solution, in absence of stratification, no internal tide can developped. In the second solution, a clear drop of amplitude (hence of potential energy) can be seen above the internal tide generation area. This drop of amplitude not only depicts the consequence of barotropic energy conversion, but also shows that small scales changes can appear in barotropic tides amplitude above the internal tide generation area. This is something to remember when trying to isolate barotropic and baroclinic sea surface signatures by using horizontal scales filtering.

6.7.5 Modal decomposition versus depth-averaging decomposition

In the preceding section, the separation of barotropic and baroclinic quantities has been operated by modal separation (i.e. the barotopic mode is identified as the modal "fast" component, and the baroclinic mode is the summation of any other "slow" modes). Another approach, widely used in literature, consists in assuming that the barotropic dynamics obey the depth-integrated Navier-Stokes equations. The baroclinic dynamics is then deduced by make the difference between 3D dynamics and the so-obtained barotropic one.

Differences between the two approaches can be considered as subtle, and to some extent both methods differ only by the choice of a weighting function in vertical integration operator. However, the modal separation should be preferred for two reasons. First, it is based upon truly dynamical considerations on wave celerity. Second, it opens the way to investigate more precisely the internal tides properties, this means not only offering a simple barotropic versus baroclinic separation but also a full modal separation. As length scales of modes spread on a great range, it allows to examine not only the physical contents but also the numerical characteristics of models at those various length scale. Of course, depth-averaging approach is often chosen because its great simplicity and effortless workout, and vertical modes are not proven to be pertinent in sloping topography regions. However, depth-averaging approach can be awfully misleading when investigating some details that need a rigorous methodology to be properly captured. As an example, Fig. 6.14 shows the depth-integrated baroclinic energy flux computation based on modal and averaging separation techniques.

While the modal separation diagnostics show the expected uniform barotropic and baroclinic fluxes above the abyssal plain (ot of the relaxation buffer zone), the depth-averaging separation diagnostics show anomalous (and compensating) oscillations that would lead to the conclusion that barotropic and baroclinic modes exchange energy in flat bottom conditions. There are no mechanism to do so in T-UGOm (friction-less and diffusion-less) solutions. This is the sign that barotropic and baroclinic dynamics are not properly separated by depth-averaging separation. The oscillations amplitude reaches less than 10 per cent of the baroclinic energy flux value, which is not so bad at first glance, but it will blur any defect in the model numerics. And testing model numerics are what test cases are made for.

6.8 Conclusions

Internal tides simulations have been successfully achieved from the NEMO and T-UGOm numerical codes. Results from both models are quite similar, still showing some significant differences The diffusion-free T-UGOm solutions are much noisier than NEMO ones, which reversely are somehow too smooth. For the latter, it seems that explicit vertical diffusion plus some numerical implicit diffusion are responsible for NEMO smooth solutions. The examination of the baroclinic energy flux in NEMO solution indicates a clear baroclinic energy decrease from the generation region (continental slope) toward the abyssal domain limit. The decrease of barotropic energy from the western open limit, both above the abyssal plain and shelf, is even more striking in a frictionless context. The cause of barotropic energy dissipation is not known, but might be linked to the time-splitting technique used in NEMO.

Despite inherent limitations, mostly linked to linearization, vertical modes are a powerful tool to decompose and analyze internal tides simulations and to provide a deep insight in the model through time-averaged energy examination. Proper vertical modes computation and model decomposition need a careful approach, as energy-related quantities are quite sensitive to numerical details.

In this test case, the separation of barotropic and baroclinic quantities has been operated by modal separation (i.e. the barotopic mode is identified as the modal ”fast” component, and the baroclinic mode is the summation of any other ”slow” modes). We have compared this separation approach with the usual depth-averaging approach. At first glance, differences are limited, the most significant being associated with energy quantities. For instance, depth-averaging technique is showing some unrealistic features in energy fluxes estimates, comparably to what was found in Kelly et al., 2010 investigations. But in the perspective of using energy budget to investigate (and hopefully correct) numerical deficiencies, we do want to emphasize that the modal approach should be preferred as it is more physically consistent, despite increased complexity.

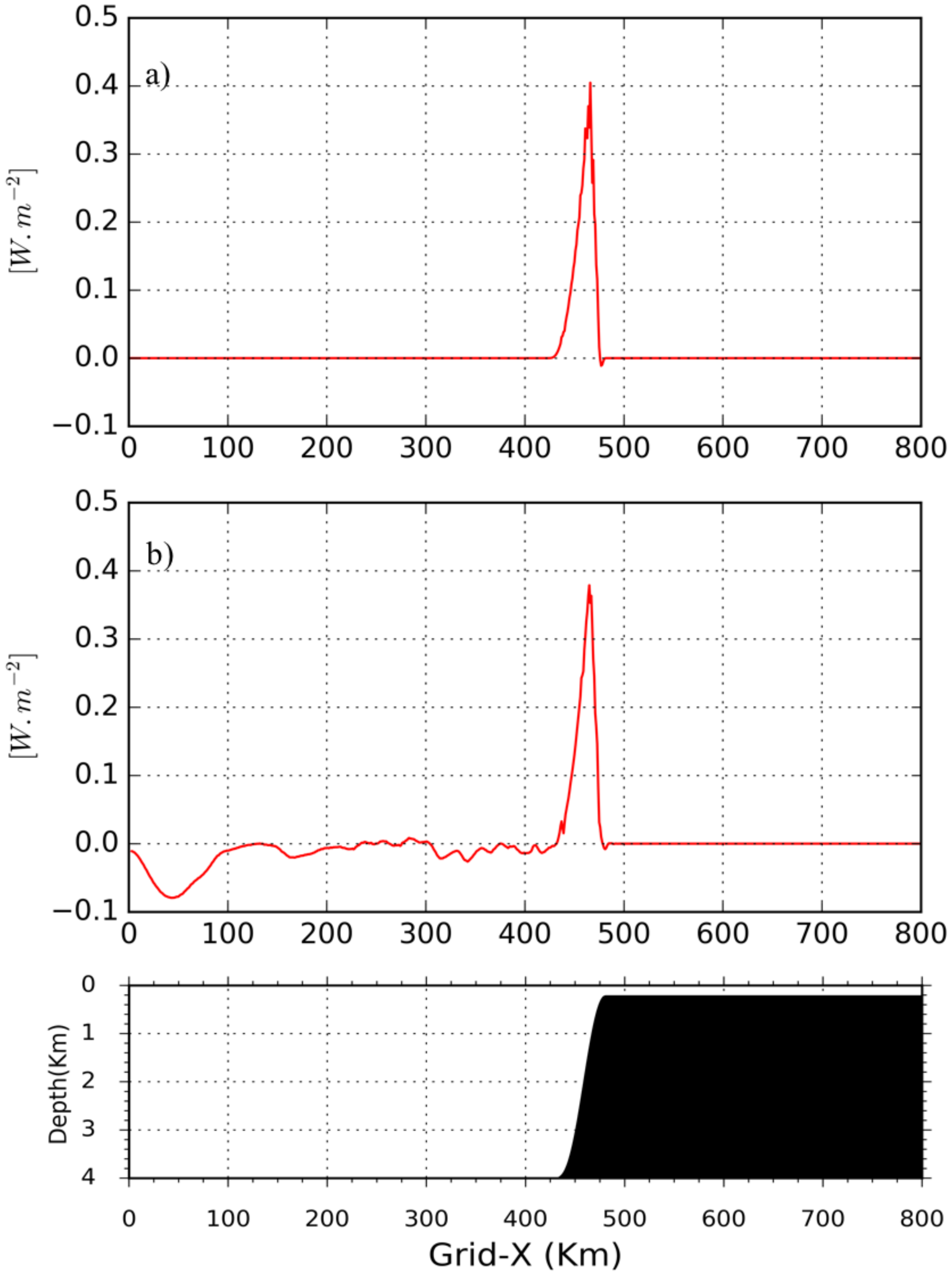

Figure 6.10: Tidally averaged depth integrated energy fluxes for NEMO. (a) Conversion, (b) Internal tides flux divergence. Units are Wm^{-2}

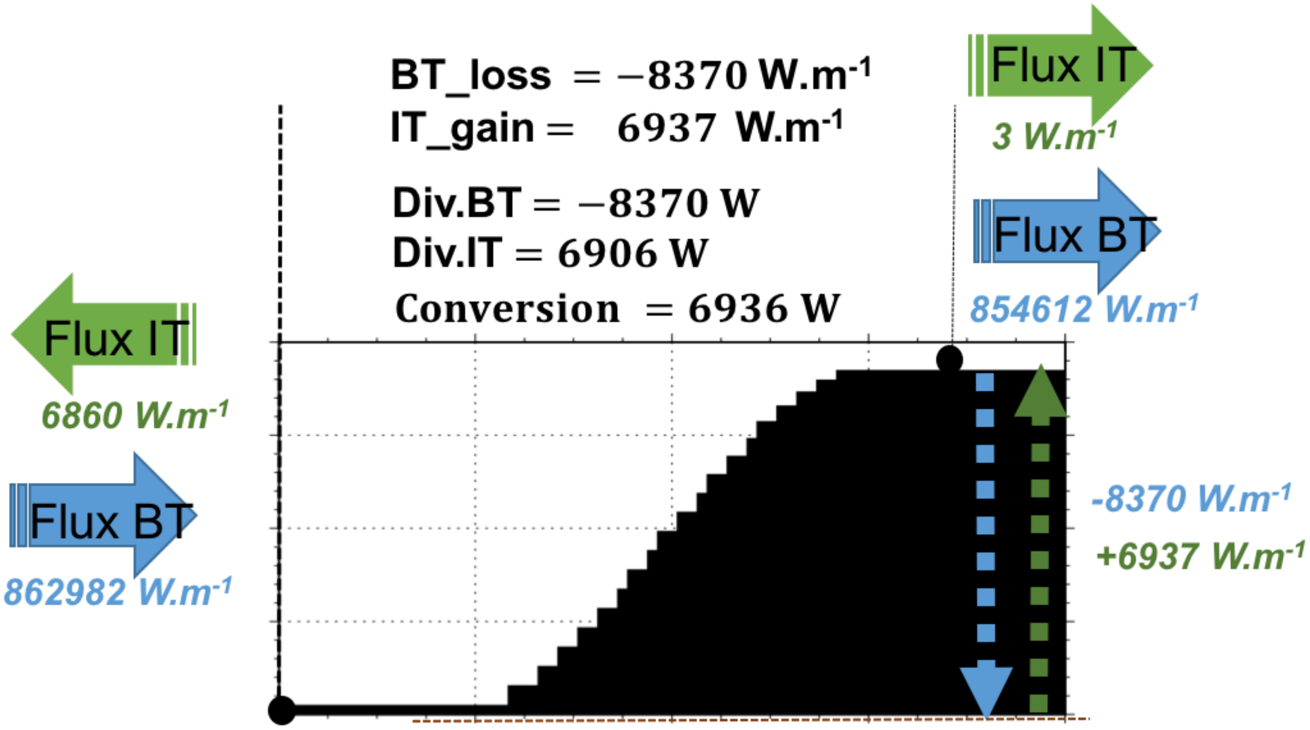

Figure 6.11: Diagrams of the internal tides energy budget above the ridge. The Conversion, $\nabla \cdot F_{bt}$, $\nabla \cdot F_{bc}$ and $Diss$ denote the area-integrated conversion rate from barotropic to baroclinic tidal energy, divergence of barotropic and baroclinic energy flux, and dissipation rate of the baroclinic energy (GW), respectively.

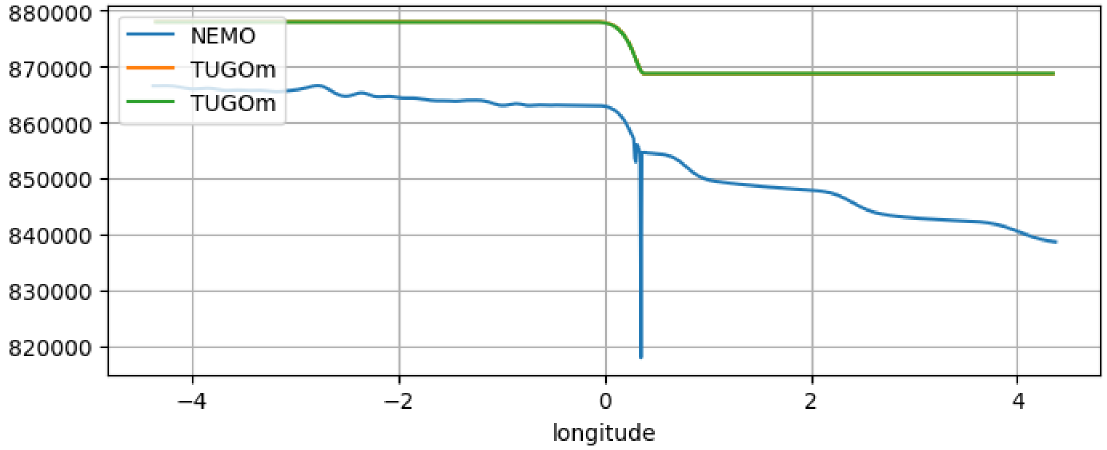

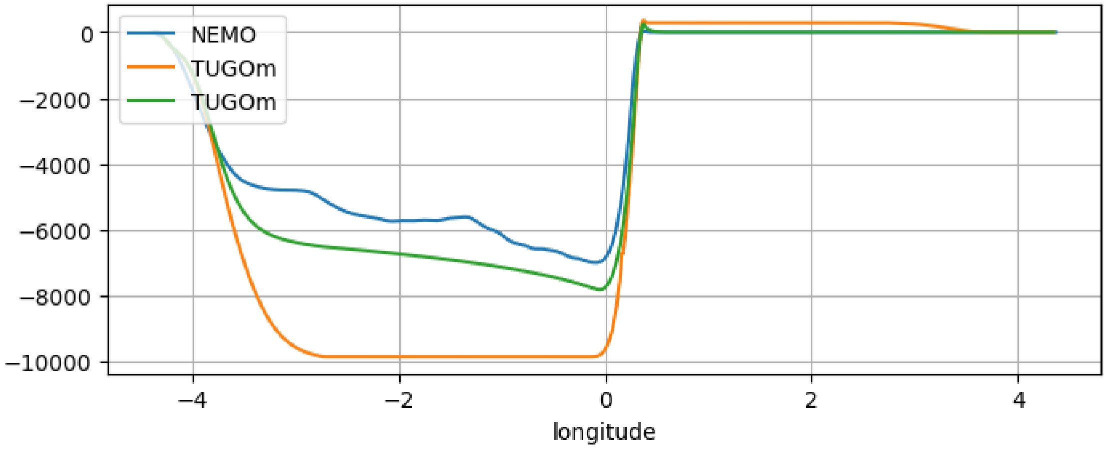

Figure 6.12: Comparison of barotropic flux (top) and baroclinic flux(bottom) for NEMO (blue lines), TUGO without diffusion(red lines) and TUGO with ($k_v = 5e^{-2}$) diffusion(green lines). Units are Wm^{-1}

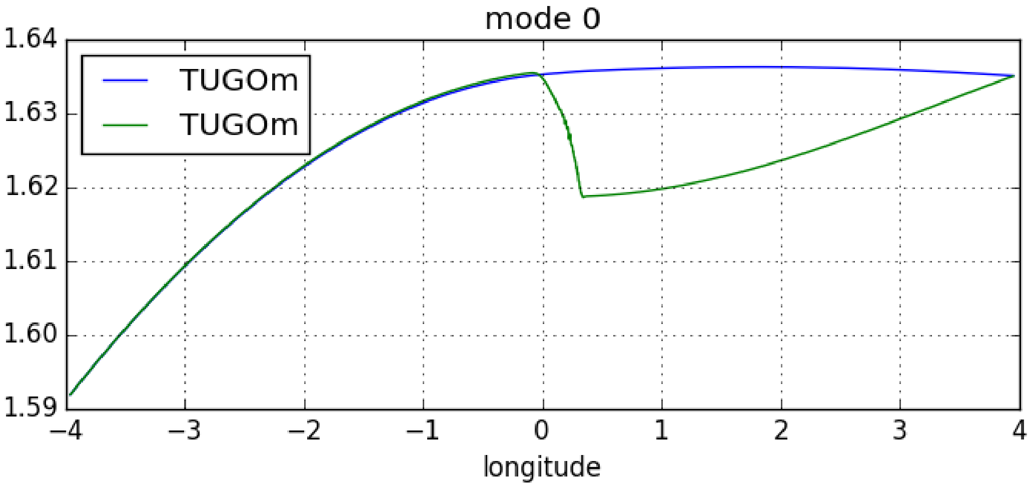

Figure 6.13: S2 free surface, mode 0 (barotropic) amplitude. T-UGOm uniform density simulation (blue) and uniform N simulation (test case) (green))

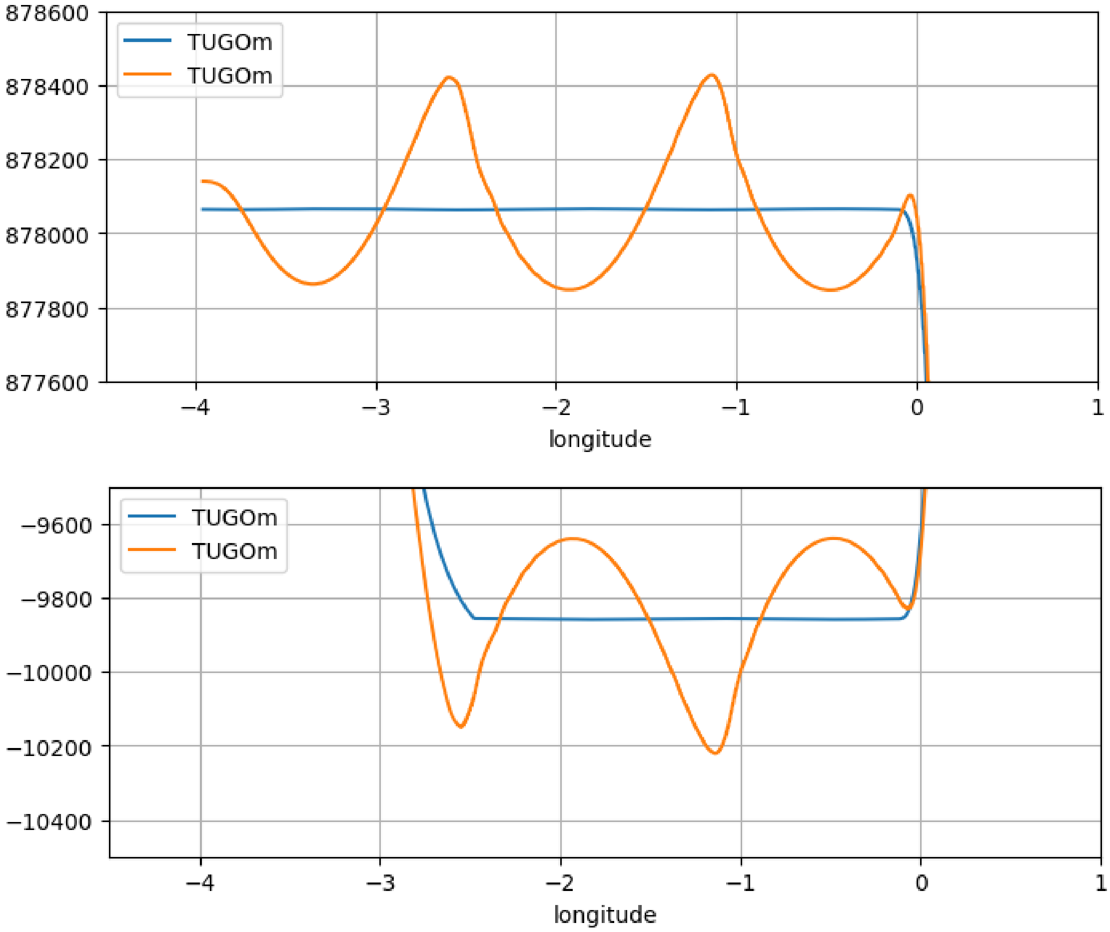

Figure 6.14: T-UGOm solution, comparison of barotropic depth-integrated x-flux (top) and baroclinic x-flux (bottom) from average method (red lines) and vertical modes decomposition (blue lines). Units are Wm^{-1}

Bibliography

Aiki, H., Matthews, J. P., and Lamb, K. G. (2011). Modeling and energetics of tidally generated wave trains in the Lombok Strait: Impact of the Indonesian Throughflow. *Journal of Geophysical Research: Oceans*, 116(3):1–17.

Aldrian, E. and Dwi Susanto, R. (2003). Identification of three dominant rainfall regions within Indonesia and their relationship to sea surface temperature. *International Journal of Climatology*, 23(12):1435–1452.

Alford, M. H., Gregg, M. C., and Ilyas, M. (1999). Diapycnal mixing in the Banda Sea: Results of the first microstructure measurements in the Indonesian Throughflow. *Geophysical Research Letters*, 26(17):2741.

Alford, M. H., MacKinnon, J. a., Nash, J. D., Simmons, H., Pickering, A., Klymak, J. M., Pinkel, R., Sun, O., Rainville, L., Musgrave, R., Beitzel, T., Fu, K.-H., and Lu, C.-W. (2011). Energy Flux and Dissipation in Luzon Strait: Two Tales of Two Ridges. *Journal of Physical Oceanography*, 41(11):2211–2222.

Alford, M. H., Peacock, T., MacKinnon, J. a., Nash, J. D., Buijsman, M. C., Centuroni, L. R., Chao, S.-Y., Chang, M.-H., Farmer, D. M., Fringer, O. B., Fu, K.-H., Gallacher, P. C., Graber, H. C., Helfrich, K. R., Jachec, S. M., Jackson, C. R., Klymak, J. M., Ko, D. S., Jan, S., Johnston, T. M. S., Legg, S., Lee, I.-H., Lien, R.-C., Mercier, M. J., Moum, J. N., Musgrave, R., Park, J.-H., Pickering, A. I., Pinkel, R., Rainville, L., Ramp, S. R., Rudnick, D. L., Sarkar, S., Scotti, A., Simmons, H. L., St Laurent, L. C., Venayagamoorthy, S. K., Wang, Y.-H., Wang, J., Yang, Y. J., Paluszkiewicz, T., and (David) Tang, T.-Y. (2015). The formation and fate of internal waves in the South China Sea. *Nature*, 521(7550):65–69.

Allen, G. R. and Werner, T. B. (2002). Coral reef fish assessment in the 'coral traingle' of Southeastern Asia. *Environmental Biology of Fishes*, 65:209–214.

Arbic, B. K., Richman, J. G., Shriver, J. F., Timko, P. G., Metzger, E. J., and Wallcraft, A. J. (2012). Global modeling of internal tides within an eddying ocean general circulation model. *Oceanography*, 25(2):20–29.

Arbic, B. K., Wallcraft, A. J., and Metzger, E. J. (2010). Concurrent simulation of the eddying general circulation and tides in a global ocean model. *Ocean Modelling*, 32(3-4):175–187.

Aumont, O. (2004). PISCES biogeochemical model WARNING : This document is not intended to be an exhaustive description of PISCES and is still incomplete. pages 1–16.

Baines, P. (1982). On internal tide generation models. *Deep Sea Research Part A. Oceanographic Research Papers*, 29(3):307–338.

Baines, P. G. (1973). The generation of internal tides by fiat-bump topography. 20(February 1972):179–205.

Buijsman, M., Arbic, B., Green, J., Helber, R., Richman, J., Shriver, J., Timko, P., and Wallcraft, a. (2015). Optimizing internal wave drag in a forward barotropic model with semidiurnal tides. *Ocean Modelling*, 85:42–55.

Carrere, L. (2012). A new global tidal model taking taking advantage of nearly 20 years of altimetry. *Proceedings of meeting "20 Years of Altimetry"*.

Carrere, L., Lyard, F., Cancet, M., Guillot, A., and Picot, N. (2016). FES 2014, a new tidal model - Validation results and perspectives for improvements, presentation to ESA Living Planet Conference. Technical report, Prague.

Carter, G., Fringer, O., and Zaron, E. (2012). Regional Models of Internal Tides. *Oceanography*, 25(2):56–65.

Carter, G. S., Merrifield, M. a., Becker, J., and Gregg, M. C. (2008). Energetics of M 2 Barotropic to Baroclinic tidal conversion at the Hawaiian Islands. *Journal of Physical Oceanography*, 38:2205–2223.

Castruccio, F. S., Curchitser, E. N., and Kleypas, J. a. (2013). A model for quantifying oceanic transport and mesoscale variability in the Coral Triangle of the Indonesian/Philippines Archipelago. *Journal of Geophysical Research: Oceans*, 118(11):6123–6144.

Chang, C. P., Wang, Z., McBride, J., and Liu, C. H. (2005). Annual cycle of Southeast Asia - Maritime continent rainfall and the asymmetric monsoon transition. *Journal of Climate*, 18(2):287–301.

Chao, S.-Y., Ko, D. S., Lien, R.-C., and Shaw, P. T. (2007). Assessing the West Ridge of Luzon Strait as an Internal. *Journal of Oceanography*, 63(2004):897–911.

Clement, A. C., Seager, R., and Murtugudde, R. (2005). Why are there tropical warm pools? *Journal of Climate*, 18(24):5294–5311.

da Silva, J., New, A., Srokosz, M., and Smyth, T. (2002). On the observability of internal tidal waves in remotely-sensed ocean colour data. *Geophysical Research Letters*, 29(12):10–13.

Eden, C., Czeschel, L., and Olbers, D. (2014). Toward Energetically Consistent Ocean Models. *Journal of Physical Oceanography*, 44(12):3160–3184.

Egbert, G. D. and Erofeeva, S. Y. (2002). Efficient inverse modeling of barotropic ocean tides. *Journal of Atmospheric and Oceanic Technology*, 19(2):183–204.

Egbert, G. D. and Ray, R. D. (2001). Estimates of \mathrm{M_2} tidal energy dissipation from {TOPEX/Poseidon} altimeter data. *J. Geophys. Res.*, 106(C10):22,422–475,502.

Ffield, A. and Gordon, A. L. (1992). Vertical Mixing in the Indonesian Thermocline.

Ffield, A. and Gordon, A. L. (1996). Tidal Mixing Signatures in the Indonesian Seas.

Ffield, A. and Robertson, R. (2008). Temperature finestructure in the Indonesian seas. *Journal of Geophysical Research: Oceans*, 113(9):1–19.

Fieux, M., Andrié, C., Delecluse, P., Ilahude, A. G., Kartavtseff, A., Mantisi, F., Molcard, R., and Swallow, J. C. (1994). Measurements within the Pacific-Indian oceans throughflow region. *Deep-Sea Research Part I*, 41(7):1091–1130.

Franks, P. J. and Chen, C. (1996). Plankton production in tidal fronts: A model of Georges Bank in summer. *Journal of Marine Research*, 54(4):631–651.

Gerkema, T. and van Haren, H. (2007). Internal tides and energy fluxes over Great Meteor Seamount. *Ocean Science Discussions*, 4:371–398.

Godfrey, J. S. (1996). The effect of the Indonesian throughflow on ocean circulation and heat exchange with the atmosphere: A review. *Journal of Geophysical Research*, 101(C5):12217.

Gordon, A. (2005). Oceanography of the Indonesian Seas. *Oceanography*, 18(4):13–13.

Gordon, A. L. (1986). Interocean exchange of thermocline water. *J. Geophys. Res.*, 91(6):5037–5046.

Gordon, A. L. and Fine, R. a. (1996). Pathways of water between the Pacific and Indian oceans in the Indonesian seas.

Gordon, A. L., Giulivi, C. F., and Ilahude, A. G. (2003). Deep topographic barriers within the Indonesian seas. *Deep-Sea Research Part II: Topical Studies in Oceanography*, 50(12-13):2205–2228.

Gordon, a. L., Sprintall, J., Van Aken, H. M., Susanto, D., Wijffels, S., Molcard, R., Ffield, a., Pranowo, W., and Wirasantosa, S. (2010). The Indonesian throughflow during 2004-2006 as observed by the INSTANT program. *Dynamics of Atmospheres and Oceans*, 50(2):115–128.

Hatayama, T. (2004). Transformation of the Indonesian throughflow water by vertical mixing and its relation to tidally generated internal waves. *Journal of Oceanography*, 60(3):569–585.

Hautala, S. L., Sprintall, J., Potemra, J. T., Chong, J. C., Pandoe, W., Bray, N., and Ilahude, a. G. (2001). Velocity structure and transport of the Indonesian Throughflow in the major straits restricting flow into the Indian Ocean. *Journal of Geophysical Research*, 106(C9):19527.

Holloway, G. and Denman, K. (1989). Influence of internal waves on primary production. *Journal of Plankton Research*, 11(2):409–413.

Holloway, P. E. (1996). A Numerical Model of Internal Tides with Application to the Australian North West Shelf.

Jackson, C. (2007). Internal wave detection using the Moderate Resolution Imaging Spectroradiometer MODIS. *Journal of Geophysical Research*, 112(C11):C11012.

Jan, S. and Chen, C. T. A. (2009). Potential biogeochemical effects from vigorous internal tides generated in Luzon Strait: A case study at the southernmost coast of Taiwan. *Journal of Geophysical Research: Oceans*, 114(4):1–14.

Jan, S., Chern, C. S., Wang, J., and Chao, S. Y. (2007). Generation of diurnal K1 internal tide in the Luzon Strait and its influence on surface tide in the South China Sea. *Journal of Geophysical Research: Oceans*, 112(6):1–13.

Jan, S., Lien, R. C., and Ting, C. H. (2008). Numerical study of baroclinic tides in Luzon Strait. *Journal of Oceanography*, 64(5):789–802.

Jeon, C., Park, J.-h., Varlamov, S. M., Yoon, J.-h., Kim, Y. H., Seo, S., Park, Y.-g., Min, H. S., Lee, J. H., and Kim, C.-h. (2014). Journal of Geophysical Research : Oceans. *Journal of Geophysical Research: Oceans*, 119:2843–2859.

Jochum, M. and Potemra, J. (2008). Sensitivity of tropical rainfall to Banda Sea diffusivity in the Community Climate System Model. *Journal of Climate*, 21(23):6445–6454.

Johnston, T. M. S., Rudnick, D. L., Alford, M. H., Pickering, A., and Simmons, H. L. (2013). Internal tidal energy fluxes in the South China Sea from density and velocity measurements by gliders. *JOURNAL OF GEOPHYSICAL RESEARCH: OCEANS*, 118:3939–3949.

Jouanno, J., Capet, X., Madec, G., Roullet, G., Klein, P., and Masson, S. (2016). Dissipation of the energy imparted by mid-latitude storms in the\r\nSouthern Ocean. *Ocean Science Discussions*, pages 1–49.

Kang, D. (2010). Energetics and Dynamics of Internal Tides in Monterey Bay Using Numerical Simulations a Dissertation Submitted To the Department of Civil and Environmental Engineering and the Committee on Graduate Studies of Stanford University in Partial Fulfillment of. (November):170.

Kang, D. and Fringer, O. (2012a). Energetics of Barotropic and Baroclinic Tides in the Monterey Bay Area. *Journal of Physical Oceanography*, 42(2):272–290.

Kang, D. and Fringer, O. (2012b). Energetics of Barotropic and Baroclinic Tides in the Monterey Bay Area. *Journal of Physical Oceanography*, 42(2):272–290.

Kartadikaria, a. R., Miyazawa, Y., Varlamov, S. M., and Nadaoka, K. (2011). Ocean circulation for the Indonesian seas driven by tides and atmospheric forcings: Comparison to observational data. *Journal of Geophysical Research: Oceans*, 116(9):1–21.

Kawamura, R. and Matsuura, T. (2003). A mechanism of the onset of the South Asian summer monsoon. 81:563–580.

Kelly, S. M. and Nash, J. D. (2010). Internal-tide generation and destruction by shoaling internal tides. *Geophysical Research Letters*, 37(23):1–5.

Kelly, S. M. and Nash, J. D. (2011). Reply to comment by T. Gerkema on “Internal-tide energy over topography”. *Journal of Geophysical Research*, 116(C9):2010–2012.

Kelly, S. M., Nash, J. D., and Kunze, E. (2010). Internal-tide energy over topography. *Journal of Geophysical Research: Oceans*, 115(6):1–13.

Kelly, S. M., Nash, J. D., Martini, K. I., Alford, M. H., and Kunze, E. (2012). The Cascade of Tidal Energy from Low to High Modes on a Continental Slope. *Journal of Physical Oceanography*, 42(7):1217–1232.

Kerry, C. G., Powel, B. S., and Carter, G. S. (2013). Effects of Remote Generation Sites on Model Estimates of M 2 Internal Tides in the Philippine Sea *. pages 187–204.

Khatiwala, S. (2003). Generation of internal tides in an ocean of finite depth: Analytical and numerical calculations. *Deep-Sea Research Part I: Oceanographic Research Papers*, 50(1):3–21.

Kida, S. and Richards, K. J. (2009). Seasonal sea surface temperature variability in the Indonesian Seas. *Journal of Geophysical Research: Oceans*, 114(6):1–17.

Kida, S. and Wijffels, S. (2012). The impact of the Indonesian Throughflow and tidal mixing on the summertime sea surface temperature in the western Indonesian Seas. *Journal of Geophysical Research: Oceans*, 117(9):1–14.

Koch-Larrouy, A., Atmadipoera, A., van Beek, P., Madec, G., Aucan, J., Lyard, F., Grelet, J., and Souhaut, M. (2015). Estimates of tidal mixing in the Indonesian archipelago from multidisciplinary INDOMIX in-situ data. *Deep-Sea Research Part I: Oceanographic Research Papers*, 106:136–153.

Koch-Larrouy, A., Lengaigne, M., Terray, P., Madec, G., and Masson, S. (2010). Tidal mixing in the Indonesian seas and its effect on the tropical climate system. *Climate Dynamics*, 34(6):891–904.

Koch-Larrouy, A., Madec, G., Bouruet-Aubertot, P., Gerkema, T., Bessières, L., and Molcard, R. (2007). On the transformation of Pacific Water into Indonesian Throughflow Water by internal tidal mixing. *Geophysical Research Letters*, 34(4):1–6.

Koch-Larrouy, A., Madec, G., Iudicone, D., Atmadipoera, A., and Molcard, R. (2008). Physical processes contributing to the water mass transformation of the Indonesian throughflow. *Ocean Dynamics*, 58(3-4):275–288.

Kundu, P., Cohen, M. I., and Hu, H. H. (2004). *Fluid mechanics*. Elsevier Academic Press, Amsterdam.

Kunze, E., Rosenfeld, L. K., Carter, G. S., and Gregg, M. C. (2002). Internal Waves in Monterey Submarine Canyon. *Journal of Physical Oceanography*, 32(6):1890–1913.

Kurapov, A. L., Egbert, G. D., Allen, J. S., Miller, R. N., Erofeeva, S. Y., and Kosro, P. M. (2003). The M 2 Internal Tide off Oregon: Inferences from Data Assimilation. *Journal of Physical Oceanography*, 33(8):1733–1757.

Large, W. G. and Yeager, S. G. (2004). Diurnal to decadal global forcing for ocean and sea–ice models: {The} data sets and flux climatologies. *NCAR Tech. Note*, TN–460+ST(May):105pp.

Le Provost, C. (2003). Ocean tides after a decade of high precision satellite altimetry. *Presentation in Swt JASON 1, Arles November 18-21.*

Lee, T., Fukumori, I., Menemenlis, D., Xing, Z., and Fu, L.-L. (2002). Effects of the Indonesian Throughflow on the Pacific and Indian Oceans. *Journal of Physical Oceanography*, 32(5):1404–1429.

Lehodey, P., Senina, I., and Murtugudde, R. (2008). A spatial ecosystem and populations dynamics model (SEAPODYM) - Modeling of tuna and tuna-like populations. *Progress in Oceanography*, 78(4):304–318.

Lévy, M., Ferrari, R., Franks, P. J. S., Martin, A. P., and Rivière, P. (2012). Bringing physics to life at the submesoscale. *Geophysical Research Letters*, 39(14).

Lewis, M. R., Glen Harrison, W., Oakey, Neil, S., Hebert, D., and Platt, T. (1976). Vertical Nitrate Fluxes in the Oligotrophic Ocean. *Science*, 234:870–873.

Lorenzo, E. D. (2006). Numerical and analytical estimates of M 2 tidal conversion at steep oceanic ridges. *Journal of physical . . .* , (2001):1072–1084.

Lu, Y., Wright, D. G., and Brickman, D. (2001). Internal tide generation over topography: Experiments with a free-surface z-level ocean model. *Journal of Atmospheric and Oceanic Technology*, 18(6):1076–1091.

Lukas, R., Yamagata, T., and McCreary, J. (1996). Pacific low-latitude western boundary currents and the Indonesian throughflow. *Journal of Geophysical Research C: Oceans*, 101(5):12209–12216.

Lyard, F., Carrere, L., Cancet, M., and Guillot, A. (2017). FES2014, a new finite elements tidal model for global ocean. *Ocean Dynamics,in preparation.*

Lyard, F., Lefevre, F., Letellier, T., and Francis, O. (2006). Modelling the global ocean tides: Modern insights from FES2004. *Ocean Dynamics*, 56(5-6):394–415.

Lyard, F., Roblou, L., and Allain, D. (2012). FES 2012, 4th PROJECT MEETING. Technical report, LEGOS, Toulouse.

Madec, G. (2008). NEMO ocean engine. (27).

Maraldi, C., Lyard, F., Testut, L., and Coleman, R. (2011). Energetics of internal tides around the Kerguelen Plateau from modeling and altimetry. *Journal of Geophysical Research: Oceans*, 116(6):1–10.

Matthews, J. P., Aiki, H., Masuda, S., Awaji, T., and Ishikawa, Y. (2011). Monsoon regulation of Lombok Strait internal waves. *Journal of Geophysical Research: Oceans*, 116(5):1–14.

Mattias Green, J. a. and Nycander, J. (2012). A comparison of tidal conversion parameterizations for tidal models. *Journal of Physical Oceanography*, (2004):121015111501009.

Melet, A., Nikurashin, M., Muller, C., Falahat, S., Nycander, J., Timko, P. G., Arbic, B. K., and Goff, J. a. (2013). Internal tide generation by abyssal hills using analytical theory. *Journal of Geophysical Research: Oceans*, 118(11):6303–6318.

Meyers, G. (1996). Variation of Indonesian throughflow and the El Niño-Southern Oscillation. *Journal of Geophysical Research: Oceans*, 101(C5):12255–12263.

Mitnik, L., Alpers, W., and Hock, L. (2000). Thermal plumes and internal solitary waves generated in the Lombok strait studied by ERS SAR. *European Space Agency, (Special Publication) ESA SP*, (461):1834–1842.

Molcard, R., Fieux, M., and Syamsudin, F. (2001). The throughflow within Ombai Strait. *Deep-Sea Research Part I: Oceanographic Research Papers*, 48(5):1237–1253.

Moore, S. E. and Lien, R.-C. (2007). Pilot Whales Follow Internal Solitary Waves. *Marine Mammal Science*, 23(January):193–196.

Mora, C., Chittaro, P. M., Sale, P. F., Kritzer, J. P., Ludsin, S. a., and Africa, S. (2003). Patterns and processes in reef fish diversity. *Nature*, 421(February):933–936.

Muller, M., Cherniawsky, J. Y., Foreman, M. G. G., and Von Storch, J. S. (2012a). Global M 2 internal tide and its seasonal variability from high resolution ocean circulation and tide modeling. *Geophysical Research Letters*, 39(19):L19607.

Muller, M., Cherniawsky, J. Y., Foreman, M. G. G., and Von Storch, J. S. (2012b). Global M 2 internal tide and its seasonal variability from high resolution ocean circulation and tide modeling. *Geophysical Research Letters*, 39(19):1–6.

Murray, S. P. and Arief, D. (1988). Throughflow into the Indian Ocean through the Lombok Strait, January 1985–January 1986. *Nature*, 333(6172):444–447.

Nagai, T. and Hibiya, T. (2015). Internal tides and associated vertical mixing in the Indonesian Archipelago. *Journal of Geophysical Research C: Oceans*, pages 3373–3390.

Neale, R. and Slingo, J. (2003). The Maritime Continent and its role in the global climate: A GCM study. *Journal of Climate*, 16(5):834–848.

Niwa, Y. (2004). internal tides in the East China Sea. *Journal of Geophysical Research*, 109(C4):1–14.

Niwa, Y. and Hibiya, T. (2001a). Numerical study of the spatial distribution of the M 2 internal tide in the Pacific Ocean. 106.

Niwa, Y. and Hibiya, T. (2001b). Numerical study of the spatial distribution of the M2 internal tide in the Pacific Ocean. *Journal of Geophysical Research*, 106:22441–22449.

Niwa, Y. and Hibiya, T. (2011). Estimation of baroclinic tide energy available for deep ocean mixing based on three-dimensional global numerical simulations. *Journal of Oceanography*, 67(4):493–502.

Niwa, Y. and Hibiya, T. (2014). Generation of baroclinic tide energy in a global three-dimensional numerical model with different spatial grid resolutions. *Ocean Modelling*, 80:59–73.

Nugroho, D., Koch-Larrouy, A., Gaspar, P., Lyard, F., Reffray, G., and Tranchant, B. (2017). Modelling Explicit tides in the Indonesian seas : an important process for surface sea water properties, in revision. *Submitted to Marine Pollution Bulletin.*

Park, J.-h. and Watts, D. R. (2005). Internal Tides in the Southwestern Japan / East Sea. pages 1–37.

Pichon, A. and Maze, R. (1990). Internal Tides over a Shelf Break: Analytical Model And Observations. *American Meteorological Society*, pages 657–671.

Potemra, J. T. (1999). Seasonal Variations of Upper Ocean Transport from the Pacific to the Indian Ocean via Indonesian Straits*. *Journal of Physical Oceanography*, 29(11):2930–2944.

Rainville, L., Lee, C. M., Rudnick, D. L., and Yang, K. C. (2013). Propagation of internal tides generated near Luzon Strait: Observations from autonomous gliders. *Journal of Geophysical Research: Oceans*, 118(9):4125–4138.

Ramp, S. R., Tang, T. Y., Duda, T. F., Lynch, J. F., Liu, A. K., Chiu, C. S., Bahr, F. L., Kim, H. R., and Yang, Y. J. (2004). Internal solitons in the northeastern South China Sea Part I: Sources and deep water propagation. *IEEE Journal of Oceanic Engineering*, 29(4):1157–1181.

Ray, R., Egbert, G., and Erofeeva, S. (2005). A Brief Overview of Tides in the Indonesian Seas. *Oceanography*, 18(4):74–79.

Robertson, R. (2010). Tidal currents and mixing at the INSTANT mooring locations. *Dynamics of Atmospheres and Oceans*, 50(2):331–373.

Robertson, R. and Ffield, A. (2005). M2 Baroclinic Tides in the Indonesian Seas. *Oceanography*, 18(4):62–73.

Robertson, R. and Ffield, A. (2008). Baroclinic tides in the Indonesian seas: Tidal fields and comparisons to observations. *Journal of Geophysical Research: Oceans*, 113(7):1–22.

Sari Ningsih, N. (2008). INTERNAL WAVES DYNAMICS IN THE LOMBOK STRAIT STUDIED BY A NUMERICAL MODEL. *International Journal Of Remote Sensing And Earth Sciences*, 5.

Sasaki, H., Sasai, Y., Nonaka, M., Masumoto, Y., and Kawahara, S. (2006). An Eddy-Resolving Simulation of the Quasi-Global Ocean Driven by Satellite-Observed Wind Field – Preliminary Outcomes from Physical and Biological Fields –. *Journal of the Earth Simulator*, 6(October):35–49.

Schiller, A. (2004). Effects of explicit tidal forcing in an OGCM on the water-mass structure and circulation in the Indonesian throughflow region. *Ocean Modelling*, 6(1):31–49.

Shang, X., Liu, Q., Xie, X., Chen, G., and Chen, R. (2015). Deep-Sea Research I Characteristics and seasonal variability of internal tides in the southern South China Sea. *Deep-Sea Research Part I*, 98:43–52.

Shriver, J. F., Arbic, B. K., Richman, J. G., Ray, R. D., Metzger, E. J., Wallcraft, a. J., and Timko, P. G. (2012). An evaluation of the barotropic and internal tides in a high-resolution global ocean circulation model. *Journal of Geophysical Research: Oceans*, 117(10):1–14.

Simmons, H. L., Hallberg, R. W., and Arbic, B. K. (2004). Internal wave generation in a global baroclinic tide model. *Deep-Sea Research Part II: Topical Studies in Oceanography*, 51(25-26 SPEC. ISS.):3043–3068.

Song, Q. and Gordon, A. L. (2004). Significance of the vertical profile of the Indonesian Throughflow transport to the Indian Ocean. *Geophysical Research Letters*, 31(16).

Souza, A. J. and Pineda, J. (2001). Tidal mixing modulation of sea-surface temperature and diatom abundance in Southern California. *Continental Shelf Research*, 21(6-7):651–666.

Sprintall, J., Gordon, A. L., Koch-Larrouy, A., Lee, T., Potemra, J. T., Pujiana, K., Wijffels, S. E., and Wij, S. E. (2014). The Indonesian seas and their role in the coupled ocean–climate system. *Nature Geoscience*, 7(7):487–492.

Sprintall, J., Wijffels, S. E., Molcard, R., and Jaya, I. (2009). Direct estimates of the indonesian throughflow entering the indian ocean: 2004-2006. *Journal of Geophysical Research: Oceans*, 114(7):2004–2006.

St. Laurent, L. and Garrett, C. (2002). The Role of Internal Tides in Mixing the Deep Ocean. *Journal of Physical Oceanography*, 32(10):2882–2899.

Susanto, R. D. and Gordon, A. L. (2005). Velocity and transport of the Makassar Strait throughflow. *Journal of Geophysical Research: Oceans*, 110(1):1–10.

Susanto, R. D., Mitnik, L., and Zheng, Q. (2005). Ocean Internal Waves Observed in the Lombok Strait. *Oceanography*, 18(4):80–87.

Talley, L. D. and Sprintall, J. (2005). Deep expression of the Indonesian Throughflow: Indonesian Intermediate Water in the South Equatorial Current. *Journal of Geophysical Research C: Oceans*, 110(10):1–30.

Tranchant, B., Reffray, G., Greiner, E., Nugroho, D., Koch-Larrouy, A., and Gaspar, P. (2016). Evaluation of an operational ocean model configuration at 1/12 spatial resolution for the Indonesian seas . Part I : ocean physics. pages 1–49.

Umlauf, L. and Burchard, H. (2003). A generic length-scale equation for geophysical. *Journal of Marine Research*, 61(2):235–265.

van Aken, H. M., Brodjonegoro, I. S., and Jaya, I. (2009). The deep-water motion through the Lifamatola Passage and its contribution to the Indonesian throughflow. *Deep-Sea Research Part I: Oceanographic Research Papers*, 56(8):1203–1216.

Veron, J., Devantier, L. M., Turak, E., Green, A. L., Kininmonth, S., Stafford-Smith, M., and Peterson, N. (2009). Delineating the Coral Triangle. *Galaxea, Journal of Coral Reef Studies*, 11(2):91–100.

Vranes, K., Gordon, A. L., and Ffield, A. (2002). The heat transport of the Indonesian throughflow and implications for the Indian Ocean heat budget. *Deep-Sea Research Part II: Topical Studies in Oceanography*, 49(7-8):1391–1410.

Wang, J., Huang, W., Yang, J., and Zhang, H. (2011). The internal waves' distribution of whole South China Sea extracted from ENVISAT and ERS-2 SAR images. *Proceedings of SPIE - The International Society for Optical Engineering*, 8175:1–7.

Wang, X., Peng, S., Liu, Z., Huang, R. X., Qian, Y.-K., and Li, Y. (2016). Tidal Mixing in the South China Sea: An Estimate Based on the Internal Tide Energetics. *Journal of Physical Oceanography*, 46(1):107–124.

Wijffels, S. (2012). The impact of the Indonesian Throughflow and tidal mixing on the Seasonal Cycle of the Sea Surface Temperature in the Indonesian Seas Why Study the SST in the Indonesian Seas ? The role of Tidal mixing The role of the Indonesian Throughflow (ITF). (July 2012):6016.

Wijffels, S. E., Meyers, G., and stuart Godfrey, J. (2008). A 20-Yr Average of the Indonesian Throughflow: Regional Currents and the Interbasin Exchange. *Journal of Physical Oceanography*, 38:1965–1978.

Wunsch, C. and Ferrari, R. (2004). Vertical Mixing, Energy, and the General Circulation of the Oceans. *Annual Review of Fluid Mechanics*, 36(1):281–314.

Xu, Z. and Yin, B. (2016). Long - range propagation and associated variability of internal tides in the South China LR. *Journal Of Geophysical Research*, (November).

Zhao, Z., Alford, M., and Girton, J. (2012). Mapping Low-Mode Internal Tides from Multisatellite Altimetry. *Oceanography*, 25(2):42–51.

Zilberman, N. V., Becker, J. M., Merrifield, M. a., and Carter, G. S. (2009). Internal Tide Generation over Mid-Atlantic Ridge Topography. *Journal of Physical Oceanography*, 39(10):2635–2651.

Chapter 7

Conclusion

contents

7.1 Conclusion

The Indonesian archipelago is one of the most important reservoirs of marine biodiversity on the planet, which supports tremendous activities in fisheries, aquaculture and tourism. The need of monitoring and forcasting is thus vital. This challenging objective was made possible through the INDESO (Infrastructure Development of Space Oceanography) project funded by the Indonesian Ministry of Marine Affairs and Fisheries. It gives Indonesia a new system for the monitoring and management of its marine living resources. In this project, physical and biogeochemical coupled ocean models are used to constrain a tuna population dynamics model.

My thesis is part of this immense project, and focuses on the NEMO model, which was used to simulate the ocean circulation in the Indonesian Seas. The main objectives of my thesis is to investigate the origine and the fate of the tides produced by the model when it is force by explicit tidal forcing; and more particularly its mixing, its realism and its impact on water mass and on surface properties as they may in turn impact biogeochemical model and tuna distribution.

It has been already shown that introducing explicit tides in the model produce mixing that improves water masses in the Indonesian seas [Castruccio et al. (2013); Kartadikaria et al. (2011); Nagai and Hibiya (2015)]. What we don't know yet is precisely how much and how it happens in the model and how it compares to previous parameterization formulation [Koch-Larrouy et al. (2007)] or in-situ data [Koch-Larrouy et al. (2015)]. In this thesis the mixing induced by the explicit forcing of the tides in NEMO is quantified, both by comparing simulation with and without tides and by using specific diagnostics applied on a simple test case. When possible generation and dissipation energy are compared to the FES2014 model and to the previous parameterization and to in-situ observations.

I first contributed to a study that aimed at validating the INDESO ocean model (NEMO) against several observation data sets. In a second and third study, we investigated the mixing produced in the model by explicit tidal forcing and its impact on water mass. Overall, the mean circulation induced by the main equatorial and coastal currents (i.e. NGCC, SEC, NECC, SJC) is well reproduced by the INDESO ocean model. Except in coastal regions, the EKE from the model and the EKE derived from altimeter data share the same patterns. On both sides of the Luzon Strait, the weak EKE values from the model corroborates the weak SCSTF. The model estimations of complex elevation amplitudes (amplitude and phase) agree reasonably well with the TOPEX/POSEIDON, JASON 1 and JASON2 crossover observations, with better agreement for the diurnal constituents K1 than the semidiurnal constituent M2. These Amplitudes and Phases compare well with the hydrodynamic assimilated model FES2014 [Carrere et al. (2016)]. We note some biases for M2 over the Australian shelf and in the Pacific before entering Luzon Strait, as well as in Flores Sea and Makassar Strait, while for K1, the larger bias is mainly in the South China Sea. These biases are comparable to the one obtain by other studies with similar resolution [Kartadikaria et al. (2011)] at such resolution.

Also, the model reproduces qualitatively well the direction of propagation coming from Luzon, Sangihe and Sibuttu in Sulawesi Sea and Ombai strait when comparing to previous study [Jackson (2007); Wang et al. (2011, 2016)] using SAR images. This validation is only qualitative, since it does not allow to quantify how much energy is radiated away from the generation sites and validation using in-situ data, such as gliders or current meters or dedicated analysis of altimetry data, would be needed to properly validate the propagation of the internal tides in the model. In this thesis, we show, as previous studies [Castruccio et al. (2013); Kartadikaria et al. (2011); Nagai and Hibiya (2015)] that introducing internal tides improves the water mass transformation in the Indonesian Through Flow. In fact, we show that it produces results similar to those obtained with the dedicated parameterization constructed by Koch-Larrouy et al. (2007).

The salinity maximum of the Pacific Subtropical Water is eroded at almost the same rate for both PARAM and EXPL, and the model is able to reproduce at the exit of the archipelago the homohaline water characteristic of the Indonesian Water. It also produces a significant cooling of 0.3 °C with maxima of 0.8°C at the location of internal tides energy. The impact of this cooling is stronger during austral winter.

We then try to quantify the energy generation and dissipation associated to the tides. The model generates 75% of the expected internal tides energy (215 GW for NEMO and 295 GW calculated by the hydrodynamical model FES2014 with assimated data). This result is in good agreement with a previous study [Niwa and Hibiya (2011)].

In the archipelago, the dissipation due to the internal tides (22GW) for EXPL is in relative good agreement with PARAM (16 GW) may explain the very similar water mass transformation along the ITF path of both simulations. Most of it (85%) is dissipated by horizontal kinetic dissipation (19GW), while only 15% is dissipated through vertical shear. This result is anti-intuitive, since we would have expected that internal tides would dissipate through vertical shear. Finally, most of the dissipation occurs over (55%) or near (25%) generation sites, and only 20% remains for far field dissipation mainly in Banda and Sulawesi Sea. Over Spring tides, dissipation is 60 to 125% larger than the mean in the Luzon strait and Sulawesi Sea, whereas it has a smaller variation in the eastern part of the archipelago. The cycle of spring tides and neap tides produces modulate the surface cooling impact by 0.1°C to 0.3°C. Both climate and ecosystem may be sensitive to this cooling/upwelling at tidal frequencies.

The model dissipation agrees well with the spatial finestructure obtained by Ffield and Robertson (2008) for Ombai, Dewakang and Lifamatola straits, and Molucca and Flores seas. It is also in very good agreement with the recent INDOMIX microstructure estimates [Koch-Larrouy et al. (2015)], above the three straits measured (station St1, St3 and St5 of INDOMIX). However, the model produces too strong mixing in regions far away from the generation sites (Banda Sea) where INDOMIX and also Alford et al. (1999) found NO evidence of intensified mixing. Also, below 200m, in station St2 the model produces stronger mixing compared to the observation. These biases might come from the fact that the model doesn't have any specific set up to dissipate the internal tides once generated. More work has to be done in order to solve this problem.

I dedicated the last part of my thesis to the quantification of tidal energy sinks in NEMO. I first worked on a simple academic case: the COMODO internal tides test case, which analyses the behaviour of a vertically stratified fluid forced by a barotropic flow interacting over an idealized abyssal plain/slope/shelf topography without bottom friction. The results of the finite element T-UGOm hydrodynamic model are compared with those of NEMO. Internal tides are similar between the two models. The diffusion-free T-UGOm solutions are much noisier than NEMO ones, which reversely are somehow too smooth. For the latter, it seems that explicit diffusion plus some numerical implicit diffusion are responsible for NEMO smooth solutions.

The examination of the baroclinic energy flux in NEMO solution indicates a clear baroclinic energy decrease from the generation region (continental slope) toward the abyssal domain limit. The decrease of barotropic energy from the western open limit, both above the abyssal plain and shelf, is even more striking in a frictionless context. The cause of barotropic energy dissipation is not known, but might be linked to the time-splitting technique used in NEMO. In this last study, I participate to the development of an original method for separating barotropic and baroclinic tides based on the projection on vertical modes. Despite inherent limitations, mostly linked to linearization, vertical modes are a powerful tool to decompose and analyze internal tides simulations and to provide a deep insight in the model through time-averaged energy examination.

Proper vertical modes computation and model decomposition need a careful approach, as energy-related quantities are quite sensitive to numerical details. We have compared this separation approach with the usual depth-averaging approach. At first glance, differences are limited, the most significant being associated with energy quantities. For instance, depth-averaging technique is showing some unrealistic features in energy fluxes estimates, comparably to what was found in Kelly et al. (2010) investigations. While the modal separation diagnostics show the expected uniform barotropic and baroclinic fluxes above the abyssal plain (off the relaxation buffer zone), the depth-averaging separation diagnostics show anomalous (and compensating) oscillations that would lead to the conclusion that barotropic and baroclinic modes exchange energy in flat bottom conditions. There are no mechanisms to do so in T-UGOm (friction-less and diffusion-less) solutions. This is the sign that barotropic and baroclinic dynamics are not properly separated by depth-averaging separation.

Furthermore, this method opens the way to investigate more precisely the internal tides properties, this means not only offering a simple barotropic versus baroclinic separation but also a full modal separation. As length scales of modes spread on a great range, it allows examining not only the physical contents but also the numerical characteristics of models at those various length scale. As an example, it allows us to identify an important bias for NEMO: for mode 4 and 5 NEMO wavelengths are shorter that the ones from T-UGOm simulations. This is of some surprise, as diffusion could alter the horizontal wave-number, but not by increasing it (i.e. by shortening the horizontal wavelengths) but the reverse. This is an issue that would need further investigations in NEMO simulations. Thus, in the perspective of using energy budget to investigate numerical deficiencies, modal approach in contrast to averaging approach should be preferred as it is more physically consistent and more precise, despite increased complexity.

This precision will prove to be useful for the future SWOT mission.

7.2 Conclusion (in French)

L'archipel Indonésien est l'un des réservoirs de la biodiversité marine le plus important sur la Terre. Il permet de nombreuses activités liées à la pêche à l'aquaculture et au tourisme. Le besoin de surveiller et de prévoir les stocks est donc essentiel. Ce difficile objectif est rendu possible grâce au projet INDESO (Developpement de l'infrsactructure de l'océanographie spatiale). Ce projet est financé par le Ministère des affaires étrangères et des pêches Indonésien. Dans ce projet un système de modèles coupés physique et biogéochimique est utilisé pour forcé un modèle de dynamique de population de Thons.

Ma thèse fait partie de cet immense projet et se concentre sur le modèle NEMO, qui a été utilisé pour les simulations océaniques des mers Indonésiennes. Le principal objectif de ma thèse est de mieux comprendre l'origine et le devenir des ondes internes lorsque le modèle est forcé par la marée explicite, avec une attention particulière sur le mélange : son réalisme, son impact sur les masses d'eau et sur les propriétés de surface.

Il a déjà été montré, par de précédentes études qu'introduire le forçage de la marée explicite produit un mélange important qui permet d'améliorer les masses d'eau dans les mers Indonésiennes [Kartadikaria et al. (2011); Castruccio et al. (2013)]. Ce qui n'avait pas été étudié encore jusqu'à ce jour, était de savoir précisément comment cela a lieu dans le modèle et de le quantifier ainsi que le comparer avec la précédente paramétrisation [Koch-Larrouy et al. (2007)] ou les données in-situ [Koch-Larrouy et al. (2015)]. Dans cette thèse, nous quantifions le mélange induit par le forçage explicite de la marée dans NEMO en comparant des simulations sur la région Indonésienne avec et sans marée dans un premier temps et en utilisant des diagnostiques spécialement développés que nous avons testé dans un cas test idéalisé. Nous avons aussi comparé les énergies de génération et de dissipation au modèle hydrodynamique avec assimilation de données ainsi qu'à la paramétrisation et aux données in-situ.

Au début de ma thèse j'ai contribué à une étude visant à valider le modèle océanique d'INDESO grâce à plusieurs jeux de donnée. Dans une seconde et troisième étude le mélange induit par la marée explicite et son impact sur les masses d'eau a été étudié. De manière générale, la circulation moyenne induite par les principaux courants équatoriaux et côtiers (i.e. NGCC, SEC, NECC, SJC) est bien reproduite par le modèle INDESO. A part pour les régions côtières, l'Energie cinétique tourbillonnaire (EKE) est bien reproduite par le modèle en comparaison avec les données altimétriques. De part et d'autre du détroit de Luzon, les faibles valeurs de l'EKE du modèle sont cohérentes avec le SCSTF. Les amplitudes et phases des hauteur de mers sont en général bon accord avec données de point de croisement des altimètres TOPEX/POSEIDON, JASON 1 and JASON2, avec un meilleur accord pour la composante diurne de la marée K1 que pour la composant semi-diurne M2. Ces mêmes amplitudes et phases sont aussi en bon accord avec le modèle assimilé FES2014 [Carrere (2012)]. On note cependant un léger biais au dessus du talus continental Australien et dans l'océan Pacifique, en amont du détrit de Luzon, ainsi que la mer de Flores et le détroit de Makassar pour M2. Par ailleurs, pour K1 des biais plus importants se retrouvent principalement dans la mer de Chine. Ces biais restent comparables à ceux trouvés par les précédentes études effectuées sur la région avec les mêmes résolutions que celles que nous utilisons [Kartadikaria et al. (2011)].

Par ailleurs, le modèle reproduit bien de manière qualitative la direction de propagation des ondes internes induites par le forçage explicit de la marée qui partent des détroits de Luzon, Sibuttu ou Ombai ou de la chaine d'iles de Sangihe lorsque l'on compare aux études précédentes utilisant les données des images SAR [Jackson (2007); Wang et al. (2011, 2016)]. Cette validation n'est que qualitative car elle ne pemet pas de vérifier que la quantité d'énergie se propageant loin des sources de generation est en bon accord avec la réalité. Des données in-situ seraient nécessaires pour valider proprement la propagation des ondes créées induites par la prise en compte de la marée explicite dans le modèle. Dans cette thèse, comme dans de précédentes études [Kartadikaria et al. (2011); Castruccio et al. (2013); Nagai and Hibiya (2015)], l'on retrouve que la marée explicite produit un mélange considérable qui améliore les masses d'eau. Nous montrons ici qu'il s'agit en fait du même impact sur les masses d'eau que ceux produits par la paramétrisation [Koch-Larrouy et al. (2007)].

Le maximum de salinité des eaux subtropicales de l'océan Pacifique est érodé à la même vitesse pour EXPL et pour PARAM, qui sont capables de reproduire l'eau homogène en salinité caractéristique de l'eau Indonésienne. Un refroidissement de surface de 0.3°C est aussi trouvé avec des mamximas à 0.8°C au dessus des sites de génération. L'impact de ce refroidissement est plus fort en été austral. Nous avons cherché ensuite à quantifier l'énergie de génération et de dissipation associées à la marée. Le modèle génère 75% de l'énergie attendue associée aux ondes internes (215 GW pour NEMO and 295 GW calculée par le modèle hydrodynamic avec assimilation de données FES2014). Ce résultat est en parfait accord avec la précédente estimation de Niwa and Hibiya (2011).

Nous avons calculé que dans l'archipel Indonésien la dissipation due aux ondes internes (22GW) pour EXPL est en relativement bon accord avec PARAM (16GW), ce qui explique sûrement le bon accord pour la transformation des masses d'eau. La plupart (85%) est perdue par dissipation horizontale cinétique (19GW). Le reste (15%) est dissipé grâce au cisaillement vertical. Finalement, la plupart de la dissipation a lieu au dessus (55%) ou près (25%) des sites de génération avec 20% d'énergie se dissipant loin des sources de génération dans les mers de Banda et de Sulawesi. Pendant les vives eaux, la dissipation est plus forte de 60 à 125% que la moyenne sur le cycle dans le détroit de Luzon et dans la mer de Sulawesi. Les variations snot plus faibles dans l'est de l'archipel. Cette modulation lors du cycle des vives eaux/mortes eaux module aussi le refroidissement de surface par des valeurs entre 0.1 et 0.3°C. Il est certain que le climat et l'ensemble de l'écosystème doivent être sensibles à ces modulations à la fréquence de la marée.

La dissipation du modèle est en bon accord avec les estimation faites par Ffield and Robertson (2008) utilisant des données de finestructures qui prévoient une intensification du mélange pour les détroits de Ombai, Dewakang et Lifamatola ainsi que dans les mers de Molucca et Flores. Au dessus de zones de génération, le modèle est aussi en très bon accord avec les récents estimés issus de la campagne INDOMIX à partir de données de microstructures [Koch-Larrouy et al. (2015)]. Cependant, le modèle surestime le mélange par 2 ordre de grandeur dans les région plus loin des sites de génération comme par example dans Banda, où Alford et al. (1999) ne trouve pas de mélange significatif non plus, et sous 200 dans la mer d'Halmahera. Ces biais sont certainement le résultats du fait que le modèle ne contient aucune paramétrisation spécifique pour la dissipation des ondes internes de marée. Il sera important dans de futures études de travailler pour améliorer cette prise en compte.

J'ai consacré la dernière partie de ma thèse à la quantification précise des puits d'énergie dans NEMO. J'ai tout d'abord travaillé sur un cas test simplifié, le cas test de marée interne de COMODO qiu analyse le comportement d'un fluide stratifié forcé par la marée à la rencontre d'un talus continental. Le domaine est composé d'une plaine abyssale, d'un talus et d'un plateau. Les résultats du modèle hydrodynamique T-UGOm sont comparés avec ceux de NEMO. Les ondes internes de marée sont assez similaires dans les deux modèles. Le modèle T-UGOm qui est non diffusif fournit des solutions qui sont plus bruitées que NEMO. A l'inverse, les solutions de NEMO paraissent un peu trop diffuses. Pour ce dernier il apparaît que la diffusion explicite plus de la diffusion numérique implicite sont responsables pour les solutions très diffuses de NEMO. L'examination des flux d'energie barocline dans NEMO montrent une très claire perte d'énergie barocline depuis la zone de génération (le talus continental) jusqu'au dessus de la plaine abyssale. Par ailleurs, La marée barotrope perd aussi beaucoup d'énergie sur la plaine abyssale et sur le plateau, ce qui est d'autant plus intriguant que cette configuration n'a pas de friction. La raison ce la perte d'énergie barotrope n'est pas connue, mais l'on pourrait suspecter les techniques du découpage du schéma temporel pour les modes rapides (barotropes) et les modes lents (baroclines).

Dans cette dernière étude, j'ai participé au développement d'une méthode originale pour séparer la marée barotrope de la marée barocline, qui repose sur la projection des modes normaux. A part quelques limitations inhérentes à la méthode, principalement des hypothèse de linéarisation, les modes verticaux sont des outils puissants pour décomposer et analyser des simulations d'onde internes, car ils fournissent des détails précis lorsque l'on regarde l'énergie de la marée moyenne. Les énergies intégrées de la marée sont très sensibles aux calculs successifs de décomposition en modes propre et de bilan d'énergie. Par exemple, la méthode classique de séparation en utilisant la moyenne verticale, montre des résultats irréalistes dans le cas test COMODO, s'agissant des flux d'énergie, qui sont comparables aux résultats trouvés par Kelly and Nash (2010). En effet, la décomposition en mode normaux permet d'obtenir les flux uniformes de marées barotrope et barocline comme attendu, alor que la méthode de moyenne presente des oscillations compensées incorrectes qui pourraient faire croire à des échanges d'énergie entre le barotrope et le barocline dans la plaine abyssal en fond plat. C'est en fait le signe d'une mauvaise séparation par la méthode de la moyenne. Par ailleurs cette méthode nous permet de pousser plus loin les analyses en offrant une séparation modes par modes. Comme les échelles spatiales des modes couvrent un grand spectre de valeurs, cela permet d'examiner non seulement le contenu physique mais aussi les caractéristiques numériques des modèles sur ces différentes échelles spatiales. Par exemple, cela nous permet d'identifier un biais important pour NEMO qui reproduit des longueurs d'onde pour les modes élevés (4 et 5) qui sont trop courtes par rapport à T-UGOm. C'est assez surprenant car la diffusion peut réduire le nombre d'onde (et donc augmenter la longueur d'onde). Ce résultat ouvre la porte à de nouvelles recherches pour essayer de comprendre les raisons d'un tel comportement. Nous avons donc démontré que dans la perspective de réaliser des bilans d'énergie précis pour chercher les défauts numériques, la méthode utilisant les modes normaux est préférable à celle utilisant la moyenne sur la verticale. La précision que l'on aquièrera ainsi sera précieuse pour la future mission SWOT.

Chapter 8

Discussion/perspective

contents

8.1 Discussion/perspective

The first limitation of this study is the resolution of the model, which does not allow reproducing correctly the internal tides. As shown in Niwa and Hibiya (2011) and also found in this study, the model with 1/12° resolution is able of reproducing only 75% of the internal tides generation due to both insufficient resolution of the bathymetry slopes and of the tidal currents. Furthermore, once generated, the internal tides are dissipated by the model by parameterisations or numerical set up that are NOT specifically adapted to the physics of the tides, but rather to the larger scale processes or to eddy diffusivity. Thus it might not dissipate them as observed and produces unrealistic mixing. In reality, where internal waves dissipate and cause mixing is not really known. It is thought that non-linear wave-wave interactions and scattering when internal waves reflect off the ocean floor cause low vertical wavenumber modes to cascade to higher wavenumbers. At higher vertical wavenumbers, there is increased vertical shear and eventually a shear instability, and hence mixing, results. Of course OGCM are not able to correctly resolve this energy cascade.

Our results show that most of the dissipation in the model occurs through horizontal shear. This result is anti-intuitive, since we would have expected that internal tides would dissipate through vertical shear. We thus identify a significant bias of this model that may also be found in all general circulation models since actually there is no special care to take into account internal tides in such models.

On main conclusion is also of this thesis is that the model produces too much far-field dissipation (20%). Indeed, when comparing the model to the recent INDOMIX cruise, the model produces higher background mixing in Banda Sea, region where in reality no mixing as been found [Alford et al. (1999); Koch-Larrouy et al. (2015)], and below 200m in the inner Halmahera Sea.

In addition, we found also that the model produces too much mixing of the barotropic tides on a flat abyssal plain without friction in the COMODO test case and unrealistic wavelength at higher modes. Some work are in progress in order to quantify this energy budget using the method tested in the COMODO test case, over the entire INDESO domain with NEMO. Two other simulations forced only by the tides, with (INDESO barotropic test case) and with stratification (INDESO baroclinic test case) have been performed that are under analysis, as well as the INDESO simulation previously describe.

Our study offers at least few new clews of how to improve internal tides dissipation. In future research, work has to be done so that the dissipation occurs through vertical processes and at the right rate. We maybe need to established new parameterisation for the partially resolved internal tides. Knowing these limitations, we also show that the model reproduce part of the internal tides in qualitatively good agreement for its propagation (in Sulawesi) or its intensity, which is in surprising very good agreement in region of high mixing (at St1, St3 and St5 of INDOMIX stations). In addition, the water mass properties are well reproduced compare to observations. This model would be worth to use to study the impact of the tidal mixing and its variability on biogeochemical surface properties. Indeed, we show that they have an important impact on sea surface temperature. The results can be easily transposable for nutrients and biomass as shown in previous studies [eg: Franks and Chen (1996); Souza and Pineda (2001); da Silva et al. (2002); Jan and Chen (2009)] since the vertical mixing would upwell deeper layer richer in nutrients at the surface. Microscale turbulence maintains well-mixed biomass and nutrients within the turbulent surface boundary layer as well as driving nutrient fluxes into the mixed layer [e.g. Lewis et al. (1976)]. Also when the internal tides propagate it could generate vertical displacement of the base of the mixed layer that would produce blooms of phytoplankton, by periodically heaving biomass into the euphotic zone [da Silva et al. (2002); Holloway and Denman (1989)].

Finally, tidal fronts can also produce phytoplankton blooms [Franks and Chen (1996)]. We can thus assume that where the mixing is intensified and there is a surface cooling, this mixing would also modulate at annual, seasonal and intraseasonal timescale the nutrients enrichment of the surface layers. Also we can assume from figure 3 (in chapter 4) that the propagation of the internal tides will eventually produce blooms of phytoplankton along their route.

In future work, this study shows that it would be worth to improve the resolution and the representation of the dissipation of the internal tides in the model, as it may improve the realism of the tides, which are important for nutrients upwelling at mixing site, on propagation route of internal tides or at tidal front, as well as for connectivity (larvae transport) and diversity, which are sensitive to temperature and currents and thus the whole ecosystem chain. This may also be of some importance for generating better the submesoscales fronts as shown in Lévy et al. (2012).

8.2 Discussion/perspective (in French)

La première limitation de cette étude est la résolution du modèle, qui ne permet pas de reproduire la marée interne correctement. Comme précédemment montré par Niwa and Hibiya (2011) et que l'on retrouve dans cette thèse le modèle au 1/12° est capable de reproduire 75% de la génération attendue des ondes internes, à cause d'une résolution insufficante des pentes de la bathymétrie et des courants de marée. Par ailleurs, une fois générées, la marée interne est dissipée dans le modèles par des paramétrization ou par une représentation explicit du mélange qui ne prend pas en compte les modes rapides de la marée barotropes ni les spécificités de la marée barocline, mais plutôt adaptés à une physique plus grande échelle et plus lente. En conséquence, il n'y a aucune raison pour que le modèle produise une dissipation proche des observations. Dans la réalité, on pense que les interactions non linéaires ondes-ondes et la dispersion lors de la réflexion des ondes internes sur le fond marin pourrait forcer l'énergie contenue dans les faibles nombres d'onde à être transférer vers des nombres d'onde plus élevés. Et pour ces nombres d'ondes élevés, le cisaillement vertical est plus élevé ce qui peut provoquer des instabilités verticales et donc du mélange. Bien sûr les OGCMs ne sont pas capables de résoudre cette cascade d'énergie.

Nos résultats montrent que la plupart de la dissipation intérieure du modèle a lieu grâce à des processus de diffusion horizontale. Ce résultat est contre intuitif, car dans la réalité on s'attend à une marée interne qui se dissiperait grâce à des processus de cisaillement verticaux. Nous avons donc identifié une important biais du modèle qui pourrait aussi se retrouver dans d'autres OGCMs.

Une autre conclusion importante de ce travail de thèse est que le modèle produit trop de dissipatoin far field. (20%). En effet, dans les mers de Banda et d'Halmahera en comparant au résultats des données d'INDOMIX et d'une ancienne campagne [Alford et al. (1999); Koch-Larrouy et al. (2015)], le modèle montre un mélange résiduel trop fort alors que les sites de génération sont relativement éloignés.

De plus, nous avons quantifié dans le cas test COMODO, que le modèle produisait un mélange trop important qui erode la marée barotrope et barocline. Pour la marée barootrope c'est assez surprenant car il n'y a aucun processus physique permettant de l'expliquer, sur un fond plat. Un travail est en cours pour appliquer les outils de diagnostiques des flux d'énergie sur le domaine entier d'INDESO. Pour cela j'ai réalisé deux simulations supplémentaires forcées uniquement par la marée sans stratification (le cas test barotrope d'INDESO) et avec une stratification idéalisée (le cas test barocline d'INDESO).

Notre étude offre de nouvelles pistes de réflexions de comment améliorer le modèle en identifiant précisément ces biais. Bien sûr un long travail reste à faire pour améliorer le modèle grâce à de nouvelles paramétrisations ou formulations adaptées aux ondes internes. Malgré toutes ces limitations et ces biais identifiés, un autre résultat auquel on ne s'attendait pas, est que le modèle reproduit le mélange associé à la marée interne en très bon accord avec les observations in-situ dans les endroits de génération. De même, les masses d'eau sont en très bon accord avec les observations, ce qui donne confiance en le modèle (à part peut-être dans les mers intérieures) pour étudier l'impact de ce mélange et de sa variabilité sur les champs biogéochimiques. En effet l'impact que nous avons décrit sur le refroidissement de surface peut être facilement transposable au flux biogéochimiques de nutriment ou de biomasse comme montré dans d'autres études (e.g.: Franks and Chen (1996); Souza and Pineda (2001); da Silva et al. (2002); Jan and Chen (2009) . En effet le mélange à la base de la couche de mélange peut apporter en surface les nutriments présents dans les couches plus profondes en surface. La turbulence de microéchelle permet de maintenir la biomasses et les nutriments dans la couche de mélange bien homogène ainsi que les flux vers la couche de mélange [e.g. Lewis et al. (1976)]. De plus quand les ondes internes se propagent, elle peuvent générer un déplacement vertical à la base de la couche de mélange qui peut produire des floraison printanière de phytoplancton, grâce à des incursion périodiques de biomasse dans la couche euphotique zone [da Silva et al. (2002); Holloway and Denman (1989)].

Il est donc légitime de s'attendre à ce que partout où nous avons trouvé un fort mélange et un refroidissement important en surface induit par la marée, ce mélange puisse aussi moduler à des échelles annuelle, saisonnière et intrsaisonnière (spring/neap tides) les flux biogéochimiques. On peut aussi faire l'hypothèse que lorsque le modèle reproduit une propagation des ondes internes, celle-ci pourrait produire des floraisons printanière le long du chemin de propagation. On peut-être imaginer qu'en validant la couleur de l'eau le long de ces chemins de propagation on puisse avoir une autre validation (ou infirmation) de la quantité d'énergie se propageant au loin. Mais ce dernier point est aussi sensible à beaucoup d'autres paramètres du modèle.

Dans des travaux futures, cette étude montre qu'il sera important de tester ces résultats à plus haute résolution, et d'avoir des études dédiées pour l'amélioration de la prise en compte de la dissipation de la marée dans NEMO. En effet ce dernier point pourrait améliorer le réalisme de la marée dans le modèle qui important pour les flux verticaux de nutriment, le long de la propagation et dans les front de marée, ainsi que pour la connectivité (transport des larves) et diversité, qui sont eux même sensibles aux températures et aux courants et donc pourrait avoir une influence sur toute la chaine de l'écosystème. La résolution peut aussi avoir un impact direct sur la meilleure représentation de fronts de sub-mesoéchelle [Lévy et al. (2012)].

Bibliography

Aiki, H., Matthews, J. P., and Lamb, K. G. (2011). Modeling and energetics of tidally generated wave trains in the Lombok Strait: Impact of the Indonesian Throughflow. *Journal of Geophysical Research: Oceans*, 116(3):1–17.

Aldrian, E. and Dwi Susanto, R. (2003). Identification of three dominant rainfall regions within Indonesia and their relationship to sea surface temperature. *International Journal of Climatology*, 23(12):1435–1452.

Alford, M. H., Gregg, M. C., and Ilyas, M. (1999). Diapycnal mixing in the Banda Sea: Results of the first microstructure measurements in the Indonesian Throughflow. *Geophysical Research Letters*, 26(17):2741.

Alford, M. H., MacKinnon, J. a., Nash, J. D., Simmons, H., Pickering, A., Klymak, J. M., Pinkel, R., Sun, O., Rainville, L., Musgrave, R., Beitzel, T., Fu, K.-H., and Lu, C.-W. (2011). Energy Flux and Dissipation in Luzon Strait: Two Tales of Two Ridges. *Journal of Physical Oceanography*, 41(11):2211–2222.

Alford, M. H., Peacock, T., MacKinnon, J. a., Nash, J. D., Buijsman, M. C., Centuroni, L. R., Chao, S.-Y., Chang, M.-H., Farmer, D. M., Fringer, O. B., Fu, K.-H., Gallacher, P. C., Graber, H. C., Helfrich, K. R., Jachec, S. M., Jackson, C. R., Klymak, J. M., Ko, D. S., Jan, S., Johnston, T. M. S., Legg, S., Lee, I.-H., Lien, R.-C., Mercier, M. J., Moum, J. N., Musgrave, R., Park, J.-H., Pickering, A. I., Pinkel, R., Rainville, L., Ramp, S. R., Rudnick, D. L., Sarkar, S., Scotti, A., Simmons, H. L., St Laurent, L. C., Venayagamoorthy, S. K., Wang, Y.-H., Wang, J., Yang, Y. J., Paluszkiewicz, T., and (David) Tang, T.-Y. (2015). The formation and fate of internal waves in the South China Sea. *Nature*, 521(7550):65–69.

Allen, G. R. and Werner, T. B. (2002). Coral reef fish assessment in the 'coral traingle' of Southeastern Asia. *Environmental Biology of Fishes*, 65:209–214.

Arbic, B. K., Richman, J. G., Shriver, J. F., Timko, P. G., Metzger, E. J., and Wallcraft, A. J. (2012). Global modeling of internal tides within an eddying ocean general circulation model. *Oceanography*, 25(2):20–29.

Arbic, B. K., Wallcraft, A. J., and Metzger, E. J. (2010). Concurrent simulation of the eddying general circulation and tides in a global ocean model. *Ocean Modelling*, 32(3-4):175–187.

Aumont, O. (2004). PISCES biogeochemical model WARNING : This document is not intended to be an exhaustive description of PISCES and is still incomplete. pages 1–16.

Baines, P. (1982). On internal tide generation models. *Deep Sea Research Part A. Oceanographic Research Papers*, 29(3):307–338.

Baines, P. G. (1973). The generation of internal tides by fiat-bump topography. 20(February 1972):179–205.

Buijsman, M., Arbic, B., Green, J., Helber, R., Richman, J., Shriver, J., Timko, P., and Wallcraft, a. (2015). Optimizing internal wave drag in a forward barotropic model with semidiurnal tides. *Ocean Modelling*, 85:42–55.

Carrere, L. (2012). A new global tidal model taking taking advantage of nearly 20 years of altimetry. *Proceedings of meeting "20 Years of Altimetry"*.

Carrere, L., Lyard, F., Cancet, M., Guillot, A., and Picot, N. (2016). FES 2014, a new tidal model - Validation results and perspectives for improvements, presentation to ESA Living Planet Conference. Technical report, Prague.

Carter, G., Fringer, O., and Zaron, E. (2012). Regional Models of Internal Tides. *Oceanography*, 25(2):56–65.

Carter, G. S., Merrifield, M. a., Becker, J., and Gregg, M. C. (2008). Energetics of M 2 Barotropic to Baroclinic tidal conversion at the Hawaiian Islands. *Journal of Physical Oceanography*, 38:2205–2223.

Castruccio, F. S., Curchitser, E. N., and Kleypas, J. a. (2013). A model for quantifying oceanic transport and mesoscale variability in the Coral Triangle of the Indonesian/Philippines Archipelago. *Journal of Geophysical Research: Oceans*, 118(11):6123–6144.

Chang, C. P., Wang, Z., McBride, J., and Liu, C. H. (2005). Annual cycle of Southeast Asia - Maritime continent rainfall and the asymmetric monsoon transition. *Journal of Climate*, 18(2):287–301.

Chao, S.-Y., Ko, D. S., Lien, R.-C., and Shaw, P. T. (2007). Assessing the West Ridge of Luzon Strait as an Internal. *Journal of Oceanography*, 63(2004):897–911.

Clement, A. C., Seager, R., and Murtugudde, R. (2005). Why are there tropical warm pools? *Journal of Climate*, 18(24):5294–5311.

da Silva, J., New, A., Srokosz, M., and Smyth, T. (2002). On the observability of internal tidal waves in remotely-sensed ocean colour data. *Geophysical Research Letters*, 29(12):10–13.

Eden, C., Czeschel, L., and Olbers, D. (2014). Toward Energetically Consistent Ocean Models. *Journal of Physical Oceanography*, 44(12):3160–3184.

Egbert, G. D. and Erofeeva, S. Y. (2002). Efficient inverse modeling of barotropic ocean tides. *Journal of Atmospheric and Oceanic Technology*, 19(2):183–204.

Egbert, G. D. and Ray, R. D. (2001). Estimates of \mathrm{M_2} tidal energy dissipation from {TOPEX/Poseidon} altimeter data. *J. Geophys. Res.*, 106(C10):22,422–475,502.

Ffield, A. and Gordon, A. L. (1992). Vertical Mixing in the Indonesian Thermocline.

Ffield, A. and Gordon, A. L. (1996). Tidal Mixing Signatures in the Indonesian Seas.

Ffield, A. and Robertson, R. (2008). Temperature finestructure in the Indonesian seas. *Journal of Geophysical Research: Oceans*, 113(9):1–19.

Fieux, M., Andrié, C., Delecluse, P., Ilahude, A. G., Kartavtseff, A., Mantisi, F., Molcard, R., and Swallow, J. C. (1994). Measurements within the Pacific-Indian oceans throughflow region. *Deep-Sea Research Part I*, 41(7):1091–1130.

Franks, P. J. and Chen, C. (1996). Plankton production in tidal fronts: A model of Georges Bank in summer. *Journal of Marine Research*, 54(4):631–651.

Gerkema, T. and van Haren, H. (2007). Internal tides and energy fluxes over Great Meteor Seamount. *Ocean Science Discussions*, 4:371–398.

Godfrey, J. S. (1996). The effect of the Indonesian throughflow on ocean circulation and heat exchange with the atmosphere: A review. *Journal of Geophysical Research*, 101(C5):12217.

Gordon, A. (2005). Oceanography of the Indonesian Seas. *Oceanography*, 18(4):13–13.

Gordon, A. L. (1986). Interocean exchange of thermocline water. *J. Geophys. Res.*, 91(6):5037–5046.

Gordon, A. L. and Fine, R. a. (1996). Pathways of water between the Pacific and Indian oceans in the Indonesian seas.

Gordon, A. L., Giulivi, C. F., and Ilahude, A. G. (2003). Deep topographic barriers within the Indonesian seas. *Deep-Sea Research Part II: Topical Studies in Oceanography*, 50(12-13):2205–2228.

Gordon, a. L., Sprintall, J., Van Aken, H. M., Susanto, D., Wijffels, S., Molcard, R., Ffield, a., Pranowo, W., and Wirasantosa, S. (2010). The Indonesian throughflow during 2004-2006 as observed by the INSTANT program. *Dynamics of Atmospheres and Oceans*, 50(2):115–128.

Hatayama, T. (2004). Transformation of the Indonesian throughflow water by vertical mixing and its relation to tidally generated internal waves. *Journal of Oceanography*, 60(3):569–585.

Hautala, S. L., Sprintall, J., Potemra, J. T., Chong, J. C., Pandoe, W., Bray, N., and Ilahude, a. G. (2001). Velocity structure and transport of the Indonesian Throughflow in the major straits restricting flow into the Indian Ocean. *Journal of Geophysical Research*, 106(C9):19527.

Holloway, G. and Denman, K. (1989). Influence of internal waves on primary production. *Journal of Plankton Research*, 11(2):409–413.

Holloway, P. E. (1996). A Numerical Model of Internal Tides with Application to the Australian North West Shelf.

Jackson, C. (2007). Internal wave detection using the Moderate Resolution Imaging Spectroradiometer MODIS. *Journal of Geophysical Research*, 112(C11):C11012.

Jan, S. and Chen, C. T. A. (2009). Potential biogeochemical effects from vigorous internal tides generated in Luzon Strait: A case study at the southernmost coast of Taiwan. *Journal of Geophysical Research: Oceans*, 114(4):1–14.

Jan, S., Chern, C. S., Wang, J., and Chao, S. Y. (2007). Generation of diurnal K1 internal tide in the Luzon Strait and its influence on surface tide in the South China Sea. *Journal of Geophysical Research: Oceans*, 112(6):1–13.

Jan, S., Lien, R. C., and Ting, C. H. (2008). Numerical study of baroclinic tides in Luzon Strait. *Journal of Oceanography*, 64(5):789–802.

Jeon, C., Park, J.-h., Varlamov, S. M., Yoon, J.-h., Kim, Y. H., Seo, S., Park, Y.-g., Min, H. S., Lee, J. H., and Kim, C.-h. (2014). Journal of Geophysical Research : Oceans. *Journal of Geophysical Research: Oceans*, 119:2843–2859.

Jochum, M. and Potemra, J. (2008). Sensitivity of tropical rainfall to Banda Sea diffusivity in the Community Climate System Model. *Journal of Climate*, 21(23):6445–6454.

Johnston, T. M. S., Rudnick, D. L., Alford, M. H., Pickering, A., and Simmons, H. L. (2013). Internal tidal energy fluxes in the South China Sea from density and velocity measurements by gliders. *JOURNAL OF GEOPHYSICAL RESEARCH: OCEANS*, 118:3939–3949.

Jouanno, J., Capet, X., Madec, G., Roullet, G., Klein, P., and Masson, S. (2016). Dissipation of the energy imparted by mid-latitude storms in the\r\nSouthern Ocean. *Ocean Science Discussions*, pages 1–49.

Kang, D. (2010). Energetics and Dynamics of Internal Tides in Monterey Bay Using Numerical Simulations a Dissertation Submitted To the Department of Civil and Environmental Engineering and the Committee on Graduate Studies of Stanford University in Partial Fulfillment of. (November):170.

Kang, D. and Fringer, O. (2012a). Energetics of Barotropic and Baroclinic Tides in the Monterey Bay Area. *Journal of Physical Oceanography*, 42(2):272–290.

Kang, D. and Fringer, O. (2012b). Energetics of Barotropic and Baroclinic Tides in the Monterey Bay Area. *Journal of Physical Oceanography*, 42(2):272–290.

Kartadikaria, a. R., Miyazawa, Y., Varlamov, S. M., and Nadaoka, K. (2011). Ocean circulation for the Indonesian seas driven by tides and atmospheric forcings: Comparison to observational data. *Journal of Geophysical Research: Oceans*, 116(9):1–21.

Kawamura, R. and Matsuura, T. (2003). A mechanism of the onset of the South Asian summer monsoon. 81:563–580.

Kelly, S. M. and Nash, J. D. (2010). Internal-tide generation and destruction by shoaling internal tides. *Geophysical Research Letters*, 37(23):1–5.

Kelly, S. M. and Nash, J. D. (2011). Reply to comment by T. Gerkema on “Internal-tide energy over topography”. *Journal of Geophysical Research*, 116(C9):2010–2012.

Kelly, S. M., Nash, J. D., and Kunze, E. (2010). Internal-tide energy over topography. *Journal of Geophysical Research: Oceans*, 115(6):1–13.

Kelly, S. M., Nash, J. D., Martini, K. I., Alford, M. H., and Kunze, E. (2012). The Cascade of Tidal Energy from Low to High Modes on a Continental Slope. *Journal of Physical Oceanography*, 42(7):1217–1232.

Kerry, C. G., Powel, B. S., and Carter, G. S. (2013). Effects of Remote Generation Sites on Model Estimates of M 2 Internal Tides in the Philippine Sea *. pages 187–204.

Khatiwala, S. (2003). Generation of internal tides in an ocean of finite depth: Analytical and numerical calculations. *Deep-Sea Research Part I: Oceanographic Research Papers*, 50(1):3–21.

Kida, S. and Richards, K. J. (2009). Seasonal sea surface temperature variability in the Indonesian Seas. *Journal of Geophysical Research: Oceans*, 114(6):1–17.

Kida, S. and Wijffels, S. (2012). The impact of the Indonesian Throughflow and tidal mixing on the summertime sea surface temperature in the western Indonesian Seas. *Journal of Geophysical Research: Oceans*, 117(9):1–14.

Koch-Larrouy, A., Atmadipoera, A., van Beek, P., Madec, G., Aucan, J., Lyard, F., Grelet, J., and Souhaut, M. (2015). Estimates of tidal mixing in the Indonesian archipelago from multidisciplinary INDOMIX in-situ data. *Deep-Sea Research Part I: Oceanographic Research Papers*, 106:136–153.

Koch-Larrouy, A., Lengaigne, M., Terray, P., Madec, G., and Masson, S. (2010). Tidal mixing in the Indonesian seas and its effect on the tropical climate system. *Climate Dynamics*, 34(6):891–904.

Koch-Larrouy, A., Madec, G., Bouruet-Aubertot, P., Gerkema, T., Bessières, L., and Molcard, R. (2007). On the transformation of Pacific Water into Indonesian Throughflow Water by internal tidal mixing. *Geophysical Research Letters*, 34(4):1–6.

Koch-Larrouy, A., Madec, G., Iudicone, D., Atmadipoera, A., and Molcard, R. (2008). Physical processes contributing to the water mass transformation of the Indonesian throughflow. *Ocean Dynamics*, 58(3-4):275–288.

Kundu, P., Cohen, M. I., and Hu, H. H. (2004). *Fluid mechanics*. Elsevier Academic Press, Amsterdam.

Kunze, E., Rosenfeld, L. K., Carter, G. S., and Gregg, M. C. (2002). Internal Waves in Monterey Submarine Canyon. *Journal of Physical Oceanography*, 32(6):1890–1913.

Kurapov, A. L., Egbert, G. D., Allen, J. S., Miller, R. N., Erofeeva, S. Y., and Kosro, P. M. (2003). The M 2 Internal Tide off Oregon: Inferences from Data Assimilation. *Journal of Physical Oceanography*, 33(8):1733–1757.

Large, W. G. and Yeager, S. G. (2004). Diurnal to decadal global forcing for ocean and sea–ice models: {The} data sets and flux climatologies. *NCAR Tech. Note*, TN–460+ST(May):105pp.

Le Provost, C. (2003). Ocean tides after a decade of high precision satellite altimetry. *Presentation in Swt JASON 1, Arles November 18-21.*

Lee, T., Fukumori, I., Menemenlis, D., Xing, Z., and Fu, L.-L. (2002). Effects of the Indonesian Throughflow on the Pacific and Indian Oceans. *Journal of Physical Oceanography*, 32(5):1404–1429.

Lehodey, P., Senina, I., and Murtugudde, R. (2008). A spatial ecosystem and populations dynamics model (SEAPODYM) - Modeling of tuna and tuna-like populations. *Progress in Oceanography*, 78(4):304–318.

Lévy, M., Ferrari, R., Franks, P. J. S., Martin, A. P., and Rivière, P. (2012). Bringing physics to life at the submesoscale. *Geophysical Research Letters*, 39(14).

Lewis, M. R., Glen Harrison, W., Oakey, Neil, S., Hebert, D., and Platt, T. (1976). Vertical Nitrate Fluxes in the Oligotrophic Ocean. *Science*, 234:870–873.

Lorenzo, E. D. (2006). Numerical and analytical estimates of M 2 tidal conversion at steep oceanic ridges. *Journal of physical . . .* , (2001):1072–1084.

Lu, Y., Wright, D. G., and Brickman, D. (2001). Internal tide generation over topography: Experiments with a free-surface z-level ocean model. *Journal of Atmospheric and Oceanic Technology*, 18(6):1076–1091.

Lukas, R., Yamagata, T., and McCreary, J. (1996). Pacific low-latitude western boundary currents and the Indonesian throughflow. *Journal of Geophysical Research C: Oceans*, 101(5):12209–12216.

Lyard, F., Carrere, L., Cancet, M., and Guillot, A. (2017). FES2014, a new finite elements tidal model for global ocean. *Ocean Dynamics,in preparation.*

Lyard, F., Lefevre, F., Letellier, T., and Francis, O. (2006). Modelling the global ocean tides: Modern insights from FES2004. *Ocean Dynamics*, 56(5-6):394–415.

Lyard, F., Roblou, L., and Allain, D. (2012). FES 2012, 4th PROJECT MEETING. Technical report, LEGOS, Toulouse.

Madec, G. (2008). NEMO ocean engine. (27).

Maraldi, C., Lyard, F., Testut, L., and Coleman, R. (2011). Energetics of internal tides around the Kerguelen Plateau from modeling and altimetry. *Journal of Geophysical Research: Oceans*, 116(6):1–10.

Matthews, J. P., Aiki, H., Masuda, S., Awaji, T., and Ishikawa, Y. (2011). Monsoon regulation of Lombok Strait internal waves. *Journal of Geophysical Research: Oceans*, 116(5):1–14.

Mattias Green, J. a. and Nycander, J. (2012). A comparison of tidal conversion parameterizations for tidal models. *Journal of Physical Oceanography*, (2004):121015111501009.

Melet, A., Nikurashin, M., Muller, C., Falahat, S., Nycander, J., Timko, P. G., Arbic, B. K., and Goff, J. a. (2013). Internal tide generation by abyssal hills using analytical theory. *Journal of Geophysical Research: Oceans*, 118(11):6303–6318.

Meyers, G. (1996). Variation of Indonesian throughflow and the El Niño-Southern Oscillation. *Journal of Geophysical Research: Oceans*, 101(C5):12255–12263.

Mitnik, L., Alpers, W., and Hock, L. (2000). Thermal plumes and internal solitary waves generated in the Lombok strait studied by ERS SAR. *European Space Agency, (Special Publication) ESA SP*, (461):1834–1842.

Molcard, R., Fieux, M., and Syamsudin, F. (2001). The throughflow within Ombai Strait. *Deep-Sea Research Part I: Oceanographic Research Papers*, 48(5):1237–1253.

Moore, S. E. and Lien, R.-C. (2007). Pilot Whales Follow Internal Solitary Waves. *Marine Mammal Science*, 23(January):193–196.

Mora, C., Chittaro, P. M., Sale, P. F., Kritzer, J. P., Ludsin, S. a., and Africa, S. (2003). Patterns and processes in reef fish diversity. *Nature*, 421(February):933–936.

Muller, M., Cherniawsky, J. Y., Foreman, M. G. G., and Von Storch, J. S. (2012a). Global M 2 internal tide and its seasonal variability from high resolution ocean circulation and tide modeling. *Geophysical Research Letters*, 39(19):L19607.

Muller, M., Cherniawsky, J. Y., Foreman, M. G. G., and Von Storch, J. S. (2012b). Global M 2 internal tide and its seasonal variability from high resolution ocean circulation and tide modeling. *Geophysical Research Letters*, 39(19):1–6.

Murray, S. P. and Arief, D. (1988). Throughflow into the Indian Ocean through the Lombok Strait, January 1985–January 1986. *Nature*, 333(6172):444–447.

Nagai, T. and Hibiya, T. (2015). Internal tides and associated vertical mixing in the Indonesian Archipelago. *Journal of Geophysical Research C: Oceans*, pages 3373–3390.

Neale, R. and Slingo, J. (2003). The Maritime Continent and its role in the global climate: A GCM study. *Journal of Climate*, 16(5):834–848.

Niwa, Y. (2004). internal tides in the East China Sea. *Journal of Geophysical Research*, 109(C4):1–14.

Niwa, Y. and Hibiya, T. (2001a). Numerical study of the spatial distribution of the M 2 internal tide in the Pacific Ocean. 106.

Niwa, Y. and Hibiya, T. (2001b). Numerical study of the spatial distribution of the M2 internal tide in the Pacific Ocean. *Journal of Geophysical Research*, 106:22441–22449.

Niwa, Y. and Hibiya, T. (2011). Estimation of baroclinic tide energy available for deep ocean mixing based on three-dimensional global numerical simulations. *Journal of Oceanography*, 67(4):493–502.

Niwa, Y. and Hibiya, T. (2014). Generation of baroclinic tide energy in a global three-dimensional numerical model with different spatial grid resolutions. *Ocean Modelling*, 80:59–73.

Nugroho, D., Koch-Larrouy, A., Gaspar, P., Lyard, F., Reffray, G., and Tranchant, B. (2017). Modelling Explicit tides in the Indonesian seas : an important process for surface sea water properties, in revision. *Submitted to Marine Pollution Bulletin.*

Park, J.-h. and Watts, D. R. (2005). Internal Tides in the Southwestern Japan / East Sea. pages 1–37.

Pichon, A. and Maze, R. (1990). Internal Tides over a Shelf Break: Analytical Model And Observations. *American Meteorological Society*, pages 657–671.

Potemra, J. T. (1999). Seasonal Variations of Upper Ocean Transport from the Pacific to the Indian Ocean via Indonesian Straits*. *Journal of Physical Oceanography*, 29(11):2930–2944.

Rainville, L., Lee, C. M., Rudnick, D. L., and Yang, K. C. (2013). Propagation of internal tides generated near Luzon Strait: Observations from autonomous gliders. *Journal of Geophysical Research: Oceans*, 118(9):4125–4138.

Ramp, S. R., Tang, T. Y., Duda, T. F., Lynch, J. F., Liu, A. K., Chiu, C. S., Bahr, F. L., Kim, H. R., and Yang, Y. J. (2004). Internal solitons in the northeastern South China Sea Part I: Sources and deep water propagation. *IEEE Journal of Oceanic Engineering*, 29(4):1157–1181.

Ray, R., Egbert, G., and Erofeeva, S. (2005). A Brief Overview of Tides in the Indonesian Seas. *Oceanography*, 18(4):74–79.

Robertson, R. (2010). Tidal currents and mixing at the INSTANT mooring locations. *Dynamics of Atmospheres and Oceans*, 50(2):331–373.

Robertson, R. and Ffield, A. (2005). M2 Baroclinic Tides in the Indonesian Seas. *Oceanography*, 18(4):62–73.

Robertson, R. and Ffield, A. (2008). Baroclinic tides in the Indonesian seas: Tidal fields and comparisons to observations. *Journal of Geophysical Research: Oceans*, 113(7):1–22.

Sari Ningsih, N. (2008). INTERNAL WAVES DYNAMICS IN THE LOMBOK STRAIT STUDIED BY A NUMERICAL MODEL. *International Journal Of Remote Sensing And Earth Sciences*, 5.

Sasaki, H., Sasai, Y., Nonaka, M., Masumoto, Y., and Kawahara, S. (2006). An Eddy-Resolving Simulation of the Quasi-Global Ocean Driven by Satellite-Observed Wind Field – Preliminary Outcomes from Physical and Biological Fields –. *Journal of the Earth Simulator*, 6(October):35–49.

Schiller, A. (2004). Effects of explicit tidal forcing in an OGCM on the water-mass structure and circulation in the Indonesian throughflow region. *Ocean Modelling*, 6(1):31–49.

Shang, X., Liu, Q., Xie, X., Chen, G., and Chen, R. (2015). Deep-Sea Research I Characteristics and seasonal variability of internal tides in the southern South China Sea. *Deep-Sea Research Part I*, 98:43–52.

Shriver, J. F., Arbic, B. K., Richman, J. G., Ray, R. D., Metzger, E. J., Wallcraft, a. J., and Timko, P. G. (2012). An evaluation of the barotropic and internal tides in a high-resolution global ocean circulation model. *Journal of Geophysical Research: Oceans*, 117(10):1–14.

Simmons, H. L., Hallberg, R. W., and Arbic, B. K. (2004). Internal wave generation in a global baroclinic tide model. *Deep-Sea Research Part II: Topical Studies in Oceanography*, 51(25-26 SPEC. ISS.):3043–3068.

Song, Q. and Gordon, A. L. (2004). Significance of the vertical profile of the Indonesian Throughflow transport to the Indian Ocean. *Geophysical Research Letters*, 31(16).

Souza, A. J. and Pineda, J. (2001). Tidal mixing modulation of sea-surface temperature and diatom abundance in Southern California. *Continental Shelf Research*, 21(6-7):651–666.

Sprintall, J., Gordon, A. L., Koch-Larrouy, A., Lee, T., Potemra, J. T., Pujiana, K., Wijffels, S. E., and Wij, S. E. (2014). The Indonesian seas and their role in the coupled ocean–climate system. *Nature Geoscience*, 7(7):487–492.

Sprintall, J., Wijffels, S. E., Molcard, R., and Jaya, I. (2009). Direct estimates of the indonesian throughflow entering the indian ocean: 2004-2006. *Journal of Geophysical Research: Oceans*, 114(7):2004–2006.

St. Laurent, L. and Garrett, C. (2002). The Role of Internal Tides in Mixing the Deep Ocean. *Journal of Physical Oceanography*, 32(10):2882–2899.

Susanto, R. D. and Gordon, A. L. (2005). Velocity and transport of the Makassar Strait throughflow. *Journal of Geophysical Research: Oceans*, 110(1):1–10.

Susanto, R. D., Mitnik, L., and Zheng, Q. (2005). Ocean Internal Waves Observed in the Lombok Strait. *Oceanography*, 18(4):80–87.

Talley, L. D. and Sprintall, J. (2005). Deep expression of the Indonesian Throughflow: Indonesian Intermediate Water in the South Equatorial Current. *Journal of Geophysical Research C: Oceans*, 110(10):1–30.

Tranchant, B., Reffray, G., Greiner, E., Nugroho, D., Koch-Larrouy, A., and Gaspar, P. (2016). Evaluation of an operational ocean model configuration at 1/12 spatial resolution for the Indonesian seas . Part I : ocean physics. pages 1–49.

Umlauf, L. and Burchard, H. (2003). A generic length-scale equation for geophysical. *Journal of Marine Research*, 61(2):235–265.

van Aken, H. M., Brodjonegoro, I. S., and Jaya, I. (2009). The deep-water motion through the Lifamatola Passage and its contribution to the Indonesian throughflow. *Deep-Sea Research Part I: Oceanographic Research Papers*, 56(8):1203–1216.

Veron, J., Devantier, L. M., Turak, E., Green, A. L., Kininmonth, S., Stafford-Smith, M., and Peterson, N. (2009). Delineating the Coral Triangle. *Galaxea, Journal of Coral Reef Studies*, 11(2):91–100.

Vranes, K., Gordon, A. L., and Ffield, A. (2002). The heat transport of the Indonesian throughflow and implications for the Indian Ocean heat budget. *Deep-Sea Research Part II: Topical Studies in Oceanography*, 49(7-8):1391–1410.

Wang, J., Huang, W., Yang, J., and Zhang, H. (2011). The internal waves' distribution of whole South China Sea extracted from ENVISAT and ERS-2 SAR images. *Proceedings of SPIE - The International Society for Optical Engineering*, 8175:1–7.

Wang, X., Peng, S., Liu, Z., Huang, R. X., Qian, Y.-K., and Li, Y. (2016). Tidal Mixing in the South China Sea: An Estimate Based on the Internal Tide Energetics. *Journal of Physical Oceanography*, 46(1):107–124.

Wijffels, S. (2012). The impact of the Indonesian Throughflow and tidal mixing on the Seasonal Cycle of the Sea Surface Temperature in the Indonesian Seas Why Study the SST in the Indonesian Seas ? The role of Tidal mixing The role of the Indonesian Throughflow (ITF). (July 2012):6016.

Wijffels, S. E., Meyers, G., and stuart Godfrey, J. (2008). A 20-Yr Average of the Indonesian Throughflow: Regional Currents and the Interbasin Exchange. *Journal of Physical Oceanography*, 38:1965–1978.

Wunsch, C. and Ferrari, R. (2004). Vertical Mixing, Energy, and the General Circulation of the Oceans. *Annual Review of Fluid Mechanics*, 36(1):281–314.

Xu, Z. and Yin, B. (2016). Long - range propagation and associated variability of internal tides in the South China LR. *Journal Of Geophysical Research*, (November).

Zhao, Z., Alford, M., and Girton, J. (2012). Mapping Low-Mode Internal Tides from Multisatellite Altimetry. *Oceanography*, 25(2):42–51.

Zilberman, N. V., Becker, J. M., Merrifield, M. a., and Carter, G. S. (2009). Internal Tide Generation over Mid-Atlantic Ridge Topography. *Journal of Physical Oceanography*, 39(10):2635–2651.